# Chemiresistive Percolation Sensors Based on Conjugated Polymers

*A thesis submitted for the degree of Doctor of Philosophy*




**Weishuo Li**

St Anne's College

Department of Materials, University of Oxford

Supervised by

Professor Martin R. Castell

Trinity Term 2023

# Preface

The research work described in this thesis was carried out by the author, under the supervision of Prof. Martin R. Castell, at the Department of Materials at the University of Oxford, from October 2019 to June 2023. All the work is original and has not been previously submitted for any degree or qualification at this university or any other institute of education. Where the work of other researchers is drawn upon, it has been referenced and acknowledged. Parts of the work described in Chapters 4, 5, and 6 have been presented at international conferences and/or published in peer-reviewed journals as follows:

***Conferences***

**Weishuo Li**, Yu Wang, Liren Wang, Abigail M. Lister and Martin R. Castell. "Resistive sensors based on PEDOT/PS nanocomposites: site percolation and multifunctional sensing", **ACS Spring 2023 National Meeting & Exposition**, American Chemical Society, Indianapolis, U.S.A., 2023. (Poster)

**Weishuo Li**, Merel J. Lefferts, Yu Wang, Abigail M. Lister and Martin R. Castell. "Chemiresistive polymer percolation network gas sensor created with a nanosphere template", **Electrochem 2022 & 63rd Corrosion Science Symposium**, Royal Society of Chemistry, Edinburgh, U.K., 2022. (Poster)

**Weishuo Li**, Merel J. Lefferts, Abigail M. Lister, Ben I. Armitage and Martin R. Castell. "In Situ Electrochemical Approach to Reproducible Percolation Networks for Chemiresistors", **239th ECS Meeting & the 18th International Meeting on Chemical Sensors**, Electrochemical Society, Online, 2021. (Oral)

***Journal papers***

**Weishuo Li***, Merel J. Lefferts, Yu Wang, Abigail M. Lister, Axel Forssberg, Runze Chen, Liren Wang, Martin R. Castell*, Chemiresistive Polymer Percolation Network Gas Sensor Created with a Nanosphere Template, **Advanced Materials Interfaces**, 2023, 10, 2202042.

**Weishuo Li**, Merel J. Lefferts, Ben I. Armitage, Krishnan Murugappan, and Martin R. Castell*, Polypyrrole Percolation Network Gas Sensors: Improved Reproducibility through Conductance Monitoring during Polymer Growth, **ACS Applied Polymer Materials**, 2022, 4, 2536–2543.

Approximate word count of this thesis: 39,000 words.

# Acknowledgements

I have always believed that one of the most significant motivations for many individuals pursuing DPhil careers for several years is the desire to develop their own ways to further understand themselves and the world. I must also admit that this journey can be a colourful but tough one, filled with surprises and anxieties. After around four years, I am now grateful to have survived at the end of this journey and discovered new paths in my life. Honestly, I attribute a part of this achievement to my luck.

I'm lucky to have been born in a warm family. Honestly, I wouldn't be writing these words here without the love and support from my families. They've not only provided me with a happy life but also the opportunity to receive good education. My parents often say they're proud of me, but I really believe they're the ones we should be proud of. Even after completing my DPhil, I can't say for sure that I'll always handle the challenges in my future life with the same optimism and strength they have.

I’m lucky to have excellent professors throughout my academic journey. Without a doubt, Martin, my supervisor, has been the most influential person since I entered Oxford. His continuous support has been invaluable, and the most significant lesson I've learned from him is critical thinking. Just like most university students in China know the old saying: “believing everything in a book is worse than without that book”, almost all the researchers know the power of critical thinking. However, a person that can play football may not be a good player like Leo Messi. Martin is that exceptional coach showing me how to be a good player of critical thinking. Each challenging moment during our discussions became an opportunity for me to learn from him, and I genuinely enjoyed those moments. So I really hope to keep finding issues in my thesis year after year, which means I'm continually striving to be a good player. I also want to express my deep gratitude to Prof. Harish Bhaskaran and Prof. Peter Bruce, my

assessors, who not only encouraged me a lot but also provided inspiring advice during my DPhil study. Additionally, I'm thankful to Prof. Hong Meng, Prof. Igor Perepichka, Prof. Dmytro Perepichka, Prof. Xiaomeng Li, and Prof. Haizheng Zhong. They not only ignited my passion for scientific research but also generously supported my admission to Oxford.

I'm lucky to work in a friendly environment. Merel and Ben helped me a lot at the beginning of my DPhil career, with their experience and suggestions. When carrying out my own studies, I always feel so grateful to my teammates, Abi, Axel, Yu, Liren, and Runze, for their friendly suggestions and generously technical support. I'm also thankful to Tairu, Sisheng, Yingrui, Liwei, and Liquan, who encouraged me and provided helpful information during my studies.

I'm lucky to have met many interesting and optimistic people at Oxford. I really enjoyed every trip and dinner with Zhihang, Liang, and Jin in UK, and witnessing Xiner's continuous improvement in tennis skills was truly exciting. I am grateful for the colourful memories shared with other friends at Oxford over these four years. I'm also thankful to my present roommate, Fanmiao, for his generous help at my final stage of DPhil career. Additionally, I want to express my gratitude to Zongrui, Kecen, Yizhou, Peilin, and Miao. Despite the distance between the UK and China, our friendship has remained strong.

Honestly, I wasn't always lucky. I also encountered problems in both my daily life and research, especially during the COVID-19 pandemic. But I'm still thankful to them, which provided chances to challenge and improve myself. Of course, I couldn't deal with everything. But on a positive side, I have a warm family, excellent professors, helpful teammates, and optimistic friends.

Last but not least, I'm thankful to each reader of my thesis. I really hope some of my ideas can help your research and I'm always looking forward to your suggestions.

Thank everything and everyone I have met and will meet, and thank life.

# Abstract

Detecting chemicals is crucial in various fields, spanning from household and industrial safety to systematic monitoring of processes and environments. Among the various techniques for chemical detection, developing chemiresistive sensors based on conjugated polymers (CPs) has emerged as a promising approach to achieve desirable sensing performance at room temperature. It has been demonstrated that the sensing performance of these CP-based chemiresistors can be further improved through the introduction of electrical percolation. However, despite the progress made, challenges and gaps remain in the development of CP-based percolation chemiresistors, impeding their further investigations and practical implementation in real-life applications.

The aim of this thesis is to explore the methods to further understand electrical percolation in CP-based chemiresistors and to improve their sensing performance. In this thesis, polypyrrole (PPy) and poly(3,4-ethylenedioxythiophene) (PEDOT) have been selected as the sensing materials, while ammonia ($NH_3$) and nitrogen dioxide ($NO_2$) have been employed as the major analytes. To improve the device-to-device reproducibility of the percolation chemiresistors prepared via electropolymerisation, a current-controlled method based on the in situ conductance monitoring technique has been introduced. Through this method, PPy-based percolation sensors with similar device resistances exhibit similar performance for $NH_3$ detection. For sensitivity and limit of detection, nanosphere templating has been introduced to create PPy-based percolation networks with well-ordered nanostructures. The nanostructured percolation sensors exhibit improved performance compared to their counterparts without templates. Beyond sensing layers solely based on conjugated polymers, furthermore, this thesis has systematically studied the effects of electrical percolation on nanocomposite-based sensing layers. The research demonstrates that electrical percolation can improve the sensing

performance of PEDOT-based nanocomposites for $NO_2$ detection. Interestingly, these PEDOT-based nanocomposites also exhibit extended sensing capabilities to other stimuli, including temperature and airflow rate. Lastly, this thesis has explored in situ solid-state polymerisation as a method to prepare PEDOT-based percolation networks. Electrical percolation can be observed during this polymerisation process, and it can also be achieved by employing varying amounts of monomers for the polymerisation. PEDOT prepared by the in situ solid-state polymerisation demonstrates responsiveness to $NO_2$ gas.

The research studies in this thesis have provided potential solutions to address some challenges and gaps in the development of CP-based percolation chemiresistors. Many of these solutions could also be applicable to other sensing materials, opening the way for further investigations on electrical percolation networks and their broader applications in chemical detection. However, limitations in these solutions have revealed new challenges and gaps, requiring new ideas and potential solutions in future research endeavours.

# Contents

**Preface** ..... **I**

**Acknowledgements** ..... **III**

**Abstract** ..... **V**

**Contents** ..... **VII**

**1. Introduction** ..... **1**

**2. Background: Conjugated polymers, chemiresistors, and electrical percolation** ..... **8**

2.1 Conjugated polymer ..... 9

2.1.1 Conducting mechanism ..... 9

2.1.2 Synthesis methods ..... 10

2.1.3 Deposition methods ..... 14

2.2 Conjugated polymer based chemiresistors ..... 17

2.2.1 Sensing mechanism ..... 17

2.2.2 Measurement techniques ..... 20

2.2.3 Parameters of performance ..... 22

2.2.4 Sensing applications ..... 25

2.3 Conjugated polymer based electrical percolation ..... 34

2.3.1 Electrical percolation in materials science ..... 34

2.3.2 Filler-in-matrix strategy based on conjugated polymer ..... 38

2.3.3 Conductor-on-substrate strategy based on conjugated polymers ..... 53

2.4 Summary ..... 61

**3. Methodology** ..... **65**

3.1 Materials and substrates ..... 66

3.2 Material synthesis and deposition ..... 67

3.2.1 Electrochemical polymerisation ..... 67

3.2.2 In situ solid-state polymerisation ..... 69

3.2.3 Solution processing methods ..... 70

3.3 Characterisation ..... 72

3.4 Sensor testing setups ..... 74

3.4.1 Gas sensing ..... 74

3.4.2 Temperature sensing ..... 77

3.4.3 Flow rate sensing ..... 78
3.5 Summary ..... 79
**4. Improved sensor reproducibility through in situ conductance monitoring ..... 80**
4.1 Motivation and solution ..... 81
4.2 Experimental section ..... 82
4.2.1 Electrochemical experiments ..... 82
4.2.2 Sensing experiments ..... 83
4.3 Results and discussion ..... 84
4.3.1 Drain current curves ..... 84
4.3.2 In situ time-controlled method ..... 85
4.3.3 In situ current-controlled method ..... 87
4.3.4 Sensor performance ..... 89
4.4 Conclusion and outlook ..... 94
**5. Nanostructured percolation sensors via a nanosphere template ..... 96**
5.1 Motivation and solution ..... 97
5.2 Experimental section ..... 98
5.2.1 Preparation of nanosphere templates ..... 98
5.2.2 Electropolymerisation of polypyrrole ..... 99
5.2.3 Sensing experiments ..... 100
5.3 Results and discussion ..... 101
5.3.1 Preparation of nanostructured polypyrrole ..... 101
5.3.2 Electrical percolation ..... 104
5.3.3 Sensor performance ..... 108
5.4 Conclusion and outlook ..... 117
**6. Percolation sensors based on nanocomposites ..... 120**
6.1 Motivation and solution ..... 121
6.2 Experimental section ..... 123
6.2.1 Fabrication of nanocomposite-based sensors ..... 123
6.2.2 Sensing experiments ..... 124
6.3 Results and discussion ..... 126
6.3.1 Electrical percolation ..... 126
6.3.2 Gas sensing ..... 131
6.3.3 Temperature sensing ..... 137
6.3.4 Airflow rate sensing ..... 142

6.4 Conclusion and outlook ..... 147
**7. Electrical percolation via in situ solid-state polymerisation ..... 150**
7.1 Motivation and solution ..... 151
7.2 Experimental section ..... 153
7.2.1 In situ solid-state polymerisation (ISSP) ..... 153
7.2.2 Electrochemical experiments ..... 154
7.2.3 Sensing experiments ..... 155
7.3 Results and discussion ..... 156
7.3.1 Electrical percolation observed during ISSP ..... 156
7.3.2 Electrical percolation observed after ISSP ..... 158
7.3.3 Gas sensing ..... 164
7.4 Conclusion and outlook ..... 168
**8. Summary and perspective ..... 171**
8.1 Issues and potential solutions ..... 172
8.2 Research crossroads and future work ..... 174
**References ..... 182**
**Appendix ..... 212**

# Chapter 1

# Introduction

Detecting chemicals has been crucial in various fields, spanning from household and industrial safety to systematic monitoring of processes and environments.[1,2] With the rapid advancement of science and technology, three main approaches have been employed to obtain the required information and implement relevant applications (Figure 1.1). The first approach involves training animals to perform various detection tasks. For example, dogs have been successfully trained to detect drugs and explosives, with olfactory sensitivities as low as 1.14 parts per trillion (ppt).[3,4] Other animals with similar capabilities, such as bees, rats and moths, have also been studied for similar applications.[5-7] However, this animal-based approach has limitations as it generally provides qualitative feedback. Additionally, it may not be practical for both the trainers and animals to perform 24-hour detection. The second approach based on lab analytical instruments, such as mass spectrometers and ultraviolet–visible spectrometers, has been extensively developed to offer both quantitative measurement and durability. In comparison to animals, chemical concentrations can be obtained using internal or external standard methods based on these instruments, and these instruments can work around the clock to analyse and monitor relevant information without being influenced by handlers.[8] However, many of them have shown unavoidable disadvantages as well. Although spectrometry and other instrument-based techniques are capable of detecting trace chemicals,[9,10] chemical samples must first be prepared and then sent to the lab analytical instruments. This means that they cannot perform real-time and direct detection in the same way that animals can. The third approach, based on sensors, offers advantages that go beyond the combination of animals and instruments. These advantages include tuneable device performance, ease of miniaturization, and low power consumption,[2] showing more potential for sensors in chemical detection.

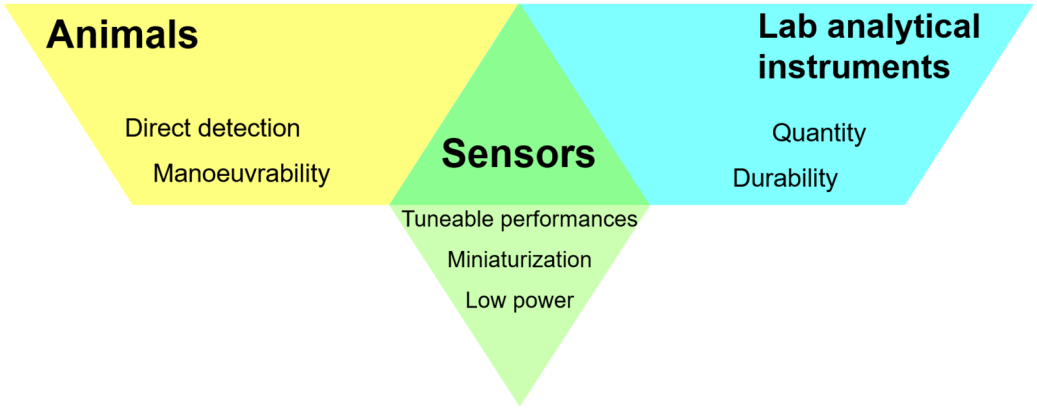



**Figure 1.1.** Three main approaches to chemical detection. Sensors offer advantages that go beyond the combination of animals and lab analytical instruments.

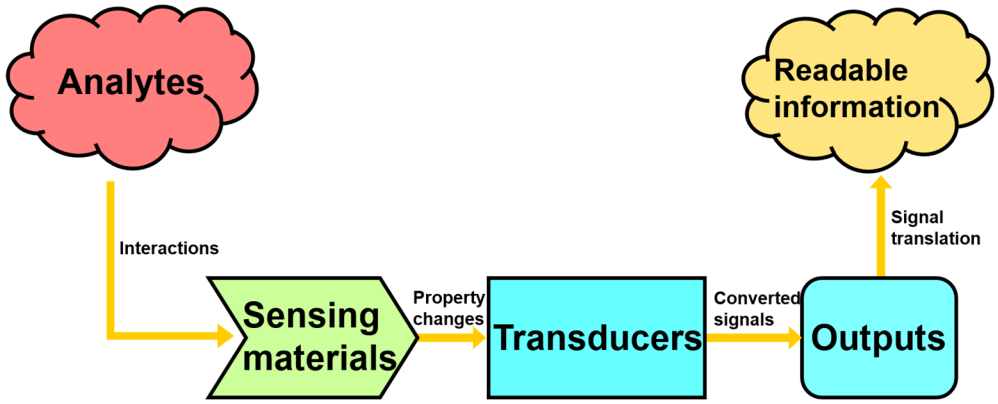



**Figure 1.2.** Schematic representation of sensing processes to detect chemicals. The properties of sensing materials can be altered through interactions between the sensing materials and analytes, and this in turn triggers signals to be produced by the transducers and transmitted via the outputs into readable digital information.

Sensors are devices or subsystems designed to detect analytes in specific environments. They consist of sensing materials, transducers, and outputs. As illustrated in Figure 1.2, the properties of sensing materials can be altered through interactions between the sensing materials and analytes, and this in turn triggers signals to be produced by the transducers and transmitted via the outputs to other electronics or systems, where the signals can be translated into readable digital information.[11] An ideal sensor should meet the following criteria: firstly, it should be sensitive to the property being measured; secondly, it should be insensitive to any

other properties; and lastly, it should not influence the property being measured.[12] Sensing materials play a crucial role in fulfilling these requirements and are the key to the sensing process. Various materials have been extensively studied and successfully used in chemical sensors, including silicon,[13] metal oxides,[14] conjugated polymers,[15] and carbon materials.[16]

Conjugated polymers (CPs) have attracted considerable attention since the discovery of the conducting polyacetylene by Shirakawa, MacDiarmid, and Heeger in the 1970s.[17] For their groundbreaking work in this field, the three scientists were jointly awarded the Nobel Prize in Chemistry in 2000. In recent decades, CPs have demonstrated a range of attractive advantages including tuneable properties, convenient processing, light weight, and flexibility.[18,19] They have now been used in various applications including light-emitting diodes,[20] transistors,[21] solar cells,[22] electrochromic devices,[23] supercapacitors,[24] and sensors.[25] In the field of chemical sensors, CPs have been regarded as promising sensing materials owing to their favourable sensitivity at room temperatures.[15] This has led to a growing interest in the development of CP-based chemical sensors.

A variety of CP-based chemical sensors have been developed, with their device configurations generally classified into chemiresistors, thin-film transistors, electrochemical transistors, diode sensors, optical devices, and piezoelectric crystal sensors (Figure 1.3).[15,26] Chemiresistors, the most common type, provide fast sensing simply through the conductance changes of CPs. Chemical sensors based on thin-film transistors, electrochemical transistors, and diode sensors offer more detailed information during the sensing process, as they have more electrical and electrochemical parameters than chemiresistors. However, these devices also show their complexity during fabrication and/or measurement. Suitable electrolytes and electrodes must be carefully selected for electrochemical transistors, while the effects of metals or semiconductors contacting CPs should be taken into consideration for diode sensors. Moreover, the introduction of gate voltage in transistors may increase the power consumption

of the sensor. The optical properties of CPs have also been studied for the development of sensors. With changes in conductance, the spectral absorbance and transmittance of polymer films may also change during the sensing process, making optical devices a viable option. Although the simplest sensor can be created by simply covering a piece of glass with polymer films, optical devices have low sensitivities and require corresponding spectrometers. Piezoelectric crystal sensors detect trace analytes by being highly sensitive to changes in the mass of CPs, but they lack selectivity. Despite using the same series of sensing materials, chemical sensors based on aforementioned configurations have different transducers due to their different sensing principles. Taking their advantages and disadvantages into account, chemiresistors have been identified as one of the best options for the future of sensors due to their simple fabrication, low cost, and desirable performance.[25]

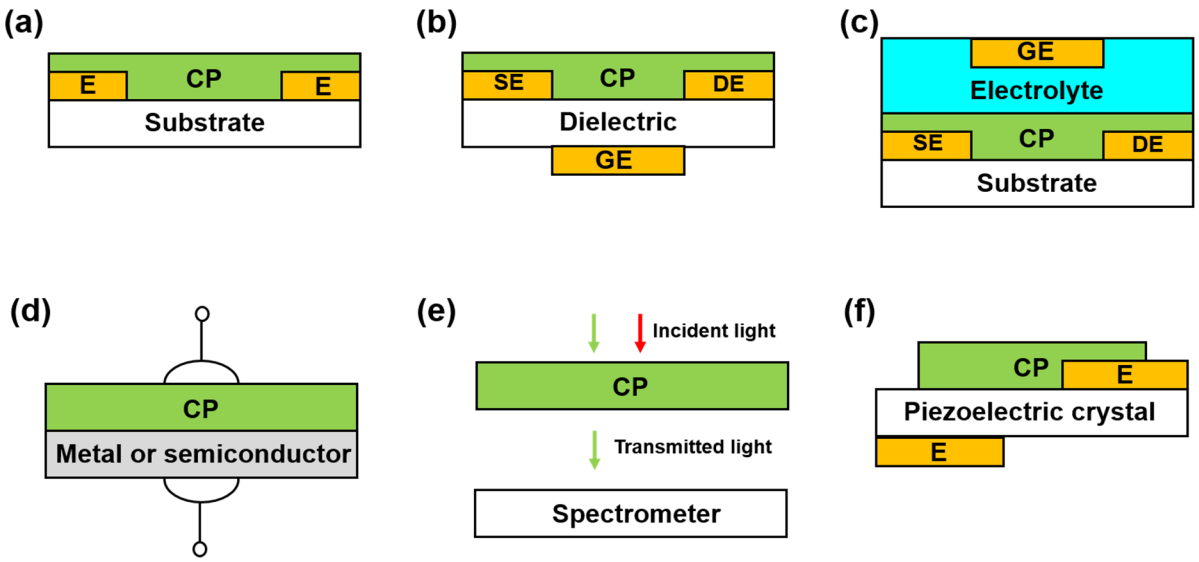



**Figure 1.3.** Representative configurations of CP-based (a) chemiresistors, (b) thin-film transistors, (c) electrochemical transistors, (d) diode sensors, (e) optical devices, and (f) piezoelectric crystal sensors for chemical detection. (CP: conjugated polymer; E: electrode; SE: source electrode; DE: drain electrode; GE: gate electrode.)

The unique advantages of CPs and CP-based chemiresistors make it possible to create miniaturized and lightweight sensors that can detect a variety of chemicals. Their sensitivity to specific analytes is a crucial factor in determining the sensing performance. One of the most effective strategies is to increase the surface area-to-volume ratio of the sensing layer. To accomplish this, CPs have been fabricated into various forms through elaborate processes, including ultra-thin films, porous thin films, and carefully designed nanostructures.[25,27] Despite these efforts, it remains a challenge to attain ultra-high sensitivity at low analyte concentrations under the parts per million (ppm) level through straightforward processing methods. Recently, it has been shown that electrical percolation materials have significantly increased sensitivity over their thin-film counterparts.[28-30] For the CP-based chemiresistors, electrical percolation is identified by the abrupt increase in conductance between two electrodes connected with conducting pathways. This phenomenon can be observed during the preparation of either CPs or CP-based composites. The percolation networks are known to be more sensitive to analytes compared to thin films, which can achieve effective detection at the parts per billion (ppb) level. Previous studies have demonstrated that percolation networks of polypyrrole (PPy) and poly(3,4-ethylenedioxythiophene) (PEDOT) can exhibit improved sensitivities and lower limits of detection for ammonia, nitrogen dioxide, and ammonium nitrate/fuel oil compared to traditional thin-film chemiresistive sensors.[31-36] However, it is important to acknowledge that challenges and gaps still exist in this field, which limit the further understanding of CP-based percolation sensors and their practical implementation in real-life applications. Efforts have been made in this thesis to address some of these issues.

This thesis starts with an overview of the basic knowledge required for the investigation on CP-based percolation chemiresistors. This interdisciplinary knowledge presented in Chapter 2 covers conjugated polymers, chemiresistors, and electrical percolation, establishing the

theoretical and experimental foundations of this thesis. At the end of this chapter, challenges and gaps that this thesis aims to address are pinpointed.

The next chapter, Chapter 3, introduces the methods used to carry out the work in this thesis. The chemicals and interdigitated electrodes used are described at the beginning of this chapter. Then, this chapter presents necessary approaches to material synthesis, deposition, and characterisation. Lastly, all the sensor testing setups are illustrated, as well as experimental protocols for corresponding sensing tests.

Chapters 4 to 7 focus on developing specific solutions to the issues raised at the end of Chapter 2. To improve the device-to-device reproducibility of the percolation chemiresistors prepared via electropolymerisation, Chapter 4 provides a current-controlled method based on the in situ conductance monitoring technique. Through this method, percolation sensors with similar device resistances exhibit similar performance for ammonia detection. For sensitivity and limit of detection, in Chapter 5, nanosphere templating is introduced to create percolation networks with well-ordered nanostructures. The nanostructured percolation sensors exhibit improved performance compared to their counterparts without templates. Beyond sensing layers solely based on conjugated polymers, furthermore, Chapter 6 systematically studies the effects of electrical percolation on nanocomposite-based sensing layers. The research demonstrates that electrical percolation can improve the sensing performance of the nanocomposites for nitrogen dioxide detection. In this chapter, these nanocomposites also exhibit extended sensing capabilities to other stimuli, including temperature and airflow rate. Lastly, Chapter 7 explores in situ solid-state polymerisation as a method to prepare percolation networks. Electrical percolation can be observed during this polymerisation process, and it can also be achieved by employing varying amounts of monomers for the polymerisation. Polymers prepared in this chapter demonstrate responsiveness to nitrogen dioxide.

Finally, Chapter 8 provides a summary of the results achieved in this thesis. With further discussion on the development of CP-based percolation chemiresistors, in the end, some suggestions built upon the results and discussion are provided for future work.

# Chapter 2

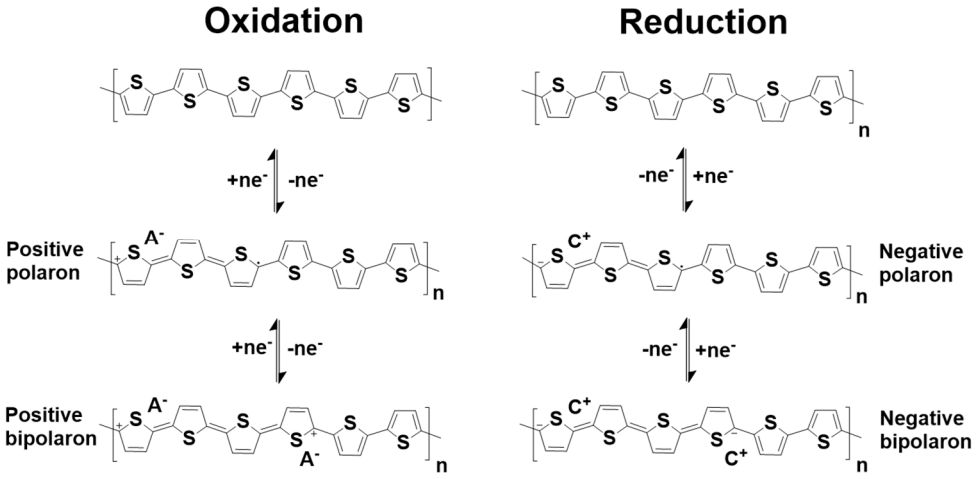
# Background: Conjugated polymers, chemiresistors, and electrical percolation

Developing chemiresistive percolation sensors based on conjugated polymers requires interdisciplinary knowledge covering conjugated polymers (CPs), chemiresistors, and electrical percolation. This chapter provides an overview of these three fundamental concepts to establish the background for this thesis. Firstly, fundamental concepts of conjugated polymers are introduced in section 2.1, including conducting mechanism, synthesis methods, and deposition methods. This section provides a necessary understanding of sensing materials used in CP-based chemiresistors. Then, section 2.2 starts with the sensing mechanism for CP-based chemiresistors. In the same section, relevant measurement techniques and parameters of sensing performance are presented and reported sensing applications are summarised. Furthermore, the basic concepts of electrical percolation are introduced in section 2.3. Two approaches to yield CP-based percolation pathways are then further presented and discussed, including the filler-in-matrix strategy and the conductor-on-substrate strategy. Lastly, all this background is summarised in section 2.4, highlighting the research motivation behind this thesis.

## 2.1 Conjugated polymer

### 2.1.1 Conducting mechanism

Conjugated polymers (CPs) have unique molecular structures with alternating single and double chemical bonds, leading to broad π-electron conjugation along their backbone and mobility of delocalized electrons. However, their low conductivity is due to limited number of carriers for intra- and inter-chain transport. This can be improved by doping, which is recognized as the key factor in distinguishing CPs from other polymers.[37]




**Scheme 2.1.** Doping processes of both oxidation and reduction for polythiophene. ($A^-$: counter anion; $C^+$: counter cation.)

CPs are normally doped through chemical or electrochemical redox reactions, which involve the removal or injection of electrons. These reactions lead to the creation of cation or anion radicals on the backbone of the CPs. At the same time, counter anions ($A^-$) or cations ($C^+$) are introduced near the polymer backbone to maintain charge balance. The radicals on the backbone are called polarons and further doping can result in bipolarons.[38] Each bipolaron is a bound pair of polarons occupying a conjugated polymer segment.[39] Both polarons and bipolarons act as charge carriers and contribute to the conductivity of the polymer.[40,41] For

example, chemical or electrochemical oxidation can create positive polarons and bipolarons in polythiophene, while reduction can produce negative carriers (Scheme 2.1). On the other hand, polyaniline can be doped through protonation, but it requires a specific structural component for it to be conductive.[15]

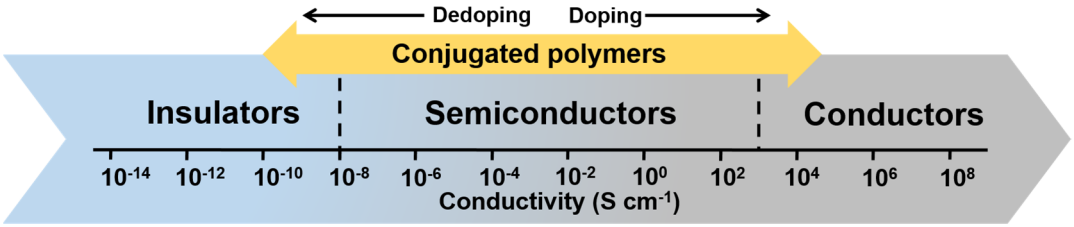



**Figure 2.1.** Conductivity range of conjugated polymers. The conductivities of conjugated polymers can increase or decrease through the doping or dedoping processes, respectively.

The doping process of CPs is reversible and adjustable, meaning that their electrical conductivity can be altered through chemical or electrochemical reactions. This ability to vary their conductivity between insulating and conducting states (Figure 2.1) has opened up a wide range of applications. For instance, CPs in semiconducting states can be used as active layers in thin-film transistors, light-emitting diodes, and solar cells, while those in conducting states can be used as conductive layers in thermoelectric devices and transparent electrodes. On the other hand, their redox properties can be utilised in applications that require redox reactions, such as supercapacitors and electrochromic devices. These redox processes are also fundamental to the sensing mechanism of chemiresistive sensors.

### 2.1.2 Synthesis methods

CPs can be simply synthesised via electrochemical reactions. With the rapid advancement in organic chemistry, furthermore, various chemical synthesis methods based on different mechanisms have been thoroughly studied and applied in the field of organic electronics in

recent years. All these methods serve as the first step in fabricating chemiresistive sensors. Some representatives have been shown as follows:

***Electrochemical oxidative polymerisation.*** Electrochemical oxidative polymerisation (i.e. electropolymerisation) is one of the most common ways to prepare CPs.[42] This method requires a system consisting of three electrodes, an electrolyte with monomers, and an electrochemical workstation (Figure 2.2a). Monomers are oxidised on the surface of the working electrode and then polymerised onto this electrode. The doping and dedoping processes can be easily controlled, and suitable polymer films can be prepared during polymerisation. Chemiresistive sensors can be easily obtained by using interdigitated microelectrodes as the working electrodes (Figure 2.2b).[43] However, this method has some disadvantages, such as the limited type of monomers that can be used, difficulty in modifying polymers after polymerisation, and less practicality for large-scale production compared to chemical methods.

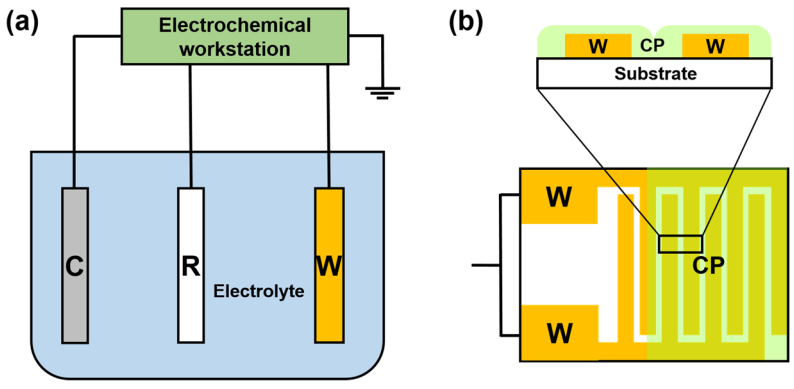
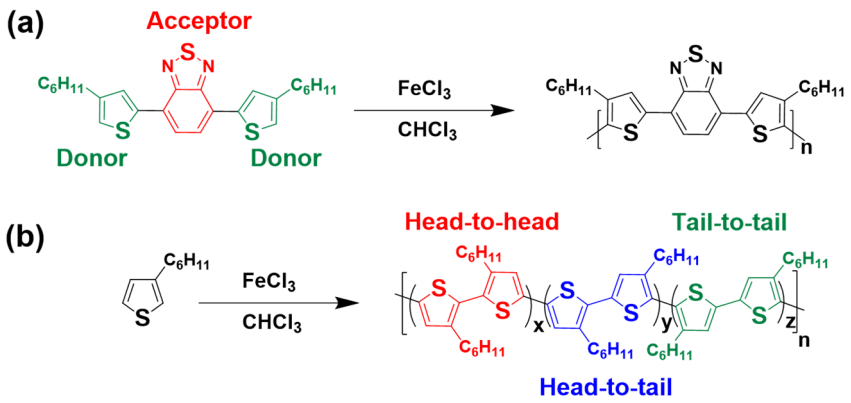


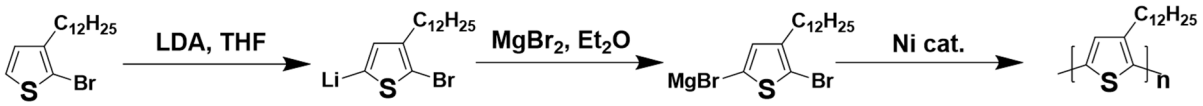

**Figure 2.2.** Schematic representation of (a) a three-electrode system and (b) an interdigitated microelectrode for electrochemical polymerisation. (C: counter electrode; R: reference electrode; W: working electrode; CP: conjugated polymer.)

***Chemical oxidative polymerisation.*** Chemical oxidative polymerisation is one of the most straightforward methods for preparing CPs. Doped polymers can be synthesised in solutions by mixing suitable monomers and oxidants, and their corresponding undoped polymers can be

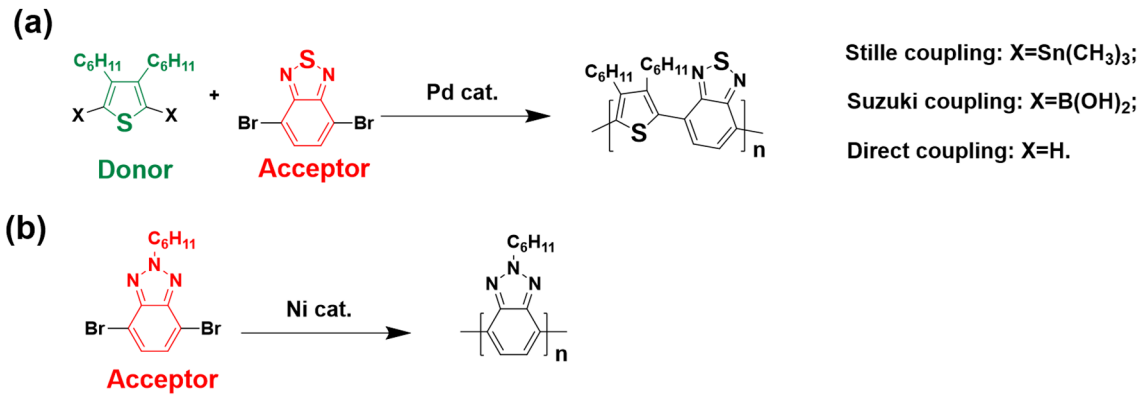
obtained through chemical or electrochemical post-treatment. The mechanism for synthesis is similar to that of electrochemical oxidative polymerisation, however, the oxidation is generated by the oxidant rather than a potential bias. The molecular weight of the polymer can be influenced by the oxidant, solvent, reaction time and temperature. Despite the potential for large-scale production of doped or undoped CPs, this method has some limitations. The choice of monomers is limited, much like with electropolymerisation, and the preparation of donor-acceptor polymers requires the prior design and synthesis of complex donor-acceptor-donor monomers, as oxidative polymerisation generally applies to suitable donors that can be easily oxidised (Scheme 2.2a). This method can thus mainly provide limited p-type or ambipolar polymers rather than n-type polymers that are fully constructed from electron acceptors. Additionally, the polymers synthesised by this method often exhibit poor regioregularity due to a lack of monomer regioselectivity. For example, poly(3-hexylthiophene) (P3HT) synthesised through oxidation usually consists of diverse segments with head-to-head, head-to-tail, and tail-to-tail couplings (Scheme 2.2b). However, only head-to-tail coupled P3HT exhibits desirable properties, as its regioregularity greatly contributes to molecular self-assembly in both solution and solid states.[44]




**Scheme 2.2.** Synthesis routes of (a) the donor-acceptor polymer poly(4,7-Bis(4-hexylthiophen-2-yl)benzo[*c*][1,2,5]thiadiazole) and (b) the regiorandom poly(3-hexylthiophene) (P3HT) by chemical oxidative polymerisation.




**Scheme 2.3.** Synthesis routes of the regioregular poly(3-dodecylthiophene) (PDDT) by Kumada coupling.




**Scheme 2.4.** Representative synthesis routes of (a) the donor-acceptor polymer poly(2,1,3-benzothiadiazole-4,7-diyl(3,4- dihexyl-2,5-thiophenediyl))by different coupling methods and (b) the n-type polymer poly(2-hexylbenzotriazole) by Yamamoto coupling.

***Coupling polymerisation.*** Many CPs have been synthesised thanks to the development of coupling polymerisation. Monomers that have been modified with functional groups can react with each other and construct polymer chains in solutions aided by specific metal catalysts. Undoped polymers are prepared using this method, and they can be chemically or electrochemically doped via post-treatment. Although coupling polymerisation generally requires higher temperatures, longer time, or more complex reaction systems than chemical oxidative polymerisation, it has shown significant advantages in both structural regioregularity and material diversity. For instance, highly regioregular poly(3-dodecylthiophene) (PDDT) has been synthesised by Kumada coupling (Scheme 2.3).[45] Its ideal head-to-tail structure leads to an average conductivity of 600 S $cm^{-1}$, which is almost 60-fold higher than PDDT prepared by electrochemical or chemical oxidative methods. Without complex monomers, donor-acceptor polymers can be effectively synthesised by Stille, Suzuki, or direct coupling methods (Scheme

2.4a).[46-48] Moreover, n-type polymers can be obtained by Yamamoto coupling (Scheme 2.4b).[49] However, by-products from coupling polymerisation are unavoidable, which may affect the properties of CPs. Some hazardous by-products, such as organostannane compounds, may increase the costs from the environment and safety issues during the large-scale production.[50]

CPs can also be prepared using other methods, such as vapour polymerisation and in situ solid-state polymerisation,[51-54] although these methods require appropriate monomers. Furthermore, the morphologies of polymers depend on both the synthesis methods and their reaction conditions.[42,55-57] To obtain ideal sensing materials, it is important to carefully design and choose the appropriate monomers, synthesis methods, and synthesis conditions. This is because they have significant impacts on the properties of the polymer, the fabrication process, and the performance of the device.

### 2.1.3 Deposition methods

The configuration of the chemiresistor determines that most CPs should be deposited as sensing layers onto suitable substrates after the material synthesis. Various deposition methods have been developed and act as the second step in fabricating chemiresistive sensors. Some representatives have been shown as follows:

***Electrochemical deposition.*** CPs can be electrochemically deposited onto substrates, and their film properties are tuneable and favourable for improving device performance.[42] This method can control film thickness and form porous surfaces, improving device performance. Identical to electropolymerisation, monomers for electrochemical deposition are limited, or they require complex preparation. Although the obtained polymer films are uniform and tuneable, the formed films are not as reproducible as expected. This disadvantage arises from the uncertainty of the changing conditions during electrochemical deposition. The composition of the electrolyte keeps changing after repeated deposition due to the consumption of

monomers, the appearance of oligomers, and the evaporation of the solvent. Therefore, it is difficult to electrochemically obtain reproducible polymer films, posing a great challenge for fabricating chemiresistors with reproducible performance. Another drawback concerns substrate applicability. Electrochemical deposition requires substrates with conducting materials that act as working electrodes.

***Drop-casting.*** As the simplest solution-processing method, drop-casting should be the most straightforward way to deposit polymers onto substrates. The polymer solution or dispersion is dropped onto a target substrate, and a polymer film can be obtained after the solvent evaporation.[58,59] All the polymers in the drops are utilised to form the sensing layers, and the film thickness is controlled by the polymer concentration and the number of drops. However, this method does not routinely provide uniform films due to the coffee-ring effect.[60]

***Spray-coating.*** Visibly uniform films can be prepared by spraying polymer solutions or dispersions onto target substrates.[61] The film thickness can be controlled by various factors such as polymer concentration, spraying time, and nozzle parameters. Moreover, patterned films can be easily achieved using this method with the assistance of masks.[62,63] However, it remains challenging to achieve uniform film morphology through spray-coating, as this technique is not precise enough. In addition, spray-coating inevitably results in a waste of material due to the large area required to cover the target substrates.

***Spin-coating.*** Spin-coating is a highly effective and widely used method for preparing polymer films with uniform morphology. It involves spreading a polymer solution or dispersion onto a spinning substrate and allowing the solvent to evaporate, resulting in the formation of a film. [64] The thickness of the film can be controlled by adjusting parameters such as polymer concentration, spin time, and spin speed. The film morphology can be improved through thermal annealing or solvent annealing.[65,66] However, spin-coating is suitable for small

substrates and may require substrate modification prior to deposition. Additionally, spin-coating typically results in significant material wastage, as only a fraction of the polymers deposited during the process remain on the target substrate.

***Dip-coating.*** Dip-coating enables larger areas of deposition and minimizes material wastage compared to spin-coating. In this method, the substrate is immersed into a polymer solution or dispersion and withdrawn at a controlled extraction speed, resulting in the formation of a polymer film after the solvent evaporates during the substrate extraction process.[67] The properties of the film are controlled by both the polymer concentration and the extraction speed. When combined with the roll-to-roll process, dip-coating allows for large-area fabrication in the industry. While dip-coating can yield uniform films, the film thickness may vary from the top to the bottom of the substrate, which can impact the film reproducibility.

***Doctor-blade coating***. The doctor-blade method has become a popular technique for depositing CP-based films in recent years. In this method, a blade is used to spread a solution or dispersion of the CP onto a substrate, with excess material being removed by the blade.[68] The film thickness is controlled by the gap between the blade and the substrate, and the film properties depend on factors such as solvent, polymer concentration, gap height, and removing speed. The advantages of this method include its simplicity, low cost, and scalability for large-area coating. However, it is difficult for this method to offer the nanoscale uniformity or extreme thin films like spin coating can and it shows limited applicability to non-planar or flexible substrates. Reproducibility may also be an issue in large-scale fabrication.

It should be noted that the choice of a deposition method generally depends on the synthesis method of the CPs. Electrochemical deposition can be accomplished during electrochemical polymerisation. Solution-processing methods, including drop-casting, spray-coating, spin-coating, dip-coating, and doctor-blade coating, are applicable for soluble or dispersible

polymers prepared by chemical polymerisation. Additionally, substrates must be taken into account when selecting a suitable deposition method. Details about the deposition methods mentioned above have been summarised in Table 2.1.

**Table 2.1.** Deposition methods to obtain sensing layers.

| Method | Polymer utilisation | Film uniformity | Reproducibility | Substrate applicability | Influencing factor |
|---|---|---|---|---|---|
| Electrochemical deposition[a] | All deposited | Nanoscale | Limited | Substrates with conducting electrodes | Solvent; monomer concentration; potential |
| Drop-casting[b] | All deposited | Poor | Poor | Various substrates | Solution concentration; number of drops |
| Spray-coating[b] | Partial amounts deposited | Visible | Moderate | Various substrates | Solution concentration; spraying time; nozzle parameters |
| Spin-coating[b] | Small amounts deposited | Nanoscale | Good | Small substrates | Solution concentration; spin time; spin speed |
| Dip-coating[b] | All deposited | Nanoscale | Moderate | Various substrates | Solution concentration; extraction speed |
| Doctor-blade coating[b] | Partial amounts deposited | Visible | Moderate | Planar and rigid substrates | Solvent; solution concentration; gap height; removing speed |

[a]Polymers for this method come from electrochemical oxidative polymerisation. [b]This method belongs to solution-processing deposition and requires polymers synthesised from chemical polymerisation.

## 2.2 Conjugated polymer based chemiresistors

### 2.2.1 Sensing mechanism

Following the general sensing principle (Figure 1.2), the sensing mechanism of CP-based chemiresistors depends on their device configuration and is determined by the interactions between sensing polymers and analytes. A CP-based chemiresistor is a resistor consisting of doped polymers between one or more pairs of electrodes. A constant potential or current is

applied across it, and the resistance change can be measured when the doped polymers interact with the analytes. Based on this, the CP-based chemiresistor establishes a relationship between the analyte concentration and its resistance. The total resistance of the chemiresistor ($R$) can be divided into two parts as follows:

$$R = R_p + R_c \tag{2.1}$$

where $R_p$ represents the resistance of the doped polymers and $R_c$ represents the contact resistance between polymers and electrodes. Chemical detection can be achieved by chemically or physically changing these two parts independently or synergistically (Figure 2.3).

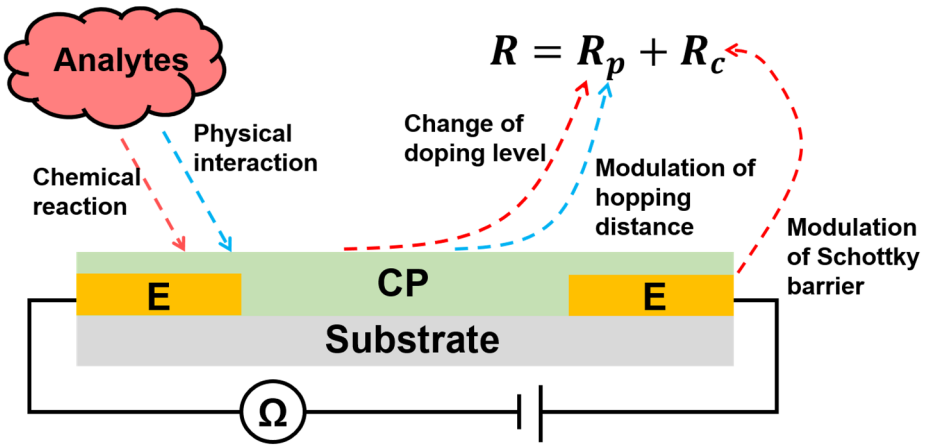



**Figure 2.3.** Schematic representation of the sensing mechanism of conjugated polymer (CP) based chemiresistors. The resistance of CPs ($R_p$) can be altered by the chemical reactions and/or physical interactions between the CPs and the analytes, while the contact resistance ($R_c$) at CP/electrode (E) contact may be changed via the reaction with analytes. Changes in both $R_p$ and $R_c$ determine the overall change in the total resistance ($R$) during the sensing process.

The resistance of CPs ($R_p$) is dependent on their doping levels ($L_D$). The doping levels can be altered via chemical reactions with analytes, and different electron transfer processes lead to different sensing responses (Table 2.2).[15,25] Many p-type CPs, such as polythiophene (PTh),

polypyrrole (PPy), polyaniline (PANI), and their derivatives, have been utilised in CP-based chemiresistors. When reacting with electron-withdrawing analytes, such as nitrogen dioxide ($NO_2$) and oxygen ($O_2$), electrons are removed from the polymer backbones, enhancing the doping levels and decreasing their resistances. Conversely, their doping levels decrease, and their resistances increase when reacting with electron-donating analytes, such as ammonia ($NH_3$). These electron-transferring processes also occur in n-type polymers, albeit only a few n-type polymers have been used in chemiresistors possibly due their ambient instability.[69-71]

**Table 2.2.** Sensing responses of p-type and n-type polymers to different analytes.

| Sensing response | Electron withdrawing analyte | Electron donating analyte |
|---|---|---|
| p-type polymer | $L_D$ increases<br>$R_p$ decreases | $L_D$ decreases<br>$R_p$ increases |
| n-type polymer | $L_D$ decreases<br>$R_p$ increases | $L_D$ increases<br>$R_p$ decreases |

Note: $L_D$ = doping level; $R_p$ = resistance of conjugated polymer.

The resistance of CPs ($R_p$) can also be altered by the physical interactions between the CPs and the analytes. The absorption of analytes may enhance the potential barrier at the grain boundaries or change the crystallinity of the CPs.[72,73] Swelling may occur and change the inter-chain distance.[74] Moreover, it has been reported that hydrogen bonding and dipole-dipole interactions may also impact the sensing process of CP-based chemiresistors.[75] These physical interactions can alter the intermolecular hopping distance of CPs, enabling chemical detection.

When the analytes chemically react with the CPs, electron transfer can also change the work function of the CPs. Previous studies have reported that the difference in the work function of the CP and the metal electrode determines the Schottky barrier height at the CP/metal interface in CP-based chemiresistors.[76,77] This modulation of barrier height induced by the interaction with the analytes leads to a change in conductivity at the CP/metal electrode contact. Therefore,

the contact resistance ($R_c$) can be altered during the sensing process, and it may also contribute to the total resistance ($R$).

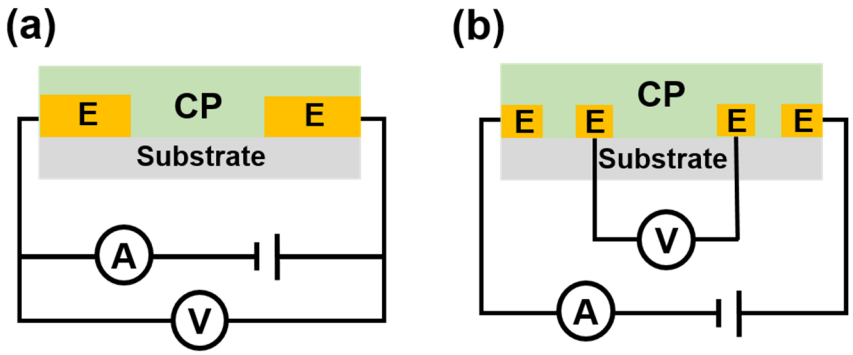



**Figure 2.4.** Configurations of (a) two-electrode and (b) four-electrode measurement techniques. (CP: conjugated polymer; E: electrode; V: voltmeter; A: ammeter.)

### 2.2.2 Measurement techniques

There are several techniques available for measuring the resistance changes of CP-based chemiresistors. These measurement techniques have undergone a long evolution, from the simplest two-electrode technique to more sophisticated measurement systems.[26] In order to improve sensor performance, it is important to ensure that the device fabrication and measurement conditions meet specific requirements. Herein, two representatives have been introduced as follows:

***Two-electrode technique.*** The simplest and most common method for measuring the total resistance ($R$) of CP-based chemiresistors is the two-electrode technique. In this technique, CPs are deposited within a small gap between two electrodes, and a constant potential or current is applied between the electrodes (Figure 2.4a). Before measuring the resistance, it is important to choose appropriate electrodes, film thickness, and substrates. Typically, platinum (Pt) or gold (Au) thin films are used as the electrodes owing to their high conductivity and ambient

stability. The thickness of the thin-film electrode is generally around 200 nm.[26] Additionally, it has been reported that pre-treatment of Au electrodes with thiol-modified monomers can reduce the contact resistance.[78] The gaps between electrodes are generally between 1.5 and 100 μm.[26] Narrower gaps require a smaller amount of polymers to cover. During electrochemical polymerisation, narrower gaps can lead to thinner films across the gaps, which may improve device sensitivity to analytes.[79] Moreover, pre-treatment of substrates with hydrophobic silanes can improve the lateral growth of CPs over the gaps.[80] During resistance measurement, the applied potential or current must be carefully considered, as a constant potential or current may cause irreversible changes that can affect device stability.[26] High currents across the chemiresistors can cause self-heating, making the device sensitive to other parameters such as airflow,[81] but can also improve the signal-to-noise (S/N) ratio. Therefore, a suitable potential or current must be applied in the two-electrode technique to keep a balance between sensitivity and the S/N ratio.

***Four-electrode technique.*** The negative effects of contact resistance ($R_c$) can pose a challenge for the two-electrode technique. High $R_c$ values that are insensitive to analytes may limit device performance. To overcome this challenge, a four-electrode technique has been developed to measure the changes in polymer resistance ($R_p$) without the interference from $R_c$.[75,78] This technique uses two pairs of electrodes, where the outer electrodes apply a constant current and the potential between the inner electrodes is measured using a high-impedance voltmeter (Figure 2.4b). The CP-based chemiresistors can therefore reflect changes in $R_p$.

Some other measurement techniques have been developed as well. For instance, Mirsky *et al*. introduced a simultaneous two and four-point (s24) method,[78,82] allowing for the measurement of total resistance and polymer resistance as well as the determination of contact resistance. Despite the availability of various measurement techniques, the majority of studies have utilised the two-electrode technique for sensing tests due to its simplicity and convenience.

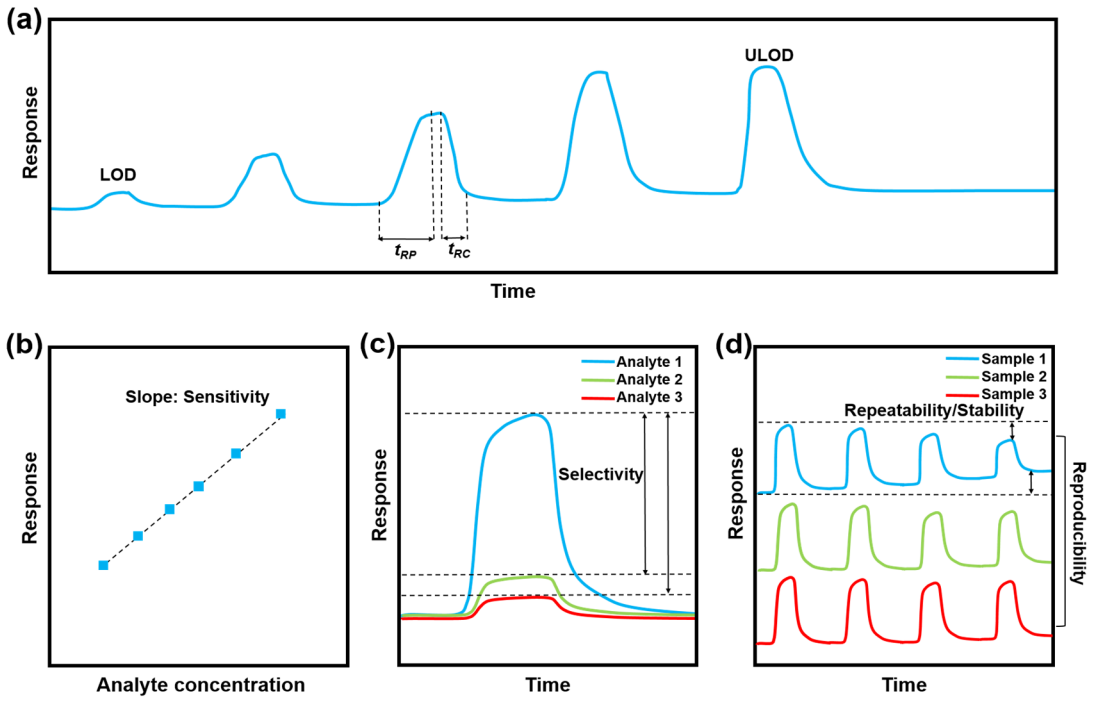



**Figure 2.5.** Graphic representation of performance parameters in (a) a sample exposed to increasing concentrations of analyte, (b) a plot of the sensor response as a function of the analyte concentration, (c) a sample exposed to different analytes with the same concentration, and (d) samples repeatedly tested under the same condition. ($t_{RP}$: response time; $t_{RC}$: recovery time; LOD: limit of detection; ULOD: upper limit of detection.)

### 2.2.3 Parameters of performance

The simple two-electrode technique is generally employed to acquire readable information and assess the performance of a CP-based chemiresistor. To begin, a sample of the chemiresistor is connected to a constant power supply and multimeter. Prior to testing, the sample is generally allowed to stabilise in the measurement environment for a certain duration set by researchers. Subsequently, the sample is exposed to known analyte concentrations for a defined duration spanning from minutes to hours, followed by a period of recovery. One or more periods of signal curves recorded by the multimeter can illustrate the resistance changes during the response and recovery processes. Analysis of these curves (Figure 2.5) can be employed to assess various performance parameters, and several factors that can influence

these parameters have been systematically discussed and summarised in relevant reviews.[15,25,26] Some fundamental parameters have been introduced as follows:

***Sensor response and sensitivity***. The evaluation of sensor response to analytes is paramount in assessing the sensitivity of chemical detection, making it the most important performance parameter. The sensor response (*SR*) is normally defined as follows:

$$SR = \frac{R_a - R_0}{R_0} \times 100\ \% \tag{2.2}$$

where $R_a$ represents the device resistance in the presence of analytes and $R_0$ represents the intrinsic device resistance without analytes.[15,25] Different responses can be observed when a sensor is exposed to varying concentrations of an analyte (Figure 2.5a), and these responses can be represented as a function of the concentration (Figure 2.5b). In an ideal scenario, the sensor responses should exhibit a linear relationship with the analyte concentrations. The slope of the linear output curve serves as an evaluation parameter for the device sensitivity.[83]

***Response and recovery time.*** The response time ($t_{RP}$) is the duration required to reach 90 % of the total response during exposure, while the recovery time ($t_{RC}$) is the duration required to recover to 90 % of the initial signal during the recovery process (Figure 2.5a).[25,84] These parameters provide insights into the speed of sensor response and recovery during and after exposure. Sufficient recovery time should be taken to allow the sample to return to its original state for further testing. However, some samples may not recover to their original states owing to their poor reversibility or stability.

***Limit of detection.*** The limit of detection (LOD) of a CP-based chemiresistor is typically described as the lowest analyte concentration it can detect.[84] The ideal lowest concentration should be determined based on the lowest acceptable signal-to-noise ratio (SNR). Typically, the LOD is defined as three times the standard deviation of the baseline noise level (σ) divided

by the sensitivity. Additionally, if the concentration of the analyte is sufficiently high, the sample may become saturated, thereby halting further device response and establishing an upper limit of detection (ULOD). Although researchers tend to focus more on the lower concentration range in order to achieve higher sensitivity and lower detection limits, it is also important to consider the upper limit to provide a comprehensive detection range.

***Selectivity.*** Selectivity refers to the capability of a sensor to detect a single analyte and differentiate it from others in a mixture.[83,84] However, achieving this exclusivity with CP-based chemiresistors is challenging as CPs can respond to various chemical and physical interactions. Thus, device selectivity is typically evaluated by comparing the signals with different resolutions after exposing the sensor to different analytes (Figure 2.5c).

***Repeatability.*** Repeatability describes the ability of a CP-based chemiresistor to generate consistent and dependable responses when measuring an identical concentration of analyte under the same conditions (Figure 2.5d). A chemiresistor that exhibits high repeatability will produce responses with minimal variation during repeated tests. It guarantees the accuracy and consistency of the measurements they produce, which is essential in numerous fields, including manufacturing, quality control, and scientific research.

***Stability.*** Stability refers to the capability of a CP-based chemiresistor to exhibit consistent and dependable responses under the same test conditions over an extended period of time.[85] It is analogous to repeatability but is assessed over a more extensive working period. The simplest way to assess stability is to compare the response provided by an aged device with its initial response. A more comprehensive evaluation of stability can be performed by examining the response retention during a repeated test over an extended time. A reversible device with ideal repeatability may exhibit favourable stability over the lifespan of this device. The lifetime of the device can be determined by the lower limit of acceptable retention.

***Reproducibility.*** Reproducibility is an essential aspect of both laboratory experiments and large-scale production. It can be evaluated by analysing the variation in response signals generated by device samples under the same test conditions (Figure 2.5d). Reproducibility is heavily dependent on the reproducibility of material preparation and device fabrication, underscoring the significance of standardising experimental or industrial protocols.

## 2.2.4 Sensing applications

Many classic CPs, such as PTh, PPy, PANI, and their derivatives, have been utilised as sensing materials in chemiresistors for detecting a wide range of analytes. The targeted analytes for CP-based chemiresistors are typically gaseous chemicals that originate from hazardous gases, volatile compounds, and warfare chemicals. In addition, some CP-based chemiresistors are capable of sensing biomolecules and ions. Various strategies have been employed to investigate these target analytes.

### 2.2.4.1 Hazardous gas detection

Plenty of research related to CP-based chemiresistors focuses on detecting hazardous gases for two primary reasons. Firstly, hazardous gases produced by rapid modernization and industrialization pose a significant threat to human health and the environment. For example, nitrogen oxides ($NO_x$) from vehicle emissions can cause respiratory problems and contribute to acid rain. Secondly, many hazardous gases are electron-donating or -withdrawing chemicals that can significantly affect the doping levels of CPs. For instance, ammonia ($NH_3$) and hydrogen sulfide ($H_2S$) are electron-donating analytes, while nitrogen oxides ($NO_x$) are electron-withdrawing analytes. Therefore, developing CP-based chemiresistors for hazardous gas detection is crucial and feasible.

Among all hazardous gases, $NH_3$ is one of the most extensively studied analytes due to its detrimental effects on human health and the environment.[86] $NH_3$ can be detected at trace levels

by almost all classic CPs, and PPy and PANI have been well-developed to improve device sensitivity and response time. More recently, PPy and PANI-based polymers have been fabricated into nanofibers,[87-90] nanowires,[55] and nanoparticles.[91] These nanostructured materials exhibit better sensing performance than their thin film counterparts,[92-94] as finely designed nanostructures with high surface-to-volume ratios can enhance the diffusion of gas molecules. Some other methods have yielded surprising results, such as PPy multilayer architecture or PANI treatment.[90,94,95] Additionally, recent research has shown that introducing electrical percolation can provide an ideal response to $NH_3$.[31] Compared to PPy and PANI, only a few PTh and its derivatives have been used for $NH_3$ detection due to their lower responses.[96,97]

Moreover, $NO_x$ gases, particularly $NO_2$, have been extensively researched. PPy thin films have been developed for the detection of $NO_2$,[98] and the sensor response and response time can be improved by introducing appropriate dopants.[99] This suggests that dopants may enhance the performance by modulating the doping level and morphology of the polymer films. PANI can also detect $NO_2$ with desirable performance when fabricated into a thin film or a nanofibrous thin film.[100-102] Some response values based on PANI are negative, as the resistance decreases when interacting with $NO_2$. Moreover, PTh and its derivatives can detect $NO_2$ with similar performance to PPy.[103-105] Also, NO can be detected by poly(3,4-ethylenedioxythiophene) polystyrene sulfonate (PEDOT:PSS), although the sensor response is not desirable.[106]

Additionally, PPy and PANI have demonstrated their ability to detect other hazardous gases, including hydrogen chloride (HCl),[107] hydrogen sulfide ($H_2S$),[108] carbon monoxide (CO),[109] carbon dioxide ($CO_2$),[110] and sulfur dioxide ($SO_2$).[111] However, they displayed limited responses. Table 2.3 summarises the representative CP-based chemiresistors that have been developed for each hazardous gas mentioned above. Unfortunately, the differences in test conditions make it challenging to systematically compare their performance.

**Table 2.3.** Representative CP-based chemiresistors to different hazardous gases.

| Gas | Material | Detection range | Performance[a] | | | Ref. |
|---|---|---|---|---|---|---|
| | | | Response[b] | Response time | Recovery time | |
| $NH_3$ | PPy thin film | 5 – 100 ppm | 0.14 @ 20 ppm | 20 s @ 20 ppm | 15 min @ 20 ppm | 92 |
| | PPy nanofibers | 20 – 150 ppm | 0.53 @ 150 ppm | 15 s @ 20 ppm | - | 87 |
| | PPy multilayer thin film | 5 – 200 ppm | 77.75 @ 50 ppm | 12 s @ 50 ppm | 52 s @ 50 ppm | 95 |
| | PPy nanowire array | 1.5 – 77 ppm | 0.26 @ 77 ppm | 60 s @ 77 ppm | - | 55 |
| | Urchi-like PPy nanoparticles | 0.01 – 10 ppm | 0.03 @ 10 ppm | < 1 s @ 0.1 ppm | ~ 30 s @ 0.1 ppm | 91 |
| | PANI thin film | 1 – 100 ppm | 0.65 @ 50 ppm | 10 s @ 50 ppm | 70 s @ 50 ppm | 93 |
| | HCl doped PANI film | - | 9.08 @ 100 ppm | 173 s @ 100 ppm | 294 s @ 100 ppm | 94 |
| | PANI nanofibrous thin film | 0.5 – 20 ppm | 2.25 @ 20 ppm | 60 s @ 20 ppm | 60 s @ 20 ppm | 88 |
| | PANI nanofiber | 5 – 200 ppm | 1.06 @ 50 ppm | 60 s @ 50 ppm | 60 s @ 50 ppm | 89 |
| | HCl treated PANI nanofibers | 1 – 200 ppm | 10 @ 50 ppm | 1 s @ 50 ppm | - | 90 |
| | PTh pellet | 25 – 650 ppm | 0.50 @ 300 ppm | - | - | 96 |
| | PEDOT nanorods | 10 – 100 ppm | 0.28 @ 100 ppm | 10 s @ 100 ppm | ~ 70 s @ 100 ppm | 97 |
| $NO_2$ | PPy thin film | 10 – 100 ppm | 0.36 @ 100 ppm | 126 s @ 100 ppm | 2170 s @ 100 ppm | 98 |
| | CSA doped PPy thin film | 10 – 100 ppm | 0.52 @ 100 ppm | 81 s @ 100 ppm | 2070 s @ 100 ppm | 99 |
| | PANI thin film | - | −0.995 @ 20 ppm | - | - | 100 |
| | PANI thin film | 50 – 250 ppb | 2.0 @ 250 ppb | - | - | 101 |
| | PANI nanofibrous thin film | 10 – 100 ppm | −0.995 @ 50 ppm | ~ 23 s @ 50 ppm | 2 min @ 50 ppm | 102 |
| | PTh thin film | 10 – 100 ppm | 0.33 @ 100 ppm | 220 s @ 100 ppm | 1603 s @ 100 ppm | 103 |
| | Interconnected nanofibrous PTh thin film | 25 – 150 ppm | 0.48 @ 100 ppm | ~ 80 s @ 100 ppm | ~ 8000 s @ 100 ppm | 104 |
| | PEDOT nanotubes | 0.2 – 63 ppm | 0.55 @ 63 ppm | - | - | 105 |
| NO | PEDOT:PSS thin film | 2.5 – 10 ppm | ~ 0.06 @ 10 ppm | - | - | 106 |
| HCl | PPy nanosheets | 20 – 100 ppm | - | 13 s @ 100 ppm | - | 107 |
| $H_2S$ | PPy thin film | 10 – 100 ppm | ~ 0.35 @ 100 ppm | 13 s @ 100 ppm | 644 s @ 100 ppm | 108 |
| CO | nanocrystalline PANI thin film | 0.06 – 0.30 ppm | −0.998 @ 0.30 ppm | ~ 8 s @ 0.30 ppm | ~ 8 s @ 0.30 ppm | 109 |
| $CO_2$ | PANI thin film | 50 – 5000 ppm | −0.1 @ 1000 ppm | - | - | 110 |
| $SO_2$ | PANI nanoneedles | 10 – 75 ppm | 0.04 @ 10 ppm | ~ 180 s @ 10 ppm | ~ 180 s @ 10 ppm | 111 |

Note: PPy = polypyrrole; PANI = polyaniline; PTh = polythiophene; CSA = camphor sulfonic acid; PEDOT = poly(3,4-ethylenedioxythiophene); PEDOT:PSS = poly(3,4-ethylenedioxythiophene) polystyrene sulfonate.
[a]Operating temperature for the tests is the room temperature. [b]Response = $(R_a - R_0)/R_0$ ($R_a$: the device resistance in the presence of analytes; $R_0$: the intrinsic device resistance without analytes).

### 2.2.4.2 Volatile compound detection

Volatile compounds are chemical substances that exist as solids or liquids and can be easily vaporised under standard temperature and pressure. Similar to hazardous gases, volatile

compounds have the potential to harm human health and the environment. Furthermore, monitoring humidity caused by water vapour also plays a crucial role in various applications. Thus, the detection of volatile compounds is significant in many fields. Previous research has demonstrated that CP-based chemiresistors can detect various vapours with acceptable sensitivity and response time.[112] The performance of these sensors may depend on the type of analyte being detected. Polar molecules, for instance, can induce a screening effect between the charge carriers and the counter ions, reducing the Coulomb interaction between the polymers and the dopants. This effect can improve intermolecular hopping and lead to high and fast responses. However, CP-based chemiresistors did not exhibit clear selectivity for specific vapours due to their limited sensing diversity. This has drawn more interest towards the development of chemically diverse sensors.

Both PPy and PANI films have been extensively studied to develop chemically diverse sensors.[113] Various dopants and different doping levels have been investigated to explore their effects on device performance. The use of dopants can diversify the performance of the device. For example, in the case of PPy-based chemiresistors, the addition of nitric acid can result in different directions of resistance changes to different vapours. The impact of doping levels on device performance is contingent on the polarity of the vapours being detected. A low doping level may have little effect on non-polar molecules, as these molecules mainly induce physical interactions with the polymers rather than chemical reactions. In contrast, a suitable doping level may enhance the sensitivity of the device to polar molecules.

Molecular design can achieve chemical diversity and device selectivity through three approaches. Firstly, copolymerisation can expand the diversity of sensing materials. It has been reported that diverse devices can be fabricated by copolymerising pyrrole with different vinyl derivatives.[114,115] Statistical analysis of response patterns has demonstrated that this approach can distinguish up to 12 different vapours. The second approach is to investigate novel

polymers. For instance, polyindole (PIn) has been systematically studied to detect 8 vapours with varying molecular polarities.[116] Similar to PPy and PANI, the performance of PIn-based chemiresistors can be improved by modulating the dopants and doping levels. It has been demonstrated that PIn-based chemiresistors are highly sensitive to methanol due to the strong hydrogen bond interaction. Lastly, modifying the conjugated polymers is the third approach. PEDOT:PSS nanowires modified with different functional side chains have been reported to offer different responses to ketones, alcohols, alkanes, aromatics, and amines.[117] It is assumed that this approach can be applied to other CPs as well.

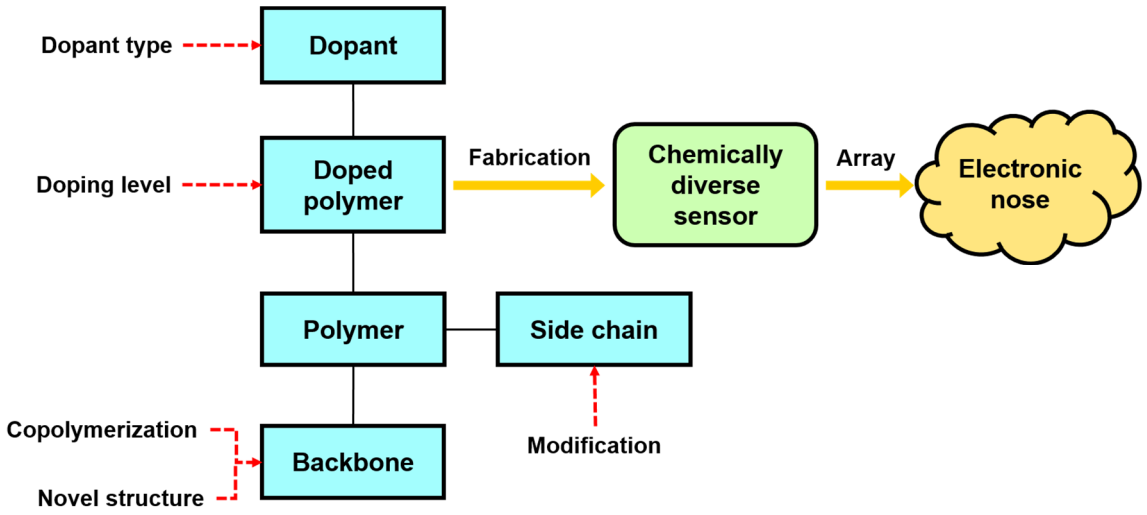


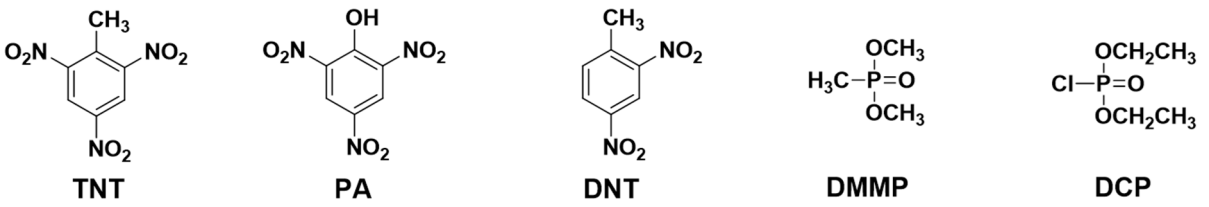

**Figure 2.6.** Approaches to the electronic nose base on conjugated polymers. Chemically diverse sensors with various sensitivities and selectivities to the analytes can be achieved through the modulation of the dopant type and doping level as well as the molecular design of the polymer backbone and side chain. An electronic nose approach based on the arrays of the chemically diverse sensors is then developed to analyse chemical mixtures.

To sum up, chemical diversity can be achieved through the modulation of doping conditions and molecular design, which can improve device sensitivity and selectivity independently or synergistically. Chemically diverse sensors can then be arrayed together to distinguish target vapours in a mixture, thereby realising an electronic nose approach (Figure 2.6). Although each

CP-based chemiresistor is not ideally selective, an array of chemically diverse sensors can provide a pattern or a plot of all their responses for further analysis to discriminate target vapours. Based on experimental results, statistical methods have been developed for the electronic nose approach to analyse multi-component vapour mixtures.[118] The electronic nose approach has also shown potential applications in daily life. For instance, it has been reported that CP-based electronic noses can distinguish virgin coconut oil from other types of coconut oil.[119] However, this approach can only distinguish a limited number of chemicals rather than more complex mixtures in the real world, revealing the challenge of transferring it to practical applications.

### 2.2.4.3 Warfare chemical detection

In regional conflicts, several types of chemical warfare agents might be deployed. Explosives are easy to use and can cause enormous damage instantly. Nerve agents, on the other hand, can cause death when people are exposed to or breathe in their vapours for several minutes. Moreover, the residues of these chemicals left behind by military operations can cause secondary damage to both human health and the environment. Therefore, there is an urgent need to detect these warfare chemicals due to fundamental global issues of anti-terrorism, human health, and the environment.




**Scheme 2.5.** Molecular structures of 2,4,6-trinitrotoluene (TNT), picric acid (PA), 2,4-dinitrotoluene (DNT), dimethyl methylphosphonate (DMMP), and diethylchlorophosphate (DCP).

Many explosives are nitroaromatic and primarily consist of 2,4,6-trinitrotoluene (TNT), picric acid (PA), and 2,4-dinitrotoluene (DNT) (Scheme 2.5). Detecting the vapours of these explosives using CP-based chemiresistors is challenging as they have extremely low vapour pressures, at or even below the parts per billion (ppb) level at room temperature.[1] Given this challenge and their immense destructive power within a short period, achieving high sensitivity and fast response is a top priority in explosive detection. The introduction of side chains with specific functional groups can enable ppb-level detection. PPy modified with n-butylamine has been studied to detect TNT and exhibited a low limit of detection (0.2 ppb) and fast responses (<1 s).[120] These desirable performances are due to the complexation of the amino end groups with the uncharged TNT molecules. Moreover, suitable substrates may lead to surprising results. PANI fibres spray-coated on filter paper can detect ppb concentrations of TNT, PA, and DNT within 10 s.[121] The high sensitivities and fast responses may be attributed to the unique interlaced flower-like structure of PANI.

Detecting nerve agents also requires high sensitivity and fast response due to their rapid lethality. Directly studying the sensing responses to nerve agents in the laboratory is not realistic, leading researchers to study their mimic chemicals. Dimethyl methylphosphonate (DMMP) and diethylchlorophosphate (DCP) are considered as two representative nerve agent mimics, with special molecular structures similar to nerve agents and organophosphate groups critical to nerve function (Scheme 2.5). To effectively detect these target groups, specific functional groups should be introduced to the backbones of CPs during material preparation. Carboxylated PPy nanotubes have been reported to detect DMMP at 0.5 ppb owing to the hydrogen bonding formed between carboxyl groups and DMMP molecules.[122] Additionally, poly(3-(9,9-dioctyl-9H-fluoren-2-yl)benzene-1,2-diamine) (PFPDA) has been developed for DCP detection, demonstrating a low detection limit of 5.88 ppb and a fast response time of 3

s.[123] Supported by DFT calculation, these desirable performances may be attributed to the dipole-dipole interaction between amine groups on PFPDA backbones and DCP molecules.

#### 2.2.4.4 Biomolecule and ion detection

Suitable CP-based chemiresistors can also detect biomolecules and ions. Biomolecule detection is essential in clinical diagnosis and treatment as it reveals the underlying biochemical processes of organisms. Ion detection, on the other hand, plays a critical role in healthcare, environmental monitoring, and industrial production. Despite the differences in the targets, the research strategies for biomolecule and ion detection share some similarities. Therefore, the applications of biomolecule and ion detection have been introduced together here.

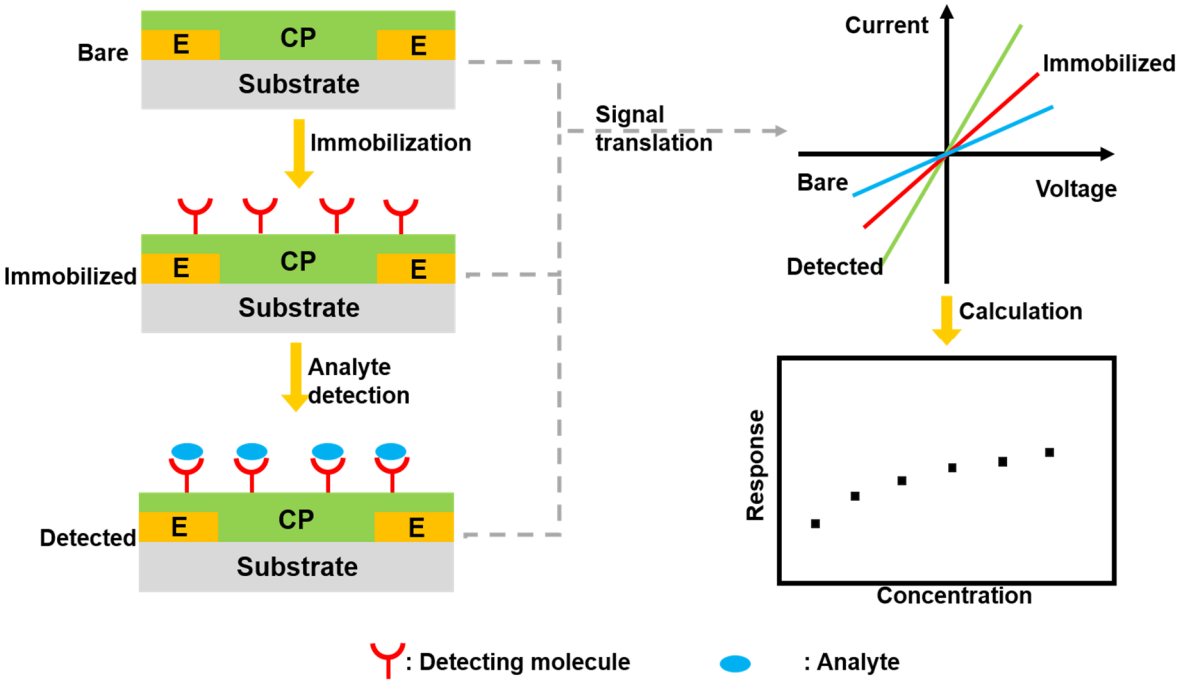



**Figure 2.7.** Schematic representation of the research procedure for biomolecule and ion detection. The resistance of the conjugated polymers (CPs) with immobilized detecting molecules, obtained from the voltage-current characteristics, can be altered by the interaction between the detecting molecules and the analytes. By analysing the different resistance changes caused by varying concentrations of analytes, a relationship between the sensor response and the concentration can be achieved through calculation. (E: electrode)

The immobilisation of detecting molecules is crucial in biomolecule and ion detection. This approach is similar to the modification for warfare chemical detection. The functional groups on detecting molecules react with end groups on polymer backbones, which immobilises detecting molecules on polymer chains (Figure 2.7). For effective detection, detecting molecules must specifically interact with target biomolecules and ions. Consequently, detecting molecules must have dual functions that facilitate the reactions with polymers and the interactions with analytes. Cosnier and Holzinger have summarised the immobilisation of electrosynthesised polymers,[124] while Lee *et al*. have expanded the scope by systematically summarising various immobilisation methods for different types of polymers.[125]

**Table 2.4.** Representative CP-based chemiresistors for biomolecule and ion detection.

| Analyte | Polymer | Detecting molecule | Detection limit | Ref. |
|---|---|---|---|---|
| His5-Syntaxin protein | PPy nanotube | Nitrilotriacetic acid | 1 ng $mL^{-1}$ in water | 126 |
| Cancer antigen 125 | PPy nanowire | Anti-CA 125 MAbs | 1 U $mL^{-1}$ in PB | 127 |
| Bacillus globigii | PPy nanowire | Anti-B. globigii MAbs | 1 CFU $mL^{-1}$ in PB | 128 |
| T7 phage | PPy nanowire | Anti-T7 antibody | $10^{-3}$ PFU in PB | 129 |
| Biotin | PEDOT-co-PTh | Avidin | ~ 1 nM in PB | 130 |
| Oligonucleotide | PEDOT nanowire | Probe oligonucleotide | $10^{-14}$ M in PB | 131 |
| Cucumber mosaic virus | PPy nanoribbon | Polyclonal anti-CMV IgG | 10 ng $mL^{-1}$ in PB | 132 |
| $Cu^{2+}$ | PPy nanotube | Nitrilotriacetic acid | $10^{-14}$ M in water | 126 |

Note: PPy = polypyrrole; PEDOT = poly(3,4-ethylenedioxythiophene); PTh = polythiophene; PB = phosphate buffer; CA 125 = cancer antigen 125; MAb = monoclonal antibody; CMV = cucumber mosaic virus; IgG = immunoglobulin G; U $mL^{-1}$ = units per millilitre; CFU $mL^{-1}$ = colony-forming units per millilitre; PFU = plaque forming unit.

Biomolecule and ion detection is carried out using the same test method. In contrast to other applications, the device resistances are obtained from the voltage-current characteristics of CP-based chemiresistors. The resistances of both bare and immobilised devices are calculated before the detection tests. The sensing layers are then covered with drops of analytes or

incubated in solutions of analytes for a specified time. The altered resistances are obtained from the corresponding voltage-current characteristics. This electrical test is repeated to record different resistance changes caused by varying concentrations of analytes. Finally, the device sensitivity is assessed by analysing the responses across various concentrations. Figure 2.7 presents the research procedure of biomolecule and ion detection. Recently, electrochemical transistors have been reported to achieve lower detection limits,[131] raising more attention to biomolecule and ion detection based on that device configuration.[125,133] Nonetheless, several studies are still based on chemiresistors,[126-132] which are summarised in Table 2.4.

## 2.3 Conjugated polymer based electrical percolation

### 2.3.1 Electrical percolation in materials science

In order to investigate the gelation processes in branched polymers, percolation was initially discussed by Flory and Stockmayer in the 1940s.[134,135] Following its mathematical description formulated by Broadbent and Hammersley in 1957,[136,137] then, this theory has been extensively developed in the field of materials science. In materials science, percolation refers to the phenomenon where a specific property of a material, such as electrical conductivity, thermal conductivity, or mechanical strength, changes as a function of the concentration or arrangement of its constituent components. This change occurs when the concentration or connectivity of one of the components reaches a critical threshold, resulting in a significant change in that particular property. This significant change typically describes that the target property appears or disappears at the threshold on a macroscopic scale. As the concentration or arrangement of the constituent components change, furthermore, percolation pathways can be formed by connecting bonds (Figure 2.8a) or sites (Figure 2.8b). The type of percolation may depend on the microscopic morphology of the constituent components.

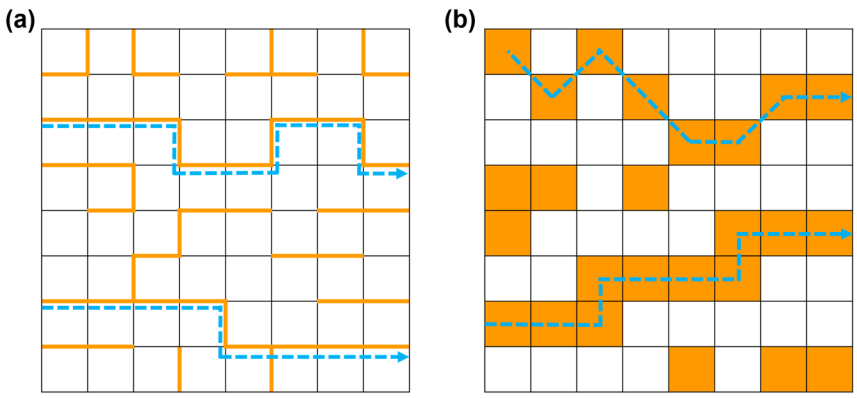



**Figure 2.8.** Schematic representation of (a) bond percolation and (b) site percolation. The bold lines and squares represent the connecting bonds and sites respectively. Formed percolation pathways from left to right sides are indicated by dash lines.

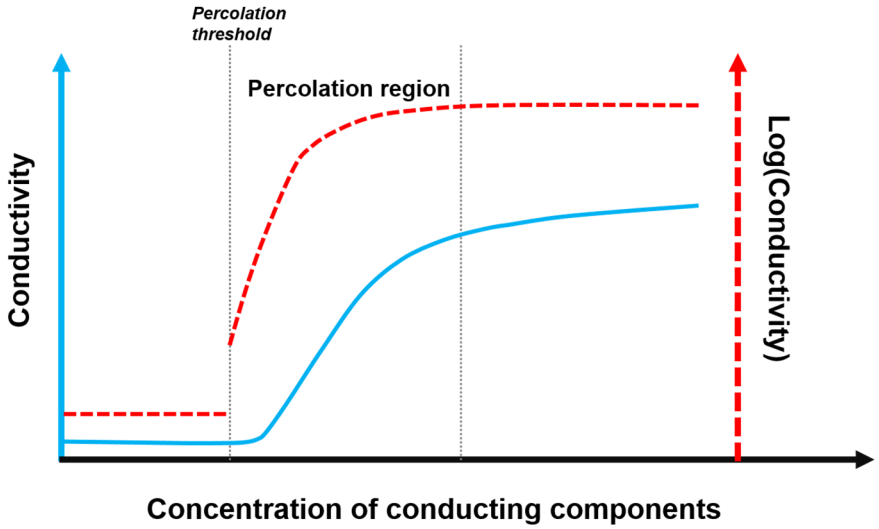



**Figure 2.9.** Schematic plot (blue line) of conductivity vs. concentration of conducting components and its semi-logarithmic plot (red dashed line). The conductivity significantly increases in the percolation region and the onset of this change is defined as the percolation threshold.

Electrical percolation is a well-studied application of percolation theory in recent decades. It describes the change in electrical conductivity as a function of the concentration of conducting bonds and/or sites within or on a medium. As the concentration of conducting components increases in an investigated system, typically, an S-shaped plot depicting the conductivity of the system can be obtained (Figure 2.9). Its semi-logarithmic plot can more

clearly present the change in conductivity and determine the boundaries of electrical percolation in practical experiments. Initially, no conducting pathways are formed due to the very low concentration of conducting components. As a result, no or extremely low conductivity can be detected in the investigated system. This insulating state persists until one or several percolation pathways are achieved through the connection of conducting bonds and/or sites. At this critical threshold, the conductivity suddenly jumps to a higher value than that in the insulating state, indicating the onset of electrical percolation. This sudden increase in conductivity is generally reflected through the discontinuous change in the semi-logarithmic plot (Figure 2.9). The conductivity then further increases rapidly as more percolation pathways are formed, and this increasing trend should depend on the increase in the number of conducting pathways. When the number of pathways is large enough, the investigated system reaches a saturated state, and the increase in conductivity slows down, indicating the end of electrical percolation.

As mentioned above, electrical percolation occurs within or on a medium. Therefore, there are generally two approaches to preparing materials that contain percolation pathways in practical experiments: the filler-in-matrix and conductor-on-substrate strategies. The preparation of filler/matrix composites is a commonly used method due to its processing simplicity and the availability of various materials. These composites can be easily obtained by introducing conductive fillers into an insulating matrix through physical blending, melt compounding, and in situ reactions. Electrical percolation occurs when the concentration of the fillers reaches a percolation threshold. Various conductive fillers have been applied to form percolation pathways, such as nanostructured metals,[138,139] carbon materials,[29,140,141] conjugated polymers, and perovskite compounds.[142,143] Insulating polymers, such as thermoplastic plastics, thermoplastic elastomers, thermosetting plastics, and rubbers, are typically used as the matrices due to their desirable processability and mechanical properties.

Composites with these polymeric matrices are considered conductive polymer composites.[144] Other studies have also shown that inorganic salts and metal organic frameworks can be used as the matrices for electrical percolation.[145,146] According to the percolation theory,[147] the electrical conductivity of the filler/matrix composite (σ) can be described by a statistical percolation model of the filler content as the following equation:

$$\sigma = c(p - p_c)^t \tag{2.3}$$

where $p$ is the weight/volume fraction of the filler and $p_c$ is the filler fraction at the percolation threshold, while $c$ is the constant. As a critical exponent, moreover, $t$ describes the dimensionality of the electrical percolation network. In filler/matrix composites, theoretically, this critical exponent takes values of approximately 1.33 for a 2D electrical conduction process and around 2 for a 3D conduction process. However, recent studies on nanostructured fillers have challenged this classical model since this model has yielded various critical exponents higher than 2.[148-151] This departure from the classical model is attributed to the fact that this model does not evaluate carrier tunnelling, filler geometry, and the interphase effects on electrical percolation.[151]

On the other hand, electrical percolation can be achieved by depositing conductors on suitable substrates. As the conducting materials grow and connect with each other on the substrate, percolation pathways are formed. Many conducting materials can be used as conductors, including carbon nanotubes,[152,153] conjugated polymers, and metal clusters.[34,154] Substrates are generally made of insulating materials, such as glass and aluminium oxides. In several studies, also, conductors have been reported to be deposited on semiconductors.[155,156] Both the filler-in-matrix and conductor-on-substrate strategies have been summarised in Figure 2.10, and relevant studies on conjugated polymers are presented in the next two sections.

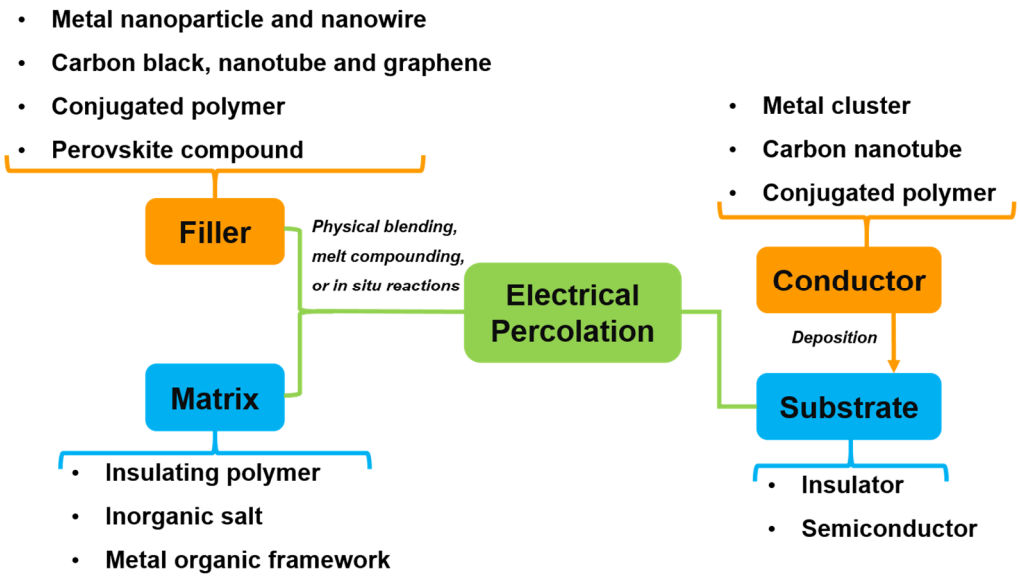



**Figure 2.10.** Schematic representation of the filler-in-matrix and conductor-on-substrate strategies to achieve electrical percolation.

## 2.3.2 Filler-in-matrix strategy based on conjugated polymer

### 2.3.2.1 Development in preparing methods (since the early 1990s)

Various CPs have been utilised as the fillers in filler/matrix composites. In the early stages of this field, dating back to the early 1990s, the primary objective of preparing such composites was to enhance the processability of CPs and/or achieve favourable mechanical properties. The threshold of electrical percolation was used to determine the boundary of conductivity. Different preparing methods were explored during this period, playing a fundamental role in advancing this field. These methods with representative studies have been summarised as follows:

***In situ polymerisation***. In situ polymerisation generally refers to the process of synthesising polymers in the presence of fillers or matrices within the same environment. Wang *et al.* employed in situ electrochemical polymerisation to study the percolation thresholds of polypyrrole/polystyrene (PPy/PS) and polypyrrole/polycarbonate (PPy/PC) composites.[157]

However, the insulating matrices had to be pre-deposited on working electrodes. To simplify the preparation, Morsli *et al*. introduced polybithiophene (PBTh) into PS matrices via in situ chemical polymerisation.[158,159] Various PBTh/PS composites were prepared by simply immersing dried PS matrix samples containing different amount of bithiophene monomers in a solution of oxidant. To improve the processability of the composites, this chemical approach was further developed using solution, emulsion, or suspension-based systems. For instance, Nicho *et al*. synthesised PANI in solutions of different insulating polymers,[160] while Mpoukouvalas *et al*. prepared PPy in PS emulsions.[161] Furthermore, this developed method proved effective for the preparation of conjugated polymer/oxide nanocomposites with percolation pathways.[162-164]

***Solution blending***. Solution blending involves the physical blending of fillers with matrices in suitable solvents. Cao *et al*. utilised this technique to incorporate PANI into poly(methyl methacrylate) (PMMA) and polyethylene (PE).[165] Owing to the adjustable solubility of PANI in its conducting emeraldine salt form or insulating emeraldine base form, further investigations have involved the preparation of various PANI-based composites using different polymers as matrices.[166-168] As more soluble conjugated polymers have been developed, other fillers have also been explored, such as PEDOT:PSS, poly(3-oylthiophene) (P3OT),[169] and poly(o-toluidine) (POT).[170] Furthermore, this method has been successfully applied to dispersible nanomaterials. For example, Mendez *et al*. achieved successful blending of PEDOT:PSS-coated cellulose nanofibers with poly(ethylene oxide) (PEO) in water and PS in dimethylformamide (DMF).[171]

***Dry mixing***. Dry mixing refers to the process of directly mixing dried fillers and matrices under high pressure. For instance, Watcharaphalakorn *et al*. achieved various PANI-based composites via dry mixing of PANI and polyimide (PI) powders.[172] The powders were mixed and ground together, and composite samples were subsequently prepared by compressing the

mixture using a hydraulic press. However, it should be noted that this method has certain limitations as the resulting composites are typically obtained in pellet form.

***Hot pressing***. Hot pressing is a method that involves blending fillers with matrices at high temperatures and under high pressure. This process requires the matrix to possess thermoplastic properties and should be carried out above the glass transition temperature of the matrix.[173] For instance, Yin *et al*. blended different PPy-coated nylon micro-fibres or PPy-coated PS micro-spheres with PE micro-spheres at 130 °C and 2950 kg $cm^{-2}$.[174-176] They successfully obtained composites with different percolation thresholds. Similarly, Zilberman *et al*. achieved the incorporation of PANI into various thermoplastic matrices using the hot pressing method.[177]

The representative CP-based filler/matrix composites prepared using the aforementioned methods have been summarised in Table 2.5. The percolation thresholds of these composites are mostly provided as weight/volume fractions of the filler relative to the total weight/volume of the composite. It is important to note that some of the mentioned methods can also be employed for other synthesis processes prior to composite preparation or as post-treatment procedures. For example, in situ polymerisation can be utilised to coat the fillers with CPs prior to composite preparation, and hot pressing can be applied as a post-treatment method to produce pellet samples after composite preparation. Additionally, it has been reported that copolymerizing CPs with insulating counterparts holds potential as a means to introduce fillers into matrices at a molecular level.[178] However, it should be noted that the conductivity of the copolymer does not adhere to the classic percolation model (equation 2.3). With the rapid advancements in organic electronics, several techniques based on in situ polymerisation and solution blending have been exclusively developed for CPs. As a result, these two methods have gradually emerged as the mainstream approaches for preparing CP-based filler/matrix composites after 2000.

**Table 2.5.** A summary of representative CP-based filler-matrix composites.

| Year | Filler | Matrix | Preparing method | Percolation threshold[a] | Ref. |
|---|---|---|---|---|---|
| 1990 | PPy | PS | In situ polymerisation | 12 wt% | 157 |
| 1990 | PPy | PC | In situ polymerisation | 7 wt% | 157 |
| 1992 | PANI | PMMA | Solution blending | 2 wt% | 165 |
| 1992 | P3OT | PE | Solution blending | 0.5 wt% | 169 |
| 1994 | PPy-coated nylon fibre | PE sphere | Hot pressing | 2 − 5 vol% | 174,175 |
| 1994 | PPy-coated PE sphere | PE sphere | Hot pressing | 10 − 20 vol% | 174,175 |
| 1996 | PBTh | PS | In situ polymerisation | ~ 0.2[b] | 158,159 |
| 1997 | PANI | PVA | Dry mixing | 10 vol% | 178 |
| 1997 | PANI | PVP | Dry mixing | 8 vol% | 178 |
| 1997 | PANI | $NH_4SO_4$ | Dry mixing | 2.5 vol% | 178 |
| 1998 | PANI | PAA | Solution blending | < 5.5 wt% | 166 |
| 1998 | PANI | PS | Solution blending | 0.6 vol% | 167 |
| 1998 | PANI | PCL | Hot pressing | 5 wt% | 177 |
| 1998 | PANI | PA | Hot pressing | 10 wt% | 177 |
| 1999 | PPy particle (100 nm) | Epoxy | Solution blending | 11 − 16 wt% | 179 |
| 1999 | PPy particle (400 nm) | Epoxy | Solution blending | 3 wt% | 179 |
| 1999 | PANI | PI | Solution blending | < 5 wt% | 168 |
| 1999 | PANI | PMMA | In situ polymerisation | ~ 4(8) wt%[c] | 160 |
| 1999 | PANI | PVK | In situ polymerisation | ~ 9(9) wt%[c] | 160 |
| 1999 | PANI | PS | In situ polymerisation | ~ 8(12) wt%[c] | 160 |
| 1999 | POT | ABS | Solution blending | 2.66 wt% | 170 |
| 2000 | PANI | PE | Solution blending | 8 wt% | 180 |
| 2002 | PANI | EVA | Solution blending | < 5 wt% | 181 |
| 2002 | PPy micro particle | PS | Hot pressing | 12 vol% | 173 |
| 2002 | PPy | PVC micro particle | In situ polymerisation | ~ 6 min[d] | 182 |
| 2002 | PPy-coated particle | PVC micro particle | Dry mixing | 20 wt% | 182 |
| 2002 | PDPA | PVDF | Solution blending | 5 wt% | 183 |
| 2003 | POT | PVDF | Solution blending | 2 wt% | 184 |
| 2005 | PPy | Pulp fibre | In situ polymerisation | 1.7 wt% | 185 |
| 2005 | PPy-coated pulp fibre | Pulp fibre | Solution blending | 0.52 wt% | 185 |
| 2005 | PANI | PAA | Solution blending | 21 wt% | 186 |
| 2005 | PANI | PI | Dry mixing | 45 wt% | 172 |
| 2007 | PANI | CTA | Solution blending | 9.5 wt% | 187 |
| 2007 | PANI | $SiO_2$ | In situ polymerisation | 1.1 wt% | 163 |
| 2007 | PANI | PU | Solution blending | 2.7 wt% | 188 |
| 2007 | PANI | PU | In situ polymerisation | 2.0 wt% | 188 |
| 2007 | PANI nanofiber | PMMA | Solution blending | 2.2 wt% | 189 |
| 2008 | PANI nanofiber | PAA | Solution blending | 20 wt% | 190 |
| 2008 | PANI powder | PAA | Solution blending | 30 wt% | 190 |
| 2009 | PPy | PS nanoparticle | In situ polymerisation | 65 vol% | 161 |
| 2009 | Nanostructured PANI | PS | In situ polymerisation | 5 wt% | 191 |
| 2009 | PANI | PS | Solution blending | > 25 wt% | 191 |
| 2009 | PPy | $SiO_2$ | In situ polymerisation | 20 wt% | 164 |
| 2010 | PANI | ABS | Solution blending | 3 wt% | 192 |

(Continued)

**Table 2.5.** (Continued)

| Year | Filler | Matrix | Preparing method | Percolation threshold[a] | Ref. |
|---|---|---|---|---|---|
| 2010 | PPy nanoparticle | CDA | Solution blending | 0.2 wt% | 193 |
| 2010 | PEDOT-coated nanofiber | PEO | Solution blending | 2 vol% | 171 |
| 2011 | PANI | PES | Solution blending | 2 wt% | 194 |
| 2011 | PANI nanofiber | PU | Solution blending | 0.3 wt% | 195 |
| 2012 | PANI | PES | Solution blending | ~ 2 wt% | 196 |
| 2012 | PPy particle | SEBS | Solution blending | 6 wt% | 149 |
| 2012 | PPy-coated $SiO_2$ fibre | SEBS | Solution blending | 1 wt% | 149 |
| 2013 | PPy nanowire | PDMS | Solution blending | 9.6 vol% | 197 |
| 2013 | PANI | Nano-cellulose | In situ polymerisation | 4.57 vol% | 150 |
| 2013 | PEDOT:PSS | Nano-cellulose & PS | Solution blending | 0.4 wt% | 198 |
| 2013 | PEDOT:PSS | PS | Solution blending | 2.2 wt% | 198 |
| 2013 | PANI | PS nanosphere | In situ polymerisation | 0.059 wt%[e] | 199 |
| 2014 | PANI | PVA | In situ polymerisation | 3 − 15 wt% | 200 |
| 2014 | PPy | PVDF | Solution blending | 3 wt% | 201 |
| 2016 | PANI | Star PAA-b-PBA | In situ polymerisation | 4.20 vol% | 202 |
| 2016 | PANI | Linear PAA-b-PBA | In situ polymerisation | 3.64 vol% | 202 |
| 2016 | P3HT nanoparticle | PS nanoparticle | Solution blending | ~24 – 30 wt% | 203 |
| 2017 | PEDOT:PSS | Commingled yarns | Solution blending | 8 – 10 wt% | 204 |
| 2017 | PANI | PVA | Solution blending | 20 vol% | 205 |
| 2017 | PDH4T | Novolac | In situ polymerisation | 6.1 wt% | 206 |
| 2017 | P3T | Novolac | In situ polymerisation | 9.7 wt% | 206 |
| 2017 | PANI | PVDF | Hot pressing | 40 – 50 vol% | 207 |
| 2017 | PEDOT:PSS | PDMS | Solution blending | 2 – 5 wt% | 208 |
| 2018 | PPy | PVDF-CTFE | Solution blending | ~7.4 wt% | 209 |
| 2019 | PEDOT:PSS | XBS nanosphere | Solution blending | ~1.6 wt% | 210 |
| 2020 | PANI | Photocurable acrylic | In situ polymerisation | ~2.9 vol% | 211 |
| 2020 | PEDOT:PSS | PU | Solution blending | 15 wt% | 212 |
| 2020 | PEDOT:PSS | PDMS | Solution blending | 1.8 wt% | 213 |
| 2021 | PANI | PVA | In situ polymerisation | 2.1 vol% | 214 |
| 2021 | POT | PVA | In situ polymerisation | 2.8 vol% | 214 |
| 2021 | POT | PAA | In situ polymerisation | 2.3 vol% | 214 |
| 2022 | PEDOT:PSS | Hydrophilic PDMS | Solution blending | 0.236 wt% | 151 |

Note: PPy = polypyrrole; PS = polystyrene; PC = polycarbonate; PANI = polyaniline; PMMA = poly(methyl methacrylate); P3OT = poly(3-oylthiophene); PE = polyethylene; PBTh = polybithiophene; PVA = poly(vinyl alcohol); PVP = poly(*N*-vinylpyrrolidone); PAA = poly(acrylic acid); PCL = poly-ε-caprolactone; PA = polyamide; PI = polyimide; PMMA = poly(methyl methacrylate); PVK = poly(vinyl carbazole); POT = poly(o-toluidine); ABS = acrylonitrile-butadiene-styrene copolymer; EVA = ethylene-vinyl acetate copolymer; PVC = polyvinyl chloride; PDPA = poly(diphenylamine); PVDF = poly(vinylidene fluoride); CTA = cellulose triacetate; CDA = cellulose diacetate; PU = polyurethane; PEO = poly(ethylene oxide); PES = poly(ether sulfone); PDMS = polydimethylsiloxane; SEBS = styrene-ethylene-butylene-styrene copolymer; PEDOT:PSS = poly(3,4-ethylenedioxythiophene) polystyrene sulfonate; P3HT = poly(3-hexylthiophene); PAA-b-PBA = poly(acrylic acid)-*block*-poly(*n*-butyl acrylate) copolymers; P3T = polyterthiophene; PDH4T = poly(dihexyl-quaterthiophene); PVDF-CTFE = poly(vinylidene fluoride-chlorotrifluoroethylene); XSB = carboxylated styrene-butadiene copolymer. [a]A wide range of thresholds exists as the threshold depends on various factors, such as the dispersion and aspect ratio of the filler, the type and surface-to-volume ratio of the matrix, and the interaction between the filler and matrix. [b]This percolation threshold was observed to be achieved at an oxidant/monomer ratio of approximately 0.2. [c]Values in brackets represent the percolation thresholds obtained from composite samples with larger surface areas. [d]This percolation threshold was observed to be achieved at approximately 6 minutes of polymerisation. [e]This percolation threshold is a theoretical value obtained from mathematical treatment.

### 2.3.2.2 Approaches to better materials (since the late 1990s)

During the 1990s, various CP-based filler/matrix composites were obtained using different preparation methods. Subsequently, systematic studies were conducted to investigate the relationship between their structures and properties. With the development of more soluble CPs and dispersible conductive nanocomposites, moreover, the challenge of polymer processability has been overcome. As a result, there has been a natural progression towards exploring approaches to achieve improved composites. Since the late 1990s, a key objective has been to prepare composites with lower percolation thresholds. The focus on this parameter is motivated by the understanding that reducing the minimum filler loading required for conductivity is the most effective way to maintain desirable physical and mechanical properties of conductive composites. By achieving lower percolation thresholds, these composites become more practical for real-life applications.

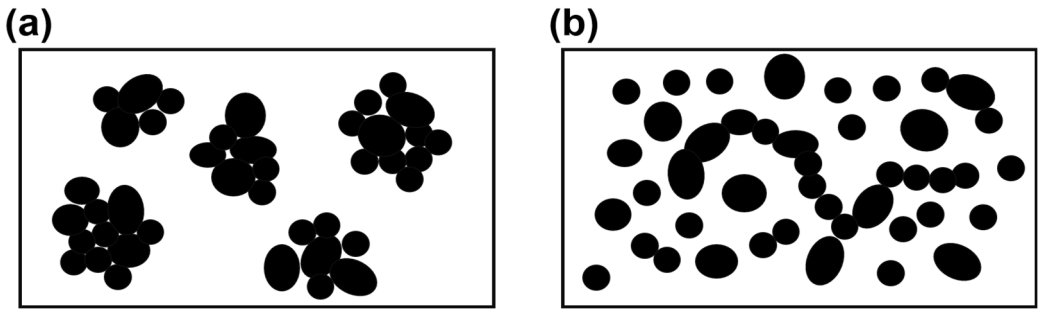



**Figure 2.11.** Illustrative scheme of two hypothetic composites containing (a) aggregated fillers and (b) fillers achieved through better dispersion. Poor dispersion in the matrix can lead to isolated clusters, hindering the formation of continuous conducting pathways.

According to Table 2.5, the attainment of lower percolation thresholds appears to be more feasible with in situ polymerisation or solution blending methods, as opposed to hot pressing and dry mixing. While this observation may be influenced by a higher prevalence of examples utilising in situ polymerisation or solution blending in the literature, one potential advantage

of these methods in composite preparation can account for this finding. In situ polymerisation and solution blending techniques offer improved dispersion of fillers within the matrices. With the aid of suitable procedures, monomers or polymers can be more easily dispersed at a smaller scale within the matrices. In comparison to aggregated fillers with the same loading, fillers achieved through better dispersion have a greater potential to form and elongate conductive percolation pathways in composites (Figure 2.11). Driven by the pressing need for lower percolation thresholds, this advantage of better filler dispersion should be another reason for the widespread adoption of in situ polymerisation and solution blending after the year 2000. Comparing in situ polymerisation with solution blending can be challenging due to the varying results reported in related studies. For instance, Huang *et al*. demonstrated a lower percolation threshold in PPy/pulp fibre composites through solution blending,[185] while Sudha *et al*. achieved a lower threshold in PANI/PS composites via in situ polymerisation.[191] These contrasting findings indicate the presence of additional factors that warrant careful consideration, as they may play significant roles in achieving lower percolation thresholds.

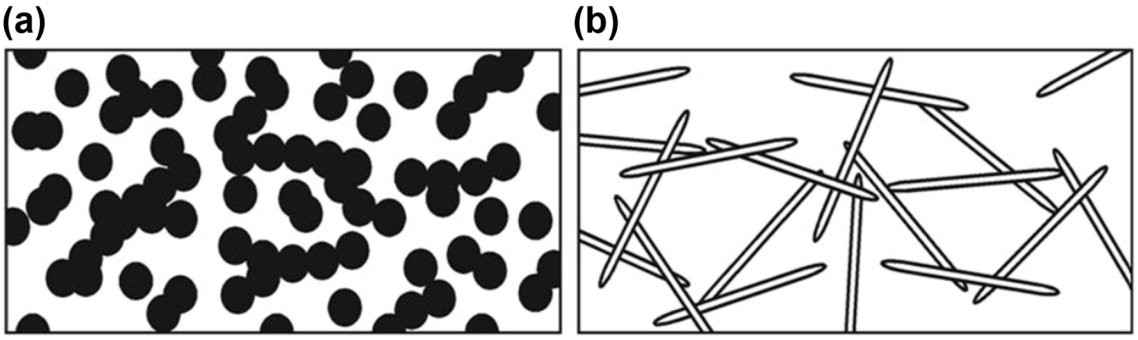



**Figure 2.12.** Illustrative scheme of two hypothetical composites with different conductive fillers geometry: (a) spheres and (b) fibers (high aspect ratio). Taken with permission from ref. 149.

Firstly, it is important to note that the characteristics of the filler plays a significant role in determining the percolation threshold of composite materials. Among these characteristics, the

aspect ratio, which refers to the length-to-diameter ratio of the filler, has been found to have a profound influence on the percolation threshold. During the early stages of developing CP-based filler/matrix composites, Yin *et al*. conducted relevant studies focusing on composites prepared via hot pressing.[174-176] They compared composites with PPy-coated nylon fibres as fillers to those with PPy-coated PE spheres as fillers. Their findings indicated that composites with higher aspect ratios, such as the ones with PPy-coated nylon fibres, exhibited lower percolation thresholds. However, there were limited subsequent studies to further explain this observation or explore additional materials until the 2000s. Since the 2000s, significant advancements have been made in the synthesis of dispersible CP-based and CP-coated fibres with higher aspect ratios.[149,171,185,189,190,195,197,209] The incorporation of these conductive fibres, particularly through solution blending, has proven to be an effective strategy for reducing percolation thresholds. For instance, Wojkiewicz *et al*. achieved a remarkably low threshold of 0.3 wt% by utilising PANI nanofibers as the filler.[195] In a comparative study between spherical particles with low aspect ratios and fibres with high aspect ratios, Merlini *et al*. elucidated the advantage of high aspect ratios in determining percolation thresholds.[149] They demonstrated that lower filler concentration is necessary to ensure adequate physical contact between fibres with high aspect ratios (Figure 2.12).

Although higher aspect ratios have been associated with lower percolation thresholds, there are limitations regarding the elaborate synthesis processes and the dispersibility of fibres in common solvents. An alternative approach is to prepare smaller conductive particles owing to their easy processing and tuneable dispersibility. Theoretical and experimental studies have consistently shown that decreasing the size of particles can result in lower percolation thresholds.[215] Similar to the influence of dispersion (Figure 2.11), smaller particles with the same loading have a higher potential to form and elongate conductive percolation pathways in composites. To achieve thresholds comparable to fibrous fillers, researchers have further

reduced the size of particles to the nanoscale, leading to remarkable results. For example, Li *et al*. achieved an exceptionally low threshold of 0.2 wt% by incorporating PPy nanoparticles in cellulose diacetate (CDA).[193] Since around 2015, the incorporation of nanoparticles has shown greater potential, owing to the development of advanced modelling methods based on CP-based particles.[216-218] Surprisingly, some researchers have demonstrated that their percolation models based on nanoparticles provide consistent results with their experimental findings.[203,219] This combination of theory and experiment holds promise for designing low threshold composites in the future. However, it is important to note that practical experiments may sometimes yield results that appear contradictory to theory. For instance, Cassignol *et al*. found that larger PPy nanoparticles led to a lower threshold.[179] Through morphology studies, they explained that smaller particles have a higher tendency to agglomerate. In other words, the agglomeration of smaller nanoparticles can form complex particles that are even larger than the larger nanoparticles, indicating that their findings are still consistent with theory. Therefore, the actual size of the filler dispersed in prepared composites should be considered a key factor in determining the percolation threshold.

As host materials in filler/matrix composites, matrices also play a significant role in determining the percolation threshold. Early studies by Wang *et al*. and Prokes *et al*. explored different insulating polymers and inorganic salts, revealing that the type of matrix can influence the percolation threshold.[157,178] Furthermore, their investigations suggested that this influence could stem from the matrix morphology and/or the interaction between the filler and matrix.

In terms of matrix morphology, Nicho *et al*. conducted further studies by preparing various composites based on PANI through in situ polymerisation.[160] They found that for matrices such as PMMA and PS, lower surface-to-volume ratios could reduce the percolation thresholds. Although not explicitly explained, this observation could be attributed to the presence of low tunnelling between domains of the insulating polymers with lower surface-to-volume ratios

(Figure 2.13). Consequently, the available space for conductive fillers within the composites would have higher aspect ratios, allowing for a greater potential to form and elongate conductive percolation pathways. This explanation finds support in studies using fibrous matrices during in situ polymerisation as well.[150,185] It is worth noting that Nicho *et al*. also observed the occurrence of surface polymerisation of monomers on insulating matrices, revealing a significant prerequisite for matrix morphology to determine the threshold. Building upon this coating process during in situ polymerisation, Vega-Rios *et al*. achieved an exceptionally low theoretical threshold of 0.059 wt% by partially coating PANI on PS nanoparticles.[199] They demonstrated that PANI growth occurred on the surface of PS nanospheres (Figure 2.14a), and electrical conduction in their system followed a mixed mechanism of tunnelling and continued electron transfer (Figure 2.14b). While most studies related to matrix morphology have focused on in situ polymerisation, solution blending can also be utilised to introduce fillers into matrices with desirable morphologies. For example, Wang *et al*. successfully achieved a remarkably low threshold of approximately 1.6 wt% by simply blending PEDOT:PSS with carboxylated styrene-butadiene (XSB) nanospheres.[210]

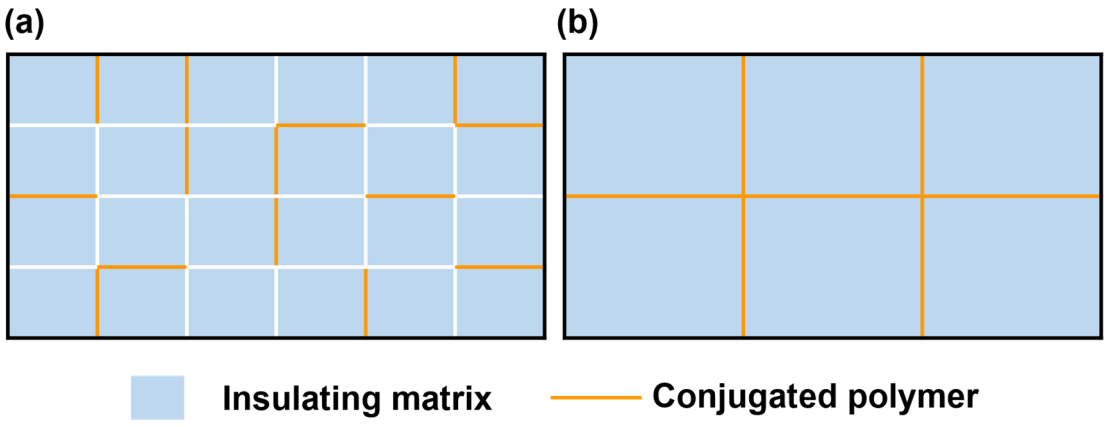



**Figure 2.13.** Illustrative scheme of two hypothetic composites consisting of (a) the matrix with a high surface-to-volume ratio and (b) the matrix with a low surface-to-volume ratio.

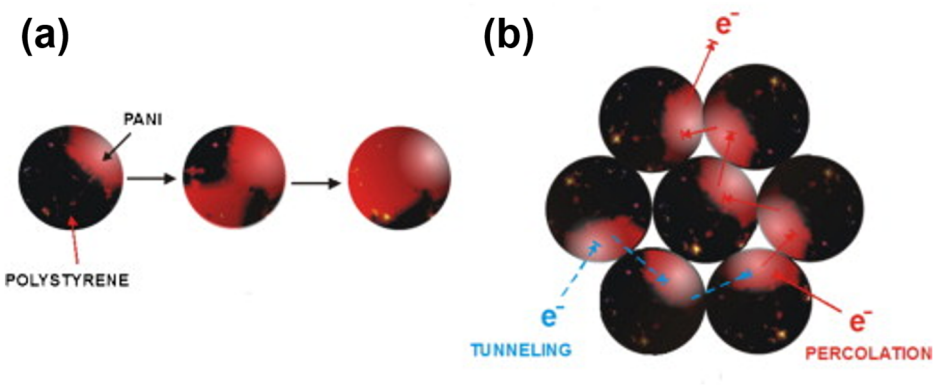



**Figure 2.14.** (a) Model of PANI in the surface of composites, PANI concentration increases from left to right. (b) Tunnelling and percolation pathways on the surface of the core-shell composites. Taken with permission from ref. 199.

Better interaction between the filler and matrix can also contribute to lower percolation thresholds. Wang *et al*. compared PPy/PC composites with PPy/PS composites and suggested that the lower threshold of PPy/PC samples could be attributed to hydrogen bonding between PPy and PC.[157] However, they did not delve into the underlying mechanism. One possible explanation is that PPy has a greater affinity for attaching to and spreading on PC due to their stronger interaction. This, in turn, allows for more controllable conducting pathways guided by the matrix morphology. Additionally, the enhanced filler-matrix adhesion resulting from the stronger interaction can reduce interfacial resistance within the composites. Furthermore, molecular functionalization can be employed to enhance the interaction between the filler and matrix, instead of solely focusing on selecting suitable filler-matrix combinations. For example, Ali *et al*. recently reported the formation of hydrogen bonding between PEDOT:PSS and functionalized polydimethylsiloxane (PDMS).[151] This molecular functionalization approach resulted in an exceptionally low percolation threshold of 0.236 wt% in their work, which is smaller compared to previously reported values in the range from 1.8 to 5 wt% for untreated PDMS.[208,213]

Over the past two decades, other approaches have also been explored to lower the percolation threshold in composite materials. These approaches include the use of suitable dopants and solvents,[180,200] the exploration of monomers with longer conjugated lengths,[206] the introduction of high aspect ratio additives as templates,[198] and the post-treatment of samples with uniaxial strain.[205] It is important to note that the aforementioned influencing factors in this section should be considered comprehensively in practical experiments, as they can have collaborative or competitive effects on percolation thresholds. Furthermore, it should be acknowledged that some of these factors can also contribute to other desirable properties of the composites. For example, a stronger interaction between the filler and matrix can improve composite stability,[183,184] while achieving ideal morphologies in copolymer-based matrices can lead to promising mechanical properties.[202]

#### 2.3.2.3 Application as chemiresistors (since 2005)

With the advancement in approaches to improve filler/matrix composites, researchers have increasingly focused on their practical applications. Since 2005, CP-based filler/matrix composites have found applications in various fields, including electromagnetic interference shielding,[186,190,191,220] sensors,[172,195,201,204,208,221] organic light-emitting diodes,[161] transparent and/or stretchable conductors,[189,202,213] and thermoelectric modules.[212] In the field of chemical sensing, these composites can be utilised as sensing layers in chemiresistors, although there have been only a few relevant studies specifically addressing this application.[172,195] It should be clarified that there is a wide range of CP-based composites specifically designed for chemiresistors.[222,223] According to their chemical composition, some of these materials can be categorized as filler/matrix composites. However, it is important to note that in many cases, these composites were primarily developed to contain a sufficient amount of conductive components to achieve ideal conductivities, and electrical percolation was not the primary focus of the relevant studies. Also, the improved sensing performances of these composites are

attributed to factors rather than electrical percolation, such as different sensing mechanisms and finely designed nanostructures. Therefore, these materials are not included in this section as they are beyond the scope of percolation composites in this thesis.

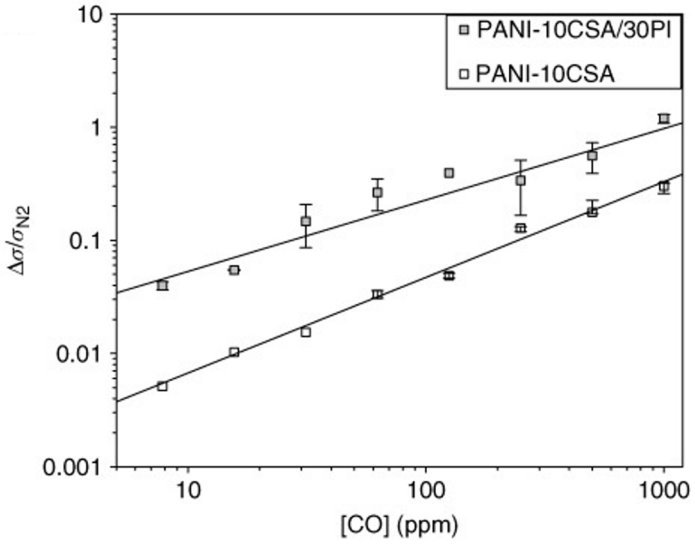



**Figure 2.15.** Sensor responses, defined as $\Delta\sigma/\sigma_{N_2}$, as a function of CO concentration at 1 atm for PANI-10CSA ($\sigma_{N_2}$ = 1.95 S cm$^{-1}$) and PANI-10CSA/30PI ($\sigma_{N_2}$ = 0.22 S cm$^{-1}$) at 25 °C, Taken with permission from ref. 172.

Watcharaphalakorn *et al*. conducted a study on carbon monoxide (CO) detection using various PANI and PANI/PI composites.[172] They explored different dopants and dopant to PANI mole ratios and found that PANI doped with camphor sulfonic acid (CSA) at a ratio of 10 (PANI-10CSA) exhibited the highest conductivity in $N_2$ carrier gas ($\sigma_{N_2}$). Subsequently, they blended PANI-10CSA with PI through dry mixing and observed percolation at a PANI-10CSA fraction of 45 wt%. The composite containing 30 wt% PI (PANI-10CSA/30PI) was used to fabricate chemiresistors for CO detection. Comparing PANI-10CSA with PANI-10CSA/30PI, the researchers found that PANI-10CSA/30PI exhibited higher responses (expressed as the relative change of conductivity, $\Delta\sigma/\sigma_{N_2}$) to CO from 3.9 to 1000 ppm (Figure 2.15). They

attributed this improved sensitivity to the fact that the conductivity of PANI-10CSA/30PI before CO exposure (i.e. $\sigma_{N_2}$) was an order of magnitude lower than the $\sigma_{N_2}$ of PANI-10CSA. Since both PANI-10CSA and PANI-10CSA/30PI showed comparable changes in conductivity ($\Delta\sigma$), the difference in $\sigma_{N_2}$ played a major role in determining the sensitivity to CO.

Furthermore, Wojkiewicz *et al*. conducted a study on the detection of ammonia ($NH_3$) by incorporating PANI nanofibers into polyurethane (PU) through solution blending.[195] Owing to the high aspect ratios of the filler, a remarkably low threshold of 0.3 wt% was observed. Subsequently, chemiresistors for $NH_3$ detection were fabricated using the composite with a PANI content of 35 wt%. Surprisingly, the sensors based on 35 wt% PANI exhibited a very low experimental limit of detection (LOD) of 20 ppb and a sensitivity of 0.8 % $ppm^{-1}$. However, it is worth noting that sensors solely based on PANI nanofibers were not fabricated for further comparison in their study.

Obviously, gaps remain when utilising CP-based filler/matrix composites as sensing layers in chemiresistors. Researchers in each study have predominantly fabricated sensors at a single filler fraction that was significantly above the percolation threshold, limiting the understanding of sensing performance within the percolation regions. To bridge this gap, it is crucial to conduct systematic studies that investigate the effects of electrical percolation across a range of filler fractions, from the percolation threshold to high filler fractions. During these studies, it is essential to consider the potential changes in the major sensing mechanism. Previous studies have demonstrated that the major sensing mechanism of sensors prepared with high filler fractions primarily rely on chemical interactions between CPs and analytes. When the filler fraction decreases, however, the majority of analytes could be absorbed within the polymeric matrices, leading to another sensing mechanism primarily driven by swelling (Figure 2.16).[224] As this change in the major sensing mechanism can complicate the

investigation of sensitivity and/or selectivity, its impact should be minimized as much as possible during the design of composites for chemiresistors.

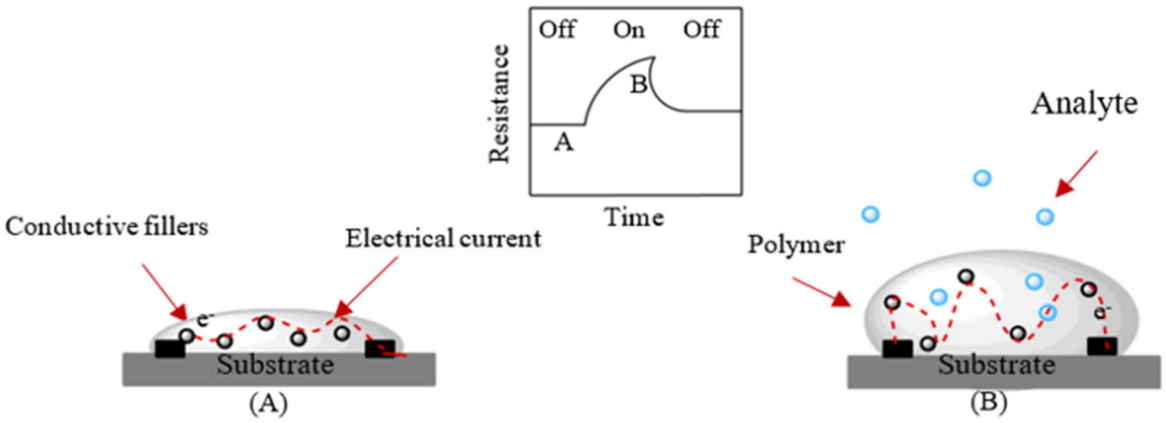



**Figure 2.16.** Schematic representation of chemiresistor mechanism based on swelling effect. The red dashed line gives the electrical current along the percolation pathway (A) before and (B) after swelling. Swelling causes an increase in the volume of the polymeric matrices, which in turn increases the distance between adjacent conductive fillers. This disrupts or destroys the conductive percolation networks, increasing the resistance of the chemiresistor. Taken with permission from ref. 224.

With the rapid advancement in organic electronics, there is increasing research interest in multifunctional sensors. However, there have been few studies to date that have explored the extension of functions in CP-based percolation chemiresistors. Utilising CP-based filler/matrix composites could be a promising approach to achieve multifunctionality in these chemiresistors, as they can be responsive to various other stimuli such as strain,[151] pressure,[201] and temperature.[225] It is important to note that developing multifunctional CP-based percolation chemiresistors is not only crucial for expanding their applications but also provides valuable insights into the effects of other stimuli on these chemiresistors. This knowledge is significant for the practical implementation of percolation sensors in real-life applications.

### 2.3.3 Conductor-on-substrate strategy based on conjugated polymers

For now, only a few studies have successfully observed electrical percolation by depositing conjugated polymers on substrates. Previous work has primarily utilised electrochemical polymerisation for preparation and interdigitated electrodes (IDEs) as substrates. During the electrical polymerisation process, percolation pathways are formed on the insulating gaps of the substrate, leading to changes in conductance or resistance across the IDEs.

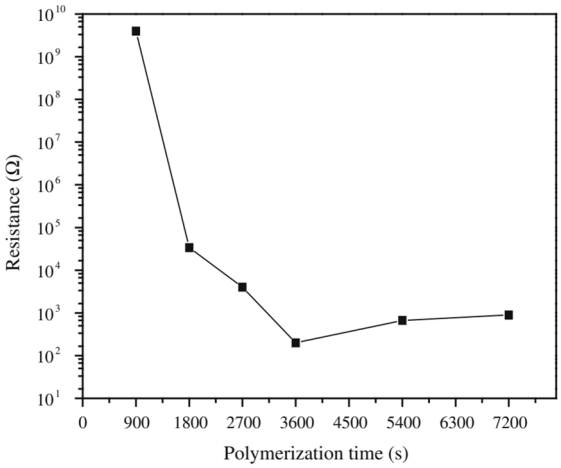



**Figure 2.17.** Resistance vs. polymerisation times for the prepared nano-PANI on the IDEs pre-treated with Au-NP islands. Taken with permission from ref. 226.

Liu *et al*. conducted early studies on the growth of nanostructured PANI deposited on a glass gap using the galvanostat method.[226] To enhance deposition speed and achieve homogeneous nano-PANI, each IDE substrate was pre-treated with Au-nanoparticle (Au-NP) islands via ion sputtering. The results of their study showed a relationship between resistance and polymerisation time (Figure 2.17), indicating the observation of electrical percolation. PANI across the pre-treated IDE was nearly insulating at 900 s of deposition, which was attributed to the isolated structure of nano-PANI aggregations on the Au-NP islands. A significant decrease in resistance was then observed until 3600 s, suggesting the generation of short nanowires that

connected the isolated aggregations. This indicated the formation of percolation pathways between 900 and 3600 s. The authors further explained that these pathways were well-established after 3600 s, and the resistance was not significantly influenced by the subsequent growth of nano-PANI. Morphology studies via scanning electron microscopy (SEM) were also conducted to examine the polymer growth on the glass gaps between 1800 and 7200 s (Figure 2.18), which correlated with the changes in resistance. To assess the function of nano-PANI, a series of chemiresistors were fabricated at different times between 1800 and 7200 s. The sensor prepared at 3600 s exhibited the best performance in detecting 4 ppm $NH_3$ (Figure 2.19), which was attributed to the presence of interconnected nanowires on the substrate surface. However, the authors did not provide further discussion on the sensor prepared at 1800 s, which also consisted of nanowires but exhibited a lower sensing response.

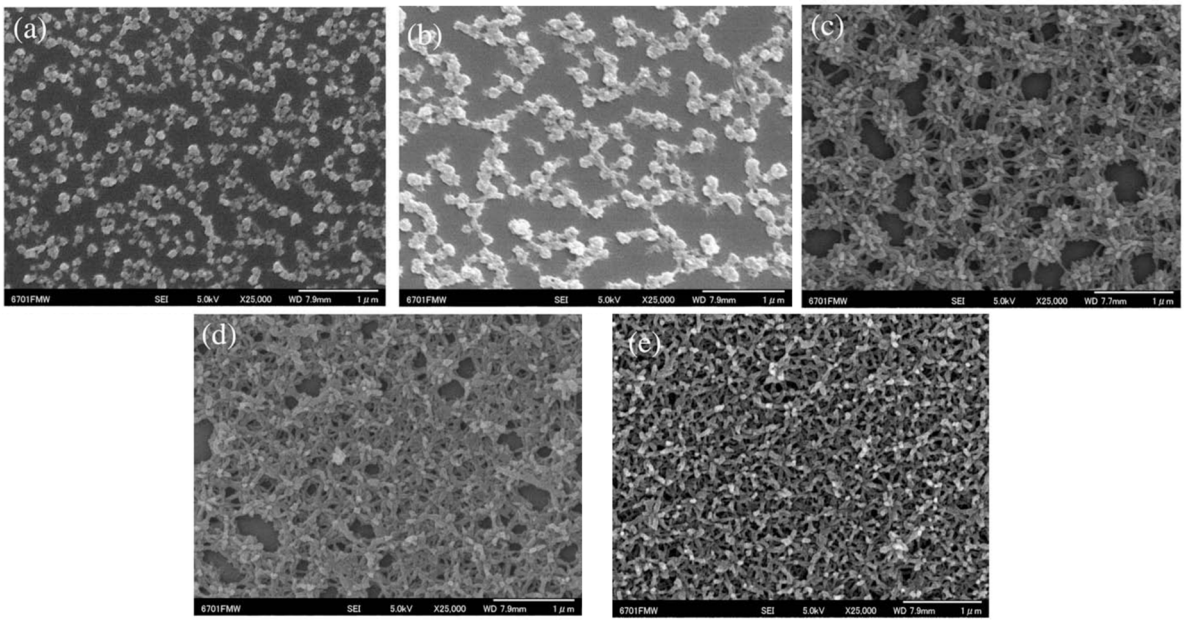



**Figure 2.18.** SEM images of PANI deposited on the insulating substrates with increasing in polymerisation time: (a) 1800 s, (b) 2700 s, (c) 3600 s, (d) 5400 s and (e) 7200 s. The gaps were pre-treated with Au-NP islands. As polymerisation proceeded, more interconnected nanowires of PANI were formed. Taken with permission from ref. 226.

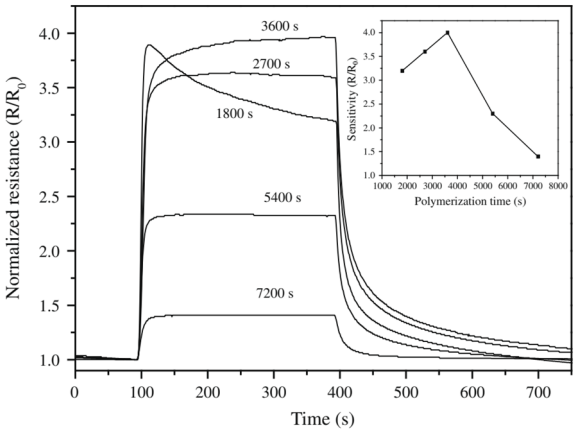



**Figure 2.19.** Real-time response of nano-PANI electrodes prepared with different polymerisation times upon exposure to 4 ppm $NH_3$ gas. Inset is the plot of sensitivity vs. polymerisation time. In this work, the sensitivity was defined as $R/R_0$. The authors attributed the superior performance of the sensors prepared at 3600 s to the presence of interconnected nanowires on the substrate surface. They claimed that the sensing response should be compromised by thicker films prepared beyond 3600 s. The increased film thickness could potentially impede the diffusion of gas into the film, leading to a decrease in sensitivity. Taken with permission from ref. 226.

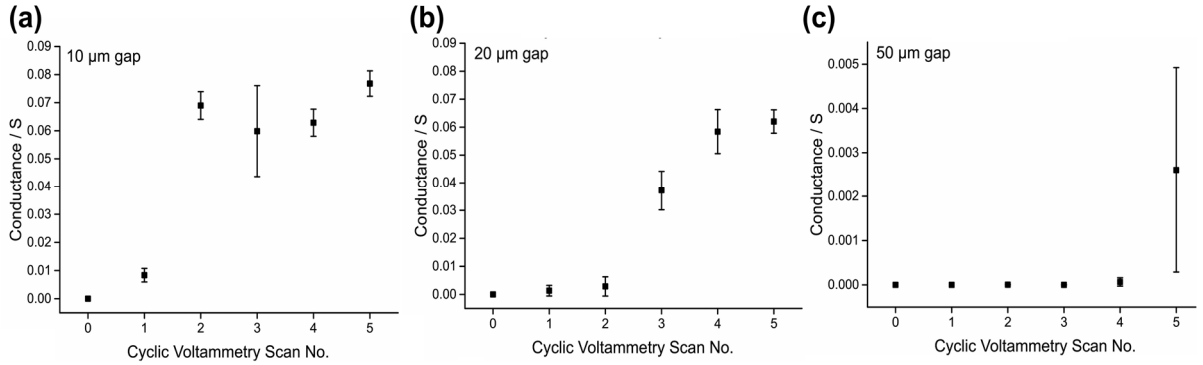



**Figure 2.20.** Conductance vs CV scans for IDEs with gap widths of (a) 10 µm, (b) 20 µm and (c) 50 µm. Error bars were obtained from the standard deviation of the conductance values of three electrode measurements for each CV scan. Dramatic increases in conductance were observed using all three types of IDEs, indicating the occurrence of electrical percolation within five scans. Among the IDEs, those with a 20 µm gap showed the most pronounced results, clearly demonstrating the entire range of the conductance change. Taken with permission from ref. 35.

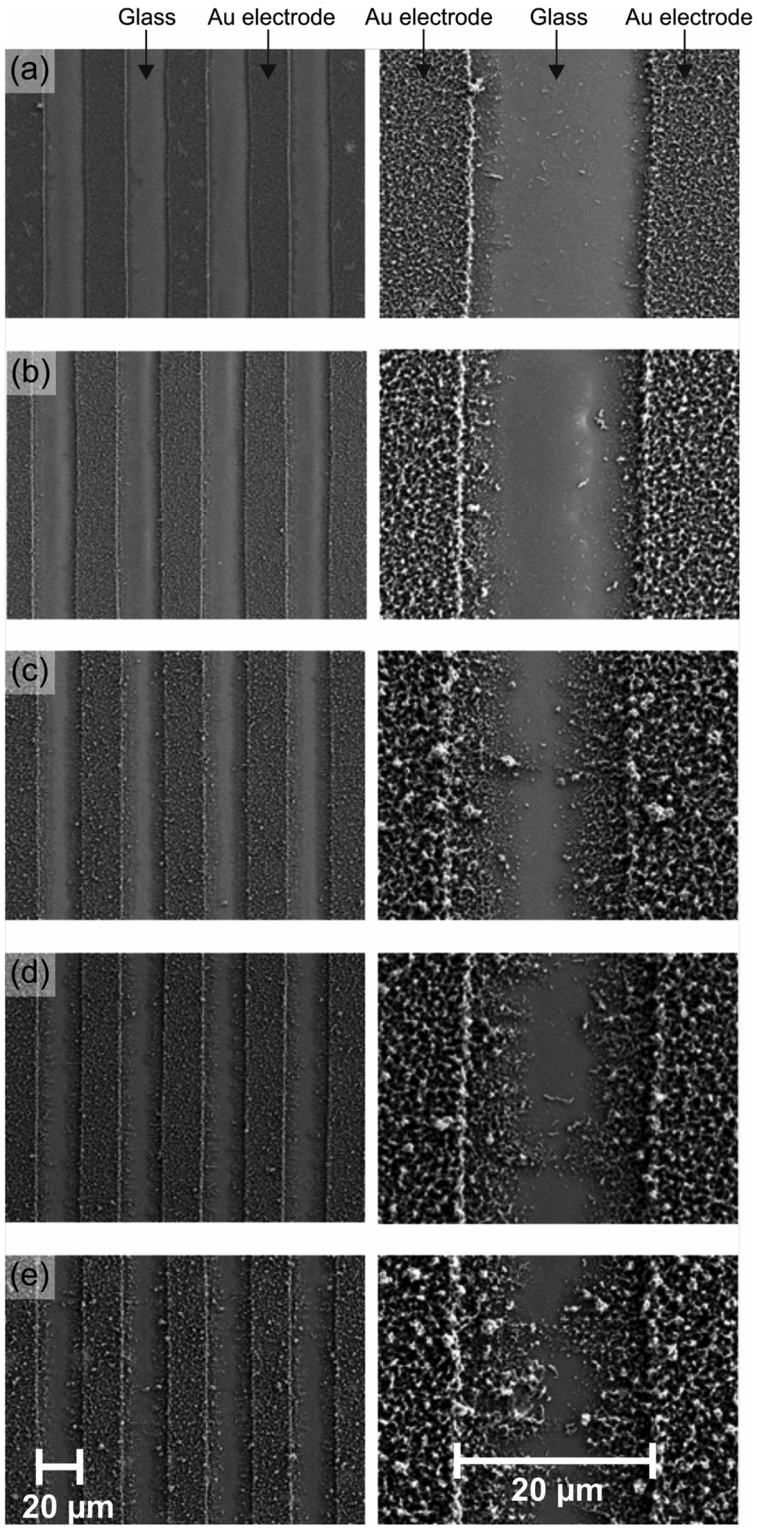



**Figure 2.21.** SEM images of 20 µm gap IDEs with (a) 1, (b) 2, (c) 3, (d) 4, and (e) 5 CV scans. The left column is at low magnification showing 5 Au electrode strips and the right at higher magnification showing individual glass gaps between the electrodes. The amount of PEDOT between the electrodes increased as a function of the number of CV scans. Taken with permission from ref. 35.

The research in this field has then been primarily led by our research group. Murugappan *et al*. conducted studies on the growth of PEDOT via cyclic voltammetry (CV).[35] Different resistance trends were observed as a function of the number of CV scans (Figure 2.20), depending on the size of the IDE gap. The most informative results, depicting the percolation behaviour, were obtained using IDEs with 20 μm gaps. Further analysis of the PEDOT morphology across the 20 μm gaps (Figure 2.21) confirmed the trends observed in conductance. Combining the conductance and morphology data, this study provided insights into the entire process of polymer deposition on IDEs, which can be divided into three regions as follows:

***Insulating region.*** The insulating region is where there are no continuous electrical connections across the IDEs. In this initial flat region, there is no conduction across the IDE because there is insufficient polymer to allow even a single electrical connection to be formed on the gaps.

***Percolation region.*** The percolation region is where isolated conducting pathways or networks have formed across the gaps. It begins with a conductance jump to a certain value, which is defined as the percolation threshold. This steep region is characterised by the non-linear relationship between the amount of deposited polymers and the conductance across the IDEs.

***Thin-film region.*** The thin-film region is where a continuous conducting film covers the IDEs. This region follows the percolation region and is characterised by a constant gradient increase in conductance. The conductance in this region is mainly influenced by the thickness of the film.

Following the primary work on PEDOT, our research expanded to explore other CPs and substrates, as well as their applications in gas detection. Armitage *et al*. investigated the use of PPy and flexible substrates to create high-performance percolation sensors for $NH_3$ detection,[31]

while Lefferts *et al*. tuned the doping state of PEDOT percolation networks on glass substrates to fabricate effective chemiresistors for $NO_2$ detection.[32] Both studies have demonstrated that sensors prepared in the percolation regions exhibit higher sensitivities rather than their counterparts prepared in the thin-film regions. The improved sensitivity in the percolation region has been attributed to the stronger interactions between the percolation networks and analytes, leading to larger changes in device resistance upon exposure to the target gases. However, it should be noted that high-resistance sensors prepared near the percolation threshold may exhibit higher noise levels. Since the limit of detection (LOD) is related to the noise, the competitive relationship between sensitivity and baseline noise was considered in these studies. Generally, the LOD initially decreases and then increases as the device resistance increases (Figure 2.22). Therefore, optimal sensors should be typically obtained within the optimum zones of the corresponding percolation regions above the percolation threshold. After pre-determining the optimum zone for PPy deposited on glass IDEs with 5 μm gaps, Lefferts *et al*. further employed PPy-based percolation chemiresistors to detect vapours of ammonium nitrate/fuel oil (ANFO).[33,36] Details about all the optimal sensors in the aforementioned studies have been summarised in Table 2.6.

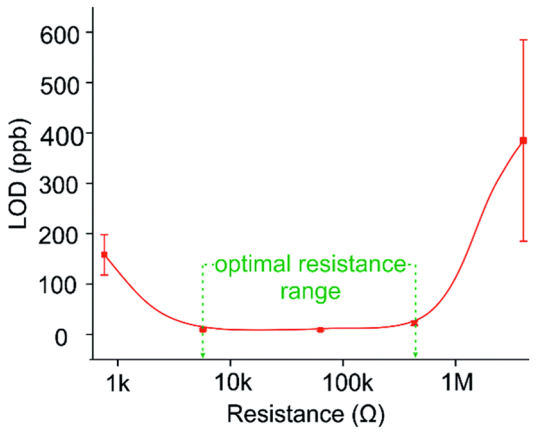



**Figure 2.22.** LODs for the PPy-based flexible sensors. The optimal resistance range represents the resistances with the highest sensitivity and lowest LOD, corresponding to the optimum zone of the percolation region. Taken with permission from ref. 31.

**Table 2.6.** CP-based percolation chemiresistors via the conductor-on-substrate strategy.

| Polymer | Substrate | Preparing method | Analyte | Detection range (ppm) | Sensitivity (% $ppm^{-1}$) | Limit of detection (ppb) | Ref. |
|---|---|---|---|---|---|---|---|
| PANI | Au/glass IDE with 100 μm Au fingers and 100 μm glass gaps | Galvanostat | $NH_3$ | 4 | - | - | 226 |
| PEDOT | Au/glass IDE with 20 μm Au fingers and 20 μm glass gaps | Cyclic voltammetry | - | - | - | - | 35 |
| PPy | Au/PET IDE with 100 μm Au fingers and 100 μm PETgaps[a] | Chronoamperometry | $NH_3$ | 0.1 − 0.7 | 39.4 | 10 | 31 |
| PEDOT | Pt/glass IDE with 5 μm Pt fingers and 5 μm glass gaps | Chronoamperometry and then re-doping | $NO_2$ | 1 − 8 | −0.4[a] | 907 | 32 |
| PPy | Pt/glass IDE with 5 μm Pt fingers and 5 μm glass gaps | Chronoamperometry | $NH_3$ | 0.1 − 2 | 10[a] | - | 33 |
| PPy | Pt/glass IDE with 5 μm Pt fingers and 5 μm glass gaps | Chronoamperometry | $NH_3$ | 1 − 8 | 1.8[a] | 73 | 36 |

Note: PANI = polyaniline; PEDOT = poly(3,4-ethylenedioxythiophene); PPy = polypyrrole; PET = polyethylene terephthalate. [a]Gradient estimated from the linear portion of the calibration curve.

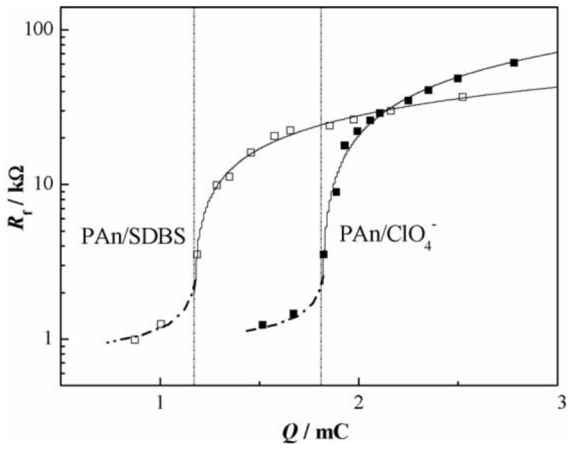



**Figure 2.23.** Plot of resistance of PANI film doped with two dopants vs. reduction charge at the same reduction potential of −0.6 V. The threshold values were obtained as 1.17 and 1.81 mC for PANI/SDBS and PANI/$ClO_4^-$, respectively. This difference is possibly due to the strong interaction between the SDBS and the amine or imine in the PANI chains. Taken with permission from ref. 227.

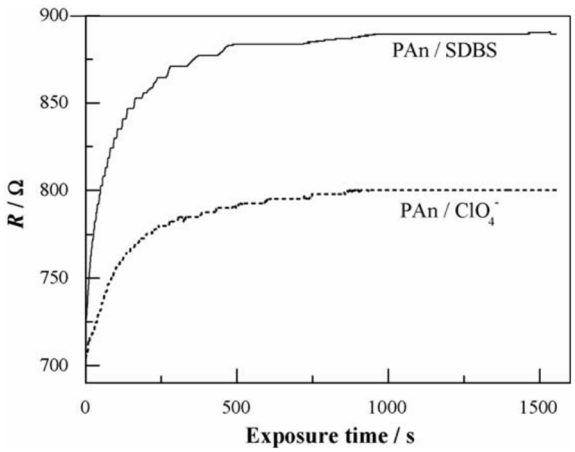



**Figure 2.24.** Response curves of PANI/DBSA and PANI/$ClO_4^-$ thin-film sensors upon exposure to 100 ppm $NH_3$. Taken with permission from ref. 227.

There was also an unconventional study on the electrical percolation within the PANI films electrochemically deposited on Pt substrates. Xu *et al*. conducted this work to study the reduction process of PANI film doped with different dopants.[227] As the reduction charge increased, a reverse percolation was observed within the PANI film, depicting the transition from the conducting state to the insulating state. The authors proposed that the percolation threshold was reached when partially reduced clusters formed a continuous partially reduced phase dispersed with retained conducting clusters. They also noted that the PANI film doped with sodium dodecylbenzene sulfonate (SDBS) exhibited a smaller reduction threshold compared to the film doped with perchlorate ($ClO_4^-$) (Figure 2.23). This finding suggested that the PANI film doped with SDBS would be more sensitive to $NH_3$, as it could be dedoped or reduced by a smaller amount of $NH_3$. Sensing experiments confirmed that the PANI film doped with SDBS showed a higher response to 100 ppm $NH_3$ (Figure 2.24). Although the focus of this work was not on percolation chemiresistors, it provided valuable insights into the effects of dopants on sensing performance.

Challenges and gaps still remain in the development of CP-based chemiresistors via electrochemical polymerisation. Firstly, the current approach for determining the percolation

region relies on plotting the electrical conductance at different deposition cycles or times, which limits continuous monitoring of the evolving conductance of the CP-based networks. This hinders a comprehensive understanding of the percolation process. Secondly, achieving reproducible results for CP layers prepared using identical procedures is challenging due to the inherent randomness of network connections.[228,229] Previous studies have demonstrated significant variations in device initial conductance within the percolation region, which could lead to inadequate device-to-device reproducibility. Furthermore, there is a lack of comprehensive studies that delve into the nanostructure morphology of percolation networks, despite the demonstrated impact of morphology on sensing performance. Understanding the morphology of these networks is crucial for optimizing sensor design and improving their overall efficiency. Last but not least, the exclusive use of electrochemical polymerisation for the conductor-on-substrate strategy leaves many opportunities for other polymer preparation techniques. All these challenges and gaps impede further investigations on CP-based percolation sensors as well as their practical implementation in real-life applications.

## 2.4 Summary

Chemiresistive percolation sensors based on CPs are created by depositing sensing layers consisting of CP-based percolation networks onto appropriate substrates. The performance of these sensors is subsequently evaluated using a range of parameters derived from advanced measurement techniques. Undertaking research in this field necessitates an interdisciplinary understanding of conjugated polymers, chemiresistors, and electrical percolation. To establish the background for this thesis, therefore, an introductory overview of these three fundamental concepts has been presented in this chapter.

The discovery of CPs marked a significant advancement in materials science, as it challenged the conventional belief that polymers were electrically insulating. Doping plays a

crucial role in the conducting mechanism of CPs. By controlling the doping processes, various applications, including chemiresistive sensors, can be realised. The fabrication of CP-based chemiresistors involves two main steps. Firstly, the polymers are synthesised and doped using electrochemical or chemical methods. The choice of synthesis method determines the properties of the CPs. Subsequently, different deposition methods are employed to form the sensing layers based on the CPs. It is important to note that the uniformity and reproducibility of the sensing layers are influenced by several factors, which significantly impact the performance of the devices.

CP-based chemiresistors are capable of detecting a wide range of chemicals by utilising the interactions between the sensing polymers and the analytes. The detection process is reflected through changes in resistance, which can be measured and represented by response curves. The resistance changes are influenced by both chemical reactions and physical interactions, affecting different components of the overall resistance. These changes can be monitored using various measurement techniques. The performance of CP-based chemiresistors is evaluated based on the response curves obtained from measurements. Different parameters are used to assess the device performance. These parameters are determined by both the inherent characteristics of the devices themselves and the specific test conditions implemented by researchers. Through advancements in measurement and evaluation methods, CP-based chemiresistors have demonstrated their effectiveness in detecting a wide range of chemicals, including hazardous gases, volatile compounds, warfare chemicals, biomolecules, and ions. Various approaches have been explored to improve device performance, such as nanostructuring sensing materials, developing chemically diverse sensors, and immobilising detecting molecules.

In materials science, percolation refers to the phenomenon where a specific property of a material changes as a function of the concentration or arrangement of its constituent

components. In the case of electrical percolation, the focus is on changes in conductivity. When a material reaches the percolation threshold, there is a sudden jump in conductivity, indicating the onset of electrical percolation. In practical experiments, there are two main approaches to creating materials with percolation pathways: the filler-in-matrix strategy and the conductor-on-substrate strategy. In most cases, CP-based percolation materials are composites where CP-based fillers are introduced into insulating matrices. The percolation threshold of these composites is influenced by the properties of both the fillers and matrices as well as the interactions between them. However, few studies have explored the effects of percolation on chemical detection in these composites. In the conductor-on-substrate strategy, percolation networks are directly formed during the electrochemical deposition on interdigitated electrodes. The percolation threshold in this case depends on the conditions of electropolymerisation. Sensors fabricated using this strategy demonstrate improved gas sensing performance within the percolation region.

Beyond the basic understanding of the research background, this overview of chemiresistive percolation sensors based on CPs reveals several motivations for further investigations in this field. While electrical percolation has shown potential in CP-based chemiresistors, there are still gaps and challenges that need to be addressed:

(1) Systematic investigations are needed to demonstrate the effects of the electrical percolation within CP-based composites on sensor performance in chemical detection.

(2) Few studies have explored the achievement of multifunctionality in percolation chemiresistors using CP-based composites.

(3) It is challenging to achieve desirable device-to-device reproducibility during electrochemical deposition for the conductor-on-substrate strategy.

(4) Further investigations are needed to focus on the morphology of percolation networks formed via the conductor-on-substrate strategy.

(5) The exclusive use of electrochemical polymerisation in the conductor-on-substrate strategy limits the exploration of other preparation techniques for forming percolation networks on substrates.

Addressing these gaps and challenges will advance the development of chemiresistive percolation sensors based on conjugated polymers, paving the way for their broader applications in chemical detection. Attempts to explore solutions to these issues are reported in this thesis.

# Chapter 3

# Methodology

Studies on chemiresistive sensors typically comprise several fundamental steps, including material synthesis, deposition, characterisation, and sensor testing. Following a brief introduction of the materials and substrates used in this thesis, this chapter presents the methods and instrumentation employed for each research step. Relevant methods of material synthesis are presented, and various methods attempted to deposit sensing materials on the substrates are discussed. Necessary instrumentation for material characterisation is then introduced. Finally, custom-made sensing setups for various device tests are described.

## 3.1 Materials and substrates

The chemicals used in this thesis were purchased from either Sigma-Aldrich or Fisher Scientific. Analyte gases (10 ppm, nitrogen fill), nitrogen gas (99.998 %, for further dilution of the analytes), and dry air (speciality grade) for sensing tests were purchased from BOC Gases UK. Details of these chemicals have been given in the Experimental sections of the following chapters. Prior to experiments, 2,5-dibromo-3,4-ethylenedioxythiophene (DBEDOT, 97 %) was further purified through recrystallisation from ethanol ($C_2H_5OH$, 99.8 %), and poly(3,4-ethylenedioxythiophene) (PEDOT) dispersion (1 wt%) and polystyrene (PS) latex (10 wt%) were sonicated for 10 minutes.

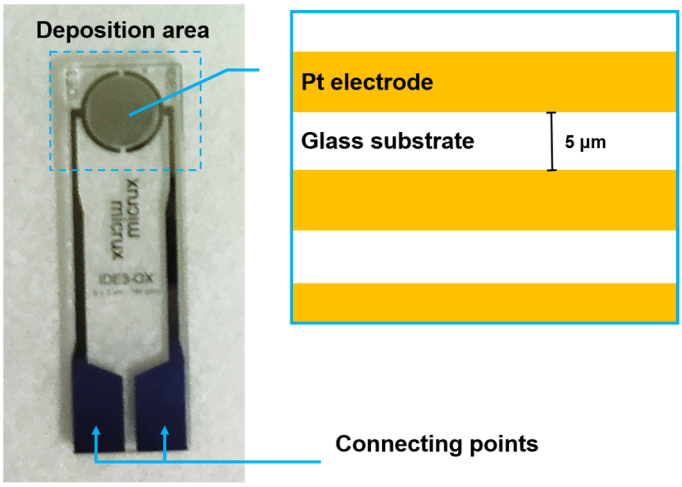



**Figure 3.1.** A Pt interdigitated electrode (IDE) substrate used in this thesis. The insulating gaps between the Pt electrodes on the glass substrates are 5 µm wide. Materials must be synthesised and/or deposited on the deposition area. Each bare IDE or device sample can be connected to other equipment via the two connecting points on the end of the IDE substrate.

Pt interdigitated electrode (IDE) substrates were purchased from Micrux (Spain). In the deposition area each substrate consists of 180 pairs of 5 µm wide and 150 nm thick Pt electrodes separated by a gap of 5 µm on an insulating glass substrate (Figure 3.1). The two connecting

points located at the end of the substrate were utilised to connect the setups for material deposition, electrical measurement, and sensing test. Prior to experiments, each Pt IDE substrate was cleaned using suitable methods corresponding to specific studies. Additionally, it can be chemically or electrochemically recycled.

## 3.2 Material synthesis and deposition

### 3.2.1 Electrochemical polymerisation

For electrochemical polymerisation, a classic three-electrode system (Figure 2.2a) was employed. Experiments were conducted using a PGSTAT204 Autolab electrochemical workstation (Eco Chemie, Netherlands) interfaced with a personal computer running NOVA version 1.11 software. The three-electrode cell consisted of a Pt coil (BASi, USA) as the counter electrode, an Ag/AgCl electrode (CH Instruments, USA) as the reference electrode, and a Pt IDE substrate as the working electrode. All these electrodes were placed in a solution containing a known concentration of monomer and 0.1 M lithium perchlorate ($LiClO_4$, 99 %) in acetonitrile ($CH_3CN$, 99 %) or deionised water. The electrochemical workstation was used to apply a predetermined potential (chronoamperometry) or scan potentials (cyclic voltammetry) to induce the electrochemical oxidative polymerisation of monomers and the deposition of corresponding polymers. During these processes, the faradaic current was monitored and recorded by the workstation. Before the polymers fully covered the deposition area and formed a thin film, electrical percolation networks were obtained by stopping the polymerisation at set times during chronoamperometry or after a few scans during cyclic voltammetry.

An in situ conductance monitoring setup was established based on the classic three-electrode system. To implement this setup, a B2902A source/measure unit (SMU, Keysight, UK) was introduced between the connecting points of the Pt IDE (Figure 3.2). Conjugated polymers

were prepared from a salt solution with monomers through chronoamperometry. The electrochemical workstation provided the faradaic current ($i_f$) and controlled the deposition process. The drain current ($i_d$) induced by the applied potential ($\Delta V$) was recorded by the SMU interfaced with a personal computer equipped with Benchvue software, thus reflecting the conductance across the IDEs in real time. Before the polymers fully covered the deposition area and formed a thin film, electrical percolation networks were obtained by stopping the polymerisation at short times or small $i_d$ changes during chronoamperometry.

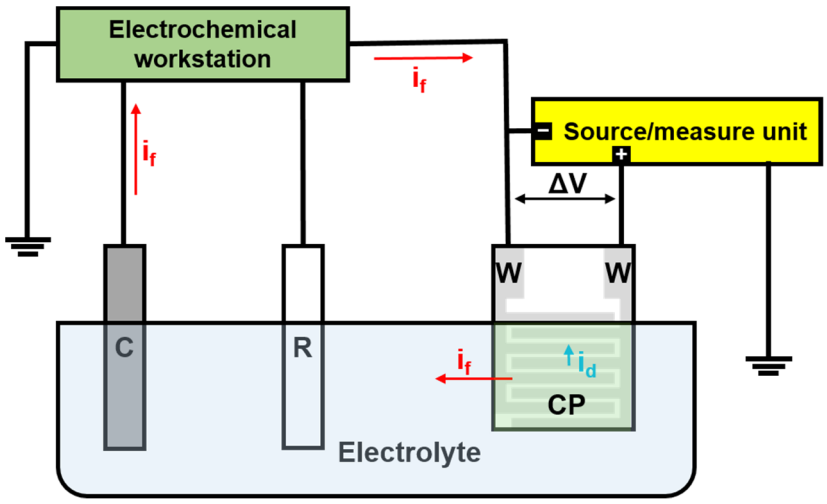



**Figure 3.2.** Schematic diagram of the in situ conductance monitoring setup during the electrochemical oxidative polymerisation of conjugated polymers (CPs). The electrochemical workstation provides the faradaic current ($i_f$) and controls the deposition process. Induced by the applied potential ($\Delta V$), the drain current ($i_d$) from one working electrode (W) to another is recorded by the source/measure unit. (C: counter electrode; R: reference electrode.)

The classic three-electrode system was applied in the research presented in Chapter 5 while the in situ conductance monitoring was employed in Chapter 4. To ensure that all the CP-based chemiresistors were tested in the same state, each sample in the same research was further stabilised through electrochemical doping. To achieve this, the deposition areas with conjugated polymers were placed in a salt solution without monomers and electrochemically

doped at a set potential for a certain time, utilising the same setup as in the corresponding research.

### 3.2.2 In situ solid-state polymerisation

After purifying and drying, the monomer DBEDOT was deposited on the deposition area of the IDE substrate using solution processing methods. Each IDE sample with the monomers was then placed in a sealed vial (5 mL) and incubated in a Garbolite PN60 natural convection oven (temperature stability: ± 0.5 ˚C) at a predetermined temperature for a certain duration. During this process, PEDOT was prepared and deposited on the deposition area.

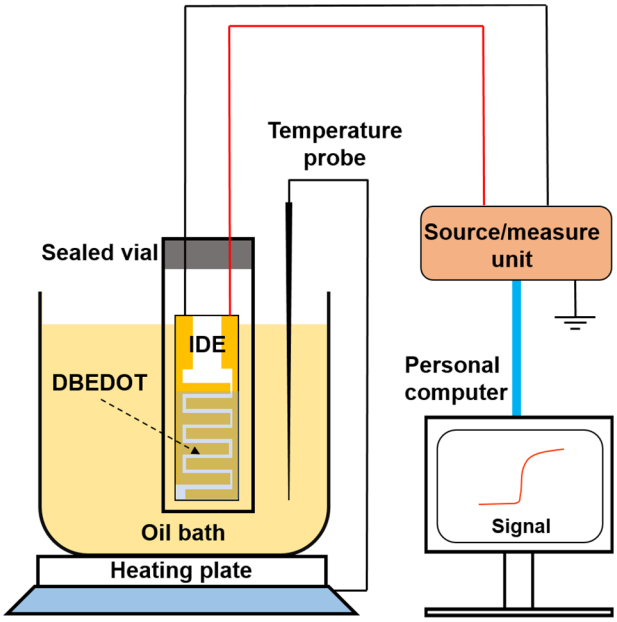



**Figure 3.3.** Schematic diagram of the in situ conductance monitoring setup for the in situ solid-state polymerisation of 2,5-dibromo-3,4-ethylenedioxythiophene (DBEDOT) on a Pt interdigitated electrode (IDE) substrate. During this process, the current across the IDE is recorded by a source/measure unit interfaced with a personal computer.

An in situ conductance monitoring setup was designed by the author of this thesis to record the current change during in situ solid-state polymerisation (Figure 3.3). The sample in a sealed

vial, connected to the B2902A source/measure unit (SMU), was incubated in an oil bath at a predetermined temperature for a certain duration, with the heating temperature being controlled via an IKA RCT Basic stirrer hotplate connected with a PT1000 temperature sensor (accuracy: ± 1 °C). The current across the IDEs was recorded by the SMU, which was interfaced with the personal computer equipped with Benchvue software.

PEDOT-based chemiresistors, prepared either in the natural convection oven or the oil bath, were further stabilised through electrochemical de- and re-doping. To accomplish this, the deposition areas with conjugated polymers were immersed in a salt solution containing $LiClO_4$ in a suitable solvent and electrochemically de- and re-doped via chronoamperometry, utilising the classic three-electrode system.

### 3.2.3 Solution processing methods

Several solution processing methods were attempted to deposit materials on the deposition areas, and self-made setups were designed for the corresponding methods. Following deposition, each sample was dried under ambient conditions for 10 minutes. Details of each method have been presented as follows:

***Drop-casting.*** A droplet of solution or emulsion was pipetted onto the deposition area of the Pt IDE substrate, and a thin film was obtained after solvent evaporation. In some cases, this process was repeated to deposit additional materials. The thickness or amount of the deposited materials were controlled by the concentration of the solution or emulsion and the total volume of droplets applied.

***Spray-coating.*** A Gocheer mini airbrush kit was utilised as the spray-coater in this thesis. The air pressure applied to the airbrush was 25 psi and the air flow rate was set to 13 L $min^{-1}$. Nozzles with different diameters were selected for different materials. A solution or emulsion, below the maximum capacity of 7 cc, was added to the cup of the airbrush. The spray-coating

was then conducted at a distance of 10.0 ± 0.1 cm from the deposition area of the Pt IDE substrate. For solvents with boiling points over 70 °C, the substrate was placed on an IKA RCT Basic stirrer hotplate (accuracy: ± 5 °C) set at 50 °C to speed up the evaporation process and avoid flooding during spraying. The spray-coating process was terminated when the solution or emulsion in the cup was completely consumed. The thickness or amount of the deposited materials were controlled by the concentration and volume of the solution or emulsion added.

***Dip-coating.*** A dip-coater was designed and made by the author of this thesis to deposit materials onto the deposition area of the Pt IDE substrate (Figure 3.4a). The dip-coater utilised a household mechanical timer as its motor, with a plastic plate affixed to the rotational switch of the timer at the same centre. A rectangular plastic strip, acting as the substrate holder, was connected to the plate via a fishing wire attached to the cylindrical surface of the plate. To prevent horizontal rotation and vibrations of the substrate during the dip-coating process, the holder was stabilised between two glass vials. The Pt IDE substrate was vertically extracted from a solution or emulsion that fully covered the deposition area, and this extraction speed was regulated by the diameter of the plastic plate. Excess solution or emulsion was allowed to drain by gravity, while solvent evaporation at room temperature resulted in the formation of a film on the deposition area. The thickness or amount of the deposited materials was controlled by the concentration of the solution or emulsion and the extraction speed of the dip-coater.

***Directed evaporation-induced self-assembly (DEISA)***. A container for DEISA was designed and made by the author of this thesis to deposit nanoparticles onto the deposition area of the Pt IDE substrate (Figure 3.4b). The container employed metal clips to hold the substrates in place, which were fixed on one face of a plastic cap by means of a ring magnet placed on the other face. The cap, along with the fixed substrates, was placed over a 50 mL glass beaker, allowing the deposition areas to be immersed in a 10 mL emulsion. Once the solvent had completely evaporated through the hole on the cap, films formed on the deposition areas. The

temperature at which the solvent evaporated was determined by the type of solvent used during DEISA. The thickness or amount of the deposited materials was controlled by the concentration of the emulsion and the evaporation temperature.

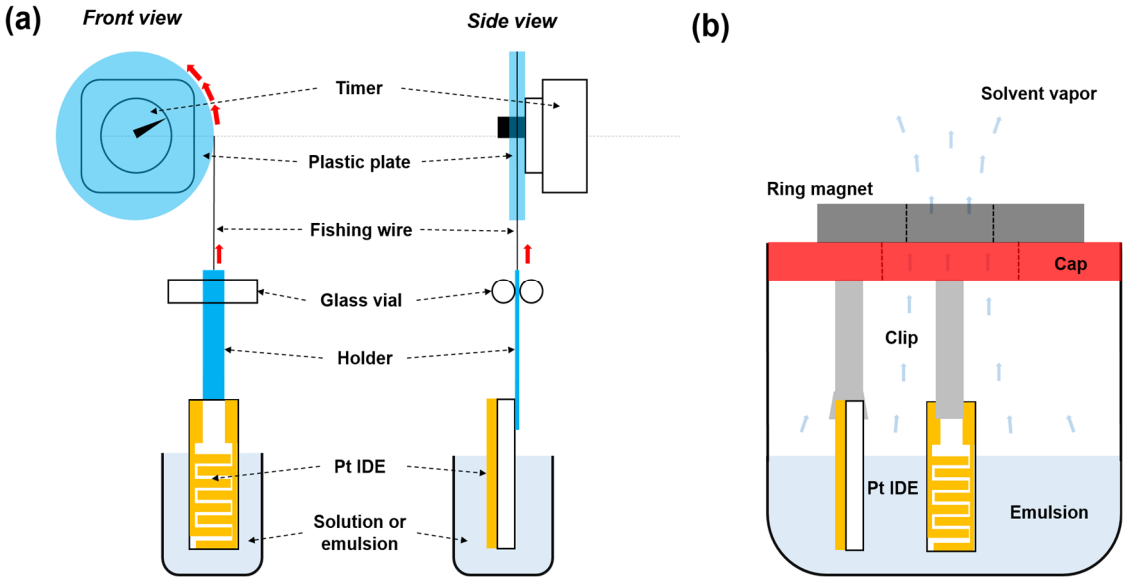



**Figure 3.4.** Schematic diagram of the solution process setups for (a) dip-coating and (b) directed evaporation-induced self-assembly (DEISA). During the dip-coating process, the Pt interdigitated electrode (IDE) substrate is vertically extracted via a fishing wire attached to the plastic plate affixed to the rotational switch of the mechanical timer. Excess solution or emulsion on the substrate is allowed to drain by gravity, while solvent evaporation at room temperature results in the formation of a film on the substrate. During the DEISA process, the Pt IDE substrates are vertically immersed in the emulsion using metal clips affixed on the cap via a ring magnet. Once the solvent of the emulsion completely evaporates through the hole on the cap, films form on the substrates.

## 3.3 Characterisation

The resistance of each CP-based chemiresistor ($R$) was measured using an RS PRO IDM 98IV handheld digital multimeter (max. measurement: 40 MΩ, resolution: 100 mΩ, accuracy: ± 0.8 % of reading) at ambient conditions. According to the description of electrical percolation

in Section 2.3.1, theoretically, the electrical conductivity ($\sigma$) should be used to investigate the percolation behaviour. The conductivity ($\sigma$) can be obtained through the following equation:

$$\sigma = \frac{L}{RA} \tag{3.1}$$

where $L$ is the length of the sensing layer covering the IDE gaps and $A$ is the cross sectional area of the sensing layer on the IDE substrate. In practical experiments, however, it is quite difficult to determine the length and the cross sectional area, especially for the dispersed percolation networks deposited on the substrates. Therefore, the conductance, the reciprocal of the measured resistance, was used to depict the electrical percolation behaviour in this thesis. Furthermore, the electrochemical analysis was performed via cyclic voltammetry using the classic three-electrode system. The deposition area with conjugated polymers was immersed in a salt solution containing $LiClO_4$ for the electrochemical analysis.

Surface morphologies of the materials on the deposition areas were investigated using a Zeiss Merlin scanning electron microscope (SEM). Samples for SEM were affixed onto a specimen stub to secure them in place. In order to enhance the surface conductivity, some samples were coated with Pt before imaging. SEM images in this thesis were taken by Yu Wang, Liren Wang, and Abigail M. Lister

In some studies, it was necessary to analyse the chemical composition of the materials on the deposition areas. Thus, Raman analysis was performed utilising a Renishaw InVia Raman microscope with a 633 nm laser. The acquisition time was set to 10 seconds, and five repetitions were obtained to enhance the signal-to-noise ratio. The Raman data in this thesis were taken by Runze Chen and then analysed by the author of this thesis. Furthermore, specific elements were analysed by Axel Forssberg using a PHI VersaProbe III X-ray photoelectron spectrometer (XPS) with monochromated Al Kα X-ray radiation (1486.6 eV), a 5 μm beam, and an analyser pass energy of 224 eV with an energy resolution of 0.28 eV.

## 3.4 Sensor testing setups

Same as in the majority of previous studies, the two-electrode technique was used for sensing tests in this thesis. A direct current (DC) potential was applied to the two interdigitated electrodes of the CP-based sensor, and the current was closely monitored to reflect the resistance change of the sensor during the sensing tests. As mentioned in Section 2.2.2, a constant potential may cause irreversible changes that can affect device stability.[26] High currents across the chemiresistors can cause self-heating, making the device sensitive to other parameters such as airflow,[81] but can also improve the signal-to-noise (S/N) ratio. Taking all these factors into comprehensive consideration, the DC potential for the sensor testing in our research group is set at 1.0 V, which was also used in all the sensing tests in this thesis. As the resistances of the sensors (R) in this thesis approximately vary between 100 Ω and 10 MΩ and the periods of time for sensing tests (t) lasted from 1 to 12 hours, the estimated Joule heat generated by the sensors ($Q = (1.0\ V)^2 \times t/R$) could span from $3.6 \times 10^{-4}$ to 432 J during the tests.

### 3.4.1 Gas sensing

Gas sensing experiments were conducted in a custom-made stainless-steel cylindrical chamber, which has an internal diameter of 21.05 ± 0.05 cm and an internal depth of 9.25 ± 0.05 cm (Figure 3.5). The sensing tests involved using analyte gases (10 ppm, nitrogen fill) and nitrogen gas (99.998 %, to further dilute the analyte). The flow rate of each gas cylinder was regulated by an Alicat mass flow controller (accuracy: ± 0.5 % of reading), with the gases being mixed at a joint before being introduced into the gas inlet of the chamber. A total flow rate of 500.0 ± 2.5 standard cubic centimetres per minute (sccm) was maintained throughout the experiments. The concentration of analyte gas was determined by the relative flow rates of the two mass flow controllers. The temperature and relative humidity in the chamber were recorded

via a Sensirion SHT31 temperature and humidity sensor (accuracy: ± 0.3 ˚C and ± 2 % RH) placed next to the CP-based chemiresistor. Each chemiresistor was fixed on a sample stage that was equipped with a heating element, and a thermocouple was affixed near its sensing layer. A thermostat system, consisting of the heating element, the thermocouple, and a Eurotherm 3216 temperature controller (accuracy: ± 0.25 % of reading), was established to determine the testing temperature in the chamber. The sensor in the chamber was connected to the B2902A source/measure unit, which was interfaced with a personal computer equipped with Benchvue software.

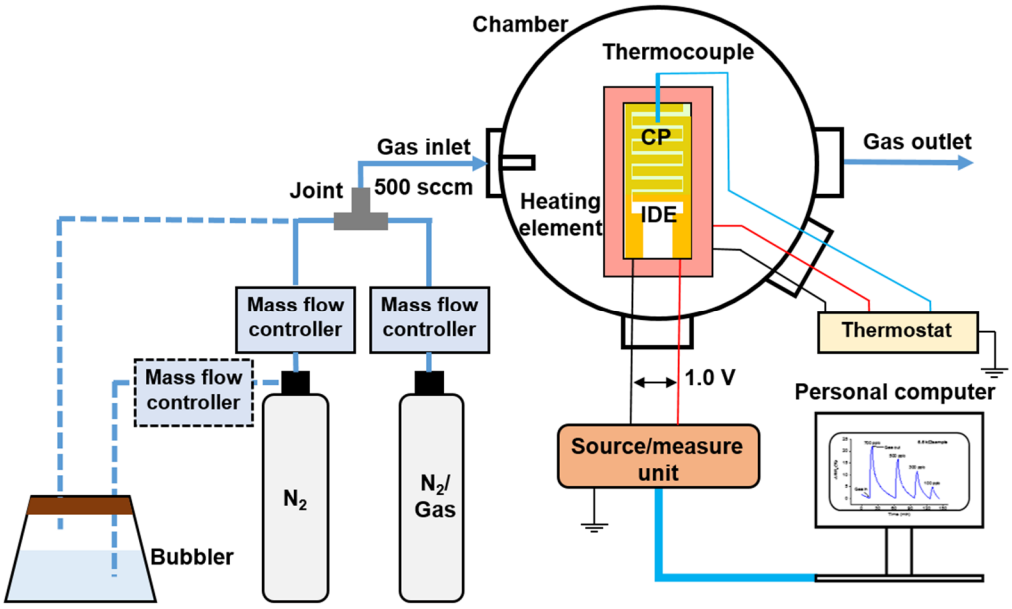



**Figure 3.5.** Schematic layout of the gas sensing setup. The sensor, consisting of the conjugated polymer (CP) deposited on an interdigitated electrode (IDE) substrate, is placed on a sample stage with a heating element in the sensing chamber. The thermostat system, comprising the heating element and the thermocouple, determines the test temperature. Gases are mixed at the joint. The analyte concentration and gas humidity are determined by the relative flow rates of the mass flow controllers connected to the gas cylinders. The current across the sensor, reflecting the gas sensing response, is recorded using the source/measure unit connected to a personal computer.

The chamber underwent an initial 30-minute purging process with nitrogen gas to remove impurities from both the chamber and the sensing layer. A DC potential of 1.0 V was applied to the two interdigitated electrodes of the CP-based chemiresistor, and the sensor resistance was closely monitored via the B2902A source/measure unit (SMU). After the purging process, the sensor was exposed to a mixture of gases containing the analyte and nitrogen for a set duration and subsequently recovered in nitrogen for another time period. The baseline of each sensor was defined as the average of the values measured within the 30-second period before the first exposure. Different concentrations of analyte gases were employed to generate distinct sensor responses. According to previous studies in our group, sensors might not recover after exposure to high concentrations above 8 ppm due to some irreversible CP-analyte reactions, such as over-oxidation. This uncertainty limited further characterisation of sensing layers after sensing tests. To avoid this potential limitation, it is recommended to conduct the gas sensing tests from high to low concentrations, and upper limits of concentration for the tests would be estimated through the first exposure. In the case of the opposite way based on tests from low to high concentrations, moreover, it would be difficult to determine a reasonable initial concentration for the sensing test of an unknown sensor due to no understanding of its lower limit of detection. Therefore, sensors in this thesis were tested from high to low concentrations. Gas sensing experiments were conducted at atmospheric pressure, and the measurements were recorded using the B2902A SMU connected to the personal computer.

In addition, a bubbler was utilised for certain experiments involving humidity. The relative humidity was determined by the relative flow rates of two mass flow controllers connected to the nitrogen cylinder. The moist nitrogen gas was then mixed with the analyte at the joint, and the total flow rate was kept at 500.0 ± 2.5 sccm. The Sensirion SHT31 temperature and humidity sensor (accuracy: ± 0.3 ˚C and ± 2 % RH) was placed next to the CP-based chemiresistor to detect the temperature and relative humidity in the chamber. Prior to the test,

the chamber was purged with moist nitrogen gas until the humidity sensor indicated a steady value of relative humidity. Sensor responses to the analyte were obtained at various relative humidity values from 1 to 55 % RH using the same testing protocols as those without the bubbler.

### 3.4.2 Temperature sensing

Temperature sensing experiments can be conducted using either the gas sensing setup illustrated in Figure 3.5 or the in situ conductance monitoring setup for in situ solid polymerisation shown in Figure 3.3. Although the thermostat system in the gas sensing setup can increase the temperature more rapidly, it takes longer time to cool down the sample stage in the chamber. Additionally, the wires and cables in the chamber are not able to withstand high temperatures above 70 ˚C. Therefore, for this thesis, the in situ setup was used for temperature sensing.

The CP-based chemiresistor, connected to the B2902A source/measure unit (SMU), was placed in a 5 mL glass vial. Dry nitrogen was purged into the vial for a period of 5 minutes to eliminate any impurities and moisture from the vial and the sensing layer. The vial was then quickly sealed to maintain a dry testing environment in nitrogen. The sensor in the sealed vial was then incubated at 30 ± 1 °C for 10 min, with the heating temperature being controlled through the IKA RCT Basic stirrer hotplate connected with a PT1000 temperature sensor (accuracy: ± 1 °C). A DC potential of 1.0 V was applied to the CP-based chemiresistor, and the sensor resistance was closely monitored. Different temperatures from 40 to 80 °C were used to generate distinct sensor responses. The baseline of each sensor was defined as the average of the values measured at 30 ± 1 °C within the 30-second period before the first increase in temperature. The measurements were recorded using the B2902A SMU connected to a personal computer interfaced with Benchvue software.

### 3.4.3 Flow rate sensing

Similar to gas sensing, flow rate sensing experiments were also carried out in the custom-made chamber (Figure 3.6). Dry air (speciality grade, 19.9 – 21.9 % oxygen with nitrogen balance) was used and its flow rate was regulated by the Alicat mass flow controller (accuracy: ± 0.5 % of reading). Each CP-based sensor was fixed on the sample stage. The sensing layer was perpendicular to the direction of airflow at a distance of 20.0 ± 0.5 mm to the head of gas inlet tube. The temperature and relative humidity in the chamber were recorded via the Sensirion SHT31 temperature and humidity sensor (accuracy: ± 0.3 ˚C and ± 2 % RH) placed next to the CP-based chemiresistor. Each CP-based sensor in the chamber was connected to the B2902A SMU interfaced with a personal computer equipped with Benchvue software.

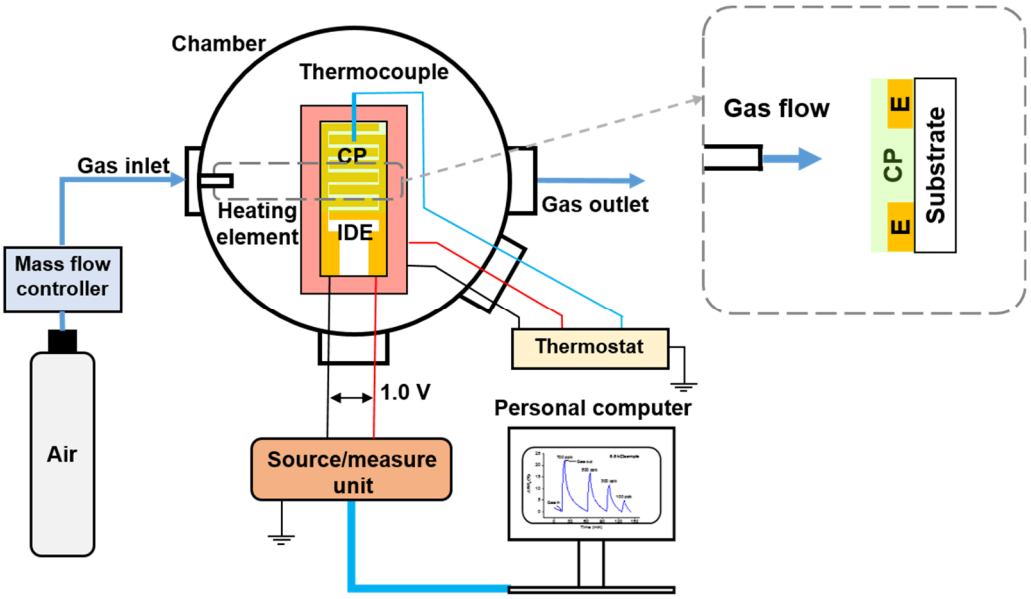



**Figure 3.6.** Schematic layout of the flow rate sensing setup. The sensor on the sample stage, consisting of the conjugated polymer (CP) deposited on an interdigitated electrode (IDE) substrate, is fixed perpendicular to the airflow direction. The thermostat system, which includes the heating element and the thermocouple, establishes the test temperature. The flow rate of dry air is regulated by a mass flow controller connected to the gas cylinder. The current across the sensor, indicating the flow rate sensing response, is recorded using the source/measure unit connected to a personal computer. (E: electrode.)

Prior to the test, the chamber was purged with dry air at a flow rate of 500.0 ± 2.5 sccm until the humidity sensor consistently indicated a very low relative humidity value under 3 % RH. Subsequently, the set value of flow rate was reduced to 0 sccm and maintained for 10 min. A DC potential of 1.0 V was applied to the sensor, and the sensor resistance was closely monitored via the B2902A SMU connected to the personal computer equipped with Benchvue software. After the 10-minute process at the set rate of 0 sccm, the sensor was exposed to various air flow rates from 20 to 800 sccm. The tests were conducted from low to high flow rates to avoid potential irreversible changes of sensing layers at high flow rate at the beginning of the tests. The baseline of each sensor was defined as the average of the values measured within the 30-second period before the first exposure.

## 3.5 Summary

Along with general information of materials used in this thesis, first, the configuration of the device substrate has been described in this chapter and each substrate should be cleaned before use. Then, various methods and instrumentation have been presented for the fabrication of the CP-based chemiresistors, including electrochemical polymerisation, in situ solid-state polymerisation, and solution processing deposition. To characterise the sensing materials on the substrate, several methods have been introduced to study their electrical, electrochemical, and surface properties. Finally, different custom-made setups have been designed to achieve gas, temperature, and flow rate sensing tests.

# Chapter 4

# Improved sensor reproducibility through in situ conductance monitoring

One of the challenges in percolation sensors prepared via the electrochemical deposition on substrates is to create percolation networks with consistent properties, so that devices based on them do not require individual calibration. To address this challenge, in this chapter, an in situ conductance technique is used during the electrochemical growth of polypyrrole (PPy) percolation networks. This technique measures the drain current ($i_d$) across interdigitated electrodes (IDEs) to determine the conductance of the PPy network during electrochemical polymerisation, allowing the percolation region to be identified. To improve the reproducibility of PPy percolation networks, an in situ current-controlled method based on the value of $i_d$ is used. The optimal percolation sensor, exhibiting the best overall performance towards ammonia, has been reproduced using this method. The device-to-device reproducibility of four optimal percolation sensors has been investigated through the coefficient of variation in both the sensor resistance and sensing performance.

## 4.1 Motivation and solution

Challenges remain when creating chemiresistive percolation sensors via the electrochemical deposition on substrates. The percolation region is typically determined by plotting the electrical conductance obtained after different numbers of deposition cycles or times, which does not allow for continuous monitoring of the conductance of the evolving CP networks. Additionally, due to the inherent randomness of network connections, it is difficult to achieve reproducible results, even for CP layers produced using identical procedures. In the percolation region, small variations in the network can have a significant effect on conductance due to the random nature of polymer growth.[228,229] As a result, conductance variations between chemiresistive percolation sensors can be up to an order of magnitude.[31,32] These variations in conductance observed in the percolation region lead to unsatisfactory device-to-device reproducibility, as the sensitivity and limit of detection are related to the initial conductance of the CP-based chemiresistor.[31] These challenges limit further studies on percolation sensors and their real-life applications. Only a few studies have discussed monitoring techniques and reproducibility issues for the electrochemical growth of CPs,[229-232] highlighting a significant gap in understanding how to overcome these problems.

In situ conductance measurement is an ideal way to gain real-time insight into the electrical properties of CP films during electrochemical growth and/or analysis,[233] bringing an opportunity to monitor or even control the process of electropolymerisation in the percolation region. As shown in Figure 3.2 in Section 3.2.1, a Keysight B2900A source/measure unit (SMU) is introduced between the IDEs on the substrate in a classic three-electrode system. The electrochemical workstation provides the faradaic current ($i_f$) and controls the deposition process or the doping state. The SMU records the drain current ($i_d$) induced by the applied potential ($\Delta V$), reflecting the conductance between the IDEs in real time. This technique has

been used in the fabrication of chemiresistors based on CP films.[43] However, to my knowledge, there was no relevant research on percolation networks.

In this chapter, in situ conductance monitoring is used to investigate CP-based percolation networks, the reproducibility of their resistances, and the device-to-device reproducibility of chemiresistive percolation sensors. As one of the most representative conjugated polymers in chemical detection, polypyrrole (PPy) is chosen to form the percolation networks via electropolymerisation. The $i_d$ curves of PPy recorded during chronoamperometry are analysed to determine their reliability in effectively estimating the percolation region. Based on the measurement of $i_d$, an in situ current-controlled method is then introduced to control the deposition process. Using this method, improved reproducibility of the resistances of PPy networks is demonstrated, and the device-to-device reproducibility for chemiresistive percolation sensors is investigated. Sensing tests are conducted using ammonia ($NH_3$) gas, as PPy has been shown to exhibit a strong response to ammonia.

## 4.2 Experimental section

### 4.2.1 Electrochemical experiments

Prior to electrochemical experiments, the Pt IDE substrates (Micrux) were cleaned with concentrated nitric acid ($HNO_3$, 90 %, Fisher Scientific) and sonicated in methanol ($CH_3OH$, 99.9 %, Sigma-Aldrich), ethanol ($C_2H_5OH$, 99.8 %, Sigma-Aldrich), and acetone ($C_3H_6O$, 99.8 %, Sigma-Aldrich) for 10 min each. Electrochemical deposition was then carried out using the in situ conductance monitoring setup (Figure 3.2). The three-electrode cell, supported by the PGSTAT204 Autolab electrochemical workstation (Eco Chemie), used the Pt coil (BASi) as the counter electrode, the Ag/AgCl (CH Instruments) as the reference electrode, and the Pt IDE as the working electrode. Pyrrole (Py, 98 %, Sigma-Aldrich) was directly used for electropolymerisation without further purification. PPy was synthesised in the deposition area

of the IDE substrate by chronoamperometry at 1.0 V from a solution containing 50 mM Py and 0.1 M lithium perchlorate ($LiClO_4$, 99 %, Sigma-Aldrich) in acetonitrile ($CH_3CN$, 99 %, Sigma-Aldrich). During deposition, the $i_d$ current was recorded via the B2902A source/measure unit (SMU, Keysight) interfaced with the personal computer equipped with Benchvue software. CP-based chemiresistors were prepared with applied potentials ($\Delta V$) from 20 to 80 mV. Devices with various conductance values were prepared by halting electropolymerisation at different deposition times or values of $i_d$. After deposition, they were washed with $CH_3CN$ and dried in air for 10 min. This washing and drying process was repeated after each device was p-doped at 1.0 V for 60 s in an electrolyte solution of 0.1 M $LiClO_4$ in $CH_3CN$.

### 4.2.2 Sensing experiments

Sensing experiments were carried out at atmospheric pressure using the gas sensing setup (Figure 3.5) and the experimental protocol described in Section 3.4.1. $NH_3$ gas (10 ppm, nitrogen fill, BOC) and nitrogen gas ($N_2$, 99.998 %, BOC, for further dilution of $NH_3$) were mixed at the T-joint before entering the gas inlet of the chamber, and a total flow rate of 500.0 ± 2.5 sccm was maintained throughout the experiments. The concentration of $NH_3$ gas was determined by the relative flow rates of the two mass flow controllers (Alicat). The temperature around the sensor was maintained at 27.0 ± 0.1 °C via the thermostat system. The sensor in the custom-made chamber was connected to the B2902A SMU interfaced with a personal computer. The DC potential of 1.0 V was applied during the experiments, and the resistance of the sensor was monitored on the personal computer equipped with Benchvue software. $N_2$ gas was initially purged for 30 min to eliminate impurities from both the chamber and the sensing layer. After the purging process, the sensor was exposed to concentrations of $NH_3$ gas ranging from 4 to 1 ppm for 1 min each. The baseline of each sensor was defined as the average of the values measured within the 30-second period before the first exposure. After each exposure,

the sensor was purged with $N_2$ until its resistance returned to the baseline before the next exposure.

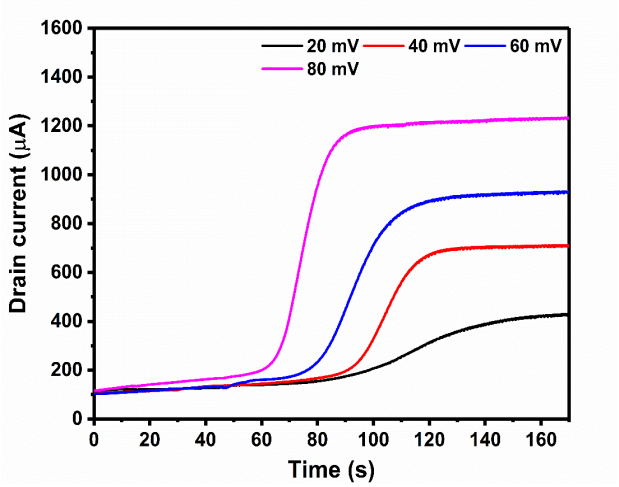



**Figure 4.1.** Measured $i_d$ curves during chronoamperometric growth of PPy on Pt IDEs with ΔV of 20, 40, 60, and 80 mV. The initial $i_d$, as the baseline of the curve, is not zero because a part of $i_f$ flows through the source/measure unit during polymerisation. The curves show an earlier onset of the current increase and a higher final $i_d$ for higher ΔVs.

## 4.3 Results and discussion

### 4.3.1 Drain current curves

PPy networks were prepared in the deposition area via chronoamperometry with ΔV of 20, 40, 60, and 80 mV. The $i_d$ current during deposition was measured to study the trend of conductance between the IDEs in the salt solution with monomers. All the $i_d$ curves exhibit similar trends from baselines to plateaus (Figure 4.1). Initially, PPy nucleates and grows on the Pt IDE fingers connected to both the electrochemical workstation and the SMU. As the SMU connects to the workstation in the in situ conductance monitoring setup (Figure 3.2), a portion of $i_f$ inducing polymerisation flows through the SMU, resulting in an initial value of $i_d$ for each curve. Therefore, the initial $i_d$, as the baseline of the curve, is not zero due to the existence of $i_f$

from the workstation. Once the Pt fingers in the deposition area are fully covered, PPy starts to grow into the insulating gaps between these fingers. As deposition proceeds, $i_d$ increases sharply owing to the formation of PPy bridges between IDE fingers. A higher ΔV results in a shorter time to reach the onset of the sharp increase in gradient because the ΔV is added onto the deposition potential for one side of electrodes and thus speeds up the deposition on that side.[233] The $i_d$ current keeps increasing until a plateau is reached, indicating the fingers are fully connected and a PPy dense thin film has formed. The height of the plateau depends on ΔV owing to Ohm's law. These $i_d$ curves are consistent with reported trends describing the conductance changes from the insulating region to the thin film region.[31,32,35] This finding suggests that the in situ method enables continuous monitoring of the polymer growth between the IDEs.

A suitable single value of ΔV requires to be decided upon before further studies are carried out on the reliability of the $i_d$ curve and the reproducibility of the percolation networks. Although a very low $i_d$ induced by a very low ΔV can avoid the overoxidation of the CP on one side of the electrode, it will result in relatively higher noise. For real-time monitoring via Benchvue software, furthermore, the change of the display range for $i_d$ should also be taken into consideration. For instance, 80 mV may not be suitable since the corresponding $i_d$ increases over 1000 μA after 80 s and the display unit of $i_d$ has to change from μA to mA. Considering these factors, both 60 mV and 40 mV are suitable, however 60 mV was chosen to obtain a better signal to noise ratio. Using a ΔV of 60 mV, the $i_d$ current starts to increase sharply after 70 s and the $i_d$ plateau is reached after 120 s (Figure 4.1).

### 4.3.2 In situ time-controlled method

A time-controlled preparation method was used to study the reliability of the $i_d$ curve. PPy was grown by chronoamperometry at 1.0 V using ΔV = 60 mV. Four samples were obtained

at each deposition time ranging between 20 and 140 s. Their resistances were recorded after the post-treatment processes including doping, washing, and drying (Figure 4.2). The semi-logarithmic plot in red is used to determine the boundary between the percolation and the thin film regions. The conductance increases sharply at first, showing the percolation behaviour. Then this increase starts to slow down at 100 s within the same order of magnitude, indicating that percolation ends after around 100 s. Some error bars in conductance for the percolation region are quite large, covering an order of magnitude. This is in agreement with previous work based on the time-controlled method.[31,35]

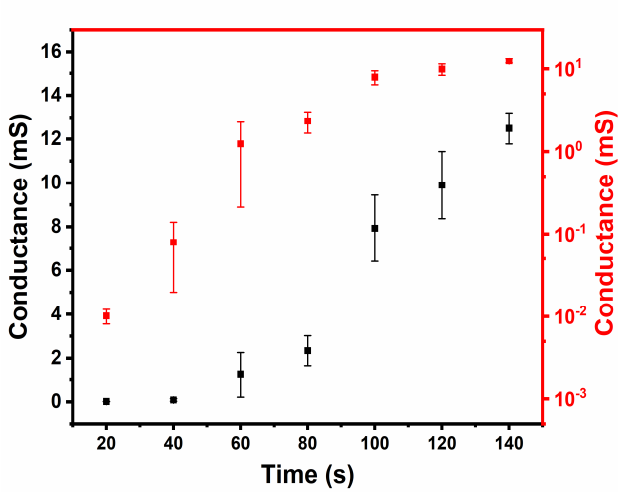



**Figure 4.2.** Plot of conductance vs. deposition time (in black) and its semi-logarithmic plot (in red) for the deposition of PPy on Pt IDEs using an in situ time-controlled method at 1.0 V and a ΔV of 60 mV for deposition times of 20 – 140 s. All the error bars are obtained from the standard deviation of the conductance values of four separate samples.

The normal plot in black determined using this time-controlled method (Figure 4.2) is similar to the percolation curve of the $i_d$ current using ΔV = 60 mV (Figure 4.1). A possible reason for any difference could be that the sample for the $i_d$ curve under 60 mV in Figure 4.1 only represents one possibility, whereas the data in Figure 4.2 represents the average of 4 independent samples. To demonstrate this, $i_d$ curves were recorded for ΔV = 60 mV for 4

independent samples (Figure 4.3). For these 4 measurements the onset of the significant current increase varies from 55 to 70 s, which is similar to the results at 60 s obtained with the time-controlled method. The variability in the onset of the current increase is attributed to the random growth of PPy. Although the difference in conductance and the variability of the $i_d$ curve are unavoidable, the $i_d$ curve is reliable enough to provide a reference range to estimate the percolation behaviour for an unknown system, improving the accuracy and efficiency for determining the percolation region in practical experiments. The variability of the $i_d$ curves in Figure 4.3 also shows the drawback of the time-controlled method, requiring an alternative method to improve the reproducibility of the initial conductance of the CP networks.

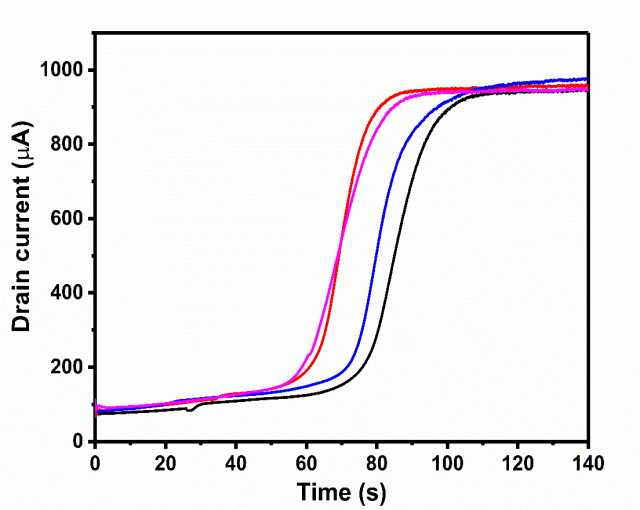



**Figure 4.3.** Drain current ($i_d$) curves for 4 independent samples during chronoamperometric growth of PPy using in situ conductance measurement with $\Delta V$ = 60 mV. The onset of the significant current increase varies from around 55 s to 70 s.

### 4.3.3 In situ current-controlled method

To improve the reproducibility of PPy percolation networks, a current-controlled method was designed, using the difference of $i_d$ between the baseline and the value during growth ($\Delta i_d$). PPy was grown via chronoamperometry at 1.0 V and $\Delta V$ = 60 mV. Instead of halting the

deposition after a predetermined time, as in the time-controlled method, samples were prepared by stopping the growth when $\Delta i_d$ reached a predetermined value between 10 and 600 μA. Then, three more repeat samples were created for each value of $\Delta i_d$. Their resistances were recorded following the post-treatment processes including doping, washing, and drying (Figure 4.4). Small measurable $\Delta i_d$ values indicate that the percolation threshold has been reached where a small number of polymer bridges have been created between the electrodes. However, for practical purposes, sensors with very low conductance values are unsuitable because their signal to noise ratios tend to be very high. Similar to the results in Figure 4.3, additionally, polymerisation time for the same $\Delta i_d$ varies due to the random growth of PPy. For instance, the time to achieve the $\Delta i_d$ of 50 μA in Figure 4.4 spans from 71 to 84 s.

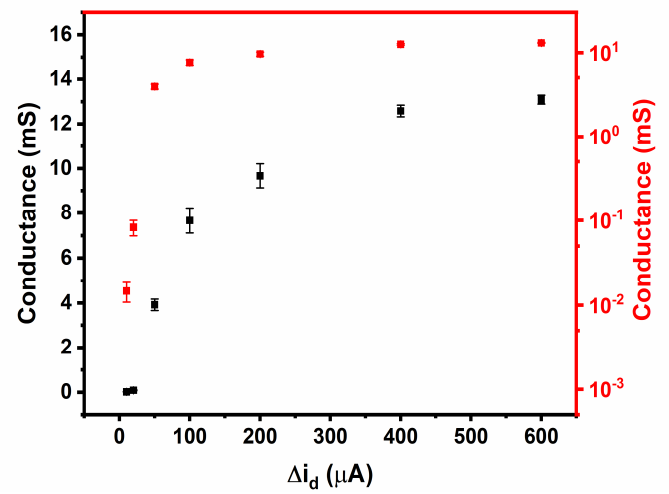



**Figure 4.4.** Plot of conductance vs. $\Delta i_d$ (in black) and its semi-logarithmic plot (in red) for the growth of PPy on Pt IDEs. All the error bars are obtained from the standard deviation of the conductance values of four separate samples.

Variations in conductance remain in the data in Figure 4.4 because the conductance is affected by post-treatment, for example when the sample is washed or doped. Compared to the time-controlled method (Figure 4.2), the current-controlled method shows smaller error bars, significantly improving the reproducibility of the conductance of the CP networks, especially

in the percolation region. These differences are more discernible in the semi-logarithmic plots. These smaller variations in conductance from the current-controlled method are attributed to a more direct way of monitoring the electrical properties of PPy during growth instead of using the deposition time to indirectly represent the amount of PPy obtained after growth.

It should be noted that the reproducibility of the conductance plays a significant role in studies of the sensing performance of the CP networks. Previous work has shown that the initial conductance affects the sensitivity.[31,32] Compared to dense thin film chemiresistive sensors with higher initial conductances, chemiresistive percolation sensors with lower initial conductances exhibit higher sensitivities. Furthermore, networks with similar values of initial conductance will exhibit similar signal-to-noise levels during sensor testing, resulting in similar limits of detection. Although percolation is a promising approach to easily obtain improved sensor performances, challenges for further studies and real-life applications remain if there is no effective way to produce percolation sensors with reliable and repeatable properties. The in situ current-controlled method makes it possible to overcome this by improving the reproducibility of the initial conductance of the CP network.

### 4.3.4 Sensor performance

The in situ current-controlled method was used to prepare PPy-based chemiresistors for sensing experiments. Sensors called $S_{400}$, $S_{50}$, $S_{35}$, $S_{20}$, $S_{10}$ and $S_5$ were fabricated by stopping growth at $\Delta i_d$ values of 400, 50, 35, 20, 10, and 5 μA, respectively. Halting PPy growth with a smaller value of $\Delta i_d$ results in sensors with lower conduction. The sensors were placed in the sensor testing chamber under $N_2$ flow and 1.0 V was applied across the IDEs. After the $N_2$ purging process for 30 min, sensors were then exposed to ammonia gas from 4 to 1 ppm for 1 min each. After each exposure, the sensor was purged with $N_2$ until its resistance returned to the baseline before the next exposure. The sensor response was recorded in Figure 4.5.

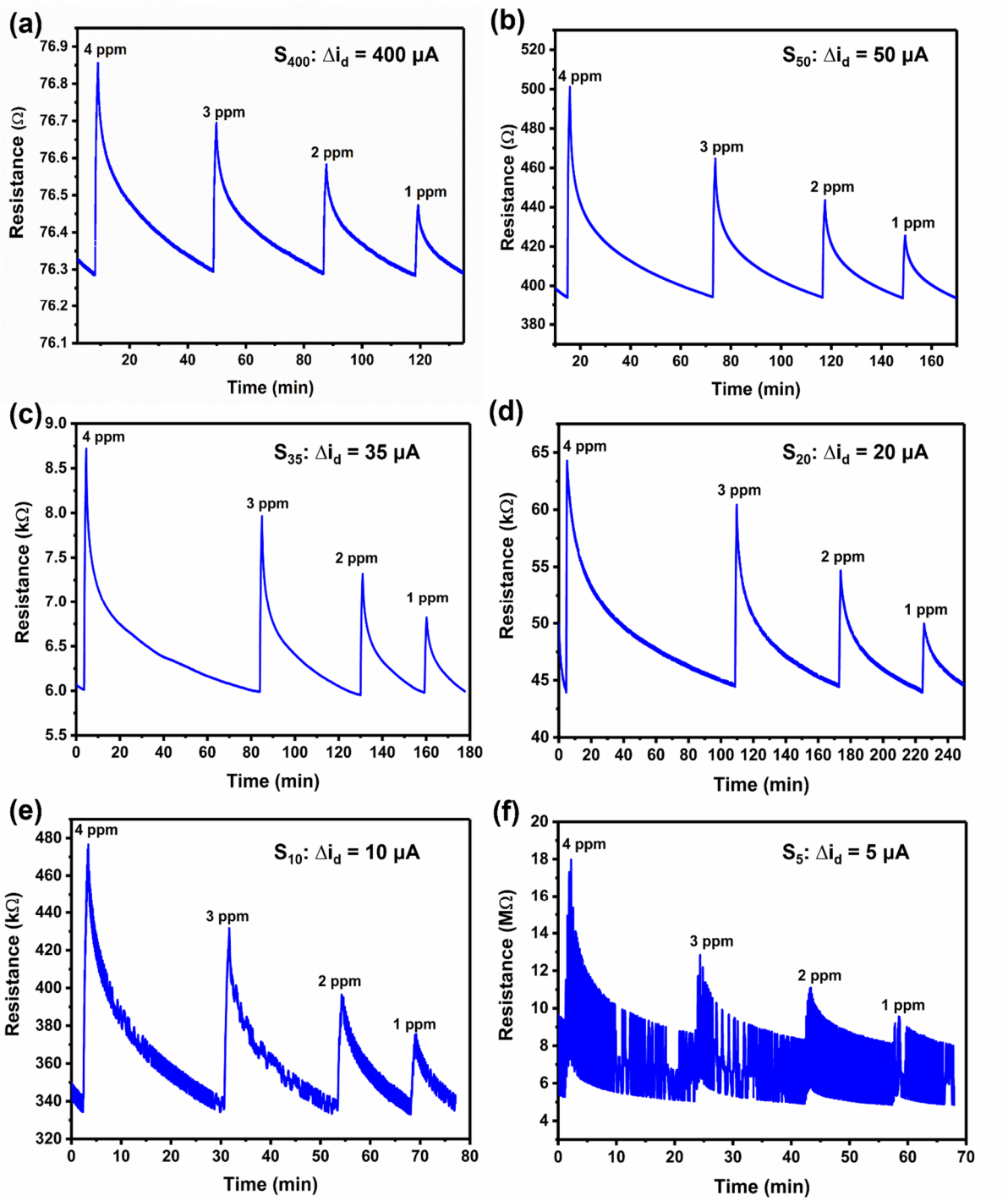
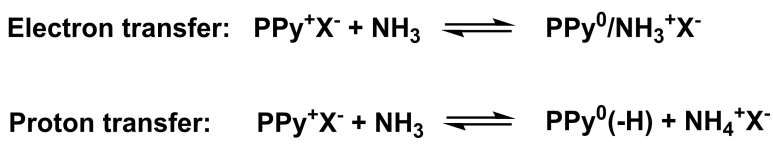



**Figure 4.5.** Sensing responses to 4, 3, 2 and 1 ppm ammonia in $N_2$ for 1 min each for PPy-based chemiresistors obtained by the in situ current-controlled method at $\Delta i_d$ values of (a) 400, (b) 50, (c) 35, (d) 20, (e) 10 and (f) 5 μA. Fresh ammonia exposures were only conducted once the sensor had recovered to the baseline. All the sensors exhibit shark fin responses, suggesting that they didn't reach the steady states within 1 min. The current value in the upper right corner of each figure represents the $\Delta i_d$ value used to fabricate the sensor.




**Scheme 4.1.** Detection mechanisms of PPy towards ammonia. ($X^-$: counterion)

As expected, the resistances increase during the exposure to ammonia gas because electron-donating ammonia molecules reduce the number of charge carriers in p-doped PPy. The resistance changes are reversible, returning to the baseline after exposure. According to the published literature,[234-239] the ammonia interaction mechanism with PPy occurs through electron transfer and/or proton transfer (Scheme 4.1). When interacting with $NH_3$ molecules, the p-doped PPy ($PPy^+$) is reduced to its neutral form ($PPy^0$) via a lone pair of electrons on the nitrogen atom of ammonia and/or the deprotonation of PPy creating ammonium salt ($NH_4^+X^-$). Additionally, sensors with higher baseline resistances displayed higher levels of noise. Among these sensors, $S_5$ with the largest resistance was not used for further experiments since it was difficult to distinguish signal from noise.

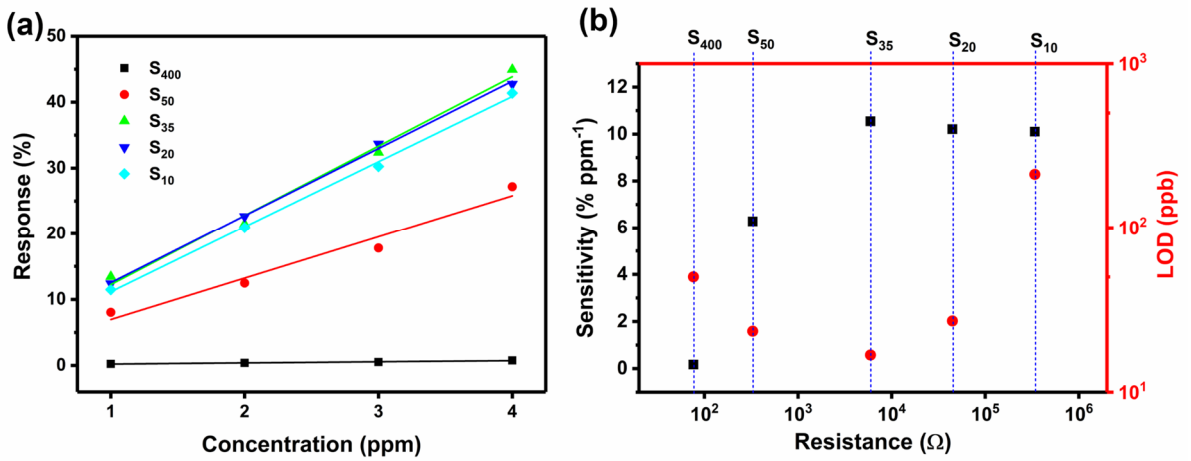



**Figure 4.6.** (a) Sensor responses, defined as $\Delta R/R_0 \times 100$ %, as a function of ammonia concentration for sensors $S_{400}$, $S_{50}$, $S_{35}$, $S_{20}$ and $S_{10}$. (b) Values of sensitivity (black squares) and limits of detection (red dots) for the five PPy-based sensors investigated.

To achieve the optimal sensor, the sensor responses of $S_{400}$, $S_{50}$, $S_{35}$, $S_{20}$, and $S_{10}$ were obtained by calculating the percentage changes to the baseline resistances ($\Delta R/R_0 \times 100$ %). For each sensor, a linear relationship was observed between the sensor response and the concentration of ammonia (Figure 4.6a). The sensitivity is defined as the slope of the linear fit in Figure 4.6a and the limit of detection (LOD) is defined as three times the standard deviation of the baseline noise level ($\sigma$) divided by the sensitivity. Figure 4.6b shows that $S_{400}$, obtained in the thin film region, exhibits the lowest sensitivity. As the sensor resistance increases, the sensitivity also increases and becomes stable above 10 % $ppm^{-1}$, where percolation networks determine the sensitivity instead of dense thin films. In the percolation region, interactions between the percolation networks and analyte molecules have a larger effect on the resistance of the networks, resulting in a significantly increased sensitivity compared to thin film-based sensors. Although $S_{20}$ and $S_{10}$ have high sensitivities, they also have higher LODs because their noise levels are relatively large compared to their sensitivity. As a result, as the baseline resistance of the sensor increases, the LOD first decreases and then increases owing to the competitive relationship between sensitivity and baseline noise. Therefore, $S_{35}$ is regarded as the optimal sensor with a sensitivity of 10.5 % $ppm^{-1}$ and a LOD of 17 ppb. This is in agreement with previous work where the percolation region was found at 1 – 10 kΩ for sensors created with the time-controlled method.[31] This demonstrates that the in situ current-controlled method, while increasing control over sensor preparation by halting polymer growth at a predetermined $\Delta i_d$ instead of deposition time, results in the same resistance range for optimal sensors.

Sensor $S_{35}$ was reproduced 3 times to study the device-to-device reproducibility. Sensors $S_{35\text{-}1}$, $S_{35\text{-}2}$, and $S_{35\text{-}3}$, were prepared and tested under the same conditions as sensor $S_{35}$. The sensor responses to 1 – 4 ppm ammonia obtained for $S_{35\text{-}1}$, $S_{35\text{-}2}$, and $S_{35\text{-}3}$ were similar to those of $S_{35}$ (Figure 4.7). In the literature, sensor responses at various concentrations were used to evaluate the device-to-device reproducibility for CP based chemiresistors.[240-243] The coefficient

of variation (CoV), defined as the standard deviation divided by the mean, for responses with desirable reproducibility vary from 0.05 to 0.10. To evaluate the device-to-device reproducibility of our percolation sensors, the CoV value for the responses at each concentration in Figure 4.7 was calculated. The average of these CoV values is 0.0870. This indicates that these percolation sensors also exhibit a desirable device-to-device reproducibility of sensing response, achieved with the in situ current-controlled method.

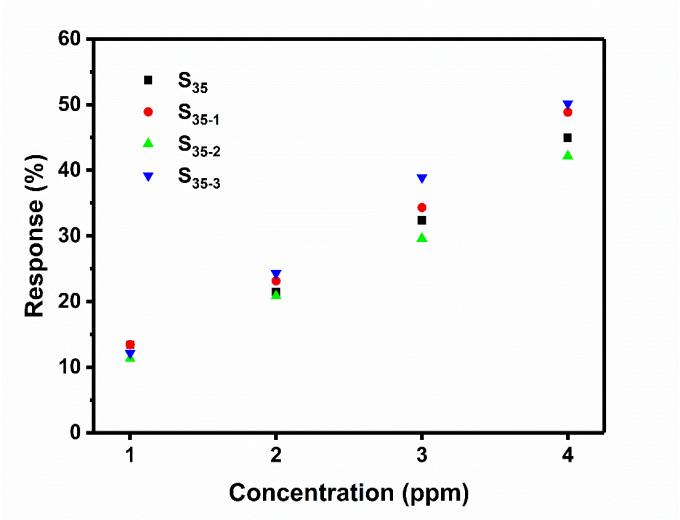



**Figure 4.7.** Sensor responses as a function of ammonia concentration for $S_{35}$, $S_{35\text{-}1}$, $S_{35\text{-}2}$, and $S_{35\text{-}3}$.

To further understand the device-to-device reproducibility of these $S_{35\text{-}x}$ sensors, CoV values for their baseline resistances, sensitivities, standard deviations in the baseline of the sensing response (σ), and LODs were calculated and summarised in Figure 4.8. Four $S_{35\text{-}x}$ sensors exhibit a CoV value of 0.1803 for their baseline resistance. This variation in resistance is attributed to the random effects from post-growth doping as well as stabilisation before the gas sensing tests. Furthermore, all four sensors have similar sensitivities with a CoV value of 0.1085, and the average sensitivity for this series of optimal sensors is 11.3 ± 1.2 % $ppm^{-1}$. This similarity is likely due to their similar resistance, resulting in a comparable number of

conducting pathways in their percolation networks, leading to similar sensing behaviour. The CoV value for σ (0.2009) is similar to that for baseline resistance because σ is related to that resistance. The difference between the CoV for σ and the CoV for resistance may be attributed to other factors that could affect σ, such as the testing setup or environment. As for the LOD, it depends on a comprehensive contribution from sensitivity and σ, resulting in a relatively larger CoV value of 0.2372 for all four percolation sensors. Their average LOD is 15.0 ± 3.6 ppb.

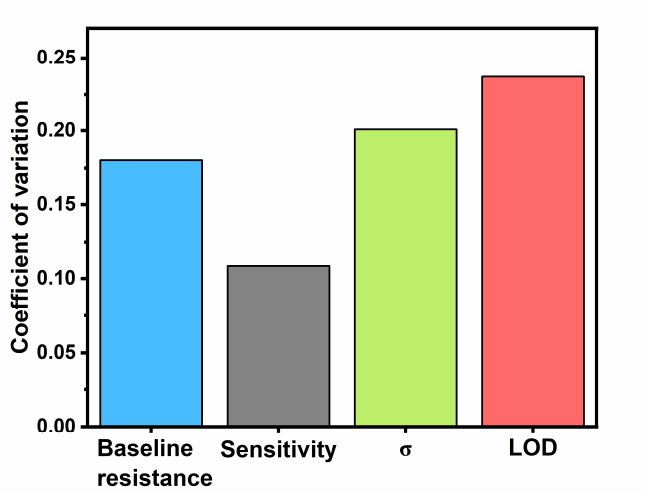



**Figure 4.8.** Coefficient of variation values for the baseline resistances, sensitivities, standard deviations in the baseline of the sensing response (σ), and LODs of four $S_{35-x}$ percolation sensors obtained by the in situ current-controlled method at $\Delta i_d$ values of 35 μA.

## 4.4 Conclusion and outlook

In this chapter, an in situ conductance technique was used to study PPy-based percolation networks, the reproducibility of their resistances, and the device-to-device reproducibility of chemiresistive gas sensors based on such percolation networks. During deposition the $i_d$ curve reflects the conductance of the PPy networks in real time, spanning from the insulating region

to the thin-film region. Compared to the conductance plot obtained by the time-controlled method, it is demonstrated that the $i_d$ curve can be used to reliably estimate the percolation region and improve the reproducibility of the initial conductance of the percolation networks. Using the current-controlled method, four optimal percolation gas sensors ($S_{35}$, $S_{35\text{-}1}$, $S_{35\text{-}2}$, and $S_{35\text{-}3}$) with an average sensitivity of 11.3 ± 1.2 % $ppm^{-1}$ and an average LOD of 15.0 ± 3.6 ppb to ammonia gas were created.

In materials science, time is conventionally used to control many preparation processes to ensure experimental reproducibility. However, electrochemical deposition suffers from inherent limitations that result in uncertainties of other parameters during this process, leading to unacceptable errors. As an alternative idea to improve reproducibility, this chapter proposes an in situ current-controlled method based on a more direct parameter of current. This method should also have the potential to be applied to the deposition of other conjugated polymers on various substrates, enabling opportunities for larger scale sensor fabrication relevant to the commercialisation of percolation sensors. Nevertheless, limitations remain, such as the potential influence of faradaic current flowing through the SMU and the cost of monitoring during large-scale fabrication, which require careful consideration in the future.

# Chapter 5

# Nanostructured percolation sensors via a nanosphere template

Nanostructuring and electrical percolation are two effective approaches to improve the sensitivity of conjugated polymer based chemiresistors. However, combining these approaches for further investigation and device improvement can be challenging. In this chapter, nanostructured polypyrrole (PPy) chemiresistive sensors for ammonia detection have been created using a nanosphere template. Polystyrene nanospheres are deposited to form a template between interdigitated electrodes, and chronoamperometry is used to grow PPy between the electrodes within the gaps of the nanospheres. The growth of PPy is controlled to create electrical percolation networks. After the removal of the nanospheres, the percolation behaviour and sensing response of the nanostructured PPy sensors are investigated. The nanostructured percolation sensors show better sensing performance to ammonia than percolation networks prepared without nanosphere templates. Optimal percolation sensors with the best overall performance are obtained from sensors prepared with and without nanosphere templates, respectively. In comparison to the optimal sensor prepared without the template, the optimal nanostructured sensor prepared with the template shows a 245 % increase in sensitivity and a 60 % decrease in the limit of detection.

## 5.1 Motivation and solution

Sensitivity is one of the most significant parameters for the sensing performance of chemiresistors based on conjugated polymers (CPs) and various approaches have to date been developed to improve it. Among all the reported approaches, nanostructuring is regarded as an effective strategy because morphologies with higher surface area-to-volume ratios can increase the sensitivity by improving the diffusion rate of gas molecules into and out of the CP-based sensing layers as well as providing more binding sites. To create nanostructured surfaces, CPs have in the past been fabricated through complex processes into different structures, including nanotubes, nanowires, nanoribbons, nanoparticles, and nanofibers.[55-57,87,91,244-249] On the other hand, electrical percolation via the conductor-on-substrate strategy can effectively improve sensitivity as well.[28-30] This is because the conductivity of an entire percolation pathway will be disrupted by the interaction of the analyte anywhere along the pathway, and this means that a small number of interactions between the analyte molecules and the CP percolation network will lead to a relatively large resistance change. Previous work has shown that electropolymerisation can be used to fabricate chemiresistors based on polypyrrole (PPy) and poly(3,4-ethylenedioxythiophene) (PEDOT) percolation networks.[31-35] The sensitivities and limits of detection of the resulting percolation networks to ammonia, nitrogen dioxide and ammonium nitrate/fuel oil are significantly improved compared to traditional thin-film chemiresistive sensors.

Although nanostructuring and electrical percolation can improve the sensitivity of CP-based chemiresistors, challenges remain for further investigation and device improvement due to their respective limitations. It is still difficult for nanostructuring to achieve ultra-high sensitivity at low analyte concentrations using easy-processing methods, while few studies focus on the

methods to tune the morphology of CP-based percolation networks. Therefore, attempts should be made to break these limitations through the combination of these two approaches.

Nanosphere templating is a well-established, cost-effective, and reproducible technique for nanofabrication that employs highly monodisperse nanospheres as deposition templates or etch masks for the fabrication of nanostructures.[250] It has previously been shown that electrochemical polymerisation can be performed between the nanospheres. After removal of the template, well-ordered CP networks with honeycomb-like or inverse-opal structures can be obtained and they can possess special surface and optical properties.[251,252] Owing to the unique properties of nanostructured polymers, electrochemical polymerisation coupled with nanosphere templating has been used in the creation of sensors, solar cells and other devices.[253-259] To combine nanostructuring and electrical percolation, this technique can be utilised to create CP percolation networks with well-ordered nanostructures for use in chemiresistors.

In this chapter, nanosphere templating is used to create CP percolation networks with well-ordered nanostructures between Pt interdigitated electrodes. PPy is used to form the percolation networks because it can be grown straightforwardly using established electrochemical techniques,[222,260] and it is known to change its electrical conductivity when exposed to ammonia gas.[25,261] This work shows that when nanostructured percolation networks are used in chemiresistive devices for the detection of ammonia ($NH_3$) they have higher sensitivities and lower LODs compared to their counterparts without nanosphere templates.

## 5.2 Experimental section

### 5.2.1 Preparation of nanosphere templates

Sulfuric acid ($H_2SO_4$, 95 %) was purchased from Sigma-Aldrich and hydrogen peroxide ($H_2O_2$, 30%) was purchased from Fisher Scientific. Prior to experiments, each Pt IDE substrate

(Micrux) in this chapter was treated with piranha solution ($H_2SO_4$ : $H_2O_2$ = 3:1, by volume; warning: piranha solution is very corrosive and must be treated with extreme care) at 50 ± 5 ℃ for 30 min to enhance its hydrophilic nature and then washed carefully with deionised water (Sigma-Aldrich) and ethanol ($C_2H_5OH$, 99.8 %, Sigma-Aldrich). The nanosphere templates were prepared via directed evaporation-induced self-assembly (DEISA) described in Section 3.2.3 (Figure 3.4b). During this process, substrates were vertically immersed in a 50 mL glass beaker containing 10 mL of $C_2H_5OH$ and 20 μL of 10 wt% latex of polystyrene (PS) nanospheres in water purchased from Sigma-Aldrich. The diameter of the PS nanospheres is 300 ± 50 nm. The beaker was then left at room temperature for 60 h until all the solvents had evaporated. After DEISA, the substrates decorated with PS nanospheres were sintered on the IKA RCT Basic hotplate at 90 ± 5 ℃ for 1 h. The surface morphologies of the nanosphere templates were imaged using a Zeiss Merlin scanning electron microscope (SEM) at an accelerating voltage of 10 kV.

## 5.2.2 Electropolymerisation of polypyrrole

Electrochemical deposition was carried out using the classic three-electrode system shown in Figure 2.2a and Section 3.2.1. The three-electrode cell, supported by the PGSTAT204 Autolab electrochemical workstation (Eco Chemie), used the Pt coil (BASi) as the counter electrode, the Ag/AgCl (CH Instruments) as the reference electrode, and the Pt IDE of the sample with a previous deposited nanosphere template as the working electrode. Pyrrole (Py, 98 %, Sigma-Aldrich) was directly used for electropolymerisation without further purification. PPy was synthesised by chronoamperometry at 0.85 V from a solution of 10 mM Py and 0.1 M lithium perchlorate ($LiClO_4$, 99 %, Sigma-Aldrich) in deionised water. Samples with various polymer coverages were prepared by halting electropolymerisation at different deposition times. After deposition, samples were carefully washed with acetonitrile ($CH_3CN$, 99 %,

Sigma-Aldrich) and dried in air for 10 min. The PS nanospheres were removed by immersing the samples in a tetrahydrofuran (THF, ≥ 99.0 %, Sigma-Aldrich) bath for 24 h followed by a THF rinse. After the removal of PS the samples were dried under ambient conditions. The same electrochemical synthesis conditions were used to deposit PPy on the substrates without nanospheres. After deposition, samples were carefully washed with $CH_3CN$ and THF and then dried in air for 10 min. The resistance of each sensor was measured using the RS PRO IDM 98IV handheld digital multimeter. The surface morphologies of the PPy networks were imaged using the Zeiss Merlin SEM at an accelerating voltage of 10 kV. The surface composition of PPy on the IDEs was studied using the Renishaw InVia Raman microscope and the PHI VersaProbe III X-ray photoelectron spectrometer (XPS) mentioned in Section 3.3.

### 5.2.3 Sensing experiments

Sensing experiments were carried out at atmospheric pressure using the gas sensing setup (Figure 3.5) and the experimental protocol in Section 3.4.1. $NH_3$ gas (10 ppm, nitrogen fill, BOC) and nitrogen gas ($N_2$, 99.998 %, BOC, for further dilution of $NH_3$) were mixed at the T-joint before entering the gas inlet of the chamber, and a total flow rate of 500.0 ± 2.5 sccm was maintained throughout the experiments. The concentration of $NH_3$ gas was determined by the relative flow rates of the two mass flow controllers (Alicat). The temperature and relative humidity in the chamber were recorded via the SHT31 temperature and humidity sensor (Sensirion) next to the PPy-based sensor. The PPy-based sensor in the custom-made chamber was connected to the B2902A source/measure unit (SMU, Keysight). The DC potential of 1.0 V was applied during the experiments, and the resistance of the sensor was monitored on a personal computer equipped with Benchvue software. $N_2$ gas was initially purged for 30 min to eliminate impurities from both the chamber and the sensing layer. After the purging process, the sensor was exposed to concentrations of $NH_3$ gas from 4 to 1 ppm for 6 min each. The

baseline of each sensor was defined as the average of the values measured within the 30-second period before the first exposure. After each exposure, the sensor was purged with $N_2$ for 15 min before the next exposure.

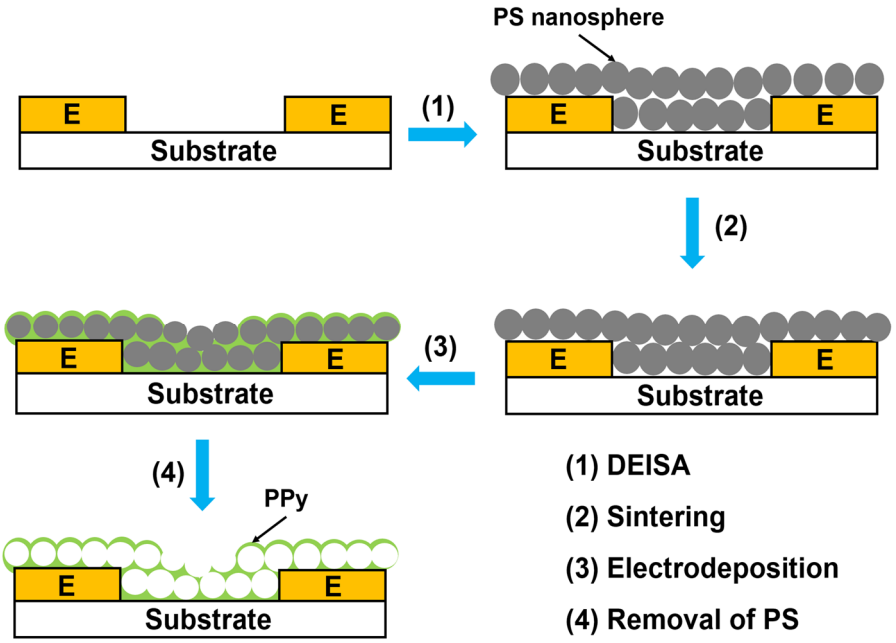



**Figure 5.1.** Schematic illustration of the preparation process of the nanostructured polypyrrole (PPy) sensor. Two electrodes (E) on a glass substrate are separated by a 5 μm gap. In step 1 polystyrene (PS) nanospheres are deposited onto the substrate via directed evaporation-induced self-assembly (DEISA). In step 2 sintering is performed. In step 3 PPy is grown electrochemically between the electrodes. In step 4 the PS nanospheres are dissolved.

## 5.3 Results and discussion

### 5.3.1 Preparation of nanostructured polypyrrole

Figure 5.1 shows a schematic of the preparation steps for the creation of the nanostructured PPy networks on Pt IDEs. Monodispersed PS nanospheres with a diameter of 300 ± 50 nm were deposited on Pt IDEs via DEISA. Although other solution processing methods in Section 3.2.3 were also attempted, DEISA exhibited the most favourable template morphology. This is

due to its ability to produce high-quality nanosphere templates with controllable thickness and geometry on substrates.[262] The IDEs decorated with PS nanospheres were then placed on a heating plate at 90 ± 5 °C for 1 h to induce moderate necking between the nanospheres. This sintering process is regarded as an effective way to improve the adhesion and stability of the nanosphere templates.[262,263] The SEM image in Figure 5.2 shows the surface morphology of a nanosphere template on IDEs. The template exhibits a close-packed structure over most of the substrate.[264] Some narrow empty regions can be found between the close-packed domains. These are defects possibly caused by the processes of DEISA and sintering. Using this method, a stable and well-ordered overlayer of PS nanospheres can be routinely obtained, which is then used as a template for the electrochemical deposition of PPy.

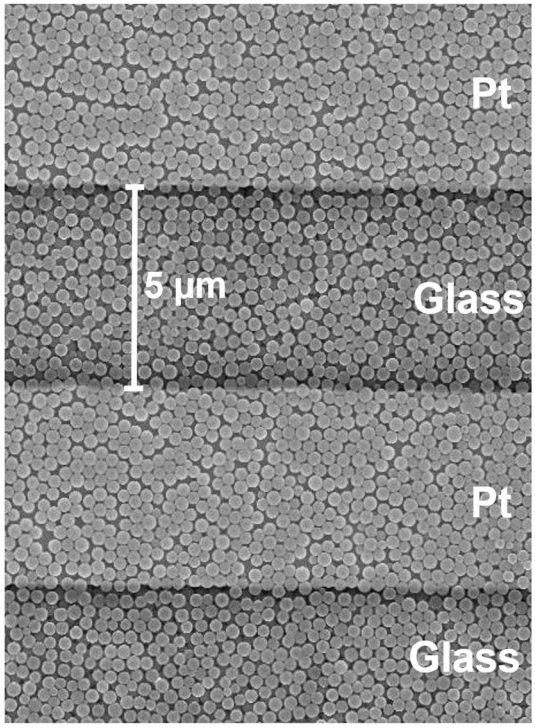



**Figure 5.2.** SEM image of a PS nanosphere template deposited on Pt IDEs. The PS nanospheres cover the electrodes and the gaps between the electrodes. Image taken by Abigail M. Lister.

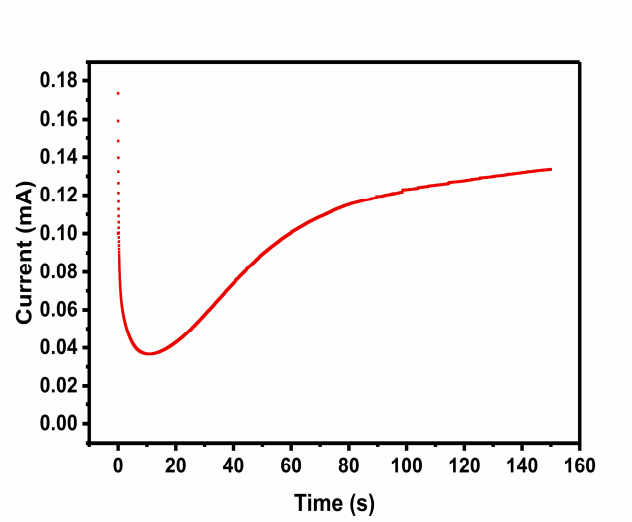



**Figure 5.3.** Chronoamperometric transient obtained for the deposition of PPy on the PS nanosphere template. The potential was set at 0.85 V and held for 150 s.

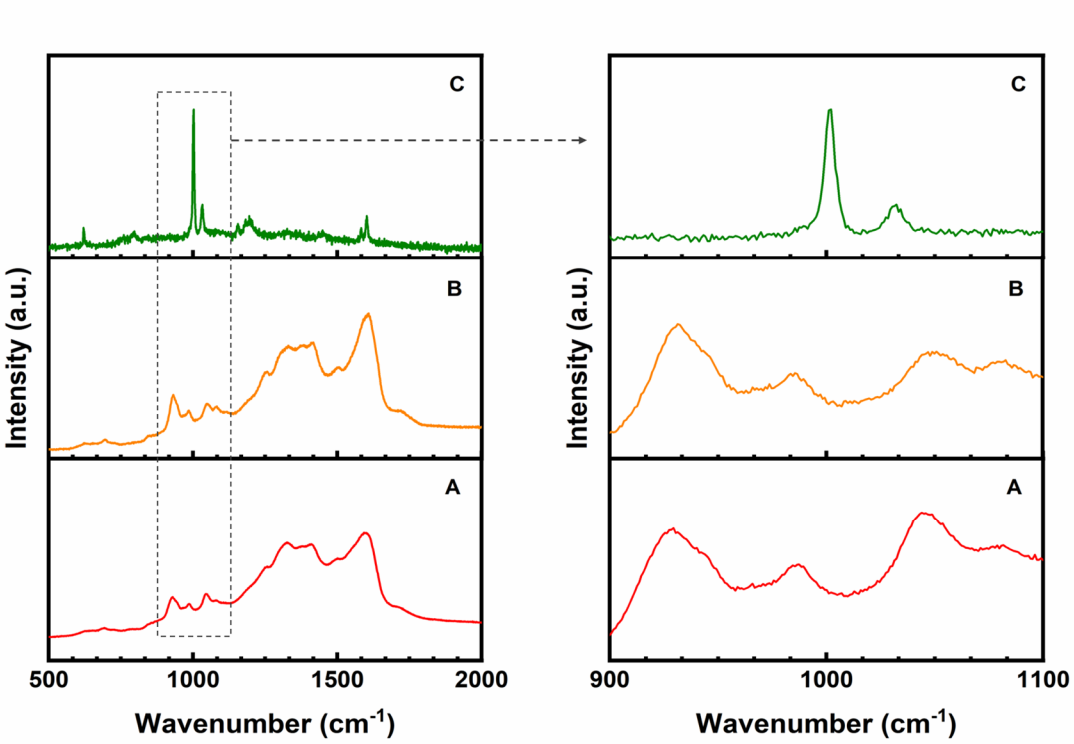



**Figure 5.4.** Raman spectra of nanostructured PPy after nanosphere removal (A), PPy prepared without the nanosphere template (B), and PS nanosphere (C) on Pt IDE substrates. Data taken by Runze Chen and then analysed by the author of this thesis.

PPy networks were grown on the PS nanosphere templates via chronoamperometry at 0.85 V. The electrochemical deposition process and electrolyte did not damage or alter the PS

nanosphere templates. Figure 5.3 shows an example of the current as a function of deposition time during chronoamperometry. Here the deposition current initially decreases from a relatively high value until approximately 10 s. This current decay could be attributed to a diffusion-controlled process involving the infiltration of Py monomers to the Pt surface through the porous templates, or possibly an indication that the interaction with the bare Pt electrodes proceeds relatively rapidly until they are covered in polymer. When the current starts to increase after around 10 s, this indicates that the polymerisation of monomers and the doping process of the polymer starts to dominate the current. In the final processing step THF is used to dissolve the PS nanospheres. The resulting deep blue PPy films are firmly attached to the IDEs without disintegrating during this process. Each sample exhibited similar electrical resistance values before and after nanosphere removal. According to the Raman spectra (Figure 5.4), no peaks related to PS were found, indicating the nanospheres on the surface of the sensing layers were fully removed through the dissolution in THF.

### 5.3.2 Electrical percolation

To study the electrical percolation behaviour, various PPy networks were prepared on the PS nanosphere templates via chronoamperometry. Four repeat samples were obtained at a variety of deposition times ranging from 80 to 150 s. The resistance values between the IDE electrode fingers were recorded after the dissolution of the PS nanospheres. The linear plot in black (Figure 5.5a) shows the conductance ranging from the insulating region to the percolation region and then the thin-film region and is consistent with previously reported trends.[31,265] The same data plotted as a semi-logarithmic plot in red is used to determine the boundaries between insulating, percolation, and thin film regions. Initially, PPy nucleates and grows between PS nanospheres on the Pt IDE fingers. After filling the voids between the PS nanospheres on the IDE fingers, PPy starts to grow into the spaces between the nanospheres on the insulating gaps

between the electrode fingers. No electrical conductance can be detected until 100 s of growth, indicating that samples prepared at 80 and 90 s belong to the insulating region. Then, from 100 s, the conductance sharply increases owing to the formation of PPy bridges between IDE fingers. This behaviour demonstrates the percolation behaviour of PPy networks prepared with the PS nanosphere templates. As deposition proceeds, the fingers are fully connected and a PPy thin film is formed. Thus, the increase in conductance is less rapid at 140 s, indicating the end of the percolation region. It should be noted that variations in conductance for samples produced with identical procedures exist in both the percolation and the thin-film regions. This is attributed to several unavoidable factors including the variation between each template, the random nature of the polymer growth,[228,229] and the influence of the post-treatment washing procedure.

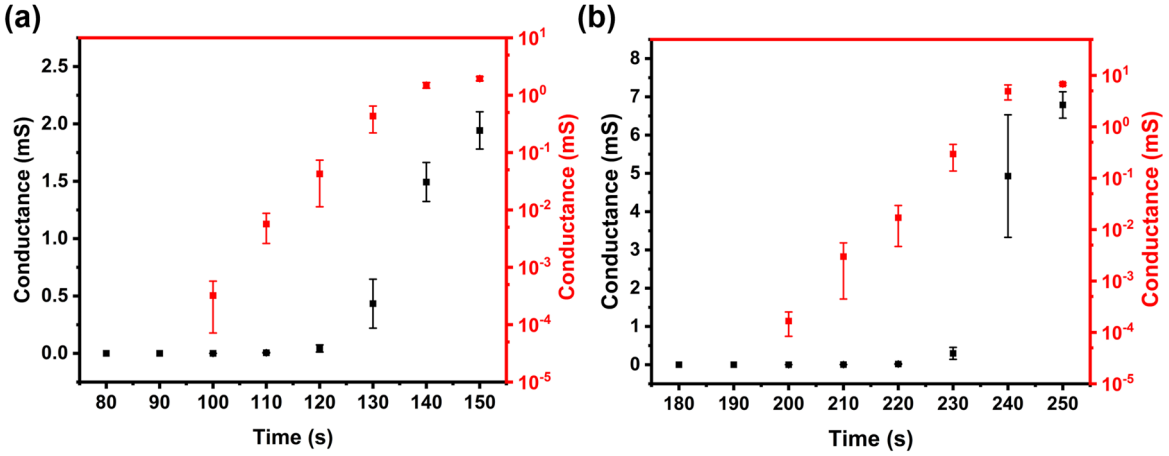



**Figure 5.5.** Plots of conductance vs. deposition time (in black) and their semi-logarithmic plots (in red) for the deposition of PPy on Pt IDEs (a) with and (b) without PS nanosphere templates via chronoamperometry. All the error bars are obtained from the standard deviation of the conductance values of four separate samples.

Samples without the PS template were prepared using the same procedure and their values of conductance were recorded from the insulating region to the thin-film region (Figure 5.5b).

The change of conductance is also consistent with previously reported trends and the estimated percolation region lies between 200 and 240 s. As the absence of PS nanospheres results in more volumes for the polymer growth on substrates, compared to the counterpart samples via nanosphere templating (Figure 5.5a), extending PPy requires more time to bridge conducting pathways between electrodes and denser PPy thin films should be obtained. Therefore, samples without templates in Figure 5.5b show a longer time for the percolation threshold and higher values of conductance in the thin-film region.

The SEM images in Figure 5.6 show the growth of PPy networks on IDEs in a nanostructured form following the dissolution of the nanospheres. PPy networks consisting of bowl-shaped pores are obtained on Pt IDE fingers when the deposition process is stopped at 80 s (Figure 5.6a). At this early stage of growth, the thickness of this nanostructured PPy is thinner than that of the templates on the IDE fingers. As more PPy is deposited between the PS nanospheres, the pore size becomes smaller and PPy expands onto the glass gaps at 90 s (Figure 5.6b). Shells in a close-packed structure can be observed on the fingers and even in some parts of the glass gaps from 100 s (Figure 5.6c – f). This suggests that the topmost layers of the templates in corresponding areas are fully covered with PPy at these stages. Otherwise, new layers of pores in a close-packed structure should appear in these areas after 100 s, changing the surface morphology of PPy networks. Figures 5.6c – f show the increasing penetration of the PPy networks across the glass gaps. Although no obvious bridges are observed in Figures 5.6c and 5.6d, some conducting bridges must have formed at 100 s and 110 s based on the non-zero conductance measurements (Figure 5.5a). The glass gaps are fully covered at 140 s, indicating that the electrical percolation regime ends at around 140 s (Figure 5.6g). This is consistent with the conductance measurements in Figure 5.5. From 140 s onwards, PPy networks close the upper layers in the middle of the gaps until a uniform overlayer is created (150 s, Figure 5.6h). Growth beyond 150 s adds to the thickness of the surface PPy film and is equivalent to a sensor

in the thin-film region, where the increase in conductance slows down since film thickness becomes the major factor controlling film conductivity.

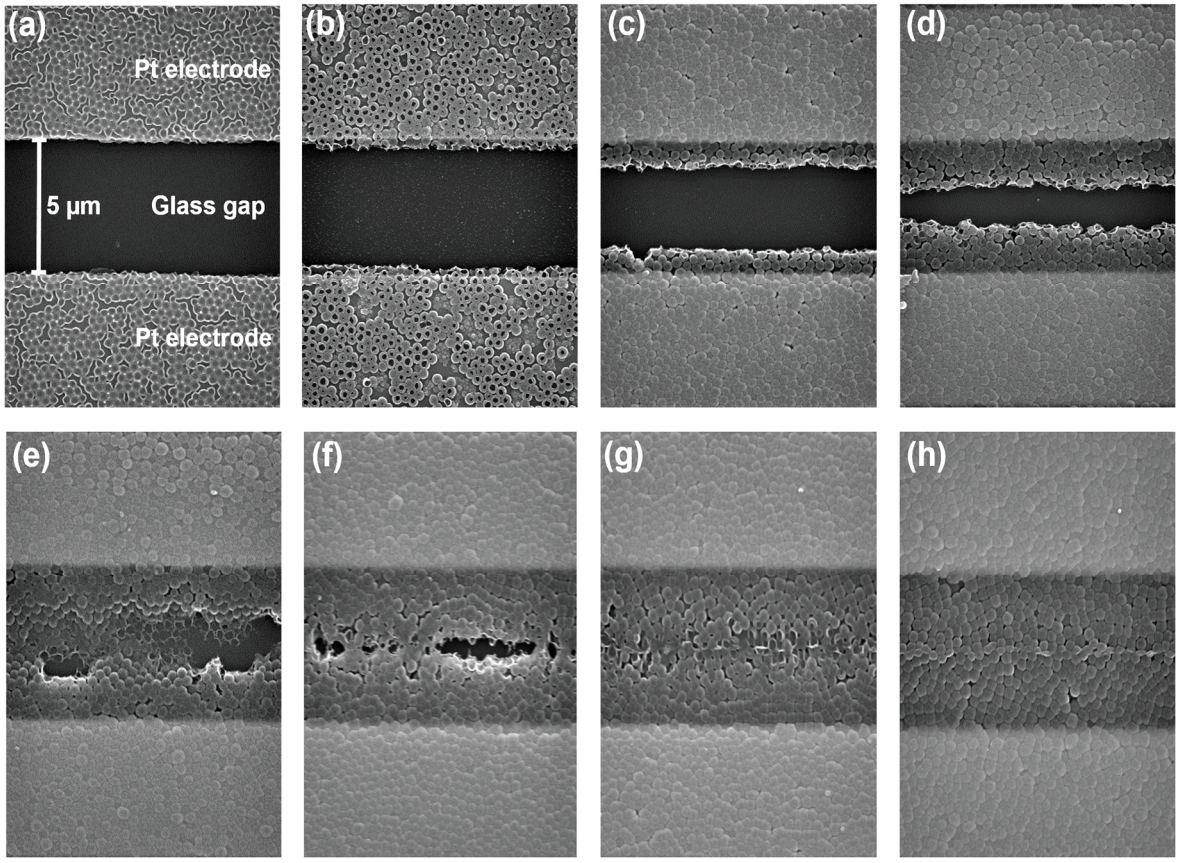



**Figure 5.6.** SEM images of nanostructured PPy prepared with the PS nanosphere templates via chronoamperometry on Pt IDEs for (a) 80 s, (b) 90 s, (c) 100 s, (d) 110 s, (e) 120 s, (f) 130 s, (g) 140 s, and (h) 150 s. As the deposition time increases, both the amount of PPy on the Pt fingers (light grey) and across the glass gaps (dark grey) increases. Images taken by Yu Wang.

Although a porous bowl-shaped surface morphology is preferred due to its ability to absorb more chemicals to the interior of the polymer networks,[266] this remains challenging. The polymer growth starts on the IDE fingers and the growth on top of the fingers happens earlier than the growth across the glass gaps. Therefore, it is likely that the topmost layers of the templates in some areas are fully covered, leading to a structure of close-packed shells of PPy,

before PPy bridges the gap between the electrodes. One possible solution would be to increase the thickness of the nanosphere templates, requiring further studies on their deposition methods.

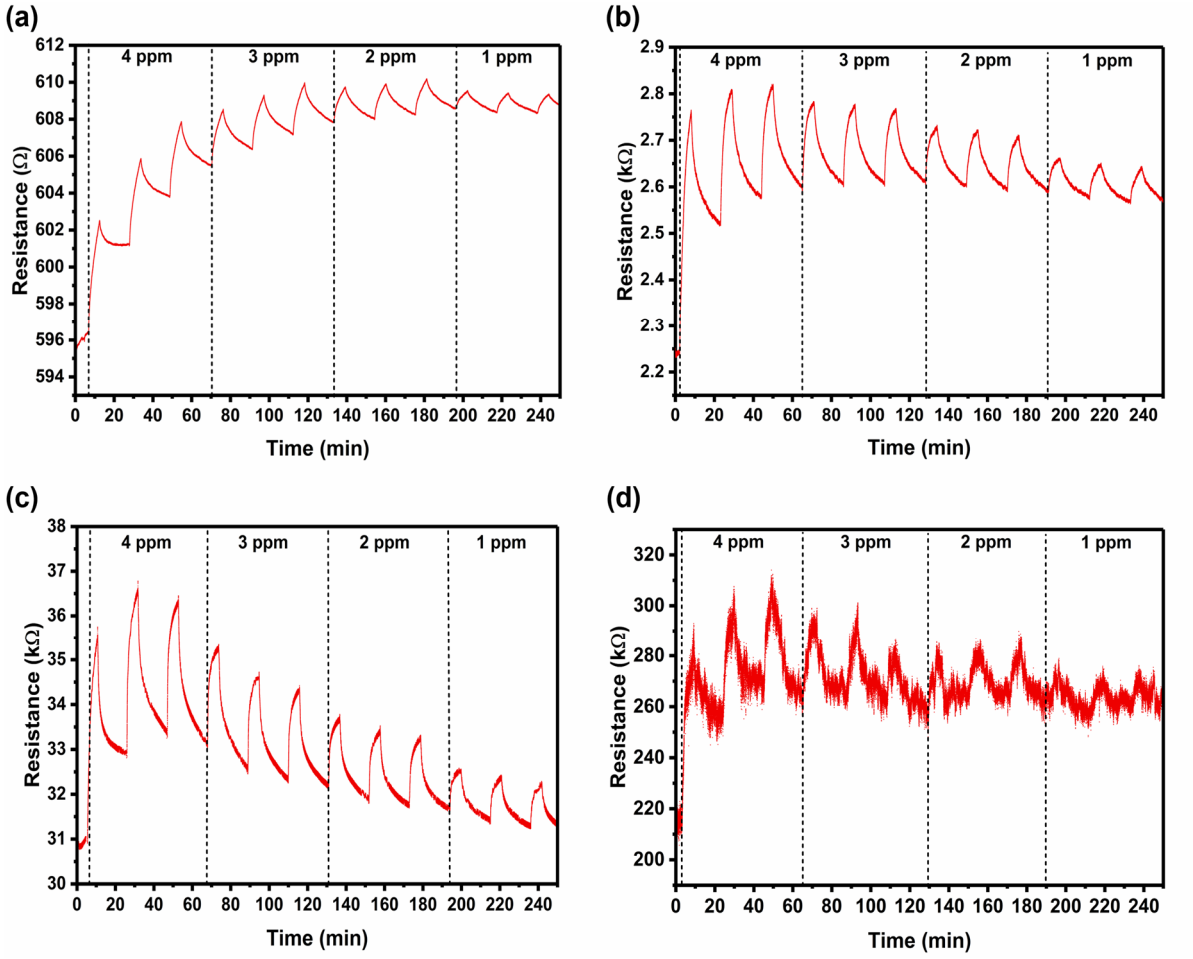



**Figure 5.7.** Sensor response to ammonia for the chemiresistors (a) $S_{N\text{-}T}$, (b) $S_{N\text{-}P1}$, (c) $S_{N\text{-}P2}$, and (d) $S_{N\text{-}P3}$ based on nanostructured PPy at deposition times of 140 s, 130 s, 120 s, and 110 s, respectively. $S_{N\text{-}T}$ was obtained in the thin-film region while $S_{N\text{-}P1}$, $S_{N\text{-}P2}$, and $S_{N\text{-}P3}$ were obtained in the percolation region. All sensors were exposed 3 times to 1, 2, 3, and 4 ppm $NH_3$ in $N_2$ for 6 minutes, with a 15 minute recovery time under pure $N_2$ flow between exposures. The test temperature is 26 ± 1 °C and the humidity is 1.22 ± 0.23 % RH.

### 5.3.3 Sensor performance

Nanostructured PPy created with the PS nanosphere template was used to fabricate chemiresistors for gas sensing experiments. Percolation sensors called $S_{N\text{-}P1}$, $S_{N\text{-}P2}$, and $S_{N\text{-}P3}$

were fabricated by stopping electrochemical deposition at 130 s, 120 s, and 110 s, respectively. For performance comparison, a thin-film sensor called $S_{N\text{-}T}$ was fabricated at 140 s with the aid of the nanosphere template. The sensors were placed in our sensor testing chamber under $N_2$ flow and 1.0 V was applied across the IDEs. Sensors were then exposed to 1, 2, 3, and 4 ppm ammonia gas diluted with $N_2$ and the resulting change in resistance was recorded (Figure 5.7).

Following the sensing mechanism in Scheme 4.1 in Section 4.3.4, as expected, the sensor resistance increases during the exposure to ammonia gas because electron-donating ammonia molecules reduce the number of charge carriers in p-doped PPy. Figure 5.7 also shows that higher ammonia concentrations result in larger resistance changes and sensors with higher resistances exhibit higher levels of noise. This is in agreement with the previous work from our research group.[31,265]

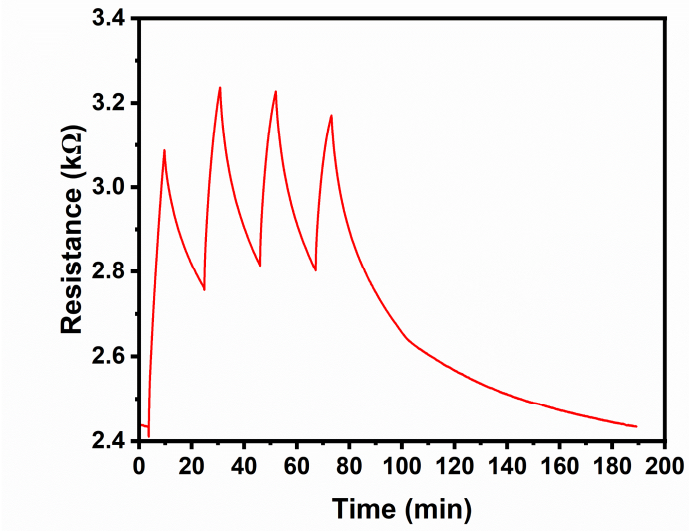



**Figure 5.8.** Sensing response to 4 ppm ammonia for the chemiresistors based on nanostructured PPy at a deposition time of 130 s. The sensor was exposed 4 times to 4 ppm $NH_3$ in $N_2$ for 6 minutes, with a 15 minute recovery time under pure $N_2$ flow between exposures. The final recovery lasted for 2 hours.

It should be noted that the resistance change during the first exposure to 4 ppm ammonia is greater than those for subsequent exposures. This higher response in the first exposure could be related to irreversible changes during gas detection. After XPS and Raman analyses on sensing layers after exposure, however, there was no evidence to support this explanation. Another possible reason for the greater change in resistance for the initial ammonia exposure could be that the interaction of nanostructured PPy networks with ammonia is not fully reversible on the time scale of the experiments (within 15 min). This means that the stated sensor reversibility and/or repeatability behaviour could be improved by a longer recovery time. This is supported by the finding that some nanostructured sensors fully recovered to the baseline after 2 hr (Figure 5.8). Similar to reported work,[267] moreover, these sensors recovered to the baseline values by heating at 100 ± 5 °C within 5 min.

For further comparison, a series of sensors called $S_{B\text{-}T}$, $S_{B\text{-}P1}$, $S_{B\text{-}P2}$, and $S_{B\text{-}P3}$ were fabricated on Pt IDEs without nanosphere templates. For each blank sample, its sensing responses were obtained using the same method for sensing experiments (Figure 5.9). With the same sensing mechanism, these thin-film counterparts show similar trends in their sensing responses to ammonia. $S_{B\text{-}T}$, $S_{B\text{-}P2}$, and $S_{B\text{-}P3}$ also show higher responses in the first exposure (Figure 5.9a, 5.9b and 5.9c), suggesting that the interaction of nanostructured PPy networks with ammonia could be not fully reversible on the time scale of these experiments. For $S_{B\text{-}T}$ and $S_{B\text{-}P1}$, furthermore, their values of recovered resistance keep decreasing since the second and the first recoveries respectively and finally drop below the initial values. This could be due to the change in chamber temperatures during the sensing experiments.

With better reversibility of the resistance change than the first exposure, the subsequent exposures for each sensor were used for further sensor evaluation and analysis. Their sensor responses were obtained by calculating the percentage changes to the starting resistances ($\Delta R/R_0 \times 100$ %). For each sensor, a linear relationship was observed between the sensor

response and the concentration of ammonia (Figure 5.10). The sensitivity is defined as the slope of the linear fit in Figure 5.10 and the limit of detection (LOD) is defined as three times the standard deviation of the baseline noise level (σ) divided by the sensitivity.

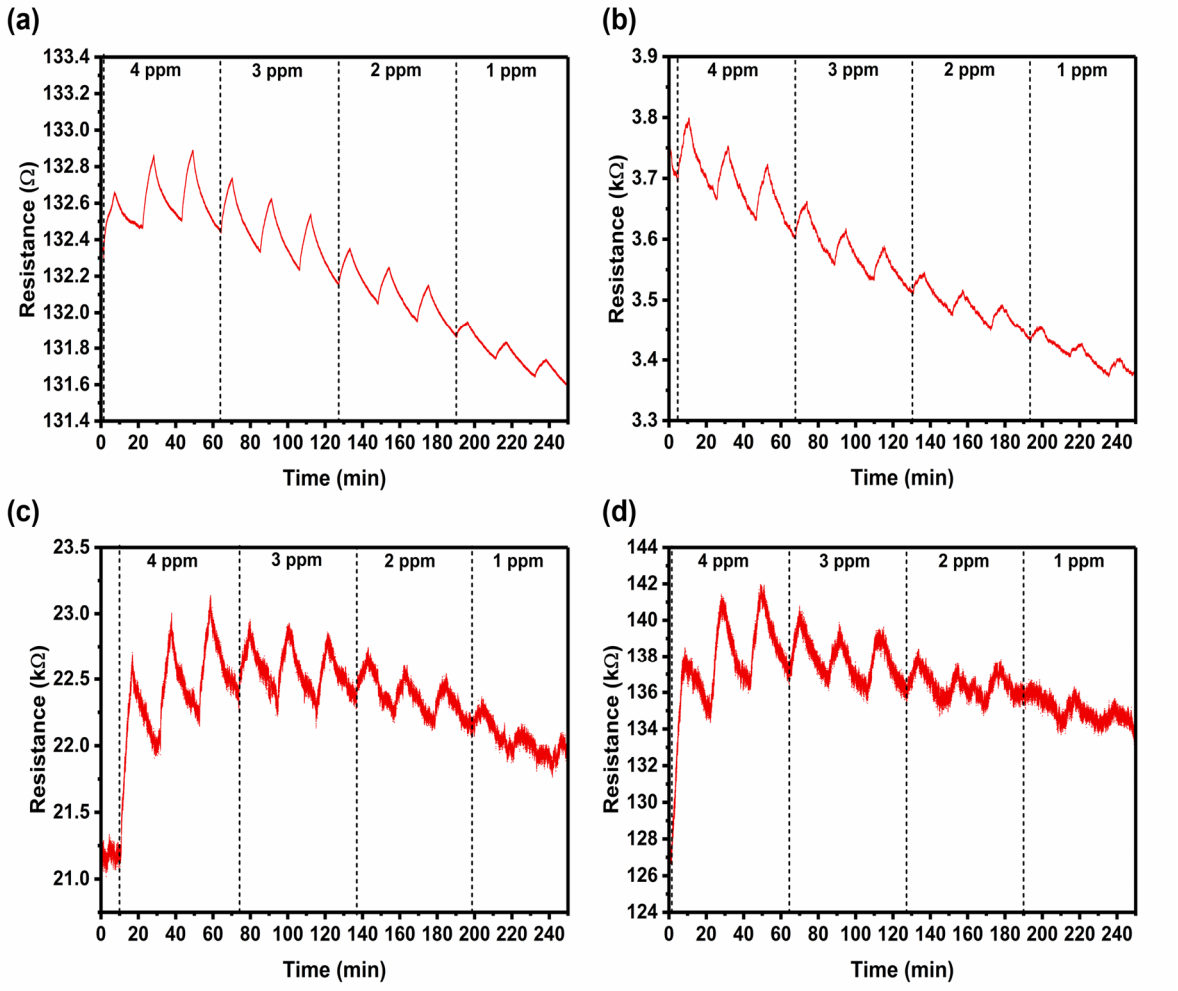



**Figure 5.9.** Sensing responses for PPy-based chemiresistors (a) $S_{B\text{-}T}$, (b) $S_{B\text{-}P1}$, (c) $S_{B\text{-}P2}$, and (d) $S_{B\text{-}P3}$ fabricated on blank Pt IDEs without PS nanosphere templates by chronoamperometry at deposition times of 240 s, 230 s, 220 s, and 210 s respectively. $S_{B\text{-}T}$ was obtained in the thin-film region while $S_{B\text{-}P1}$, $S_{B\text{-}P2}$, and $S_{B\text{-}P3}$ were obtained in the percolation region. All sensors were exposed 3 times to 1, 2, 3, and 4 ppm $NH_3$ in $N_2$ for 6 minutes, with a 15 minute recovery time under pure $N_2$ flow between exposures. The test temperature is 25 ± 1 °C and the humidity is 1.61 ± 0.41 % RH.

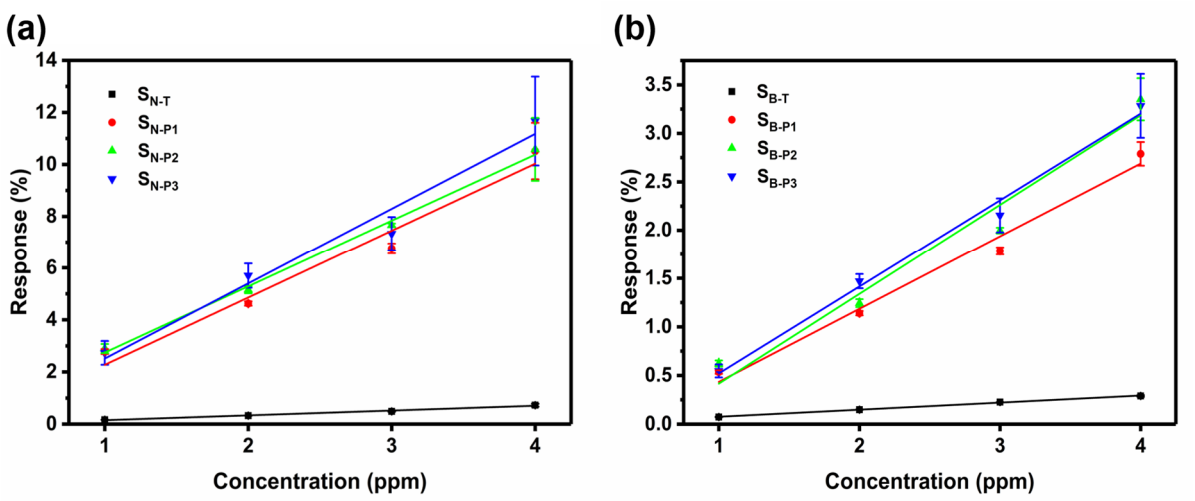



**Figure 5.10.** Sensor responses ($\Delta R/R_0 \times 100$ %) as a function of ammonia concentration for PPy-based chemiresistors prepared (a) with ($S_{N\text{-}T}$, $S_{N\text{-}P1}$, $S_{N\text{-}P2}$, and $S_{N\text{-}P3}$) and (b) without ($S_{B\text{-}T}$, $S_{B\text{-}P1}$, $S_{B\text{-}P2}$, and $S_{B\text{-}P3}$) PS nanosphere templates.

According to Figure 5.10a, the sensitivities and LODs of nanostructured sensors ($S_{N\text{-}T}$, $S_{N\text{-}P1}$, $S_{N\text{-}P2}$, and $S_{N\text{-}P3}$) were obtained. Figure 5.11 shows that $S_{N\text{-}T}$, prepared in the thin-film region, exhibits low sensitivity. As the sensor resistance increases, the sensitivity also increases and becomes stable above 2.5 % $ppm^{-1}$, where electrical percolation determines the sensitivity. In the percolation region, interactions between PPy networks and ammonia molecules have a large effect on the resistance of the networks, resulting in a significantly increased sensitivity compared to thin film-based sensors. As shown in Figure 5.7, higher baseline resistances also lead to higher levels of noise. Therefore, the LOD first decreases and then increases since it is determined by a competitive relationship between sensitivity and baseline noise, which is in agreement with our previous work for PPy percolation networks without the nanosphere templates.[31,265] Especially for the sensor $S_{N\text{-}P3}$, its high level of noise results in a very high LOD around 1 ppm, which is consistent with the result in Figure 5.7d. Among these nanostructured sensors, $S_{N\text{-}P1}$ is regarded as the optimal sensor with a sensitivity of 2.59 ± 0.20 % $ppm^{-1}$ and a LOD of 71 ± 6 ppb. For comparison, the sensitivities and LODs of the sensors without

templates ($S_{B\text{-}T}$, $S_{B\text{-}P1}$, $S_{B\text{-}P2}$, and $S_{B\text{-}P3}$) were calculated according to Figure 5.10b. As shown in Figure 5.11, these sensors exhibit similar trends in sensitivity and LOD to those based on nanostructured PPy. However, their nanostructured counterparts exhibit higher sensitivities in the percolation region, suggesting that creating nanostructured CP networks with nanosphere templates may further enhance the sensing performances of polymer percolation sensors. Compared to the optimal sensor $S_{B\text{-}P1}$ prepared without the template, the optimal nanostructured sensor $S_{N\text{-}P1}$ prepared with the templates shows a 245% increase in sensitivity and a 60% decrease in LOD. The improvement in performance might be attributed to higher surface area-to-volume ratios resulting from the introduction of nanostructuring. This explanation necessitates further experiments for verification, even though obtaining accurate surface area-to-volume ratios of trace amounts of PPy on IDE substrates might pose challenges.

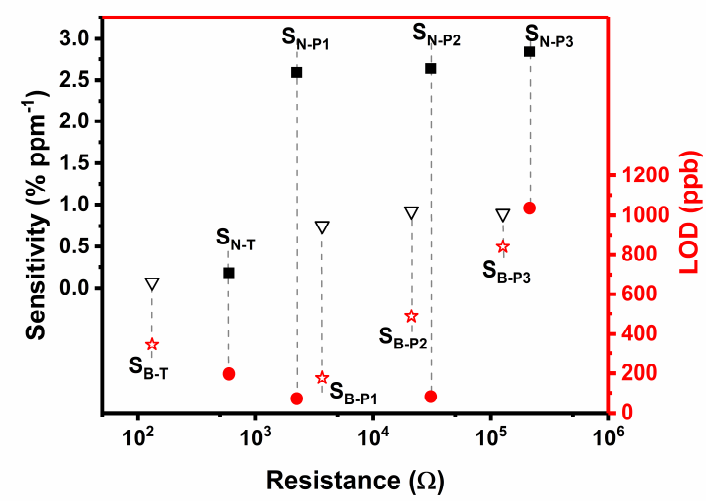



**Figure 5.11.** Values of sensitivity (black data points) and LOD (red data points) for the sensors investigated. Black filled squares are the sensitivities of the nanostructured sensors prepared with PS templates ($S_{N\text{-}T}$, $S_{N\text{-}P1}$, $S_{N\text{-}P2}$, and $S_{N\text{-}P3}$), and red filled points are the corresponding LODs. Black open triangles are the sensitivities of the sensors prepared without PS templates ($S_{B\text{-}T}$, $S_{B\text{-}P1}$, $S_{B\text{-}P2}$, and $S_{B\text{-}P3}$), and red open stars are the corresponding LODs. The dashed lines connect the sensitivity and LOD for each sensor.

**Table 5.1.** Sensing performances of representative PPy-based chemiresistors to ammonia gas from previous studies.

| Material & Morphology | Detection range | Operating temperature | Exposure time | Sensitivity (% $ppm^{-1}$) | LOD (ppm) | Response time (s) | Gas flow rate (sccm) | Ref. |
|---|---|---|---|---|---|---|---|---|
| PPy film | 100 – 1000 ppm | R.T. | 15 min | 0.0127 | - | - | 500 | 268 |
| | 1 – 40 ppm | 22 °C | 5 min | 0.71[a] | - | - | 600 | 269 |
| | 50 – 100 ppm[b] | 29 °C | - | 0.04[ac] | - | 240 (@ 50 ppm) | - | 270 |
| | 8 – 500 ppm | R.T. | 100 min | 0.11[a] | - | - | 50 | 271 |
| | 5 – 80 ppm | R.T. | - | 0.4 | - | 20 (@ 20 ppm) | - | 92 |
| | 4 – 80 ppm | R.T. | - | 0.4 | - | 20 (@ 25 ppm) | - | 272 |
| | 1 – 10 ppm | ~ 20 °C | 5 min | 0.67[a] | - | - | 50 | 242 |
| | 10 – 100 ppm | R.T. | 5 min | 0.094[a] | - | - | 100 | 273 |
| | 100 – 400 ppm[b] | R.T. | - | 0.25[ac] | - | 55 (@ 100 ppm) | - | 274 |
| PPy porous film | 45 – 90 ppm[b] | 25 °C | - | 0.53[ac] | 1.151 | 3 (@ 350 ppm) | 500 | 248 |
| Porous PPy on SEBS matrix | 10 – 40 ppm | 20 °C | 15 min | 0.6685 | - | 30 (@ 750 ppm) | - | 275 |
| PPy multilayer thin film | 5 – 50 ppm | R.T. | - | 1.036 | - | 12 (@ 50 ppm) | - | 95 |
| $Na_2SO_3$ treated PPy film | 0.5 – 5 ppm[b] | 25 °C | 2 h | 10[ac] | - | 1020 (@ 0.5 ppm) | 1000 | 51 |
| $CuF_2$ doped PPy film | 0.2 – 4 ppm | R.T. | 5 min | 1.77 | 0.02 | - | - | 236 |
| PPy-coated filter paper | 10 – 100 ppm | 28 °C | - | 0.53 | 5.2 | 20 (@ 20 ppm) | - | 52 |
| PPy nanotubes | 10 – 100 ppm | R.T. | 200 s | 0.382 | - | - | 3000 | 91 |
| Single PPy nanowire | 38 – 290 ppm | R.T. | 15 min | 0.06 | - | 900 (@ 38 ppm) | 150 | 244 |
| PPy nanowire arrays | 1.5 – 9.2 ppm[b] | R.T. | 5 min | 2.17[ac] | - | 60 (@ 77 ppm) | - | 55 |
| Single PPy nanoribbon | 0.5 – 5 ppm[b] | R.T. | 10 min | 1.77[ac] | - | - | 200 | 245 |
| PPy nanoparticles | 10 – 200 ppm[b] | R.T. | - | 0.06[ac] | - | < 1 (@ 5 ppm) | 2000 | 56 |
| | 50 – 300 ppm | R.T. | - | 0.095 | - | 200 (@ 100 ppm) | - | 246 |
| | 25 – 125 ppm | R.T. | - | 0.352 | - | 5 (@ 25 ppm) | - | 247 |
| | 45 – 90 ppm[b] | 25 °C | - | 0.96[ac] | 1.156 | 10 (@ 350 ppm) | 500 | 248 |
| Urchin-like PPy nanoparticles | 0.01 – 0.1 ppm[b] | R.T. | - | 8.85[ac] | - | < 1 (@ 0.1 ppm) | 1 – 5 | 249 |
| PPy nanospheres on silk fiber | 1 – 225 ppm | 25 ± 1 °C | - | 0.401 | - | 24 (@ 100 ppm) | - | 57 |
| PPy nanofibers | 20 – 150 ppm | R.T. | - | 0.3[a] | - | 15 (@ 20 ppm) | - | 87 |
| | 50 – 300 ppm | R.T. | - | 0.112 | - | 200 (@ 100 ppm) | - | 246 |
| | 45 – 90 ppm[b] | 25 °C | - | 0.49[ac] | 1.153 | 7 (@ 350 ppm) | 500 | 248 |
| PPy percolation networks | 100 – 700 ppb | R.T. | 5 min | 39.4 | 0.01 | < 300 (@ < 1 ppm) | 500 | 31 |
| | 1 – 4 ppm | 27 °C | 1 min | 11.3 | 0.015 | < 60 (@ 1 ppm) | 500 | 265 |

Note: R.T. = room temperature. [a]Estimated sensitivity from publication. [b]Linear portion of the whole detection range. [c]Gradient estimated from linear portion of the calibration curve.

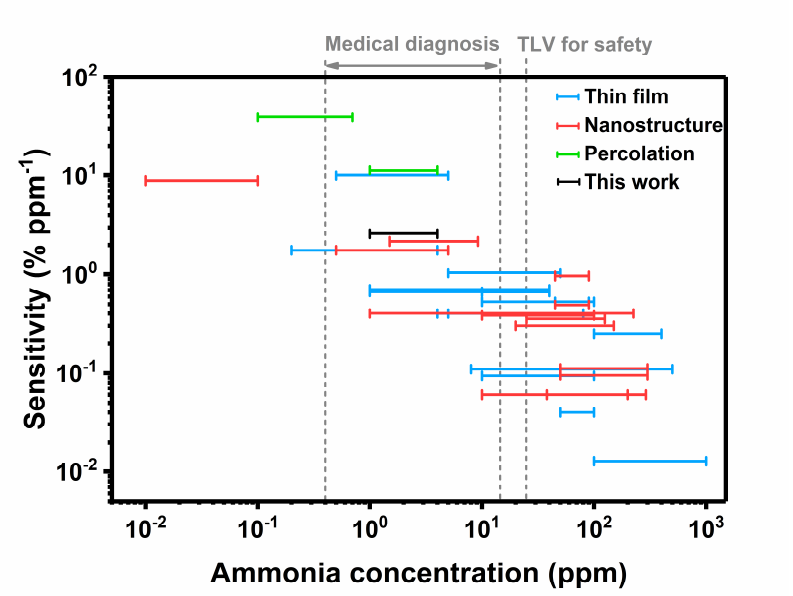



**Figure 5.12.** Sensitivities and corresponding detection ranges during sensing experiments for $S_{N\text{-}P1}$ (in black) and other PPy-based chemiresistors from previous studies. Sensors from previous studies have been classified according to Table 5.1, including thin-film sensors (in blue), sensors based on nanostructured PPy (in red), and percolation sensors (in green). Most of the sensors show desirable detection ranges covering the threshold limit value (TLV) of 25 ppm for industrial and daily safety and sensors with the detection ranges at low concentrations (0.4 – 14.7 ppm) are applicable for medical diagnosis.

Although a systematic comparison between each sensor can be difficult to accomplish since experimental conditions like temperature, response time, and analyte flow rate may vary, attempts have been made to compare the optimal nanostructured sensor $S_{N\text{-}P1}$ with representative PPy-based chemiresistors from previous studies (Table 5.1). It should be noted that $S_{N\text{-}P1}$ exhibits a lower sensitivity and a higher LOD than the PPy-based percolation sensors prepared in Chapter 4.[265] These differences should be attributed to the fact that different polymerisation conditions suitable for PS nanospheres were applied in this chapter. Upon further comparison with more sensors, as far as known, only a few sensors exhibit high sensitivities above 2 % $ppm^{-1}$ with detection ranges under 10 ppm (Figure 5.12).[31,51,55,249,265] This indicates that $S_{N\text{-}P1}$ prepared with the nanosphere template shows a desirable sensitivity

of 2.59 ± 0.20 % $ppm^{-1}$ at low concentrations. Moreover, its LOD of 71 ± 6 ppb demonstrates the ability for detection of ammonia under 100 ppb, which is competitive with other PPy-based chemiresistors.[52,248] Combining the benefits of nanostructuring and electrical percolation, creating nanostructured CP networks with nanosphere templates is a promising method to fabricate PPy-based sensors with enhanced performance. To further improve sensor performance, many factors should be considered in future work, such as the material porosity,[276] the deposition potential, and the type of the counterion.[51,277]

Figure 5.12 also shows that sensors with different performances are applicable in different fields of ammonia detection, spanning from industrial and daily safety (> 25 ppm) to medical diagnosis (0.4 – 14.7 ppm).[248,278-281] With a high sensitivity at low concentrations, $S_{N\text{-}P1}$ shows its potential in point-of-care applications for medical diagnosis. Analysing its responses to ammonia gas from human breath could be a promising approach to the early detection of many diseases, such as ulcers, hepatic injury, renal disorders and cancers.[51,236,282] Compared with instrument-based testing, a non-invasive device has various advantages including low cost, no requirement for experienced operators, time saving, and low power consumption.[283]

To further characterise the optimal sensor ($S_{N\text{-}P1}$) in this chapter, more sensors based on nanostructured percolation networks were reproduced at the deposition time of 130 s and additional performance parameters including selectivity, stability, and the influence of humidity were investigated. Figure 5.13a shows the selectivity to ammonia compared with other toxic gases such as CO and $NO_2$. This can be attributed to the different electron donating and withdrawing properties of the different analytes. Probably due to the film aging and/or the reduction in the number of unstable adsorption sites,[98,284] a slow decay of the sensing response was observed during a 2-week study (Figure 5.13b). Furthermore, as the relative humidity increases up to 20 % RH (Figure 5.13c), the sensing response to ammonia drops because the

proton transfer induced by water molecules reduces the number of the sensing sites for ammonia molecules.[285,286]

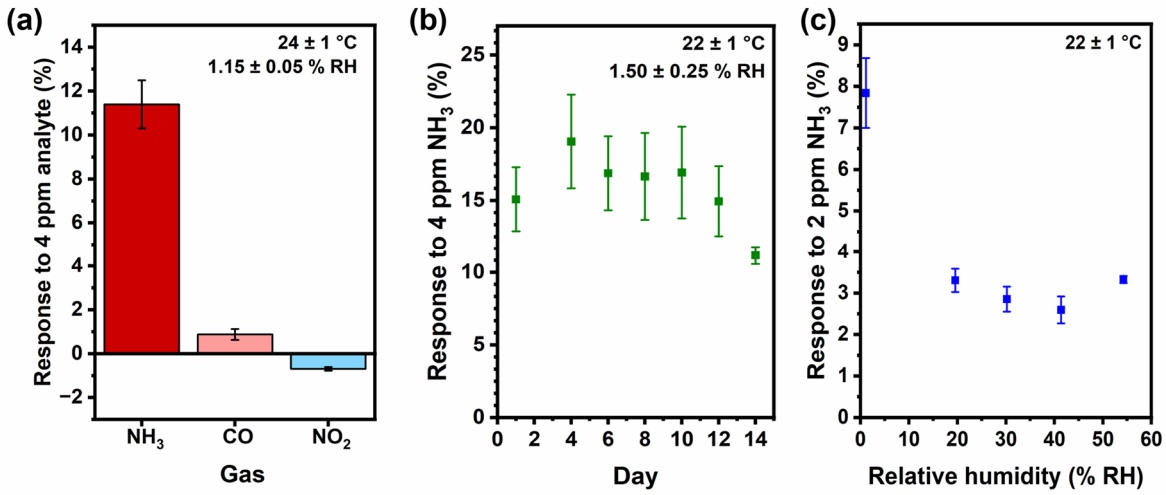



**Figure 5.13.** (a) Selectivity, (b) stability, and (c) humidity tests for nanostructured percolation sensors produced at the deposition time of 130 s. All sensors were exposed 4 times to the analytes in $N_2$ for 6 minutes, with a 15 minute recovery time under pure $N_2$ flow between exposures. For each sensor, three exposures after the first one were used for response calculation. Test conditions are shown in the upper right corner of each figure.

## 5.4 Conclusion and outlook

In this chapter, nanostructured PPy-based chemiresistors were fabricated with nanosphere templates via electrochemical polymerisation. During preparation PS nanosphere templates were created via directed evaporation-induced self-assembly and PPy networks were obtained via chronoamperometry on the nanosphere templates. After dissolution of the nanosphere templates this resulted in nanostructured PPy layers, whose composition was confirmed by Raman spectroscopy. By varying the electrochemical deposition time PPy layer densities spanning from the insulating region to the thin-film region were obtained. The electrical percolation behaviour of the nanostructured PPy networks was confirmed by electrical

measurements and SEM imaging. The sensing responses to ammonia of nanostructured PPy layers fabricated by this method in both the thin-film and percolation regions were investigated. Compared with their counterparts prepared on IDEs without templates, they exhibit better sensing performances to ammonia, suggesting that creating nanostructured CP networks with nanosphere templates may further improve the performance of percolation sensors. The optimal nanostructured sensor $S_{N\text{-}P1}$ prepared with the template shows a 245 % increase in sensitivity and a 60 % decrease in LOD compared to the optimal sensor $S_{B\text{-}P1}$ prepared without the template. With a sensitivity of 2.59 ± 0.20 % $ppm^{-1}$ and an LOD of 71 ± 6 ppb, $S_{N\text{-}P1}$ demonstrates competitive performance when compared with other PPy-based chemiresistors for ammonia detection.

With a desirable sensitivity within a suitable concentration range (Figure 5.12), the optimal sensor $S_{N\text{-}P1}$ shows potential in point-of-care applications. Therefore, more nanostructured percolation sensors can be prepared in future work to explore their capabilities of detecting ammonia in human breath. However, many factors affecting exhaled human breath analysis need be taken into account when evaluating a sensor for this application, such as humidity, temperature, and gas flow rate. Although humidity tests have been conducted in this chapter, the highest humidity that the gas sensing setup can reach is only around 55 % RH. As human exhalation has a high humidity generally above 85 % RH, it is necessary to update this setup in the future to extend the detection range to a higher humidity.

Last but not least, limitations also remain in this study. The validity of the comparison between the sensors prepared with and without the templates could be an issue because the bare IDE substrates for the sensors prepared without the templates were not strictly pre-treated with the same procedure as those prepared with templates. This procedure includes the 1-hour heating and the 24-hour THF bath. Even though accurate surface area-to-volume ratios of trace amounts of PPy in these sensors could be obtained, it is still not entirely convincing to attribute

the performance improvement to improved morphology since potential impacts from heating and THF must be considered as well. This limitation must be addressed through more carefully designed experiments in future work. As PS nanospheres are physically and chemically stable in water or some alcohol solvents, furthermore, only a few suitable monomers with desirable solubility in such solvents are applicable during nanosphere templating. Silica nanospheres could be an alternative, but highly toxic and corrosive hydrofluoric acid is required to remove these templates. Large variations in sensor resistance were also observed due to the random growth of PPy. The in situ conductance monitoring technique described in Chapter 4 could improve the device-to-device reproducibility of the nanostructured sensors in this chapter, but it requires a stable faradaic current in lab-based experiments. Only when a custom-designed program that subtracts the faradaic current is achieved can the in situ conductance monitoring technique be coupled with nanosphere templating.

# Chapter 6

# Percolation sensors based on nanocomposites

Electrical percolation materials, achieved by incorporating conjugated polymer (CP) fillers into insulating polymeric matrices, have been developed for various applications for several decades. However, gaps remain when using these materials as sensing layers in CP-based chemiresistors, including a limited understanding of sensing performance within the percolation regions and a lack of exploration in their multifunctionality. To address these issues, this chapter focuses on chemiresistors based on poly(3,4-ethylenedioxythiophene)/polystyrene (PEDOT/PS) nanocomposites. The nanocomposites are formed by combining PEDOT nanoparticles with PS nanospheres through solution blending, and CP-based chemiresistors with varying PEDOT filler fractions are then fabricated using the directed evaporation-induced self-assembly (DEISA) technique. The electrical percolation behaviour within these nanocomposites is investigated by analysing the trend in conductance and surface morphologies. Subsequently, this chapter systematically studies the response of the PEDOT-based chemiresistors to nitrogen dioxide ($NO_2$), demonstrating that electrical percolation can improve the sensing performance for $NO_2$ detection. An optimal $NO_2$ sensor with a sensitivity of $-2.29 \pm 0.05$ % $ppm^{-1}$ and a LOD of $40 \pm 1$ ppb has been obtained. Furthermore, the sensing capabilities of these PEDOT-based chemiresistors are extended through additional studies on temperature and airflow rate sensing, achieving improved sensing performance within the percolation region. Based on the percolation sensors, an impressively high temperature resolution of $0.043 \pm 0.002$ °C is accomplished, while low flow rate detection from 20 to 500 sccm is achieved.

## 6.1 Motivation and solution

CP-based percolation materials have been developed since the early 1990s,[157,165,169] primarily through the incorporation of CP-based fillers into insulating polymeric matrices. These composites have been extensively studied, leading to a comprehensive understanding of their structures and properties,[149,176,178,179,195] and demonstrating their potential in various applications.[161,172,186,204,210] In the field of chemical detection, chemiresistors based on these composite materials have shown improved sensing performance compared to chemiresistors solely based on the same fillers.[172] However, there are still gaps when using composite-based percolation materials as sensing layers in CP-based chemiresistors.

One of the gaps is related to the filler fraction employed in the composites. Researchers in previous studies focused on fabricating chemiresistors at a single filler fraction that was far above the percolation threshold,[172,195] limiting the understanding of sensing performance within the percolation regions. To address this gap, it is crucial to conduct systematic studies on the effects of electrical percolation across a range from the percolation threshold to high filler fractions. Through these studies across this range, a more comprehensive understanding of the relationship between filler fraction and sensing performance can be achieved.

Additionally, CP-based percolation composites have proven the potential to fulfil the recent research interest in multifunctional sensors.[210] These composites can be responsive to various stimuli, opening up possibilities for extending the functions of CP-based percolation chemiresistors. However, there have been limited studies exploring the extension of functions in these chemiresistors. Fortunately, this exploration can be conducted alongside the systematic studies on chemiresistors based on percolation composites, further enhancing the understanding of the effects of electrical percolation and broadening the capabilities of CP-based chemiresistors.

To facilitate the understanding of electrical percolation in CP-based composite chemiresistors and the multifunctionality of these sensors, careful considerations in composite preparation must be taken when designing the experiments. The choice of preparation method is important, and solution blending is often preferred in initial studies due to its simplicity. Composites prepared through solution blending can be easily deposited onto Pt interdigitated electrodes (IDEs) using various solution processing techniques, such as drop-casting and spray-coating. When selecting the components of the composites, furthermore, it is crucial to choose suitable fillers and matrices. CP-based nanofibers or nanoparticles that can be easily dispersed are preferred, as they can effectively form percolation pathways and exhibit desirable sensing properties. As for the matrices, it is advantageous to use dispersible nanostructured polymers instead of soluble insulating polymers. By assembling these nanostructured polymers, the potential issue of filler encapsulation within the matrices can be avoided, especially at low filler fractions. The assembly of these nanostructured polymers also ensures the presence of sufficient tunnels for analyte diffusion throughout the composites. In this way, the interactions between the fillers and the analytes can dominate the sensing mechanism across the entire range of filler fractions. In summary, during the early stage of systematic studies on CP-based percolation composites in chemiresistors and their multifunctionalization, it is recommended to prepare these composites by mixing dispersible nanostructured fillers and matrices through solution blending. Subsequently, chemiresistors can be fabricated using solution processing methods. These approaches provide a solid foundation for exploring the electrical percolation behaviour and multifunctionality of CP-based percolation composites in chemiresistors.

In this chapter, PEDOT/PS nanocomposites are prepared for the CP-based percolation chemiresistors. The nanocomposites are formed by combining PEDOT nanoparticles doped with dodecylbenzenesulfonic acid (DBSA) with PS nanospheres through solution blending. CP-based chemiresistors with varying filler fractions are then fabricated using the directed

evaporation-induced self-assembly (DEISA) technique. The electrical percolation behaviour within these nanocomposites is investigated by analysing the trend in device conductance and surface morphologies. Then, this chapter systematically studies the response of the PEDOT-based chemiresistors to nitrogen dioxide ($NO_2$). After the investigation on gas sensing, furthermore, the sensing capability of these PEDOT-based chemiresistors is extended via further studies on temperature and airflow rate sensing.

## 6.2 Experimental section

### 6.2.1 Fabrication of nanocomposite-based sensors

Sulfuric acid ($H_2SO_4$, 95 %) was purchased from Sigma-Aldrich and hydrogen peroxide ($H_2O_2$, 30%) was purchased from Fisher Scientific. Prior to experiments, each Pt IDE substrate (Micrux) in this chapter was treated with piranha solution ($H_2SO_4$ : $H_2O_2$ = 3:1, by volume; warning: piranha solution is very corrosive and must be treated with extreme care) at 50 ± 5 ℃ for 30 min to enhance its hydrophilic nature and then washed carefully with deionised water (Sigma-Aldrich) and ethanol ($C_2H_5OH$, 99.8 %, Sigma-Aldrich). DBSA-doped PEDOT nanoparticle dispersion (1 wt% in water, Sigma-Aldrich) and PS latex (10 wt% in water, Sigma-Aldrich) were subjected to ultrasonic treatment for 10 min to ensure complete dispersion before use. According to the certificates of analysis from the producer, the diameters of the PEDOT nanoparticles and monodispersed PS nanospheres are around 400 nm and 300 ± 50 nm, respectively. Further characterisations given in Appendix have shown that the purchased PEDOT nanoparticles exhibit poorly defined morphologies and the estimated size of these non-spherical nanoparticles is 322 ± 116 nm. The PEDOT dispersion and PS latex were separately diluted to 0.02 wt% with deionised water (Sigma-Aldrich) and further treated with ultra-sonication for another 10 min. Various PEDOT/PS nanocomposites were prepared via solution blending. Obtained 0.02 wt% PEDOT dispersion was mixed with 0.02 wt% PS

latex in different $m_{PEDOT-D} : m_{PS-L}$ ratios ranging from 10:0 to 0:10, and the weight fraction of PEDOT ($WF_{PEDOT}$) was calculated using the following equation:

$$WF_{PEDOT} = \frac{m_{PEDOT-D}}{m_{PEDOT-D}+m_{PS-L}} \times 100\ \% \quad (6.1)$$

where $m_{PEDOT-D}$ and $m_{PS-L}$ represent the weights of 0.02 wt% PEDOT dispersion and 0.02 wt% PS latex added in the mixture, respectively. The nanocomposite-based sensors were prepared via directed evaporation-induced self-assembly (DEISA) described in Section 3.2.3 Instead of the 50 mL glass beaker shown in Figure 3.4b, 4 mL glass vials were used to simplify the DEISA equipment and conserve materials. During the DEISA process, substrates were vertically immersed in these glass vials containing 400 µL of mixtures with different values of $WF_{PEDOT}$. The vials were then placed in the Garbolite PN60 oven at 70.0 ± 0.5 ℃ for 12 hours until all the solvents had evaporated. After the DEISA process, the resistance of each sensor was measured using the RS PRO IDM 98IV handheld digital multimeter. The surface morphologies of the PEDOT/PS nanocomposites on IDEs were imaged using a Zeiss Merlin scanning electron microscope (SEM) at an accelerating voltage of 15 kV.

## 6.2.2 Sensing experiments

### 6.2.2.1 Gas sensing

Sensing experiments were carried out at atmospheric pressure using the gas sensing setup (Figure 3.5) and the experimental protocol described in Section 3.4.1. $NO_2$ gas (10 ppm, nitrogen fill) and nitrogen gas ($N_2$, 99.998 %, BOC, for further dilution of $NO_2$) were mixed at the T-joint before entering the gas inlet of the chamber, and a total flow rate of 500.0 ± 2.5 sccm was employed throughout the experiments. The concentration of $NO_2$ gas was determined by the relative flow rates of the two mass flow controllers (Alicat). The temperature and relative humidity in the chamber were recorded via the SHT31 temperature and humidity sensor

(Sensirion) next to the nanocomposite-based sensor. The nanocomposite-based sensor in the custom-made chamber was connected to the B2902A source/measure unit (SMU, Keysight). A DC potential of 1.0 V was applied during the experiments, and the resistance of the sensor was monitored on a personal computer equipped with Benchvue software. $N_2$ gas was initially purged for 30 min to eliminate impurities from both the chamber and the sensing layer. After the purging process, the sensor was exposed to concentrations of $NO_2$ gas from 8 ppm to 200 ppb for 1 min each. The baseline of each sensor was defined as the average of the values measured within the 30-second period before the first exposure. After each exposure, the sensor was purged with nitrogen for 29 min before the next exposure.

#### 6.2.2.2 Temperature sensing

Temperature sensing experiments were conducted using the setup depicted in Figure 3.3 and following the experimental protocol outlined in Section 3.4.2. Each nanocomposite-based sensor, connected to the B2902A SMU, was placed in a 5 mL glass vial. Prior to the experiments, dry $N_2$ was purged into the vial for 5 minutes to remove any impurities and moisture from the vial and the sensing layer. The vial was then promptly sealed to maintain a dry testing environment with $N_2$. The sensor in the sealed vial was subsequently immersed in an oil bath set at 30 ℃ for 10 min, and the bath temperature was regulated using the IKA RCT Basic stirrer hotplate connected with the PT1000 temperature sensor. A DC potential of 1.0 V was applied to the sensor, and the resistance of the sensor was closely monitored. After the 10-minute incubation at 30 ± 1 ℃. The temperature was then incrementally raised by 10 ℃ every 10 min until it reached 80 ± 1 ℃. The actual temperature of the oil bath reached the designated values within 10 minutes. The resistance of each sensor was recorded during this temperature increase process using the B2902A SMU connected to the personal computer equipped with Benchvue software, and the baseline of each sensor was defined as the average of the values measured at 30 ± 1 °C within the 30-second period before the first increase in temperature.

#### 6.2.2.3 Airflow rate sensing

Airflow rate sensing experiments were carried out using the flow rate sensing setup (Figure 3.6) and following the experimental protocol outlined in Section 3.4.3. Dry air (speciality grade, 19.9 – 21.9 % oxygen with nitrogen balance, BOC) was utilised for the tests, and its flow rate was controlled by the Alicat mass flow controller. Each nanocomposite-based sensor was securely positioned on the sample stage, facing the gas inlet tube. The sensing layer was perpendicular to the direction of airflow at a distance of 20.0 ± 0.5 mm to the head of gas inlet tube. The sensor in the chamber was connected to the B2902A SMU, which was linked to a personal computer equipped with Benchvue software. The temperature and relative humidity in the chamber were recorded via the SHT31 temperature and humidity sensor placed next to the nanocomposite-based sensor. Prior to the test, the chamber was purged with dry air at a flow rate of 500.0 ± 2.5 sccm for 40 min and the humidity sensor consistently indicated very low relative humidity values below 3 % RH. Subsequently, the set value of flow rate was reduced to 0 sccm and maintained for 10 min. A direct DC potential of 1.0 V was applied to the nanocomposite-based sensor, and the resistance of the sensor was closely monitored on the personal computer with Benchvue software. After the 10-minute process at the set rate of 0 sccm, the sensor was exposed to various flow rates of dry air, ranging from 20 to 800 sccm, for a duration of 2 min each. The baseline of each sensor was defined as the average of the values measured within the 30-second period before the first exposure. Following each exposure, the set value of flow rate was reduced to 0 sccm and maintained for 8 min before the next exposure.

## 6.3 Results and discussion

### 6.3.1 Electrical percolation

To study the electrical percolation behaviour, various PEDOT/PS nanocomposites were prepared via solution blending and then deposited on the Pt IDEs via DEISA. Four repeat

samples were obtained at the weight fractions of PEDOT ($WF_{PEDOT}$) ranging from 0 to 100 wt%. The resistance values between the IDE electrode fingers were recorded under the ambient conditions. The linear plot in black (Figure 6.1) shows the trend of conductance as a function of $WF_{PEDOT}$. The same data plotted as a semi-logarithmic plot in red is used to determine the boundaries between each region. At 0 wt% of PEDOT nanoparticles, initially, no electrical conductance is detected due to the absence of conductive fillers, and the PS nanospheres do not contribute to the conductance across the IDEs. Then, conductance can be detected at 10 wt%, indicating the formation of percolation pathways within the composites. This suggests that the percolation threshold is located no more than 10 wt% of the PEDOT nanoparticles. With the formation of more percolation pathways, the conductance exhibits a sharp increase by orders of magnitude until reaching 70 wt%, defining the percolation region between 10 and 70 wt%. Beyond 70 wt%, the conductance shows a slow and gradual increase within the same order of magnitude, indicating the tendency towards saturation. This change in conductance increase should be attributed to the formation of the continuous PEDOT domains within the composites, facilitated by the presence of sufficient percolation pathways. Following the percolation region, the region where the conductance saturates below 100 wt% is referred to as the saturation region. It should be noted that variations in conductance for samples produced with identical procedures exist in both the percolation and the saturation regions. This is attributed to several unavoidable factors such as differences in the actual geometry of the composite film on IDEs and variations in the distribution of PEDOT within the composites. Furthermore, it is difficult to fit the conductance trend in Figure 6.1 using the classical percolation model (Equation 2.3), as an ununiversal critical exponent (~ 3.8) deviating from the theoretical values is obtained. This departure suggests that additional factors such as carrier tunnelling, filler geometry, or interphase effects may be influencing the percolation behaviour, highlighting the need for further investigations to fully comprehend these effects.

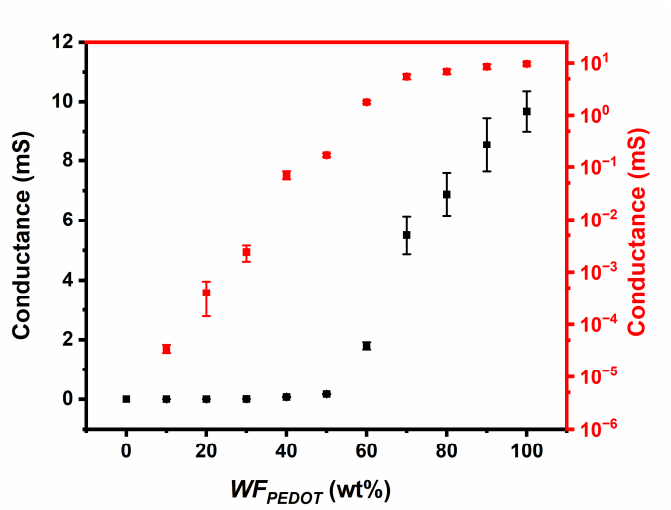



**Figure 6.1.** Plot of composite conductance vs. $WF_{PEDOT}$ and its semi-logarithmic plot (in red). All the error bars are obtained from the standard deviation of the conductance values of four separate samples.

SEM images depict the surface morphologies of the PEDOT/PS nanocomposites on the glass gaps of the Pt IDE substrates in both the percolation region (Figures 6.2a – g) and the saturation region (Figures 6.2h and 6.2i). Consistent with the morphological characterisation given in Appendix (Figure A2), non-spherical PEDOT nanoparticles and their aggregates are observed in Figure 6.2, which could potentially contribute to the deviations in the conductance trend observed in practical experiments compared to the predictions of the classical percolation model. Previous studies on PEDOT nanoparticles have also reported similar observations of the poorly defined morphologies of prepared nanoparticles,[287-291] and their morphologies should depend on the synthesis conditions. Some of these studies have demonstrated that better defined morphologies of spherical shape can be achieved through suitable surfactant-oxidant systems,[287] ideal stabilisers,[288] and bi-oxidant systems.[289,291] As shown in Figure 6.2, furthermore, all the studied materials exhibit porous structures without the encapsulation of the PEDOT nanoparticles. This ensures the presence of sufficient dispersion tunnels, allowing the analytes to directly contact the PEDOT nanoparticles. At low PEDOT weight fractions of 10

wt% and 20 wt% (Figures 6.2a and 6.2b, respectively), a limited number of PEDOT nanoparticles are randomly dispersed within the PS matrix containing closely packed nanospheres. At this stage, the morphology primarily relies on the PS matrix. Although no obvious bridges of PEDOT nanoparticles are observed in Figures 6.2a and 6.2b, some conducting percolation pathways must have formed at 10 wt% and 20 wt% based on the non-zero conductance measurements observed in Figure 6.1. With an increase in PEDOT weight fraction from 30 wt% to 70 wt%, an increasing number of PEDOT nanoparticles and formed percolation pathways are observed within the matrices based on PS nanospheres (Figures 6.2c − g), which is consistent with the sharply increase in conductance in Figure 6.1. Additionally, small PEDOT domains induced by the aggregation of PEDOT nanoparticles are observed from 40 wt% upwards. It is worth noting that the PS matrix gradually breaks into domains consisting of closely packed nanospheres at higher PEDOT weight fractions of 60 wt% and 70 wt%. At the same time, as shown in Figures 6.2f and 6.2g, small PEDOT domains containing aggregated nanoparticles begin to connect with each other. The conducting pathways within the composites are determined by the connections between these PEDOT domains interspersed with PS domains, rather than bridged PEDOT nanoparticles. This interspersing morphology ends beyond 70 wt%, where the filler-matrix relationship between PEDOT and PS reverses (Figures 6.2h and 6.2i). Continuous PEDOT domains based on aggregated nanoparticles form the matrix of the composite, while PS nanospheres become randomly dispersed fillers within the PEDOT matrix. At this stage, the major morphologies of the PEDOT/PS nanocomposites are similar to that of densely aggregated PEDOT nanoparticles (Figure 6.2j), and the PEDOT matrices provide sufficient conducting pathways throughout the nanocomposites. This is in agreement with the slow increase in conductance between 70 wt% and 100 wt% observed in Figure 6.1. The reversal of the filler-matrix relationship in the composite morphology may signify the boundary between the percolation and saturation regions.

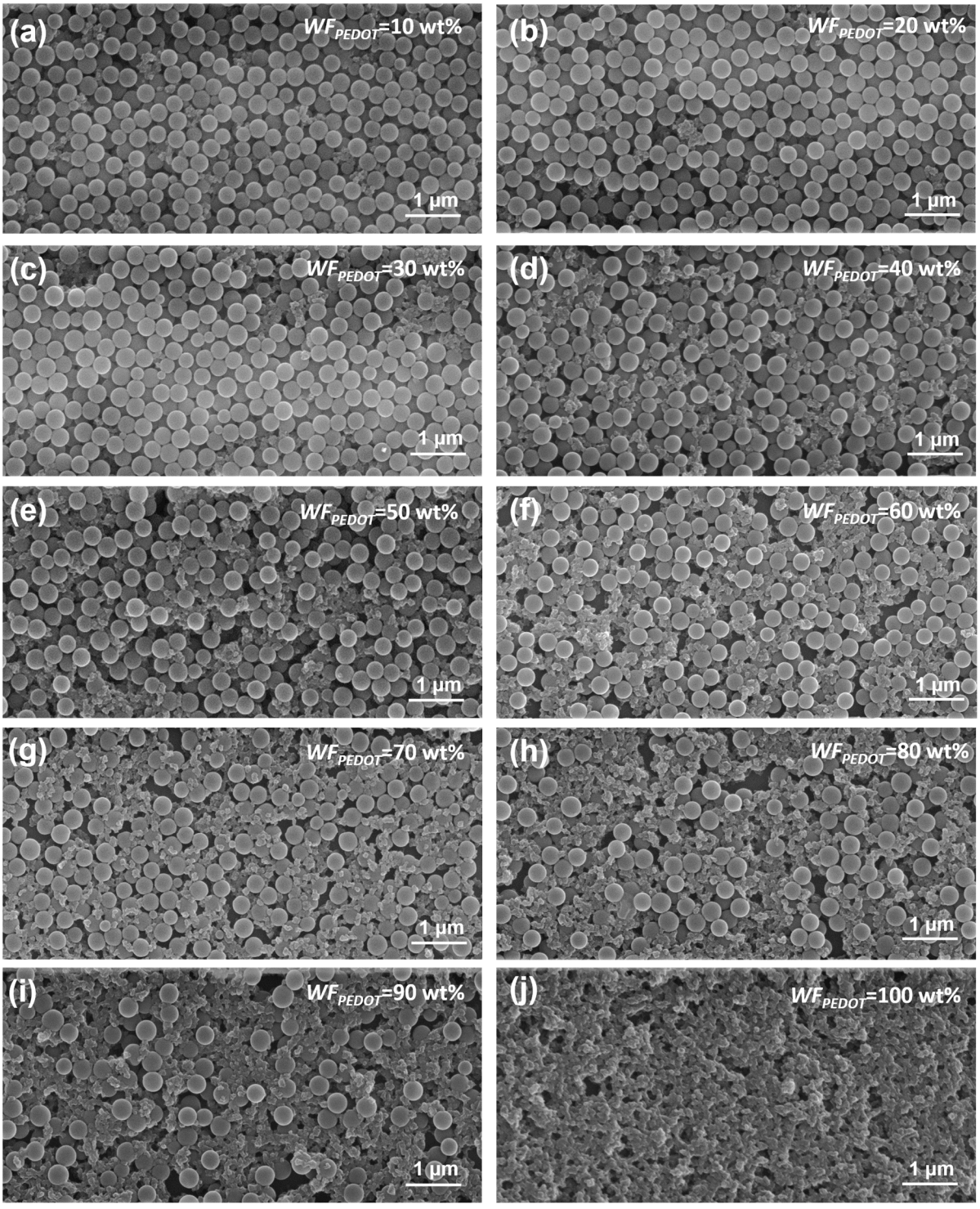



**Figure 6.2.** SEM images of PEDOT/PS nanocomposites with different $WF_{PEDOT}$ values between 10 and 90 wt% (a − i, respectively) and (j) densely aggregated PEDOT nanoparticles ($WF_{PEDOT}$ = 100 wt%) on the glass gaps of the Pt IDE substrates. The $WF_{PEDOT}$ value of the studied material is presented in the upper right corner of each figure to indicate the specific composition being depicted. Images taken by Yu Wang.

To sum up, both the percolation and saturation regions have been determined by analysing the trend of the conductance across the Pt IDEs. The formation of percolation pathways has been further confirmed through the analysis of morphology. Moreover, the transition from the percolation region to the saturation region has been found to be associated with the reversal of the filler-matrix relationship in the composite morphology. To systematically investigate the effects of electrical percolation on sensing performance, therefore, various percolation sensors, including $S_{10\text{-}P}$, $S_{20\text{-}P}$, $S_{30\text{-}P}$, $S_{40\text{-}P}$, $S_{50\text{-}P}$, and $S_{60\text{-}P}$, were then prepared via DEISA at 10, 20, 30, 40, 50, and 60 wt%, respectively. For further comparison, additionally, a saturation sensor ($S_{80\text{-}S}$) and a pure PEDOT sensor ($S_{PEDOT}$) were prepared at 80 and 100 wt%, respectively. Among these sensors, however, the sensing experiments for $S_{10\text{-}P}$ were not conducted due to its low conductivity. As the signal noise completely masked the current, it was impossible to obtain reliable measurements under the applied DC potential of 1.0 V. This interference of noise limited further investigations near the percolation threshold.

### 6.3.2 Gas sensing

Various chemiresistors were prepared using the DEISA method for the gas sensing experiments, including the percolation sensors ($S_{20\text{-}P}$, $S_{30\text{-}P}$, $S_{40\text{-}P}$, $S_{50\text{-}P}$, and $S_{60\text{-}P}$), the saturation sensor ($S_{80\text{-}S}$), and the pure PEDOT sensor ($S_{PEDOT}$). These sensors were exposed to concentrations of $NO_2$ diluted with $N_2$ ranging from 8 ppm to 200 ppb, and their resulting changes in resistance were recorded as shown in Figure 6.3. During the exposure to $NO_2$ gas, the resistances of the sensors decreased. This is because the electron-withdrawing $NO_2$ molecules act as dopants for the p-doped PEDOT. When the PEDOT interacts with $NO_2$ molecules, some neutral segments of the polymer chains are oxidised to their p-doped form (Scheme 6.1), leading to an increase in the number of charge carriers in the p-doped PEDOT. These observations also suggest that the purchased PEDOT nanoparticles were not fully p-

doped with DBSA. Otherwise, the sensor resistances would have increased due to over-oxidation caused by the $NO_2$ molecules.

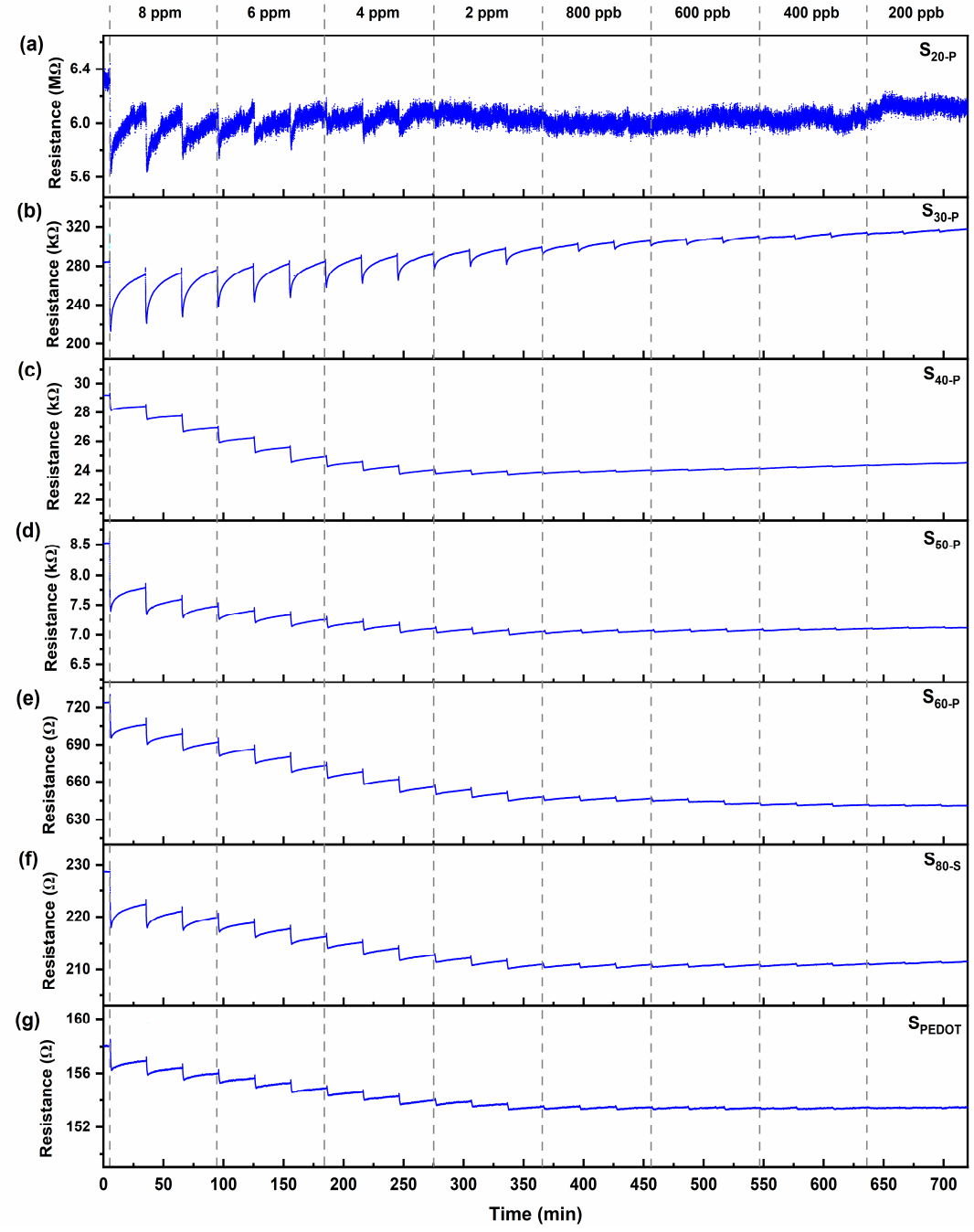
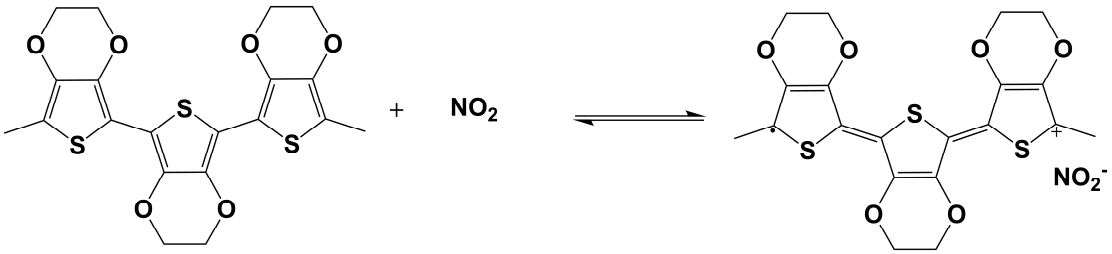



**Figure 6.3.** Sensing response to $NO_2$ gas for the chemiresistors (a) $S_{20\text{-}P}$, (b) $S_{30\text{-}P}$, (c) $S_{40\text{-}P}$, (d) $S_{50\text{-}P}$, (e) $S_{60\text{-}P}$, (f) $S_{80\text{-}S}$, and (g) $S_{PEDOT}$. The name of each sensor is presented in the upper right corner of each figure. All sensors were exposed 3 times to concentrations of $NO_2$ in $N_2$ from 8 ppm to 200 ppb for 1 min each, with a 29 minute recovery time under pure $N_2$ flow between exposures. The test temperature is 25 ± 2 °C and the humidity is 1.16 ± 0.30 % RH.




**Scheme 6.1.** Detection mechanism of PEDOT towards $NO_2$ gas.

In Figure 6.3, it is important to note that the sensor resistances do not fully recover to their initial values after the first exposure to 8 ppm $NO_2$. This results in greater responses compared to subsequent exposures at the same concentration. This observation suggests that the interaction between PEDOT nanoparticles and $NO_2$ is not fully reversible within the time frame of the experiments (within 29 minutes). While the sensor reversibility could be improved with a longer recovery time, it may not be practical in real-life applications for frequent tests. Previous studies have attributed this limitation in reversibility to the high binding energy between PEDOT and $NO_2$, which leads to the strong entrapment of $NO_2$ molecules on the sensor surface.[105,292] To overcome this limitation for practical purposes, some researchers have introduced ultraviolet (UV) light during the desorption process to reduce the recovery time.[105,293] Moreover, sensors in this section were found to recover to the baseline values by heating at 100 ± 5 °C within 5 min. In the sensing experiments from 8 ppm to 200 ppb, furthermore, percolation sensors prepared at low $WF_{PEDOT}$ values of 20 wt% and 30 wt% (Figures 6.3a and 6.3b) exhibit better reversibility below 8 ppm compared with other sensors (Figures 6.3c − g). This difference in reversibility could be related to the transition of the surface morphology of the sensing layers (Figure 6.2). At low $WF_{PEDOT}$ values (20 wt% and 30 wt%), the entrapment of $NO_2$ molecules is expected to primarily occur on the surface of dispersed nanoparticles. As the $WF_{PEDOT}$ increases over 30 wt%, however, more $NO_2$ molecules may be trapped within the PEDOT domains with aggregated nanoparticles.

Furthermore, Figure 6.3 provides additional valuable insights for further investigation. Firstly, it is observed that sensors with higher resistances exhibit higher levels of noise. Among these sensors, $S_{20\text{-}P}$ with the highest resistance was not used for further analysis as it was challenging to distinguish the signal from the noise below 6 ppm. Additionally, although $S_{30\text{-}P}$ demonstrates desirable reversibility, its final resistance increases above the initial value. This change could be attributed to the change in chamber temperature during the sensing. This observation inspires further investigations on the sensor responses to different temperatures in this study. In Figure 6.3, small positive spikes in resistance are also observed at the beginning of each exposure. These spikes could be attributed to the abrupt changes in flow rate at the initiation of $NO_2$ gas introduction. This finding prompts further investigations on the sensor responses to various flow rates in this chapter.

The sensor responses of $S_{30\text{-}P}$, $S_{40\text{-}P}$, $S_{50\text{-}P}$, $S_{60\text{-}P}$, $S_{80\text{-}S}$, and $S_{PEDOT}$ were calculated as the percentage changes relative to the starting resistances ($\Delta R/R_0 \times 100$ %). Negative responses (Figure 6.4a) were obtained owing to the decrease in resistance during exposure. For each sensor, a linear relationship was observed between the sensor response and the concentration of $NO_2$ from 200 ppb to 6 ppm. However, the data for 8 ppm were not included in the trend lines due to their deviation from the linear fit and the presence of large errors, which is attributed to the limited reversibility at 8 ppm.

The sensitivity is defined as the slope of the linear fit in Figure 6.4a. Figure 6.4b shows that both the percolation sensors ($S_{30\text{-}P}$, $S_{40\text{-}P}$, $S_{50\text{-}P}$, and $S_{60\text{-}P}$) and the saturation sensor ($S_{80\text{-}S}$) exhibit better sensitivities than the PEDOT sensor ($S_{PEDOT}$), indicating that PEDOT/PS nanocomposite layers are more sensitive to $NO_2$ than the pure PEDOT nanoparticle layer. As the $WF_{PEDOT}$ decreases, furthermore, the sensitivity keeps improving from the saturation region to the percolation region. This trend in sensitivity can be attributed to the fact that decreasing the $WF_{PEDOT}$ allows each PEDOT pathway to consume more $NO_2$ molecules under

the same exposure conditions, resulting in larger changes in conductivity. The transition in morphology (Figure 6.2) may also contribute to the improvement in sensitivity. As the $WF_{PEDOT}$ decreases, the PEDOT matrix breaks into dispersed PEDOT domains from the saturation region to the percolation region. Then, these domains further break into dispersed nanoparticles in the PS matrix when the $WF_{PEDOT}$ is low enough in the percolation region. During these processes, the decrease in the size of the conductive filler might increase the surface-to-volume ratio of the PEDOT pathway, further improving the sensitivity to $NO_2$.

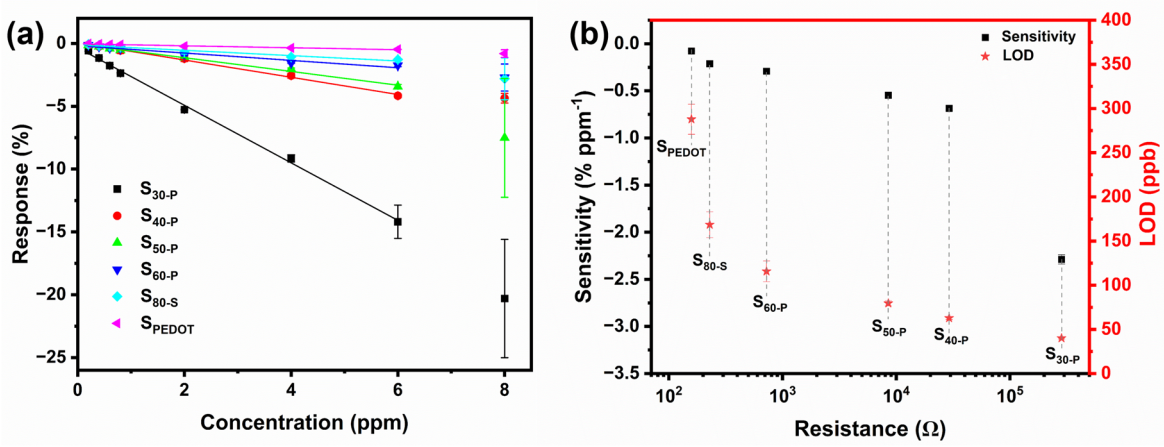



**Figure 6.4.** (a) Sensor responses ($\Delta R/R_0 \times 100$ %) as a function of $NO_2$ concentration for the percolation sensors ($S_{30\text{-}P}$, $S_{40\text{-}P}$, $S_{50\text{-}P}$, and $S_{60\text{-}P}$), the saturation sensor ($S_{80\text{-}S}$), and the PEDOT sensor ($S_{PEDOT}$). The data for 8 ppm are not included in the trend lines due to their deviation from the linear fit and the presence of large errors. (b) Values of sensitivity (black squares) and LOD (red stars) for the sensors investigated. The dashed lines connect the sensitivity and LOD for each sensor to indicate that they are from the same sensor.

In terms of the limit of detection (LOD), it is determined by a competitive relationship between sensitivity and baseline noise. The LOD is defined as three times the standard deviation of the baseline noise level (σ) divided by the modulus of the sensitivity. While higher baseline resistances lead to higher levels of noise for the sensors studied (Figure 6.3), the LOD is primarily influenced by the sensitivity, as indicated by the decreasing trend of LOD with

increasing sensor resistance (Figure 6.4b). However, it should be noted that the sensitivity only plays a dominant role in determining the LOD when the $WF_{PEDOT}$ value is between 30 wt% and 100 wt%. Figure 6.3a has already suggested that the noise dominates the LOD for the percolation sensor $S_{20\text{-}P}$ prepared below 30 wt%.

**Table 6.1.** Comparison of sensing performance of CP-based chemiresistors for $NO_2$ detection. All the sensors were operated at room temperature.

| Material | Testing range | Linear range | Exposure time | Sensitivity (% ppm$^{-1}$) | LOD | Flow rate (sccm) | Ref. |
|---|---|---|---|---|---|---|---|
| HCl doped POT | 10 – 100 ppm | 10 – 100 ppm | 2 min | 1.6[a] | - | - | 293 |
| PANI-ES nanothin film | 50 – 250 ppb | 50 – 250 ppb | - | ~3760 | ~0.6 ppb | 200 | 101 |
| PTh thin film | 10 – 100 ppm | 10 – 100 ppm | - | –0.24 | - | - | 103 |
| PPy/$WO_2$ nanocomposites | 5 – 100 ppm | 5 – 20 ppm | - | –1.6[a] | - | - | 294 |
| PEDOT nanotubes | 0.2 – 63 ppm | 0.2 – 20 ppm | - | 1.32[b] | 80 ppb | 500 | 105 |
| PPy/N-MWCNT composites | 0.25 – 9 ppm | 0.25 – 9 ppm | - | –4.17 | - | 200 | 295 |
| PPy/rGO-aryl-COOH nanocomposites | 2 – 20 ppm | 2 – 20 ppm | - | –1.01 | - | - | 296 |
| PEDOT percolation network | 1 – 8 ppm | 1 – 4 ppm | 5 min | –0.40[a] | 907 ppb | 500 | 32 |
| 1D polymer *p*PTz | 25 – 150 ppm | 25 – 150 ppm | 5 min | –0.21[a] | 5.67 ppm | 100 | 297 |
| UV-activated PANI/ZnO nanocomposites | 0.05 – 2.5 ppm | 0.05 – 1 ppm | - | 11700 | 0.2 ppb | 8 | 298 |
| Nanogranular PPy thin film | 10 – 120 ppm | 10 – 120 ppm | - | –0.38 | - | - | 299 |
| PEDOT/PS nanocomposites ($S_{30\text{-}P}$) | 0.2 – 8 ppm | 0.2 – 6 ppm | 1 min | –2.29 ± 0.05 | 40 ± 1 ppb | 500 | This work |

Note: POT = poly-o-toluidine; PANI-ES = polyaniline emeraldine salt; PTh = polythiophene; PPy = polypyrrole; N-MWCNT = nitrogen-doped multi-walled carbon nanotube; rGO-aryl-COOH = reduced graphene oxide with aryl 4-carboxybenzene diazonium salt; *p*PTz = poly[(1,4-phenylene)-*alt*-(3,6-(1,2,4,5-tetrazine)/3,6-(1,2,4,5dihydrotetrazine))]. [a]Estimated sensitivity from publication. [b]Sensitivity based the percentage changes relative to the starting current values ($\Delta I/I_0 \times 100$ %).

Among the sensors studied in this chapter, the percolation sensor $S_{30\text{-}P}$ is regarded as the optimal $NO_2$ sensor with a sensitivity of –2.29 ± 0.05 % ppm$^{-1}$ and a LOD of 40 ± 1 ppb. While it can be challenging to make a systematic comparison between each sensor due to variations in experimental conditions, attempts have been made to compare this optimal sensor ($S_{30\text{-}P}$) with other CP-based chemiresistors operating at room temperature. As shown in Table 6.1, some of these reported sensors exhibit positive values of sensitivity because of the difference

in sensing mechanism. Moreover, only a few sensors exhibit high sensitivities with the modulus over 2 % $ppm^{-1}$ and favourable LODs below the threshold limit value (TLV) for the long-term $NO_2$ exposure (100 ppb).[300] This suggests that electrical percolation within PEDOT/PS nanocomposites can provide competitive sensing performance for $NO_2$ detection. Based on Table 6.1, it should be noted that the PANI-ES nanothin film and the PANI/ZnO nanocomposites show better sensing performance than $S_{30\text{-}P}$ in terms of both sensitivity and LOD. However, there are limitations associated with their practical applications. The PANI-ES nanothin film exhibits irreversible responses,[101] while the PANI/ZnO nanocomposite sensor requires UV light activation.[298] Additionally, the PANI-ES responses above 250 ppb have not been shown in the corresponding study, and a non-linear trend of PANI/ZnO has been obtained above 1 ppm. These limitations pose challenges in achieving effective responses at 5 ppm, which is the threshold limit value (TLV) for short-term $NO_2$ exposure.[300,301] In comparison, $S_{30\text{-}P}$ offers more potential in the applications for $NO_2$ detection.

### 6.3.3 Temperature sensing

To explore the temperature sensing capabilities of the nanocomposite-based chemiresistors in this chapter, temperature sensing experiments were conducted for various percolation sensors ($S_{20\text{-}P}$, $S_{30\text{-}P}$, $S_{40\text{-}P}$, $S_{50\text{-}P}$, and $S_{60\text{-}P}$), the saturation sensor ($S_{80\text{-}S}$), and the PEDOT sensor ($S_{PEDOT}$). Measurements were taken at different temperatures ranging from 30 to 80 °C, and the resulting changes in resistance were recorded. As shown in Figure 6.5, a negative temperature coefficient (NTC) effect was observed for each sensor. This effect means that the resistance of each sensor decreases as the temperature increases. The decrease in resistance for the pure PEDOT sensor ($S_{PEDOT}$) is attributed to the NTC nature of PEDOT. As the temperature increases, the mobility of charge carriers in PEDOT increases owing to enhanced carrier hopping and/or tunnelling between polymer segments,[302-304] thereby leading to an increase in

its conductivity. This NTC behaviour should contribute to the sensing responses of the studied sensors based on PEDOT/PS nanocomposites as well. Even though, it is still necessary to consider other influencing factors of their sensing responses, requiring further comparison between the sensors studied in this section.

To further compare the sensing performance between each sensor studied, the sensor responses of $S_{20\text{-}P}$, $S_{30\text{-}P}$, $S_{40\text{-}P}$, $S_{50\text{-}P}$, $S_{60\text{-}P}$, $S_{80\text{-}S}$, and $S_{PEDOT}$ were calculated as the percentage changes relative to the resistances at 30 °C ($\Delta R/R_{30} \times 100$ %). Negative responses were obtained owing to the decrease in resistance with the increase in temperature (Figure 6.5). As shown in Figure 6.6a, both the percolation and the saturation sensors exhibit improved sensor responses compared with $S_{PEDOT}$, indicating the presence of factors enhancing the NTC effect in temperature sensing beyond the inherent NTC nature of PEDOT. Otherwise, similar sensor responses would be expected across all sensors in this section if the temperature dependence of conductivity of PEDOT dominated the NTC effect of the nanocomposites. One potential factor should be associated with the thermomechanical properties of PS nanospheres. As the temperature rises, their expansion in volume may compress the PEDOT nanoparticles, thereby enhancing the contact area between connected fillers and/or bridging more adjacent fillers. Future investigations on the contributions from the insulating matrix to the sensor responses are required to support this explanation. Furthermore, Figure 6.6a shows that the introduction of PS nanospheres may also improve the linearity of the sensor response as a function of temperature. $S_{PEDOT}$ can only achieve a desirable linearity ($R^2 \geq 0.99$) from 30 to 50 °C, which is similar to the reported work on PEDOT nanoparticles.[305] Interestingly, sensors based on nanocomposites can accomplish this level of linearity from 30 to 60 °C, extending the linear range of detection in temperature sensing. However, this observation raises an intriguing question, necessitating future studies on the relationship between the linearity of the sensor response and the specific composition of PEDOT/PS nanocomposites.

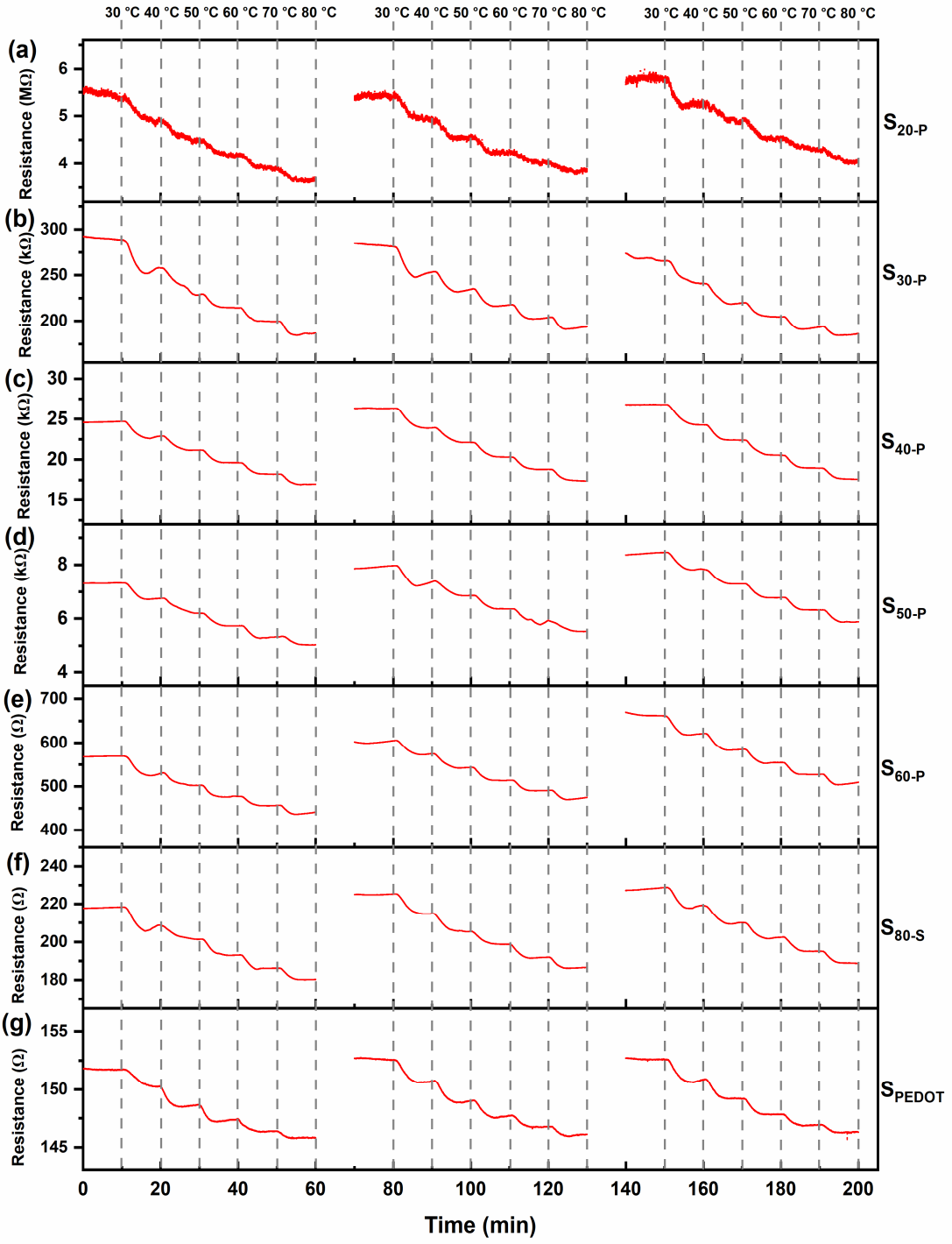



**Figure 6.5.** Temperature response for the sensors (a) $S_{20\text{-}P}$, (b) $S_{30\text{-}P}$, (c) $S_{40\text{-}P}$, (d) $S_{50\text{-}P}$, (e) $S_{60\text{-}P}$, (f) $S_{80\text{-}S}$, and (g) $S_{PEDOT}$. The name of each sensor is presented on the right of each figure. The sensing experiments were conducted 3 times for each sensor from 30 to 80 °C.

The temperature coefficient of resistance (TCR) of each sensor, defined as the slope of the linear fit, was then obtained within corresponding detection ranges to evaluate the sensitivity

in temperature sensing. Consistent with the sensor responses in Figure 6.6a, nanocomposite-based sensors exhibit improved TCRs compared to the PEDOT sensor (Figure 6.6b). In comparison to $S_{PEDOT}$ with a TCR of –0.12 ± 0.01 % °C$^{-1}$, $S_{80\text{-}S}$ exhibits a better TCR of –0.39 ± 0.02 % °C$^{-1}$. Figure 6.6b also shows that the TCR can be further improved with the decrease in $WF_{PEDOT}$ from the saturation region to the percolation region. However, the improvement of TCR almost stops below 30 wt% and similar TCRs around –0.80 % °C$^{-1}$ were obtained at 30 and 20 wt%, suggesting a potential upper limit to the improvement of TCR. Among all the sensors studied in this chapter, $S_{20\text{-}P}$ exhibits the best TCR of –0.81 ± 0.05 % °C$^{-1}$.

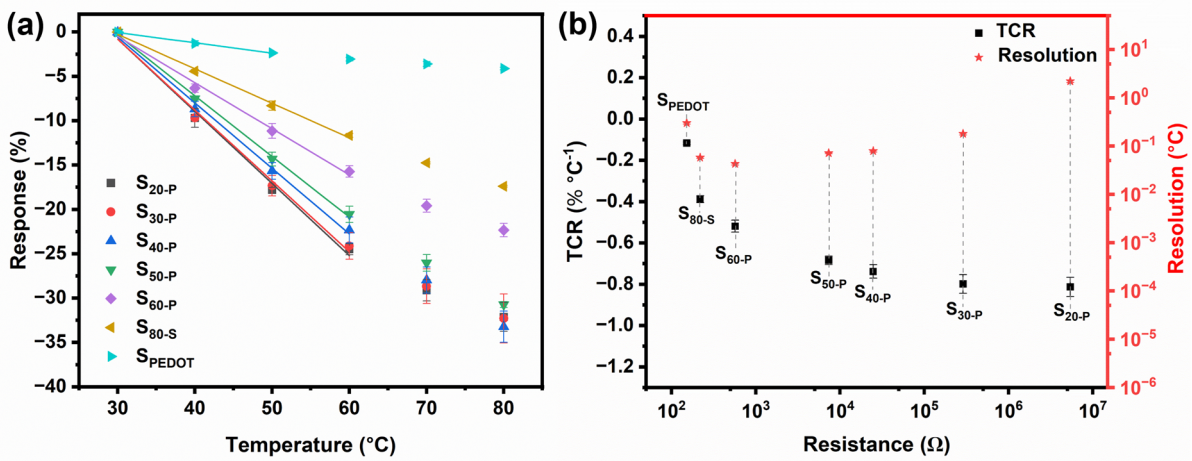



**Figure 6.6.** (a) Sensor responses ($\Delta R/R_{30} \times 100$ %) as a function of temperature for the percolation sensors ($S_{20\text{-}P}$, $S_{30\text{-}P}$, $S_{40\text{-}P}$, $S_{50\text{-}P}$, and $S_{60\text{-}P}$), the saturation sensor ($S_{80\text{-}S}$), and the PEDOT sensor ($S_{PEDOT}$). Due to the deviation from a desirable linearity ($R^2 \geq 0.99$), the data for the percolation and saturation sensors at 70 and 80 °C, as well as the data for the PEDOT sensor at 60, 70, and 80 °C, are not included in the trend lines. (b) Values of TCR (black squares) and resolution (red stars) for the sensors investigated. The dashed lines connect the TCR and resolution for each sensor.

Resolution is a significant parameter to describe the minimum detectable change in temperature, which is defined as three times the standard deviation of the baseline noise level (σ) divided by the modulus of the TCR. According to this definition, resolution is determined

by a competitive relationship between TCR and baseline noise. Since higher baseline resistances lead to higher levels of noise for the sensors studied, as the $WF_{PEDOT}$ decreases, the resolution keeps improving until 60 wt% (Figure 6.6b). This observation suggests that electrical percolation may not make positive effects to the resolution since the noise could primarily determine the resolution at low $WF_{PEDOT}$ values. Considering the significance of resolution in practical applications, therefore, a balance between TCR and noise should be carefully kept when designing percolation temperature sensors. Among all the sensors studied in this chapter, $S_{60\text{-}P}$ exhibits the best resolution of 0.043 ± 0.002 ℃.

Various PEDOT-based temperature sensors have been developed in recent years, providing valuable references for further evaluating the sensing performance of the sensors in this chapter. Therefore, it is worth attempting a comparison between the sensors studied here and those reported in the literature. Three percolation sensors, including $S_{40\text{-}P}$, $S_{50\text{-}P}$, and $S_{60\text{-}P}$, have been selected for comparison owing to their desirable comprehensive performance. Together with other PEDOT-based temperature sensors published in recent literature, the sensing performances of these percolation sensors have been summarised in Table 6.2. Although the selected percolation sensors show a relatively broad detection range compared to most of the reported sensors, their TCRs are not competitive. This observation should be related to various factors involved in designing a temperature sensor, such as the composition of the sensing layer,[306,307] the type of the substrate, [308] and post-treatment after device fabrication.[309] Further studies on these factors may lead to improvements in the TCR of PEDOT/PS nanocomposites in the future. In terms of resolution, it is noteworthy that all the selected percolation sensors demonstrate favourable results below 0.1 ℃. Particularly, $S_{60\text{-}P}$ achieves a resolution close to the highest resolution (0.04 ℃) known in the literature.[210] Therefore, the selected percolation sensors ($S_{40\text{-}P}$, $S_{50\text{-}P}$, and $S_{60\text{-}P}$) still hold the potential for temperature sensing, especially in applications requiring high accuracy.

**Table 6.2.** Comparison of sensing performance of PEDOT-based temperature sensors.

| Material | Electrode | Substrate | Detection range | TCR (% °C$^{-1}$) | Resolution (°C) | Ref. |
|---|---|---|---|---|---|---|
| PEDOT:PSS/CNT | Ag bands | $SiO_2$-coated Kapton | 22 – 49 °C | –0.61 | - | 310 |
| PEDOT:PSS | Ag bands | PEN | 20 – 70 °C | –0.90 | - | 311 |
| PEDOT:PSS/graphene | Ag | PET | 30 – 45 °C | –0.064 | - | 312 |
| PEDOT:PSS-dyed threads[a] | - | - | –50 – 80 °C | –0.48 | - | 313 |
| pNIPAM/PEDOT:PSS/CNT | Ag | PDMS | 25 – 40 °C | –2.6 | 0.5 | 306 |
| PEDOT-based VERAZOL® | Cr/Au | PEN | –15 – 35 °C | –0.75 | - | 314 |
| PEDOT:PSS/XSB[a] | - | - | 10 – 100 °C | –0.72 | 0.04 | 210 |
| PEDOT:PSS | Cu papers | Kapton | 30 – 80 °C | –0.72[b] | ~ 0.1 | 315 |
| cross-linked PEDOT:PSS | Ag bands | PEN | 25 – 50 °C | –0.77 | - | 225 |
| acid-treated PEDOT:PSS with micro-cracks | Cu wires | PDMS | 30 – 55 °C | 4.2[c] | 0.1 | 309 |
| PEDOT:PSS/rGO/PDMS[a] | - | - | 30 – 35 °C | –1.03 | - | 307 |
| silk/PEDOT:PSS | silk/PEDOT: PSS | Fibroin | 20 – 50 °C | –0.99 | - | 316 |
| PEDOT:PSS/PANI | Cu bands | PET | 32 – 42 °C | –0.803 | 0.1 | 317 |
| PEDOT:PSS | Ag pads | glossy photo paper | 28 – 50 °C | –1.67 | - | 308 |
| PEDOT:PSS | Ag IDEs | PI | 28 – 50 °C | –3.202 | - | 318 |
| PEDOT | Ag | TPU fibres | 20 – 40 °C | –0.95 | 0.2 | 319 |
| PEDOT:PSS/rGO | Al pads | Kapton | 30 – 45 °C | –3.365 | - | 320 |
| PEDOT:PSS/ZnO | Ag IDEs | PET | 30 – 60 °C | –1.06 | - | 321 |
| PEDOT/PS ($S_{40\text{-}P}$) | Pt IDEs | glass | 30 – 60 °C | –0.74 ± 0.05 | 0.078 ± 0.004 | This work |
| PEDOT/PS ($S_{50\text{-}P}$) | | | | –0.68 ± 0.03 | 0.071 ± 0.002 | |
| PEDOT/PS ($S_{60\text{-}P}$) | | | | –0.52 ± 0.03 | 0.043 ± 0.002 | |

Note: PEDOT:PSS = poly (3,4-ethylenedioxythiophene):polystyrene sulfonate; CNT = carbon nanotubes; PEN = polyethylene naphthalate; PET = polyethylene terephthalate; pNIPAM = poly(N-isopropylacrylamide); PDMS = polydimethylsiloxane; XSB = carboxylated styrene-butadiene copolymer; rGO = reduced graphene oxide; PANI = polyaniline; PI = polyimide; TPU = thermoplastic polyurethane. [a]Self-standing material without electrodes and substrates. [b]Estimated TCR from publication. [c]TCR based on a positive temperature coefficient (PTC) effect.

## 6.3.4 Airflow rate sensing

To explore the airflow rate sensing capabilities of the nanocomposite-based sensors in this chapter, airflow rate sensing experiments were conducted for various percolation sensors ($S_{20\text{-}P}$, $S_{30\text{-}P}$, $S_{40\text{-}P}$, $S_{50\text{-}P}$, and $S_{60\text{-}P}$), the saturation sensor ($S_{80\text{-}S}$), and the PEDOT sensor ($S_{PEDOT}$). Each sensor was securely positioned on the sample stage, facing the gas inlet tube. The sensing layer was perpendicular to the direction of airflow at a distance of 20.0 ± 0.5 mm to the head

of gas inlet tube. Measurements were taken at different airflow rates ranging from 20 to 800 sccm, and the resulting changes in resistance were recorded as shown in Figure 6.7.

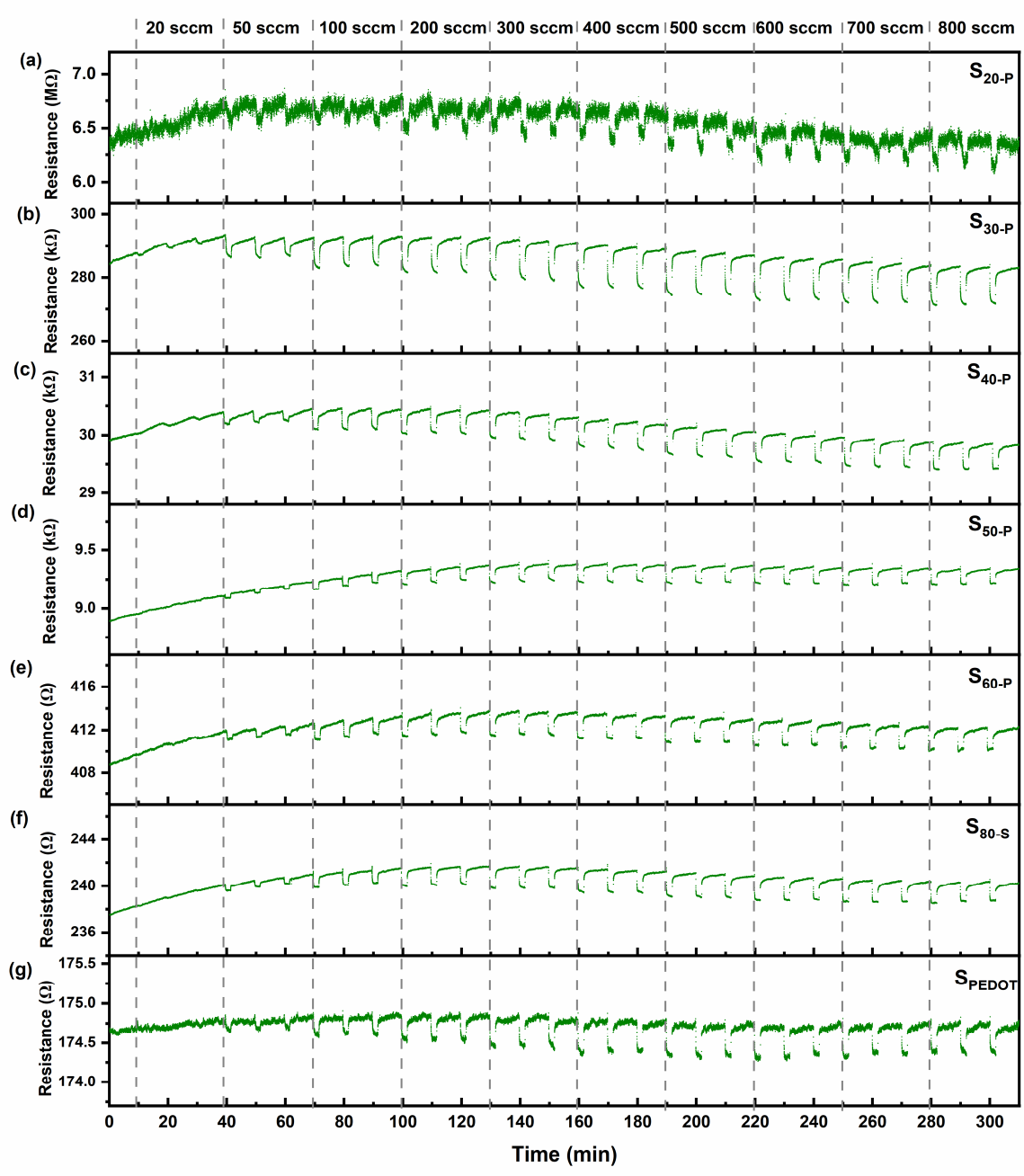



**Figure 6.7.** Airflow rate sensing response for (a) $S_{20\text{-}P}$, (b) $S_{30\text{-}P}$, (c) $S_{40\text{-}P}$, (d) $S_{50\text{-}P}$, (e) $S_{60\text{-}P}$, (f) $S_{80\text{-}S}$, and (g) $S_{PEDOT}$. The name of each sensor is presented in the upper right corner of each figure. All sensors were exposed 3 times to flow rates of dry air from 20 to 800 sccm for 2 min each, with an 8 minute recovery at 0 sccm between exposures. The test temperature is 25 ± 2 °C and the humidity is 2.23 ± 0.99 % RH.

As shown in Figure 6.7, the resistances for all the sensors decrease during the exposure periods from 50 to 800 sccm. This observation might be attributed to the piezoresistive nature of the sensing layers based on both PEDOT/PS nanocomposites and PEDOT nanoparticles. The increased surface pressure induced by the airflow compresses these sensing layers, leading to improved contact between connected PEDOT nanoparticles and/or bridging of adjacent PEDOT nanoparticles. It is also observed that sensors with higher resistances exhibit higher levels of noise. Among these sensors, $S_{20\text{-}P}$ with the highest resistance was excluded from further analysis as it was challenging to distinguish the signal from the noise effectively. Additionally, a noteworthy observation is that only $S_{30\text{-}P}$ and $S_{40\text{-}P}$ exhibit distinguishable changes in resistance at 20 sccm, indicating that electrical percolation may improve the lower limit of detection for airflow rate sensing.

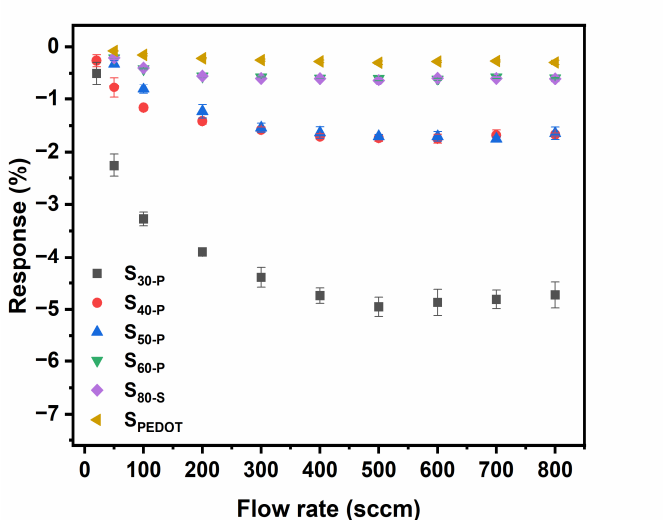



**Figure 6.8.** Sensor responses ($\Delta R/R_0 \times 100$ %) as a function of flow rate for the percolation sensors ($S_{30\text{-}P}$, $S_{40\text{-}P}$, $S_{50\text{-}P}$, and $S_{60\text{-}P}$), the saturation sensor ($S_{80\text{-}S}$), and the PEDOT sensor ($S_{PEDOT}$).

For a further understanding of electrical percolation in airflow rate sensing, the sensor responses for $S_{30\text{-}P}$, $S_{40\text{-}P}$, $S_{50\text{-}P}$, $S_{60\text{-}P}$, $S_{80\text{-}S}$, and $S_{PEDOT}$ were calculated as the percentage

changes relative to the starting resistances ($\Delta R/R_0 \times 100$ %). As shown in Figure 6.8, all these studied sensors exhibit nonlinear relationships between their sensor responses and airflow rates, presenting a challenge in evaluating their sensing performance. Further studies in the future are required to explore effective approaches to overcome this challenge. One potential solution, as suggested in the literature,[322,323] could be to attempt different flow angles inclined from the surface of the sensing layer.

Figure 6.8 also demonstrates that the sensor responses can be improved by decreasing $WF_{PEDOT}$, indicating that percolation sensors are more sensitive to airflow rate compared to the saturation sensor and the PEDOT sensor. Among all the sensors in this chapter, the percolation sensor $S_{30\text{-}P}$ exhibits the strongest sensor responses with an experimental lower limit of detection at 20 sccm. Similar to other studied sensors, however, the sensor response of $S_{30\text{-}P}$ keeps increasing with the increase in flow rate until 500 sccm, revealing an experimental upper limit of detection. Therefore, $S_{30\text{-}P}$ can operate within the detection range from 20 to 500 sccm. As 1 sccm equals to $7.45 \times 10^{-7}$ mol $s^{-1}$ and the airflow rate sensing experiments were carried out at atmospheric pressure and around 25 °C, airflow velocity in m $s^{-1}$ ($v$) was estimated from the airflow rate in sccm ($V_{sccm}$) using the following equation:

$$v = \frac{7.45 \times 10^{-7} V_{sccm} M_{dry\ air}}{\rho_{dry\ air} \pi r_i^2} \tag{6.2}$$

where $M_{dry\ air}$ repesents the mole mass of the dry air (28.96 g $mol^{-1}$), $\rho_{dry\ air}$ represents the density of the dry air at atmospheric pressure and 25 °C (1.183 g $L^{-1}$), and $r_i$ represents the internal radius of the gas inlet tube (0.25 cm). Thus, the estimated detection range for $S_{30\text{-}P}$ spans from 0.019 to 0.464 m $s^{-1}$. This detection range has been used for the comparison with other CP-based airflow rate sensors. Only a few airflow sensors have to date developed based on conjugated polymers and their composites, and their capabilities in airflow rate sensing are

attributed to the piezoresistive effect enhanced by various factors, such as hair/fluffy-like structures and favourable matrices.[324-328] As summarised in Table 6.3, although $S_{30\text{-}P}$ operates within a narrower detection range compared to most of CP-based airflow rate sensors, it exhibits the lowest limit of detection obtained in sensing experiments. This indicates that $S_{30\text{-}P}$ should be more suitable for the detection at very low flow rates. If the scope of sensing materials is extended beyond conjugated polymers, however, $S_{30\text{-}P}$ is not as competitive as expected since carbon-based materials have already exhibited excellent results in detection range. For instance, fluffy-like carbon nanotubes deposited on textiles can exhibit ideal responses from 0.05 to 7.0 m $s^{-1}$,[322] while a remarkably wide detection range from 0.0023 to 8 m $s^{-1}$ has been obtained with laser-induced graphene fibres deposited on polyimide substrates.[323] Even so, this section has proven that the concept of electrical percolation can contribute to the improvement of airflow rate sensing performance, which should work for various sensing materials. Moreover, PEDOT/PS nanocomposites obtained in the percolation region still holds some opportunities since changing the thickness of the sensing layer and/or the configuration of the sensor may improve the performance in airflow rate sensing, which requires further investigations in the future.

**Table 6.3.** Comparison between the percolation sensor $S_{30\text{-}P}$ with other CP-based airflow rate sensors.

| Material | Electrode | Substrate | Detection range | Ref. |
|---|---|---|---|---|
| PEDOT:PSS micro-hairs | Au | - | 0.424 – 2.968 m $s^{-1}$ [a] | 324 |
| PEDOT:PSS micro-hairs | Au | PDMS | 0.066 – 0.099 m $s^{-1}$ | 325 |
| fluffy-like PEDOT: PSS-$Cu^{2+}$ fibres [b] | - | - | 0.5 – 3.5 m $s^{-1}$ | 326 |
| fluffy-like PEDOT: PSS fibres [b] | - | - | 1.0 – 3.0 m $s^{-1}$ | 327 |
| PANI/PEO/graphene | Cu foils | tape | 1.69 – 6.78 m $s^{-1}$ [a] | 328 |
| PEDOT/PS nanocomposites ($S_{30\text{-}P}$) | Pt IDEs | glass | 0.019 – 0.464 m $s^{-1}$ | This work |

Note: PEDOT:PSS = poly (3,4-ethylenedioxythiophene):polystyrene sulfonate; PDMS = polydimethylsiloxane; PANI = polyaniline; PEO = polyethylene oxide. [a]Estimated detection range from publication. [b]Self-standing material without electrodes and substrates.

## 6.4 Conclusion and outlook

In this chapter, PEDOT/PS nanocomposites were prepared for the CP-based percolation chemiresistors. These nanocomposites were formed by combining PEDOT nanoparticles with PS nanospheres through a simple solution blending process. CP-based chemiresistors with varying values of $WF_{PEDOT}$ were then fabricated using the DEISA technique. The electrical percolation behaviour was investigated, and both the percolation and saturation regions were determined by analysing the trend of device conductance. The formation of percolation pathways was further confirmed through morphology analysis. The morphology analysis also revealed a reversal of the filler-matrix relationship in the composite morphology as the transition from the percolation region to the saturation region. Then, this chapter systematically studied the response of the PEDOT-based chemiresistors to $NO_2$ gas. It has been demonstrated that sensors based on PEDOT/PS nanocomposites can exhibit better sensitivities compared to their counterparts solely based on PEDOT nanoparticles, and electrical percolation has proven to further improve the sensing performance for $NO_2$ detection. An optimal $NO_2$ sensor ($S_{30\text{-}P}$) with a sensitivity of –2.29 ± 0.05 % $ppm^{-1}$ and a LOD of 40 ± 1 ppb was obtained, showing competitive performance compared to other CP-based chemiresistors for $NO_2$ detection. After the investigation on gas sensing, furthermore, the sensing capabilities of these PEDOT-based chemiresistors were extended through further studies on temperature and airflow rate sensing. The results indicate that improved sensing performance for both temperature and airflow rate detection can be obtained in the percolation region. Although the temperature sensors based on nanocomposites in this chapter exhibits moderate TCRs in a detection range with desirable linearity ($R^2 \geq 0.99$) from 30 to 60 ℃, compared with other PEDOT-based temperature sensors, the percolation sensors $S_{40\text{-}P}$, $S_{50\text{-}P}$, and $S_{60\text{-}P}$ can achieve very competitive temperature resolutions below 0.1 ℃. The highest resolution obtained in this chapter is 0.043 ± 0.002 ℃ from the percolation sensor $S_{60\text{-}P}$. As for the airflow rate sensing, unfortunately, nonlinear

relationships between sensor response and flow rate were observed. The optimal airflow rate sensor ($S_{30\text{-}P}$) exhibits a valid detection range from 20 to 500 sccm, which could be suitable for low flow rate detection. To sum up, this chapter has provided valuable insights into the development of percolation chemiresistors with CP-based composites by systematically investigating their electrical percolation behaviour and exploring their multifunctionality for different stimuli.

Limitations remain in this chapter as well. Firstly, specific studies were not conducted on the sensors prepared below the $WF_{PEDOT}$ values of 20 or 30 wt% due to the difficulty in effectively distinguishing the electrical signals from the noise. This limitation hinders a comprehensive understanding of the sensing performance near or at the percolation threshold. To overcome this challenge, approaches to lower the noise of measurement should be explored, such as lock-in techniques. Another limitation lies in the poor reversibility observed at high gas concentrations, which was also observed in Chapter 5. Although the results in Chapters 4 and 5 (Figures 4.5 and 5.8) have demonstrated that the sensors can fully recover back to their baselines with a long recovery time of one or more hours, systematic investigations are still necessary to explore and understand the influencing factors of sensor reversibility. This understanding is fundamental for optimizing the sensing performance and ensuring reliable gas detection. Furthermore, this chapter does not mention the gas selectivity and humid resistivity of the percolation sensors, which are important aspects to consider in practical applications. Relevant studies on these aspects will be carried out in the future.

Last but not least, both the two sides of multifunctionality should be carefully considered. It would be surprising and encouraging if the sensors exhibit multifunctionality, as they may bring more possibilities in various applications. On the opposite side, however, their multifunctionality also reveals concerns that more uncertainties caused by other stimuli must be considered for a specific application. For example, if the sensors in this chapter are designed

for gas detection, attempts should be made to avoid the impacts from both temperature and flow rate. During the gas sensing tests in this thesis, the gas temperatures detected via the mass flow controllers are usually 1 to 2 °C lower than the chamber temperature, and abrupt decreases in total flow rate always exist due to an unavoidable interval of change (0.1 s) between two flow controllers. As no obvious abrupt changes over 0.1 °C were observed next to the tested sensors at the start of exposure, the temperature in the sensing chamber should dominate the test temperature. Also, the total flow rate can quickly stabilise after two flow controllers completely change to set values. Thus, the steady changes in sensor resistance during the gas sensing tests in this thesis are determined by the analyte concentration. However, abrupt changes in temperature and/or total flow rate may result in spike-like changes in sensor resistance observed in Figure 6.3, potentially interfering with future tests at the ppb level. To mitigate this issue, a more stable sensing setup should be designed, and the tested sensor should be securely fixed in a position without the interference of gas flow.

# Chapter 7

# Electrical percolation via in situ solid-state polymerisation

Electrical percolation based on conjugated polymers (CPs) can be achieved through both the filler-in-matrix and the conductor-on-substrate strategies. Among these, the conductor-on-substrate strategy has shown more promise for improving the sensing performance of CP-based chemiresistors. However, this approach has to date primarily relied on electropolymerisation, a preparation method with drawbacks that limit the development of CP-based percolation sensors. To diversify the preparation method for the conductor-on-substrate strategy and address the limitations of electropolymerisation, this chapter investigates the possibility of achieving electrical percolation based on poly(3,4-ethylenedioxythiophene) (PEDOT) through in situ solid-state polymerisation (ISSP). In this exploration, monomers for ISSP are deposited on glass substrates with Pt interdigitated electrodes (IDEs) via spray coating. Electrical percolation can be observed both during an ISSP process coupled with an in situ conductance monitoring technique and after a simplified ISSP process without monitoring. PEDOT sensors prepared through the simplified process exhibit sensitivity to nitrogen dioxide ($NO_2$) gas. An electrochemical re-doping process is used to avoid the over-oxidation during $NO_2$ sensing, and the sensing response of re-doped PEDOT can be improved via electrical percolation.

## 7.1 Motivation and solution

Electrical percolation based on conjugated polymers (CPs) has demonstrated its advantages in the field of chemical detection. As discussed in Section 2.3, CP-based percolation networks can be generally realised through two approaches, including the filler-in-matrix strategy and the conductor-on-substrate strategy. However, these two approaches significantly differ in the diversity of available preparation methods. Numerous techniques have been reported for achieving percolation networks by incorporating CP-based fillers into matrices,[160,172,173,179] while the deposition of CP-based percolation networks onto substrates has predominantly relied on electrochemical polymerisation.[35,226] Compared with the filler-in-matrix strategy, furthermore, recent studies on CP-based chemiresistors have increasingly highlighted that improved sensing performance can be effectively attained by creating percolation networks through the conductor-on-substrate strategy.[31-33,36,265,329] This enhancement can be attributed to the inherent advantage of CPs deposited solely on substrates, allowing them to fully exhibit sensitivity to analytes without any interference from matrix materials. However, the primary method for implementing the conductor-on-substrate strategy, namely electrochemical polymerisation, does present certain limitations. Drawbacks such as restricted monomer and substrate choices, along with challenges in achieving large-scale production, are inherent in this approach. To address the dual concerns of methodological diversity and the material limitations of electropolymerisation, it is imperative to explore alternative preparation methods for the conductor-on-substrate strategy. Investigating these alternatives holds promise for uncovering their potential contributions to CP-based percolation chemiresistors.

In situ solid-state polymerisation (ISSP) has been regarded as a unique synthesis method for CPs without catalysts or solvents. The first instance of the CP via ISSP was reported by Meng *et al*. in 2003.[53,54] They discovered that highly conductive poly(3,4-ethylenedioxythiophene)

(PEDOT) can be obtained through the ISSP of 2,5dibromo-3,4-ethylenedioxythiophene (DBEDOT) crystals after prolonged storage at room temperature. Their subsequent studies demonstrated that this reaction can be accelerated with increasing temperature below the melting point of DBEDOT (97 °C) and can be effectively completed within several hours. Since then, many researchers have explored various monomers suitable for ISSP,[330-337] enhancing the diversity of resulting CPs. Furthermore, PEDOT via ISSP has already been applied in various fields, such as solar cells,[338-342] electromagnetic interference shielding,[343,344] batteries,[345,346] supercapacitors,[347-349] and sensors.[336,350,351]

With its ease of use and potential for large-scale preparation of CPs on diverse substrates, ISSP should be a potential method to achieve electrical percolation. Monomers can be readily deposited on various substrates using solution processing or vapour deposition methods. Subsequently, electrical percolation could be achieved either during or after the ISSP process. During the polymerisation, some obtained CPs within monomers and/or oligomers may interconnect. This implies the potential occurrence of electrical percolation during ISSP, which can be detected through an in situ conductance monitoring technique. Ideally, stopping ISSP within a detected percolation region should yield samples with varying numbers of percolation networks on substrates. Alternatively, electrical percolation could also be achieved by finely controlling the quantity of monomers deposited, as this parameter has a direct influence on the concentration of CPs present on substrates after ISSP. Although these approaches above may yield electrical percolation during and after ISSP, it is important to note that no relevant studies have been reported in this domain. In terms of application, furthermore, there have been no reported instances demonstrating the use of CP-based percolation networks via ISSP as sensing materials for chemiresistors. Consequently, it is crucial to embark on explorations to evaluate the feasibility of ISSP in the creation of percolation networks and assess their potential effectiveness as sensing materials for chemical detection.

In this chapter, attempts are made to investigate the feasibility of achieving electrical percolation through ISSP. To conduct this investigation, DBEDOT is chosen as the monomer. This choice is due to the fact that the resultant PEDOT, obtained from this monomer, is an extensively studied CP via ISSP over the past two decades. In this chapter, DBEDOT monomers are deposited on glass substrates with Pt interdigitated electrodes (IDEs) via spray coating. Subsequently, PEDOT is synthesised through ISSP at specific temperatures. An in situ conductance monitoring technique is used to investigate the percolation behaviour during ISSP. In addition to the conductance monitoring, electrical percolation observed after ISSP is also explored, which involves the control of the quantity of DBEDOT deposited onto the Pt IDE substrate. Furthermore, this work explores the sensing capability of PEDOT obtained after ISSP.

## 7.2 Experimental section

### 7.2.1 In situ solid-state polymerisation (ISSP)

Prior to ISSP, each Pt IDE substrate (Micrux) was cleaned with concentrated nitric acid ($HNO_3$, 90 %, Fisher Scientific) and then sonicated in ethanol ($C_2H_5OH$, 99.8 %, Sigma-Aldrich) for 10 min. Monomer DBEDOT (97 %, Sigma-Aldrich) was further purified through recrystallisation from $C_2H_5OH$. Following the experimental protocol in Section 3.2.3, purified DBEDOT was spray-coated onto the substrates using its solution with a concentration of 2.5 mg $mL^{-1}$ in chloroform ($CHCl_3$, ≥ 99 %, Sigma-Aldrich). This spray-coating process was carried out utilising the Gocheer mini airbrush equipped with a 0.2 mm nozzle. The air pressure applied to the airbrush was 25 psi and the airflow rate was 13 L $min^{-1}$. Under ambient conditions, the spray-coating was conducted at an approximate distance of 10.0 ± 0.1 cm between the nozzle and the deposition area of the Pt IDE substrate. This process was terminated upon complete consumption of the solution loaded in the airbrush cup.

The ISSP process coupled with an in situ conductance monitoring technique was conducted using the setup depicted in Figure 3.3 and following the experimental protocol outlined in Section 3.2.2. For each spray-coating cycle, 500 μL of the monomer solution was loaded and subsequently consumed. Each coated substrate was sealed within a 5 mL glass vial and connected to the B2902A source/measure unit (SMU, Keysight). The sealed vial was then positioned in an oil bath, maintained at a predetermined temperature for a specific duration. The temperature control was achieved using an IKA RCT Basic stirrer hotplate connected with a PT1000 temperature sensor. A DC potential of 1.0 V was applied throughout this ISSP process, and the current across the IDEs was recorded by the B2902A SMU interfaced with the personal computer equipped with Benchvue software. The resistance of each resultant sample under ambient conditions was measured using the RS PRO IDM 98IV handheld digital multimeter.

Following the experimental protocol outlined in Section 3.2.2, the ISSP process for PEDOT was also conducted using a simplified approach without the in situ conductance monitoring technique. A series of samples with varying quantities of monomer were prepared by loading distinct volumes of the monomer solution into the airbrush cup. Each coated substrate was sealed within a 5 mL glass vial. These sealed vials were then placed within the Garbolite PN60 oven maintained at 70.0 ± 0.5 ℃ for 12 hr. After this ISSP process, the resistance of each resultant sample was measured using the RS PRO IDM 98IV handheld digital multimeter. The surface morphologies of the PEDOT on the Pt IDE substrates were imaged using a Zeiss EVO scanning electron microscope (SEM) at an accelerating voltage of 20 kV.

### 7.2.2 Electrochemical experiments

All electrochemical experiments were conducted using the classic three-electrode system shown in Figure 2.2a and Section 3.2.1. The three-electrode cell, supported by the PGSTAT204

Autolab electrochemical workstation (Eco Chemie), used the Pt coil (BASi) as the counter electrode, the Ag/AgCl (CH Instruments) as the reference electrode, and the Pt IDE substrate with PEDOT as the working electrode. The electrolyte solution used for electrochemistry consisted of 0.1 M lithium perchlorate ($LiClO_4$, 99 %, Sigma-Aldrich) dissolved in acetonitrile ($CH_3CN$, 99 %, Sigma-Aldrich). The electrochemical characteristics of PEDOT prepared via ISSP were investigated through cyclic voltammetry. The working electrode underwent cycling between −1.0 and +1.5 V, utilising a scan rate of 100 mV $s^{-1}$. The re-doping process of PEDOT was conducted using the chronoamperometry technique. Each sample was de-doped at −1.0 V for 2 min, followed by doping at 0.3 V for 2 min. After this re-doping process, each sample was carefully washed with $CH_3CN$ and dried in air for 10 min.

### 7.2.3 Sensing experiments

Sensing experiments were carried out at atmospheric pressure using the gas sensing setup (Figure 3.5) and the experimental protocol described in Section 3.4.1. Analyte gas (10 ppm, BOC) and nitrogen gas ($N_2$, 99.998 %, BOC, for further dilution of analyte) were mixed at the T-joint before entering the gas inlet of the chamber, and a total flow rate of 500.0 ± 2.5 sccm was employed throughout the experiments. The concentration of analyte was determined by the relative flow rates of the two mass flow controllers (Alicat). The temperature and relative humidity in the chamber were recorded via the SHT31 temperature and humidity sensor (Sensirion) next to the PEDOT-based sensor. The PEDOT-based chemiresistor in the custom-made chamber was connected to the B2902A SMU. A DC potential of 1.0 V was applied during the experiments, and the resistance of the sensor was monitored via the SMU connected to a personal computer equipped with Benchvue software. $N_2$ gas was initially purged for 30 min to eliminate impurities from both the chamber and the sensing layer. After the purging process, the sensor was exposed to 4ppm analyte for 1 min. The baseline of each sensor was defined as

the average of the values measured within the 30-second period before the first exposure. After each exposure, the sensor was purged with nitrogen for recovery.

## 7.3 Results and discussion

### 7.3.1 Electrical percolation observed during ISSP

To investigate the electrical percolation behaviour during the ISSP process, an in situ conductance monitoring technique was introduced to observe the trend of the current across the Pt IDEs at varying temperatures. As shown in Figure 7.1, no discernible current is observed during the monitoring phase at room temperature (R.T.) within 20 hr. This absence of current is attributed to the sluggish progression of the ISSP of DBEDOT at room temperature. The existing literature has claimed that PEDOT formation via ISSP can require up to two years under these conditions.[53,54] In order to expedite the ISSP process for practical experimentation, the majority of published studies have raised the reaction temperature to at least 60 °C.

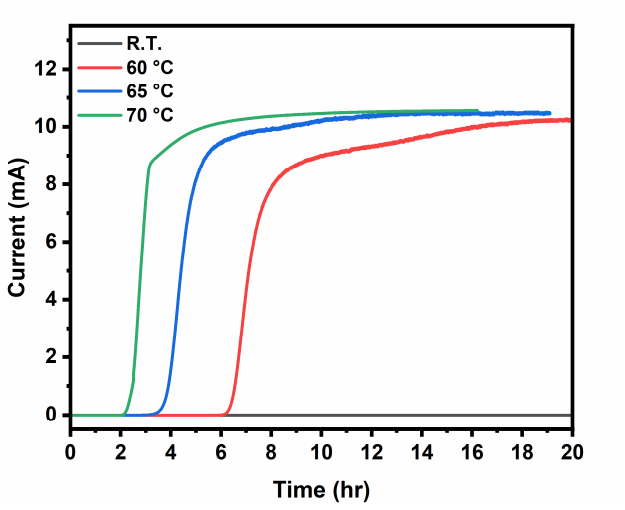



**Figure 7.1.** Measured current curves during ISSP of DBEDOT on Pt IDE substrates at room temperature (R.T.), 60 °C, 65 °C, and 70 °C. 1.0 V was applied across the Pt IDEs. The curves show earlier onsets of the current increase for higher reaction temperatures.

In this chapter, the ISSP process coupled with the in situ conductance monitoring technique was then carried out at 60, 65, and 70 ℃. As shown in Figure 7.1, the resulting current curves exhibit analogous trends throughout this ISSP process. For the curve of each heated sample, initially, no discernible current is observed across the Pt IDEs. This preliminary stage corresponds to the insulating region for each sample, wherein monomers, oligomers, and polymers coexist. Although some PEDOT networks may interconnect, the insulating region lacks sufficiently extensive PEDOT conducting pathways to bridge the gap between the electrodes. As ISSP proceeds, the current observed for each heated sample exhibits an abrupt increase. This change in current can be attributed to the further extension of PEDOT pathways across the gaps, resulting in the connection of the IDEs. A higher reaction temperature results in a shorter time to reach the onset of this sharp increase as elevated temperatures accelerate the reaction kinetics. The current keeps increasing rapidly after each onset, depicting the electrical percolation behaviour during ISSP. Subsequently, the percolation region ends when the increase in current starts to slow down. This indicates that the IDEs are fully connected with PEDOT networks via ISSP, leading to the formation of a dense conductive film. This is attributed to the saturation of conducting pathways across the gaps between IDEs. At this stage, adjacent PEDOT networks within each dense film can further interconnect, gradually enhancing the conductivity of this film. Finally, the increase in current for each heated sample stops, indicating the completion of ISSP.

Although the in situ conductance monitoring technique holds promise for studying electrical percolation behaviour during ISSP, it is difficult to obtain samples at different stages of conductance before the completion of ISSP. Taking the ISSP process of DBEDOT at 60 ℃ as an example, attempts were made to prepare PEDOT networks in the percolation region. A sample was quickly extracted from the glass vial after 6 hr and then immersed in 5 mL of $CHCl_3$ overnight. The immersion process was anticipated to dissolve and remove both the

monomers and oligomers. Unexpectedly, the resistance of the sample decreased from 14 kΩ to approximately 100 Ω, and this phenomenon was consistently observed from repeated experiments. This observation suggests that polymerisation continues during the overnight immersion, which is possible attributed to the bromine generated during ISSP that functions as the oxidant propelling this reaction.[53,54] To stop the polymerisation, one potential solution could be immersing the sample in a reducing solvent or solution to consume the bromine. A re-doping process would be required after immersion since PEDOT can be de-doped by reducing agents. Further attempts will be made in the future to develop a reliable approach to obtain PEDOT networks at any stages of ISSP. Only when this issue is fully addressed, can further investigations on morphologies and sensing capabilities be carried out for the PEDOT percolation networks prepared during ISSP.

### 7.3.2 Electrical percolation observed after ISSP

A simplified ISSP process without the in situ conductance monitoring technique was also carried out in this chapter. A series of samples with varying quantities of the DBEDOT monomer were prepared by loading distinct volumes of the monomer solution for spray coating, ensuring different quantities of PEDOT networks on Pt IDE substrates. The ISSP process was simply carried out in an oven at a set temperature of 70 ℃. The reaction time was set at 12 hr as the ISSP of DBEDOT can be completed under such conditions (Figure 7.1). After this simplified ISSP, the resistance values between the IDEs were recorded under the ambient conditions.

The plot in black (Figure 7.2) shows the trend of conductance as a function of the loading volume of the DBEDOT solution for spray coating, spanning from 60 to 500 μL. The same data plotted as a semi-logarithmic plot in red is used to determine the boundaries for the percolation region. Initially, no conductance is observed using 60 or 70 μL of the monomer

solution. This observation indicates that small quantities of PEDOT via ISSP are insufficient to establish connections across the glass gaps between the Pt IDEs. This stage is regarded as the insulating region. As the loading volume increases, conductance can be then detected at 80 µL, signifying the formation of percolation pathways across the IDEs. This suggests that the percolation threshold can be achieved using no more than 80 µL of the monomer solution for spray coating. With the formation of more percolation pathways, the conductance exhibits a sharp increase until 200 µL, thus defining the percolation region between 80 and 200 µL. Beyond 200 µL, the conductance shows a gradual increase within the same order of magnitude, indicating the tendency towards saturation. In summary, the observed trend of conductance from the insulating to the saturation regions provides evidence that electrical percolation can be achieved after the ISSP of controlled quantities of DBEDOT monomer. Nevertheless, it is important to acknowledge that the conductance error bars are large, particularly for samples near the percolation threshold. This variability between samples may result from the limited reproducibility of the spray coating process.

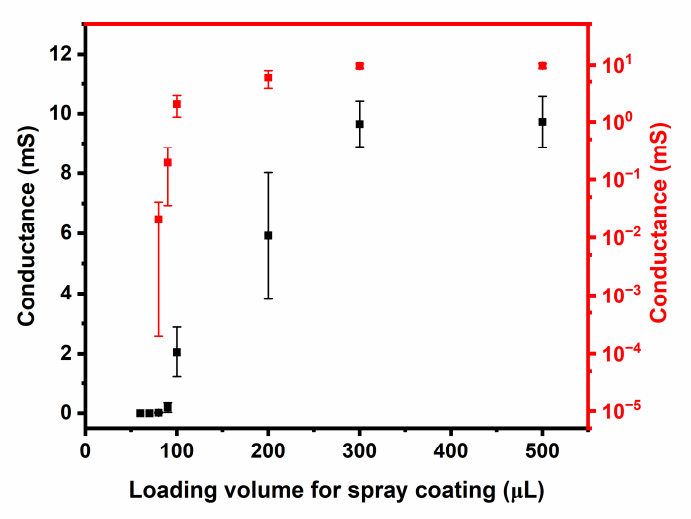



**Figure 7.2.** Plot of conductance vs. loading volume for spray coating and its semi-logarithmic plot (in red). All the error bars are obtained from the standard deviation of the conductance values of three separate samples.

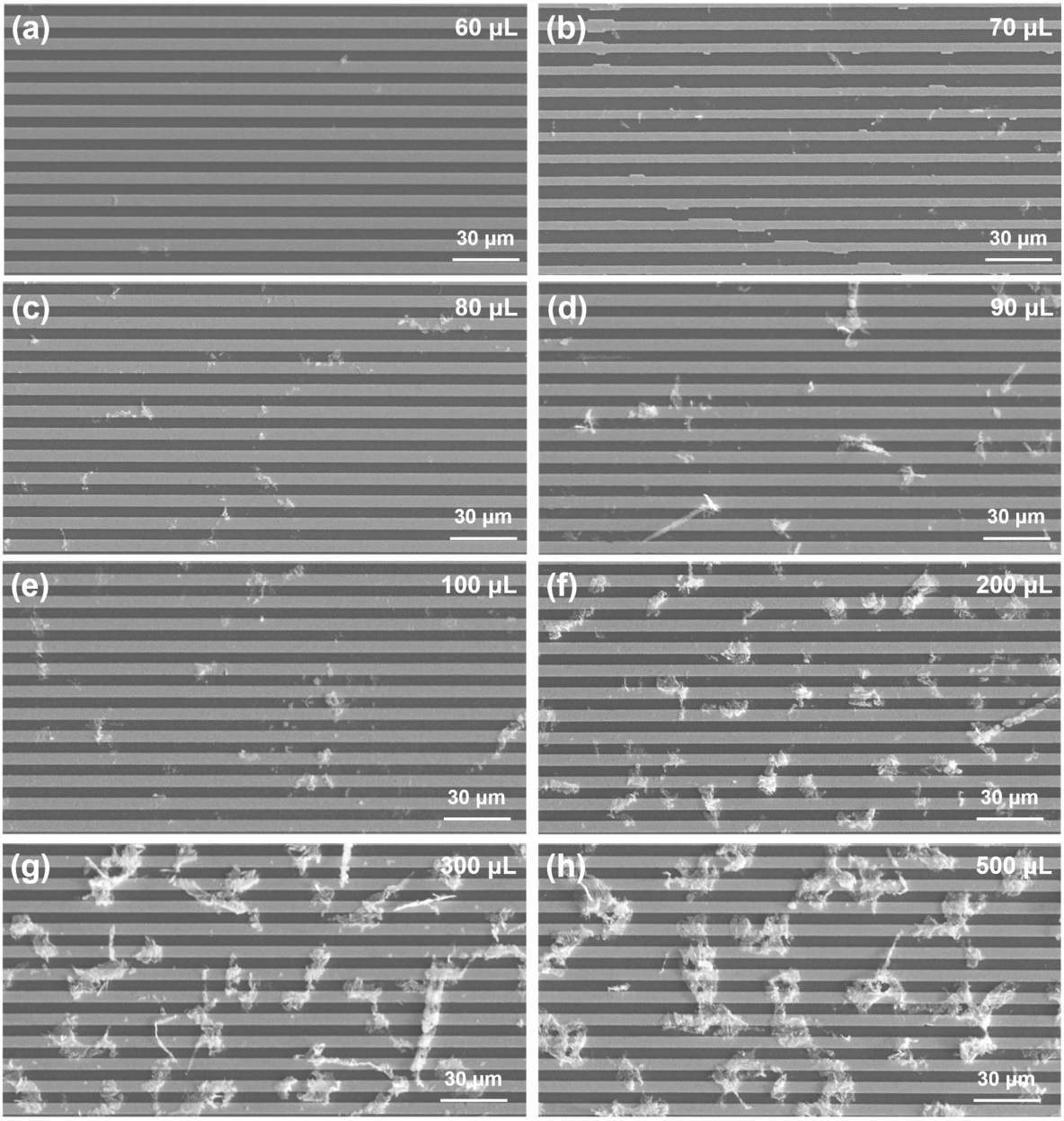



**Figure 7.3.** SEM images of PEDOT prepared on the Pt IDE substrates using different loading volumes of the DBEDOT solution from 60 to 500 µL (a − h, respectively). The loading volume is presented in the upper right corner of each figure. Images taken by Liren Wang.

SEM images illustrate the morphologies of the PEDOT via ISSP on the Pt IDE substrates within the insulating (Figures 7.3a and 7.3b), percolation (Figures 7.3c – f), and saturation regions (Figures 7.3g and 7.3h). As the loading volume of the DBEDOT solution for spray coating increases, both the density and size of the PEDOT clusters and stripes on the substrate

show augmentation. This change in density and size facilitates the bridging of insulating gaps between the Pt IDEs, resulting in the emergence of electrical percolation behaviour. Notably, Figure 7.3 consistently supports the conductance trend observed in Figure 7.2, demonstrating the correlation between morphology and electrical behaviour. Additionally, Figure 7.3b shows partial detachment of the Pt material from the IDEs, likely resulting from repetitive recycling and cleaning procedures.

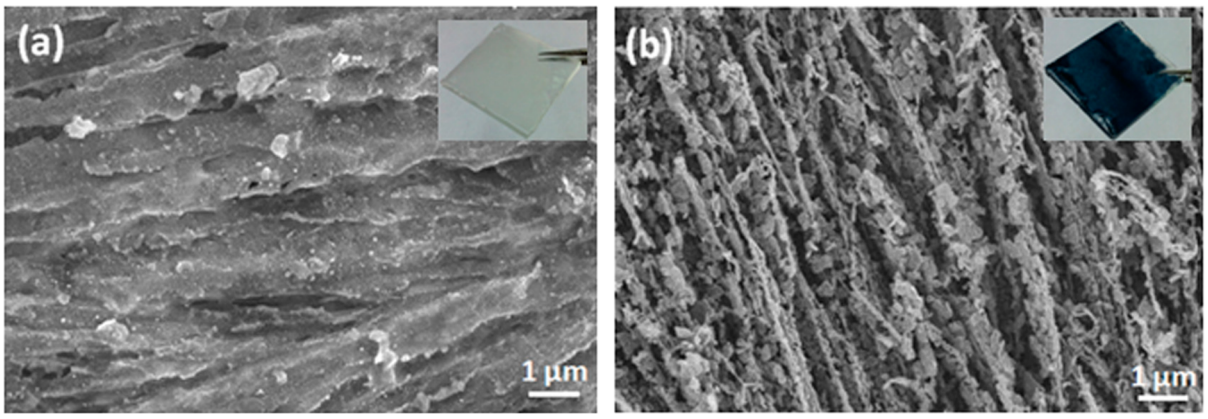



**Figure 7.4.** Photographs and FE-SEM images of (a) DBEDOT and (b) PEDOT films fabricated via solid-state polymerisation on the fluorine-doped tin oxide (FTO) substrate. Taken with permission from ref. 340.

Although results in this section have demonstrated that the electrical percolation of PEDOT can be obtained after the simplified ISSP process, it is crucial to acknowledge that the morphological study has unveiled certain issues that require further consideration. Firstly, it is puzzling that only the trace quantities of PEDOT were observed in Figures 7.3a and 7.3b. This finding contradicts the visual presence of the white thin films of monomer observed on the substrates when using 60 and 70 µL of DBEOT solution for spray coating. For samples prepared using larger volumes (Figures 7.3g and 7.3h), moreover, it adds to this perplexity that only PEDOT clusters and stripes distributed on the substrates were observed as opposed to the expected continuous films. These observations collectively suggest the disappearance of

monomers from the substrates during the simplified ISSP process. Comparing the morphologies before and after ISSP could potentially help address this issue. However, this approach appears impractical for the work in this section due to the sublimation of DBEDOT during the metal sputtering pre-treatment required for SEM analysis. Only a handful of studies have succeeded in such a comparison between DBEDOT and PEDOT through field emission scanning electron microscopes (FE-SEM).[340,343] Yin *et al*. first reported a significant change in the morphology of the materials deposited on a substrate (Figure 7.4).[340] Subsequently, Wu *et al*. assumed that this significant change in morphology might result from the formation of the polymer chain during ISSP.[343] However, this explanation seems less compelling due to the possible overestimation of the effects of polymer chains on morphology at the microscale. Moreover, it cannot elucidate the disappearance of monomers observed in this section. For a similar finding during the ISSP of a DBEDOT derivative, Gulprasertrat *et al*. presented an alternative explanation for the significant change in morphology. They assumed that the surface of their sample was destroyed probably due to the evaporation of the excess bromine released during ISSP,[352] which aligns more with the observed changes than the formation of the polymer chain. Based on this explanation, it is reasonable to further speculate that some of the monomers might have departed from the substrates before polymerisation, which is possibly induced by the flow of released bromine vapour. This speculation offers a possible explanation for the puzzling observations in this section.

Another noteworthy discovery in the morphological study is the emergence of distinct morphologies obtained in the same sample. For instance, both PEDOT stripes with large crystal flakes and PEDOT clusters with small particles were observed in the same sample prepared using 500 μL of the DBEDOT solution for spray coating (Figure 7.5). One possible explanation could be the potential impact of the heating process on the crystallisation of DBEDOT. Specifically, some small monomer crystals might merge and then become larger crystals

through thermal annealing. Considering the possible departure of monomer, another explanation could involve the re-deposition of these departed monomers onto the substrate. In this scenario, these monomers might have re-crystallised and subsequently undergone polymerisation, forming PEDOT crystal flakes at the microscale.

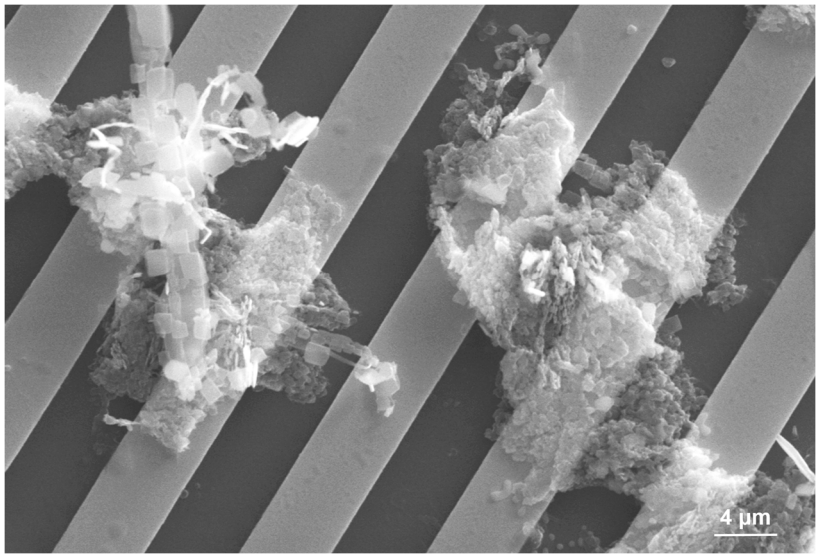



**Figure 7.5.** SEM image of PEDOT prepared on the Pt IDE substrates using 500 µL of the DBEDOT solution for spray coating. Image taken by Liren Wang.

Additionally, it should be noted that dark blue residues were observed on the inner walls of the glass vials after the simplified ISSP process. As each vial was pre-cleaned before polymerisation and each substrate only consists of Pt and glass, these residues are likely to be PEDOT prepared via ISSP. This finding should serve as evidence for both the departure and re-deposition of DBEDOT. Further studies are required to provide additional evidence to evaluate the possible explanations for some perplexing observations in this section. Such investigations could contribute to a deeper understanding of the ISSP process. This understanding holds significance for research focused on electrical percolation achieved via ISSP, as both the departure and re-deposition of DBEDOT significantly influence the formation of percolation networks. To minimize uncertainties during the preparation of percolation

networks, furthermore, it is advisable to further explore more reliable and controllable ISSP procedures that eliminate the issues of monomer departure and re-deposition.

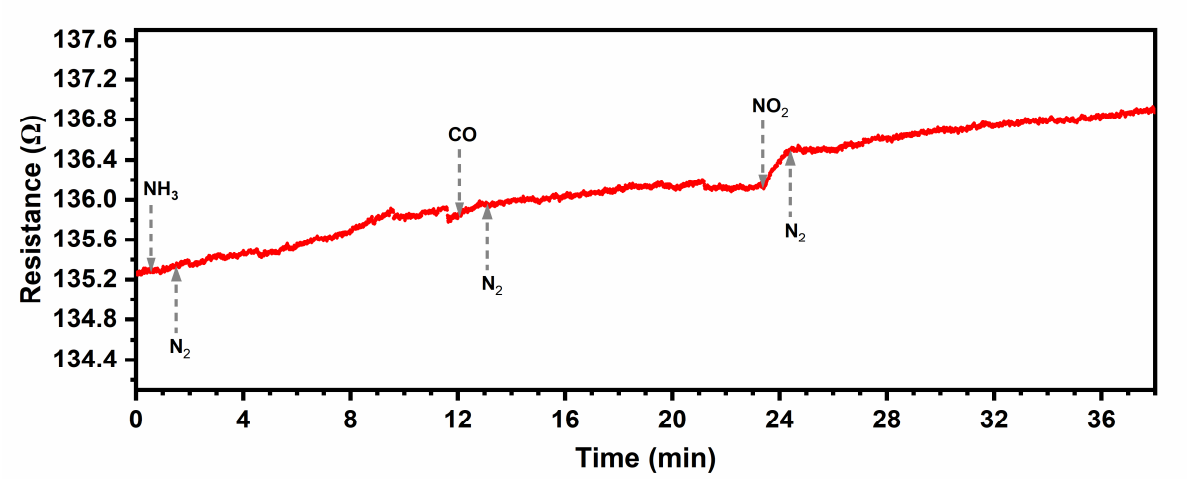



**Figure 7.6.** Sensing response to $NH_3$, CO, and $NO_2$ gases for the chemiresistors prepared using 300 µL of DBEDOT solution for spray coating. The sensor was exposed to 4ppm of the analytes for 1 min each, and it was recovered under pure $N_2$ flow for around 10 min between exposures. The test temperature is 23 ± 1 ℃ and the humidity is 1.88 ± 0.24 % RH.

### 7.3.3 Gas sensing

As electrical percolation can be achieved through the simplified ISSP process, various PEDOT-based chemiresistors were prepared using 80, 90, and 300 µL of DBEDOT solution for spray coating. To commence the exploration, the sensor prepared using 300 µL was selected to evaluate the gas sensing capabilities of PEDOT via ISSP. The sensor was placed in our sensor testing chamber under $N_2$ flow and 1.0 V was applied across the IDEs. The sensor was then exposed to 4 ppm of different analyte gases diluted with $N_2$ for 1 min each, and these analytes include ammonia ($NH_3$), nitrogen dioxide ($NO_2$), and carbon monoxide (CO). Following each exposure, the sensor was purged with nitrogen ($N_2$) for around 10 min. The resulting changes in resistance were recorded during sensing experiments. As shown in Figure

7.6, unfortunately, PEDOT via ISSP shows no discernible responses to either $NH_3$ or CO. Only an irreversible increase in resistance is observed during the exposure in $NO_2$. Due to the strong oxidising nature of $NO_2$, this irreversible response is attributed to the degradation of polymer chains caused by over-oxidation. Although the results are not desirable, Figure 7.6 demonstrates that PEDOT via ISSP may hold potential as the sensing material for chemiresistors.

Further exploration in this section focuses on the $NO_2$ sensing capability of PEDOT owing to its detectable response to this analyte (Figure 7.6). Encouragingly, previous efforts in our research group have demonstrated that a reversible PEDOT-based chemiresistor for $NO_2$ detection can be achieved through electrochemical re-doping,[32] bolstering the feasibility of this exploration. In this previous work, the electrochemical characteristics of PEDOT prepared via chronoamperometry was studied using cyclic voltammetry (CV). Then, desirable reversibility was obtained by electrochemically re-doping PEDOT at the potential of the initial anodic peak following the onset of oxidation. Beyond this peak, the sensor reversibility decreased with the increase of the re-doping potential due to higher possibilities of over-oxidation. Following a similar methodology to this previous work, the further study in this section commenced with a CV test to determine a re-doping potential. As shown in Figure 7.7, the initial anodic peak following the onset of oxidation is observed at +0.3 V, and this potential was used for the re-doping process in this section. After the de-doping process at –1.0 V for 2 min, PEDOT in each sensor was re-doped at +0.3 V for 2 min. Subsequently, sensing experiments were conducted to explore the $NO_2$ sensing capabilities of the re-doped PEDOT. Sensors with re-doped PEDOT were placed in our sensor testing chamber under $N_2$ flow and 1.0 V was applied across the IDEs. These sensors were then exposed to 4 ppm of $NO_2$ diluted with $N_2$, and the resulting changes in resistance were recorded as shown in Figure 7.8.

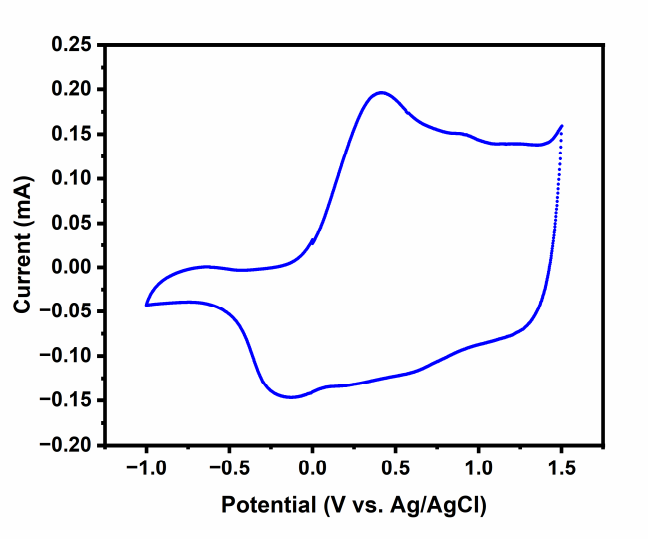



**Figure 7.7.** Cyclic voltammogram of PEDOT via ISSP on the Pt IDEs in 0.1 M $LiClO_4$/ $CH_3CN$, recorded at the scan rate of 100 mV $s^{-1}$ vs Ag/AgCl electrode.

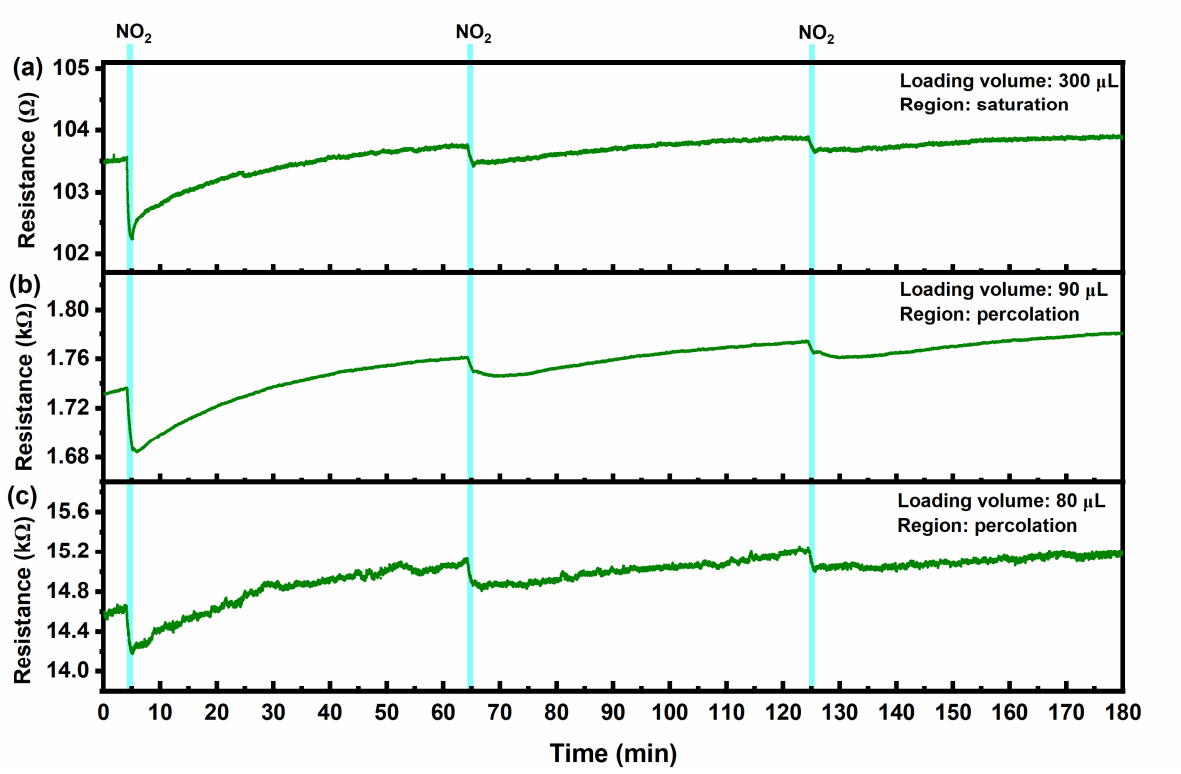



**Figure 7.8.** Sensing response to $NO_2$ gas for the chemiresistors with re-doped PEDOT prepared using (a) 300, (b) 90, and (c) 80 µL of DBEDOT solution for spray coating. The loading volume for spray coating and the region where the sensor was obtained are presented in the upper right corner of each figure. All sensors were exposed 3 times to 4 ppm of $NO_2$ in $N_2$ for 1 min each, with a 59 minute recovery time under pure $N_2$ flow between exposures. The test temperature is 23 ± 2 °C and the humidity is 1.93 ± 0.19 % RH.

As shown in Figure 7.8, the resistances of the sensors decrease during the exposure to $NO_2$ gas, following the sensing mechanism elucidated in Section 6.3.2 (Scheme 6.1). The electron-withdrawing $NO_2$ molecules act as dopants for the p-doped PEDOT. When the PEDOT interacts with $NO_2$ molecules, some neutral segments of the polymer chains are oxidised to their p-doped form, leading to an increase in the number of charge carriers in the p-doped PEDOT. Although the over-oxidation during the exposure to $NO_2$ can be avoided through electrochemical re-doping, it is important to acknowledge the poor repeatability of the sensing responses observed in Figure 7.8. Specifically, the responses to 4ppm $NO_2$ experience decay over three cycles of exposure for all the sensors in this section. This phenomenon was observed in the previous work on PEDOT prepared by electrochemical polymerisation as well,[32] which is still an open question requiring further investigations.

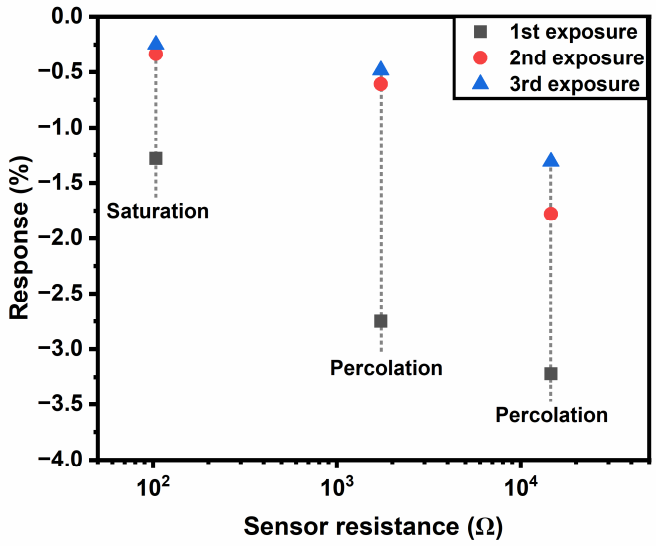



**Figure 7.9.** Sensor responses ($\Delta R/R_0 \times 100$ %) to 4 ppm $NO_2$ for the sensors investigated. The dashed lines connect the responses obtained from three cycles of exposure with the regions where the sensors were prepared.

Sensor responses for the sensors investigated in Figure 7.8 were calculated as the percentage changes relative to the starting resistances ($\Delta R/R_0 \times 100$ %). As shown in Figure 7.9, all the

sensor exhibit negative responses to 4 ppm $NO_2$ owing to the decrease in resistance during exposure. Over the three cycles of exposure, each sensor shows the decay in the sensor response to the same concentration of $NO_2$, especially between the first and the second cycles. Despite this unfavourable repeatability, it should be noted that an improving trend in the sensor response with an increase in sensor resistance can be observed when analysing the responses obtained from the same cycles of exposure. This finding demonstrates that the sensor response of re-doped PEDOT prepared via ISSP can be improved in the percolation region. Compared with the saturation region, fewer PEDOT stripes and clusters are obtained in the percolation region. This possibly allows each PEDOT pathway to consume more $NO_2$ molecules under the same exposure conditions, resulting in larger changes in conductivity.

To extend the scope of this section, the sensors with the re-doped PEDOT prepared in the percolation region were reproduced and then exposed to 4 ppm $NH_3$ and CO gases for 1 min each. With no discernible responses to these two analytes, the percolation sensors exhibited ideal selectivity to $NO_2$ gas. Furthermore, their sensor resistances were not influenced by changes in flow rate up to 800 sccm, and it has been reported that PEDOT via ISSP exhibits a limited temperature dependence of the conductivity above room temperature.[53] These observations collectively indicate that this material would not be suitable for multifunctional sensing. On a positive side, however, employing this materials should hold promise to mitigate the interference of flow and temperature during gas sensing.

## 7.4 Conclusion and outlook

In this chapter, PEDOT was prepared through the ISSP processes of the DBEDOT deposited on the Pt IDE substrates via spray coating. During the ISSP process coupled with in situ conductance monitoring, electrical percolation was observed and the percolation threshold was found to depend on the reaction temperature. However, it is still challenging to obtain samples

at different stages before the completion of this ISSP process. Encouragingly, electrical percolation based on PEDOT was also achieved after a simplified ISSP process without monitoring. In this approach, varying quantities of PEDOT on the substrates were obtained using different loading volumes of the DBEDOT solution for spray coating. The morphological study on the samples through this simplified process was further carried out, showing consistent observations with the conductance trend. However, puzzling issues of the departure and re-deposition of monomers were unveiled at the same time. Subsequently, PEDOT-based chemiresistors were prepared through the simplified ISSP process. Among the analyte gases studied in this chapter, PEDOT via ISSP only exhibited an irreversible response to $NO_2$ due to over-oxidation. To overcome this issue, PEDOT deposited on the substrate was further treated through an electrochemical re-doping process. The sensor response of re-doped PEDOT prepared via ISSP can be improved in the percolation region

This chapter has unveiled both the opportunities and the challenges in the investigation on electrical percolation via ISSP. It is surprising to observe the electrical percolation behaviour during the ISSP process. The in situ conductance monitoring technique should work for the ISSP of other monomers as well. To comprehensively understand the electrical percolation during ISSP, moreover, more influencing factors should be explored in the future, such as other reaction temperatures, applied potentials across the IDEs, and gap widths of the substrate. However, recent experiments have shown limitations in the existing setup for monitoring the ISSP process, particularly in sustaining long-term experiments beyond 60 °C. This poses uncertainties and underscores the immediate need to develop a sustainable and reliable monitoring setup for ISSP. On the other hand, future investigations on the simplified ISSP process can explore alternative deposition methods to enhance sample reproducibility. However, these efforts would be challenged by the issues arising from the departure and re-deposition of monomers discussed in this chapter. To address these issues, efforts should be

made to develop a more controllable ISSP process for DBEDOT and alternative monomers with improved stability could be considered. In terms of gas sensing, lastly, systematic investigations are still required for a comprehensive understanding of the impacts of re-doping on sensing performance.

# Chapter 8

# Summary and perspective

Chemical sensors play a pivotal role in various fields, spanning from household and industrial safety to systematic monitoring of processes and environments. Among diverse sensor configurations utilising various sensing materials, chemiresistors based on conjugated polymers (CPs) have emerged as one of the most promising options for the future of chemical sensors. Encouragingly, recent research has demonstrated that electrical percolation holds significant promise for enhancing the sensing performance of CP-based chemiresistors. However, challenges and gaps persist in the development of these percolation sensors. Following a brief summary of these issues, this chapter summarises the four solutions developed in this thesis to address corresponding issues. These solutions include in situ current-controlled solution, nanosphere templating solution, multifunctional nanocomposite solution, and in situ solid-state polymerisation solution. As these solutions have revealed both opportunities and questions, this chapter then discusses the research crossroads with various potential directions for future work following this thesis.

## 8.1 Issues and potential solutions

CP-based percolation chemiresistors hold significant promise for high-performance chemical detection. However, as discussed and summarised in Chapter 2, challenges and gaps persist in the development of these sensors. Firstly, it is challenging to achieve desirable device-to-device reproducibility during electropolymerisation, even though this method can effectively form percolation networks between electrodes. Additionally, when applying this electrochemical method, only a few studies have focused on the morphology of the resulting percolation networks and its effects on sensing performance. Although preparing CP-based composites is also a well-established approach to achieve electrical percolation, previous studies have lacked systematic investigations into the effects of percolation on chemical sensing performance and the exploration of the multifunctionality of these percolation materials. Lastly, there is still a need to explore other methods for the simple preparation of CP-based percolation networks on substrates. To address these issues, this thesis has proposed the following solutions:

***In situ current-controlled solution.*** In Chapter 4, an in situ conductance technique has been used during the electrochemical growth of PPy-based percolation networks. This technique can measure the drain current ($i_d$) across IDEs to determine the conductance of the PPy network during electrochemical polymerisation, allowing the percolation region to be identified. To improve the reproducibility of PPy percolation networks, an in situ current-controlled method based on the value of $i_d$ has been developed. A set of optimal $NH_3$ percolation sensors have been created using this method, showing low coefficients of variation in both their sensor responses and sensitivities. These results in Chapter 4 have demonstrated that the in situ current-controlled method is a promising solution to overcome the poor device-to-device reproducibility for percolation chemiresistors prepared by electropolymerisation. Instead of the

conventional idea based on time, this in situ current-controlled solution provides an effective way to control the preparation processes during electropolymerisation.

***Nanosphere templating solution.*** In Chapter 5, nanostructured PPy chemiresistors for $NH_3$ detection have been created using a nanosphere template. PS nanospheres are deposited to form a template between IDEs, and chronoamperometry is used to grow PPy between the electrodes within the gaps of the nanospheres. The growth of PPy is controlled to create electrical percolation networks. After the removal of the nanospheres, chemiresistive sensors with nanostructured PPy have been obtained. The nanostructured percolation sensors have shown higher sensitivities and lower LODs to $NH_3$ than percolation networks prepared without nanosphere templates, demonstrating that the nanosphere templating solution can further improve the sensitivity of percolation networks. The optimal nanostructured percolation sensor in this chapter has shown competitive performance relative to other PPy-based $NH_3$ sensors, further proving the value of this solution. In summary, this solution has filled the gap in controlling the morphology of percolation networks and deepen the understanding of the relationship between the morphology and sensing performance for percolation sensors.

***Multifunctional nanocomposite solution.*** Preparing composites with conductive fillers is a mainstream way to achieve electrical percolation, although only a few studies have employed it in CP-based percolation chemiresistors. To facilitate the understanding of electrical percolation in CP-based composite chemiresistors and the multifunctionality of these sensors, Chapter 6 focuses on chemiresistors based on PEDOT/PS nanocomposites. The nanocomposites have been created by combining PEDOT nanoparticles with PS nanospheres through solution blending, and CP-based chemiresistors with varying PEDOT filler fractions have then been fabricated using the DEISA technique. After observing the electrical percolation behaviour within these nanocomposites, this chapter has systematically studied their multifunctional sensing capabilities to $NO_2$, temperature, and airflow rate. The percolation

sensors in this chapter have shown competitive performance to reported ones in both $NO_2$ and temperature sensing. This nanocomposite solution has provided valuable insights into the development of CP-based percolation sensors.

***In situ solid-state polymerisation solution.*** To diversify the preparation method for electrical percolation, Chapter 8 has investigated the possibility of achieving electrical percolation based on PEDOT through in situ solid-state polymerisation (ISSP). In this exploration, monomers for ISSP are deposited on the IDE substrates via spray coating. Electrical percolation can be observed both during an ISSP process coupled with an in situ conductance monitoring technique and after a simplified ISSP process without monitoring. Furthermore, PEDOT prepared through the simplified process has exhibited sensitivity to $NO_2$. Then, an electrochemical re-doping process is used to overcome the over-oxidation of PEDOT induced by $NO_2$ during sensing exposure. The sensing response of re-doped PEDOT can be improved via electrical percolation. This ISSP solution has shown a novel way to achieve electrical percolation on IDEs, bringing more opportunities in electrical percolation and percolation sensors.

Encouragingly, these solutions should also work for other sensing materials and substrates. For instance, the in situ current-controlled and the nanosphere templating solutions can be employed in the electrochemical preparation of metal-organic frameworks. Additionally, depositing nanocomposites on plastic films can enable the creation of flexible multifunctional sensors. However, it is still necessary to state that each solution in this thesis has its limitations, which have been discussed in each corresponding chapter.

## 8.2 Research crossroads and future work

Before giving suggestions to the future work on CP-based percolation chemiresistors, it is crucial to figure out which direction these suggestions would focus on. Obviously, this thesis

has presented both opportunities and questions, which have led to various potential research directions. These directions intersect and diverge, forming research crossroads (Figure 8.1) that require decision-making for future research plans.

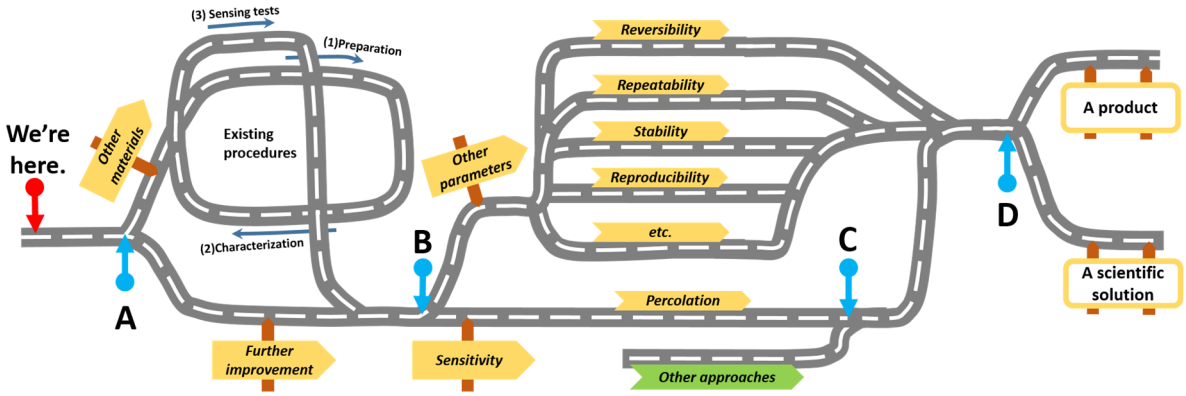



**Figure 8.1.** Schematic representation of directions and crossroads in the development of CP-based percolation chemiresistors. Crossroads A presents two optional directions for future work: conducting more studies based on other materials and further investigating improvements in previous work. Crossroads B indicates that future work could focus on either sensitivity or other sensing parameters for percolation sensors. To enhance sensitivity, other research strategies would merge with the percolation strategy at crossroads C. Finally, crossroads D outlines two research goals for future work: developing a product beyond academia and providing a scientific solution within academia.

The first step before embarking on further investigations is to establish clear goals. CP-based percolation chemiresistors in this thesis have shown some possibilities in application areas of safety and healthcare. Thus, one goal of further studies can be to bridge the gap between scientific research and a product. In addition to potential applications, this thesis has also raised new scientific questions, such as limited reversibility and repeatability in percolation chemiresistors. As another goal of further studies, addressing these issues can not only deepen our understanding of the sensing behaviours of electrical percolation networks but also contribute to the development of competitive products beyond academia. It should be noted

that these aforementioned goals determine the final achievement after the last crossroads of the further investigations on percolation sensors (crossroads D in Figure 8.1).

As shown in Figure 8.1, it is normal to encounter the first crossroads (A) showing different optional approaches to achieve a research goal. As mentioned in Section 8.1, solutions provided in this thesis should work for other materials. Thus, further investigations on other sensing materials and substrates will be carried out in the future, giving a more informative and comprehensive insight into percolation materials and sensors. For instance, more series of CPs and their nanocomposites will be prepared for the detection of ammonia and nitrogen dioxide gases. Beyond these scientific solutions for a more diverse range of analytes, furthermore, solution-processable nanocomposites will be deposited on commercial substrates to explore their opportunities in miniature sensor products with low cost and power consumption. These studies will follow an existing research procedure, including material and sensor preparation, material characterisation, and sensing tests.

Crossroads A also present another natural step for future work, focusing on further enhancing the sensing performance of the studied percolation sensors. This step is also applicable after the aforementioned studies involving other sensing materials and substrates. Then, at crossroads B, another decision must be made to determine which parameter of sensing performance to focus on. From a scientific perspective, efforts should continue to improve the sensitivity of CP-based chemiresistors. Sensitivity has always been the primary goal in most relevant studies, but only a few have achieved sensitivity levels comparable to animals at the ppt level. According to both recent publications and this thesis, CP-based percolation chemiresistors can currently only detect trace analytes at concentrations in the tens of ppb. Seemingly, these results are approaching an upper limit of the influence of electrical percolation. At crossroads C in Figure 8.1, therefore, the concept of electrical percolation should be combined with other approaches to achieve high-performance chemiresistors.

Encouragingly, Chapter 5 has already shown the feasibility of nanostructuring CP-based percolation pathways via a template. Therefore, further investigations based various templates will be conducted to finely tune the nanoscale morphologies of CPs for percolation chemiresistors. Furthermore, another strategy involving composite materials will be integrated into the percolation approach in future work. This strategy will entail the combination of CPs with metals (M) and their oxides (MO). Subsequently, electrical percolation networks based on these CP/M or CP/MO composites will be developed for ultra-sensitive detection of specific analytes. Beyond scientific solutions, it is worth noting that these future studies on ultra-sensitivity may also help explore more potential application areas for percolation chemiresistors in the sensor market.

Crossroads B also reveals other significant directions in the development of CP-based percolation chemiresistors. These directions involve the improvement of other parameters, such as reversibility, repeatability, stability, and device-to-device reproducibility. Undoubtedly, it is still necessary to systematically and comprehensively figure out the influencing factors for these parameters. These efforts will not only deepen our understanding of the sensing and recovery processes but also bring us closer to the realisation of a market-ready product. Future work will involve repeating some experiments conducted in this thesis and then delving deeper into the sensing reversibility and repeatability. During this investigation, potential factors will be considered, such as film thickness, the test environment, and the electrochemical properties of CPs. This work will contribute to the future studies involving a potential product based on commercial substrates, as achieving desirable reversibility and repeatability is one of the most fundamental requirements for a product.

Although future work will mainly focus on gas detection using CP-based percolation sensors, sensors for other stimuli will also be developed. For example, the temperature sensing capability of nanocomposite-based percolation sensors will also be further evaluated in future

studies. This is because the nanocomposites developed in Chapter 6 have shown a linear detection range covering human body temperatures, creating opportunities in healthcare. To more comprehensively understand CP-based percolation materials in temperature sensing, future work can investigate additional parameters of sensing performance, such as response and recovery time, reproducibility, and stability.

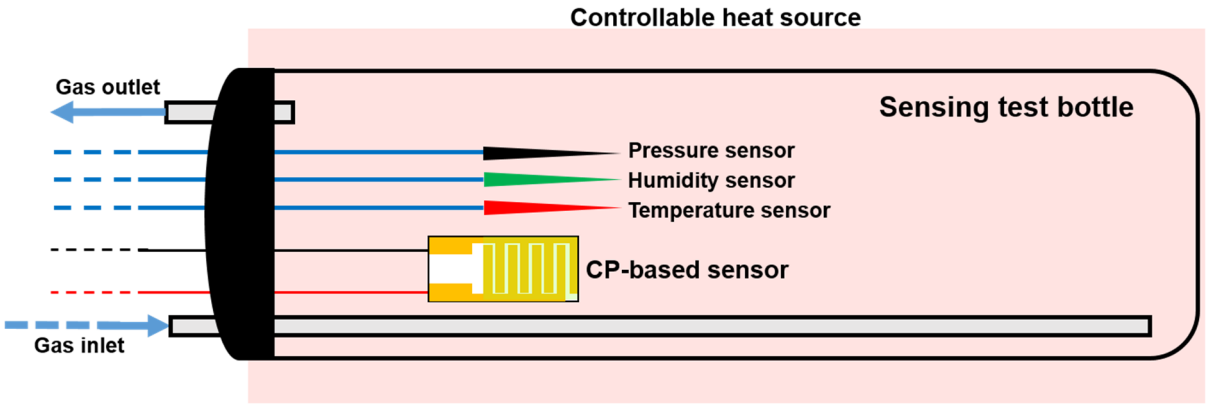



**Figure 8.2.** Schematic layout of a sensing test bottle potentially used in future studies following this thesis. The conjugated polymer (CP) based sensor is placed in the sensing test bottle. Basic parameters of the test environment, including temperature, relative humidity, and air pressure, are monitored using commercial temperature, humidity, and pressure sensors positioned adjacent to the CP-based sensor. The test temperature is regulated by a controllable heat source that fully encompasses the bottle. This sensing test bottle should be adaptable for both gas and temperature sensing tests.

Last but most significantly, efforts should be made to systematically establish more reliable sensing test setups and reasonable testing standards before conducting future work as discussed above. Many studies on CP-based sensors, including this thesis, have demonstrated the temperature dependence of material conductivity. Therefore, potential factors that may influence the test temperature should be minimized as much as possible during the sensing tests. Temperature differences between gases and the test environment may impact the test

temperature, especially at the beginning of exposure and recovery when the type and flow rate of gases need to change. Fortunately, no obvious abrupt changes over 0.1 °C were observed when using the gas sensing setup in Figure 3.5, suggesting that the temperature in the sensing chamber dominates the test temperature. For long term tests, however, this setup suffers from a temperature fluctuation of around ± 2 °C due to the difference between the temperature surrounding the CP-based sensor and the room temperature. This issue arises from the design limitation of the setup used in this thesis. The heating element, controlled by our thermostat system, only heats the sample stage rather than the entire sensing chamber. To achieve a stable and controllable environment for sensing tests, our setup should be updated using a sensing test bottle covered with a controllable heat source such as an electric heating mat or a water bath system (Figure 8.2). The bottle temperature, which dominates the test temperature, can be determined and stabilised using a thermostat system connected with the temperature sensor in the bottle and the heat source. Given that relative humidity significantly affects sensing performances, furthermore, a humidity sensor must be introduced into the sensing test bottle. The relative humidity in the bottle can be determined via the component of the mixture gases controlled by the mass flow controllers. A pressure sensor should be introduced to monitor the air pressure of the test environment as well. While it may not be explicitly clear whether air pressure can affect the sensing performance of the CP-based sensors in this thesis, it is still necessary to record this basic parameter of the test environment. To avoid potential impacts from abrupt changes in flow rate, additionally, the tested sensor should be placed opposite to the head of the gas inlet tube. It should be noted that the potential design of the sensing test bottle (Figure 8.2) can be used for both gas and temperature sensing tests.

It is also crucial to establish general standards for sensing tests. Unfortunately, all the sensing studies presented in Chapter 2 have indicated a lack of universal standards in the field of CP-based sensors. It must be acknowledged that this thesis also has this limitation, as sensors were

tested under varying conditions, such as different temperatures and exposure times. Although internal comparisons can be made within the same chapter, barriers exist when attempting to compare one chapter to another due to the absence of testing standards, limiting a more comprehensive understanding of the sensors prepared in this thesis. Therefore, reasonable standards should be designed before conducting future work. Primarily, the most fundamental requirement for designing these standards is to specify as many basic parameters for the tests as possible, including temperature, air pressure, relative humidity, flow rate, and applied potential. A stable and controllable sensing test setup, as illustrated in Figure 8.2, is the cornerstone for obtaining reliable information on these parameters. Instead of vague ranges, these basic parameters should be presented as either specific values or clear ranges, as some of them may influence the sensing performance. For instance, a specific value of the test temperature is preferable to a vague description such as "room temperature". Although achieving identical test conditions may be challenging in the field of CP-based sensors, efforts should be made to standardise them within our research group. It is recommended that general tests for both gas and temperature sensing should be conducted at 101.3 kPa and below 2 % RH. For gas sensing, the total flow rate is still set at 500 sccm, and the test temperature should be 25 °C. Then, parameters of sensing test processes would be better standardised as well. A reasonable baseline should be determined only after all the basic parameters of the test environment and the sensor resistance become stable. To quantify acceptable stability, upper limits of coefficient of variation values for these parameters should be further clarified in future work. Concerning exposure and recovery, theoretically, one exposure period should end after the sensor resistance reaches a steady state, while one recovery period should end after the resistance returns to the baseline. As some sensors may exhibit poor reversibility in practical experiments, their recovery periods should end after their resistances reach steady states. Additionally, a minimum sample size for generating valid values of standard deviation should

be suggested when evaluating device-to-device reproducibility. To enhance the understanding of the variation in both sensor resistance and performance, future investigations on reproducibility should involve a larger sample size rather than three or four samples in this thesis. An ideal approach would be to work with at least 30 separate samples via the same conditions.

# References

(1) Lefferts, M. J.; Castell, M. R. Vapour sensing of explosive materials. *Analytical Methods* **2015**, *7*, 9005-9017.

(2) Potyrailo, R. A. Multivariable Sensors for Ubiquitous Monitoring of Gases in the Era of Internet of Things and Industrial Internet. *Chemical Reviews* **2016**, *116*, 11877-11923.

(3) Walker, D. B.; Walker, J. C.; Cavnar, P. J.; Taylor, J. L.; Pickel, D. H.; Hall, S. B.; Suarez, J. C. Naturalistic quantification of canine olfactory sensitivity. *Applied Animal Behaviour Science* **2006**, *97*, 241-254.

(4) Elstein, D. Training Dogs To Smell Off-Flavor in Catfish. *Agricultural Research* **2004**, *52*, 10-11.

(5) Shaw, J. A.; Seldomridge, N. L.; Dunkle, D. L.; Nugent, P. W.; Spangler, L. H.; Bromenshenk, J. J.; Henderson, C. B.; Churnside, J. H.; Wilson, J. J. Polarization lidar measurements of honey bees in flight for locating land mines. *Optics Express* **2005**, *13*, 5853-5863.

(6) King, T. L.; Horine, F. M.; Daly, K. C.; Smith, B. H. Explosives detection with hard-wired moths. *IEEE Transactions on Instrumentation and Measurement* **2004**, *53*, 1113-1118.

(7) Otto, J.; Brown, M. F.; Long, W. Training rats to search and alert on contraband odors. *Applied Animal Behaviour Science* **2002**, *77*, 217-232.

(8) Furton, K. G.; Myers, L. J. The scientific foundation and efficacy of the use of canines as chemical detectors for explosives. *Talanta* **2001**, *54*, 487-500.

(9) Moore, D. S. Instrumentation for trace detection of high explosives. *Review of Scientific Instruments* **2004**, *75*, 2499-2512.

(10) March, R. E. An Introduction to Quadrupole Ion Trap Mass Spectrometry. *Journal of Mass Spectrometry* **1997**, *32*, 351-369.

(11) Kalantar-zadeh, K.: Introduction. In *Sensors*; Springer US: Boston, MA, 2013; pp 1-9.

(12) Mukhopadhyay, S. C.: Wireless Sensors and Sensors Network. In *Intelligent Sensing, Instrumentation and Measurements*; Smart Sensors, Measurement and Instrumentation; Springer Berlin Heidelberg: Berlin, Heidelberg, 2013; pp 55-69.

(13) Harraz, F. A. Porous silicon chemical sensors and biosensors: A review. *Sensors and Actuators B: Chemical* **2014**, *202*, 897-912.

(14) Dey, A. Semiconductor metal oxide gas sensors: A review. *Materials Science and Engineering B-Advanced Functional Solid-State Materials* **2018**, *229*, 206-217.

(15) Bai, H.; Shi, G. Gas sensors based on conducting polymers. *Sensors* **2007**, *7*, 267-307.

(16) Hughes, G.; Westmacott, K.; Honeychurch, K. C.; Crew, A.; Pemberton, R. M.; Hart, J. P. Recent advances in the fabrication and application of screen-printed electrochemical (bio) sensors based on carbon materials for biomedical, agri-food and environmental analyses. *Biosensors* **2016**, *6*, 50.

(17) Shirakawa, H.; Louis, E. J.; Macdiarmid, A. G.; Chiang, C. K.; Heeger, A. J. Synthesis of Electrically Conducting Organic Polymers - Halogen Derivatives of Polyacetylene, (Ch)X. *Journal of the Chemical Society-Chemical Communications* **1977**, 578-580.

(18) Yoshino, K.; Kaneto, K.; Takeda, S. Applications of conducting polymers as electronics and opto-electronics devices. *Synthetic Metals* **1987**, *18*, 741-746.

(19) Forrest, S. R. The path to ubiquitous and low-cost organic electronic appliances on plastic. *Nature* **2004**, *428*, 911-918.

(20) Jankus, V.; Aydemir, M.; Dias, F. B.; Monkman, A. P. Generating Light from Upper Excited Triplet States: A Contribution to the Indirect Singlet Yield of a Polymer OLED, Helping to Exceed the 25% Singlet Exciton Limit. *Advanced Science* **2016**, *3*, 1500221.

(21) Wang, C.; Dong, H.; Hu, W.; Liu, Y.; Zhu, D. Semiconducting pi-conjugated systems in field-effect transistors: a material odyssey of organic electronics. *Chemical Reviews* **2012**, *112*, 2208-2267.

(22) Dou, L.; You, J.; Hong, Z.; Xu, Z.; Li, G.; Street, R. A.; Yang, Y. 25th anniversary article: a decade of organic/polymeric photovoltaic research. *Advanced Materials* **2013**, *25*, 6642-6671.

(23) Li, W. S.; Guo, Y. T.; Shi, J. J.; Yu, H. T.; Meng, H. Solution-Processable Neutral Green Electrochromic Polymer Containing Thieno[3,2-b]thiophene Derivative as Unconventional Donor Units. *Macromolecules* **2016**, *49*, 7211-7219.

(24) Li, W.; Guo, Y.; Wang, Y.; Xing, X.; Chen, X.; Ning, J.; Yu, H.; Shi, Y.; Murtaza, I.; Meng, H. A “chain–lock” strategy to construct a conjugated copolymer network for supercapacitor applications. *Journal of Materials Chemistry A* **2019**, *7*, 116-123.

(25) Wong, Y. C.; Ang, B. C.; Haseeb, A.; Baharuddin, A. A.; Wong, Y. H. Conducting Polymers as Chemiresistive Gas Sensing Materials: A Review. *Journal of the Electrochemical Society* **2019**, *167*, 037503.

(26) Lange, U.; Mirsky, V. M. Chemiresistors based on conducting polymers: A review on measurement techniques. *Analytica Chimica Acta* **2011**, *687*, 105-113.

(27) Mkhize, N.; Murugappan, K.; Castell, M. R.; Bhaskaran, H. Electrohydrodynamic jet printed conducting polymer for enhanced chemiresistive gas sensors. *Journal of Materials Chemistry C* **2021**, *9*, 4591-4596.

(28) Sauerwald, T.; Russ, S.: Percolation Effects in Metal Oxide Gas Sensors and Related Systems. In *Gas Sensing Fundamentals*; Kohl, C.-D., Wagner, T., Eds.; Springer Series on Chemical Sensors and Biosensors; Springer Berlin Heidelberg: Berlin, Heidelberg, 2014; pp 247-278.

(29) Hu, L.; Hecht, D.; Grüner, G. Percolation in transparent and conducting carbon nanotube networks. *Nano Letters* **2004**, *4*, 2513-2517.

(30) Gao, J.; Wang, H.; Huang, X.; Hu, M.; Xue, H.; Li, R. K. Y. Electrically conductive polymer nanofiber composite with an ultralow percolation threshold for chemical vapour sensing. *Composites Science and Technology* **2018**, *161*, 135-142.

(31) Armitage, B. I.; Murugappan, K.; Lefferts, M. J.; Cowsik, A.; Castell, M. R. Conducting polymer percolation gas sensor on a flexible substrate. *Journal of Materials Chemistry C* **2020**, *8*, 12669-12676.

(32) Lefferts, M. J.; Armitage, B. I.; Murugappan, K.; Castell, M. R. PEDOT percolation networks for reversible chemiresistive sensing of $NO_2$. *RSC Advances* **2021**, *11*, 22789-22797.

(33) Lefferts, M. J.; Humphreys, L. H.; Mai, N.; Murugappan, K.; Armitage, B. I.; Pons, J.-F.; Castell, M. R. ANFO vapour detection with conducting polymer percolation network sensors and GC/MS. *Analyst* **2021**, *146*, 2186-2193.

(34) Lefferts, M. J.; Murugappan, K.; Wu, C.; Castell, M. R. Electrical percolation through a discontinuous Au nanoparticle film. *Applied Physics Letters* **2018**, *112*, 251602.

(35) Murugappan, K.; Castell, M. R. Bridging electrode gaps with conducting polymers around the electrical percolation threshold. *Electrochemistry Communications* **2018**, *87*, 40-43.

(36) Lefferts, M. J.; Castell, M. R. Influence of soil type on chemiresistive detection of buried ANFO. *Forensic Chemistry* **2022**, *27*, 100401.

(37) MacDiarmid, A. G. "Synthetic metals": A novel role for organic polymers (Nobel lecture). *Angewandte Chemie International Edition* **2001**, *40*, 2581-2590.

(38) Zozoulenko, I.; Singh, A.; Singh, S. K.; Gueskine, V.; Crispin, X.; Berggren, M. Polarons, Bipolarons, And Absorption Spectroscopy of PEDOT. *ACS Applied Polymer Materials* **2019**, *1*, 83-94.

(39) Dhanker, R.; Gray, C. L.; Mukhopadhyay, S.; Nunez, S.; Cheng, C.-Y.; Sokolov, A. N.; Giebink, N. C. Large bipolaron density at organic semiconductor/electrode interfaces. *Nature communications* **2017**, *8*, 2252.

(40) Bredas, J. L.; Street, G. B. Polarons, bipolarons, and solitons in conducting polymers. *Accounts of Chemical Research* **1985**, *18*, 309-315.

(41) Nowak, M.; Rughooputh, S. D. D. V.; Hotta, S.; Heeger, A. J. Polarons and bipolarons on a conducting polymer in solution. *Macromolecules* **1987**, *20*, 965-968.

(42) Heinze, J.; Frontana-Uribe, B. A.; Ludwigs, S. Electrochemistry of conducting polymers--persistent models and new concepts. *Chemical Reviews* **2010**, *110*, 4724-4771.

(43) Sugiyasu, K.; Swager, T. M. Conducting-Polymer-Based Chemical Sensors: Transduction Mechanisms. *Bulletin of the Chemical Society of Japan* **2007**, *80*, 2074-2083.

(44) Loewe, R. S.; Ewbank, P. C.; Liu, J.; Zhai, L.; McCullough, R. D. Regioregular, Head-to-Tail Coupled Poly(3-alkylthiophenes) Made Easy by the GRIM Method: Investigation of the Reaction and the Origin of Regioselectivity. *Macromolecules* **2001**, *34*, 4324-4333.

(45) McCullough, R. D.; Lowe, R. D. Enhanced electrical conductivity in regioselectively synthesized poly(3-alkylthiophenes). *Journal of the Chemical Society, Chemical Communications* **1992**, 70-72.

(46) Wang, X. C.; Wang, K.; Wang, M. F. Synthesis of conjugated polymers via an exclusive direct-arylation coupling reaction: a facile and straightforward way to synthesize thiophene-flanked benzothiadiazole derivatives and their copolymers. *Polymer Chemistry* **2015**, *6*, 1846-1855.

(47) Kawabata, K.; Osaka, I.; Nakano, M.; Takemura, N.; Koganezawa, T.; Takimiya, K. Thienothiophene-2,5-Dione-Based Donor-Acceptor Polymers: Improved Synthesis and Influence of the Donor Units on Ambipolar Charge Transport Properties. *Advanced Electronic Materials* **2015**, *1*, 1500039.

(48) Zhang, J.; Parker, T. C.; Chen, W.; Williams, L.; Khrustalev, V. N.; Jucov, E. V.; Barlow, S.; Timofeeva, T. V.; Marder, S. R. C–H-Activated Direct Arylation of Strong Benzothiadiazole and Quinoxaline-Based Electron Acceptors. *The Journal of Organic Chemistry* **2016**, *81*, 360-370.

(49) Shi, Y.; Mai, C.-K.; Fronk, S. L.; Chen, Y.; Bazan, G. C. Optical Properties of Benzotriazole-Based Conjugated Polyelectrolytes. *Macromolecules* **2016**, *49*, 6343-6349.

(50) Burke, D. J.; Lipomi, D. J. Green chemistry for organic solar cells. *Energy & Environmental Science* **2013**, *6*, 2053-2066.

(51) Ly, A.; Luo, Y.; Cavaillès, G.; Olivier, M.-G.; Debliquy, M.; Lahem, D. Ammonia Sensor Based on Vapor Phase Polymerized Polypyrrole. *Chemosensors* **2020**, *8*, 38.

(52) Majumdar, S.; Sarmah, K.; Mahanta, D. A Simple Route to Prepare Polypyrrole-Coated Filter Papers via Vapor Phase Polymerization and Their Gas Sensing Application. *ACS Applied Polymer Materials* **2020**, *2*, 1933-1942.

(53) Meng, H.; Perepichka, D. F.; Bendikov, M.; Wudl, F.; Pan, G. Z.; Yu, W.; Dong, W.; Brown, S. Solid-state synthesis of a conducting polythiophene via an unprecedented heterocyclic coupling reaction. *Journal of the American Chemical Society* **2003**, *125*, 15151-15162.

(54) Meng, H.; Perepichka, D. F.; Wudl, F. Facile solid-state synthesis of highly conducting poly(ethylenedioxythiophene). *Angewandte Chemie, International Edition in English* **2003**, *42*, 658-661.

(55) Zhang, L.; Meng, F.; Chen, Y.; Liu, J.; Sun, Y.; Luo, T.; Li, M.; Liu, J. A novel ammonia sensor based on high density, small diameter polypyrrole nanowire arrays. *Sensors and Actuators B: Chemical* **2009**, *142*, 204-209.

(56) Kwon, O. S.; Hong, J.-Y.; Park, S. J.; Jang, Y.; Jang, J. Resistive Gas Sensors Based on Precisely Size-Controlled Polypyrrole Nanoparticles: Effects of Particle Size and Deposition Method. *The Journal of Physical Chemistry C* **2010**, *114*, 18874-18879.

(57) She, C.; Li, G.; Zhang, W.; Xie, G.; Zhang, Y.; Li, L.; Yue, F.; Liu, S.; Jing, C.; Cheng, Y.; Chu, J. A flexible polypyrrole/silk-fiber ammonia sensor assisted by silica nanosphere template. *Sensors and Actuators A: Physical* **2021**, *317*, 112436.

(58) Ruangchuay, L.; Sirivat, A.; Schwank, J. Selective conductivity response of polypyrrole-based sensor on flammable chemicals. *Reactive and Functional Polymers* **2004**, *61*, 11-22.

(59) Choi, H. H.; Lee, J.; Dong, K.-Y.; Ju, B.-K.; Lee, W. Gas Sensing performance of composite materials using conducting polymer/single-walled carbon nanotubes. *Macromolecular Research* **2012**, *20*, 143-146.

(60) Kaliyaraj Selva Kumar, A.; Zhang, Y.; Li, D.; Compton, R. G. A mini-review: How reliable is the drop casting technique? *Electrochemistry Communications* **2020**, *121*, 106867.

(61) Schottland, P.; Bouguettaya, M.; Chevrot, C. Soluble polythiophene derivatives for $NO_2$ sensing applications. *Synthetic Metals* **1999**, *102*, 1325.

(62) Kim, K.-W.; Lee, S. B.; Kim, S. H.; Moon, H. C. Spray-coated transparent hybrid electrodes for high-performance electrochromic devices on plastic. *Organic Electronics* **2018**, *62*, 151-156.

(63) Liu, H.-S.; Chang, W.-C.; Chou, C.-Y.; Pan, B.-C.; Chou, Y.-S.; Liou, G.-S.; Liu, C.-L. Controllable Electrochromic Polyamide Film and Device Produced by Facile Ultrasonic Spray-coating. *Scientific Reports* **2017**, *7*, 11982.

(64) Prasad, G. K.; Radhakrishnan, T. P.; Kumar, D. S.; Krishna, M. G. Ammonia sensing characteristics of thin film based on polyelectrolyte templated polyaniline. *Sensors and Actuators B: Chemical* **2005**, *106*, 626-631.

(65) Liu, J.; Guo, T.-F.; Yang, Y. Effects of thermal annealing on the performance of polymer light emitting diodes. *Journal of Applied Physics* **2002**, *91*, 1595-1600.

(66) Li, G.; Yao, Y.; Yang, H.; Shrotriya, V.; Yang, G.; Yang, Y. "Solvent Annealing" Effect in Polymer Solar Cells Based on Poly(3-hexylthiophene) and Methanofullerenes. *Advanced Functional Materials* **2007**, *17*, 1636-1644.

(67) Hu, Z.; Zhang, J.; Xiong, S.; Zhao, Y. Performance of polymer solar cells fabricated by dip coating process. *Solar Energy Materials and Solar Cells* **2012**, *99*, 221-225.

(68) Glasser, A.; Cloutet, É.; Hadziioannou, G.; Kellay, H. Tuning the Rheology of Conducting Polymer Inks for Various Deposition Processes. *Chemistry of Materials* **2019**, *31*, 6936-6944.

(69) Griggs, S.; Marks, A.; Bristow, H.; McCulloch, I. n-Type organic semiconducting polymers: stability limitations, design considerations and applications. *Journal of Materials Chemistry C* **2021**, *9*, 8099-8128.

(70) Song, W.; Sun, J.; Wang, Q.; Wu, H.; Zheng, K.; Wang, B.; Wang, Z.; Long, X. n-Type boron β-diketone-containing conjugated polymers for high-performance room temperature ammonia sensors. *Materials Horizons* **2024**.

(71) Park, H.; Kim, D.-H.; Ma, B. S.; Shin, E.; Kim, Y.; Kim, T.-S.; Kim, F. S.; Kim, I.-D.; Kim, B. J. High-Performance, Flexible $NO_2$ Chemiresistors Achieved by Design of Imine-Incorporated n-Type Conjugated Polymers. *Advanced Science* **2022**, *9*, 2200270.

(72) Athawale, A. A.; Kulkarni, M. V. Polyaniline and its substituted derivatives as sensor for aliphatic alcohols. *Sensors and Actuators B: Chemical* **2000**, *67*, 173-177.

(73) Torsi, L.; Tanese, M. C.; Cioffi, N.; Gallazzi, M. C.; Sabbatini, L.; Zambonin, P. G. Alkoxy-substituted polyterthiophene thin-film-transistors as alcohol sensors. *Sensors and Actuators B: Chemical* **2004**, *98*, 204-207.

(74) Ruangchuay, L.; Sirivat, A.; Schwank, J. Polypyrrole/poly (methylmethacrylate) blend as selective sensor for acetone in lacquer. *Talanta* **2003**, *60*, 25-30.

(75) Ruangchuay, L.; Sirivat, A.; Schwank, J. Electrical conductivity response of polypyrrole to acetone vapor: effect of dopant anions and interaction mechanisms. *Synthetic Metals* **2004**, *140*, 15-21.

(76) Hangarter, C. M.; Chartuprayoon, N.; Hernández, S. C.; Choa, Y.; Myung, N. V. Hybridized conducting polymer chemiresistive nano-sensors. *Nano Today* **2013**, *8*, 39-55.

(77) Janata, J.; Josowicz, M. Conducting polymers in electronic chemical sensors. *Nat Mater* **2003**, *2*, 19-24.

(78) Hao, Q.; Kulikov, V.; Mirsky, V. M. Investigation of contact and bulk resistance of conducting polymers by simultaneous two- and four-point technique. *Sensors and Actuators B: Chemical* **2003**, *94*, 352-357.
(79) Stussi, E.; Stella, R.; De Rossi, D. Chemoresistive conducting polymer-based odour sensors: influence of thickness changes on their sensing properties. *Sensors and Actuators B: Chemical* **1997**, *43*, 180-185.
(80) Nishizawa, M.; Miwa, Y.; Matsue, T.; Uchida, I. Ultrathin polypyrrole formed at a twin-microband electrode in the presence of dodecylsulfate. *Journal of Electroanalytical Chemistry* **1994**, *371*, 273-275.
(81) Harris, P. D.; Arnold, W. M.; Andrews, M. K.; Partridge, A. C. Resistance characteristics of conducting polymer films used in gas sensors. *Sensors and Actuators B: Chemical* **1997**, *42*, 177-184.
(82) Lange, U.; Mirsky, V. M. Separated analysis of bulk and contact resistance of conducting polymers: Comparison of simultaneous two- and four-point measurements with impedance measurements. *Journal of Electroanalytical Chemistry* **2008**, *622*, 246-251.
(83) Meng, Z.; Stolz, R. M.; Mendecki, L.; Mirica, K. A. Electrically-Transduced Chemical Sensors Based on Two-Dimensional Nanomaterials. *Chemical Reviews* **2019**, *119*, 478-598.
(84) Dai, J.; Ogbeide, O.; Macadam, N.; Sun, Q.; Yu, W.; Li, Y.; Su, B.-L.; Hasan, T.; Huang, X.; Huang, W. Printed gas sensors. *Chemical Society Reviews* **2020**, *49*, 1756-1789.
(85) Vig, J. R.; Walls, F. L. A review of sensor sensitivity and stability. *Proceedings of the 2000 IEEE/EIA International Frequency Control Symposium and Exhibition* **2000**, 30-33.
(86) Pandey, S. Highly sensitive and selective chemiresistor gas/vapor sensors based on polyaniline nanocomposite: A comprehensive review. *Journal of Science: Advanced Materials and Devices* **2016**, *1*, 431-453.
(87) Yang, X.; Li, L. Polypyrrole nanofibers synthesized via reactive template approach and their $NH_3$ gas sensitivity. *Synthetic Metals* **2010**, *160*, 1365-1367.
(88) Sutar, D. S.; Padma, N.; Aswal, D. K.; Deshpande, S. K.; Gupta, S. K.; Yakhmi, J. V. Preparation of nanofibrous polyaniline films and their application as ammonia gas sensor. *Sensors and Actuators B: Chemical* **2007**, *128*, 286-292.
(89) Du, Z.; Li, C.; Li, L.; Yu, H.; Wang, Y.; Wang, T. Ammonia gas detection based on polyaniline nanofibers coated on interdigitated array electrodes. *Journal of Materials Science: Materials in Electronics* **2011**, *22*, 418-421.

(90) Chen, J.; Yang, J.; Yan, X.; Xue, Q. $NH_3$ and HCl sensing characteristics of polyaniline nanofibers deposited on commercial ceramic substrates using interfacial polymerization. *Synthetic Metals* **2010**, *160*, 2452-2458.

(91) Yoon, H.; Chang, M.; Jang, J. Sensing Behaviors of Polypyrrole Nanotubes Prepared in Reverse Microemulsions: Effects of Transducer Size and Transduction Mechanism. *The Journal of Physical Chemistry B* **2006**, *110*, 14074-14077.

(92) Chougule, M. A.; Pawar, S. G.; Patil, S. L.; Raut, B. T.; Godse, P. R.; Sen, S.; Patil, V. B. Polypyrrole Thin Film: Room Temperature Ammonia Gas Sensor. *IEEE Sensors Journal* **2011**, *11*, 2137-2141.

(93) Sharma, A. L.; Kumar, K.; Deep, A. Nanostructured polyaniline films on silicon for sensitive sensing of ammonia. *Sensors and Actuators A: Physical* **2013**, *198*, 107-112.

(94) Sengupta, P. P.; Adhikari, B. Influence of polymerization condition on the electrical conductivity and gas sensing properties of polyaniline. *Materials Science and Engineering: A* **2007**, *459*, 278-285.

(95) Su, P.-G.; Lee, C.-T.; Chou, C.-Y. Flexible $NH_3$ sensors fabricated by in situ self-assembly of polypyrrole. *Talanta* **2009**, *80*, 763-769.

(96) Tripathi, A.; Mishra, S. K.; Bahadur, I.; Shukla, R. K. Optical properties of regiorandom polythiophene/$Al_2O_3$ nanocomposites and their application to ammonia gas sensing. *Journal of Materials Science: Materials in Electronics* **2015**, *26*, 7421-7430.

(97) Jang, J.; Chang, M.; Yoon, H. Chemical Sensors Based on Highly Conductive Poly(3,4-ethylenedioxythiophene) Nanorods. *Advanced Materials* **2005**, *17*, 1616-1620.

(98) Navale, S. T.; Mane, A. T.; Chougule, M. A.; Sakhare, R. D.; Nalage, S. R.; Patil, V. B. Highly selective and sensitive room temperature $NO_2$ gas sensor based on polypyrrole thin films. *Synthetic Metals* **2014**, *189*, 94-99.

(99) Navale, S. T.; Chougule, M. A.; Patil, V. B.; Mane, A. T. Highly sensitive, reproducible, selective and stable CSA-polypyrrole $NO_2$ sensor. *Synthetic Metals* **2014**, *189*, 111-118.

(100) Kumar, R.; Singh, S.; Misra, A. Development of $NO_2$ gas sensor based on plasma polymerized nanostructure polyaniline thin film. *J. Miner. Mater. Charact. Eng* **2010**, *9*, 997-1006.

(101) Srinives, S.; Sarkar, T.; Mulchandani, A. Nanothin Polyaniline Film for Highly Sensitive Chemiresistive Gas Sensing. *Electroanalysis* **2013**, *25*, 1439-1445.

(102) Tiwari, A.; Kumar, R.; Prabaharan, M.; Pandey, R. R.; Kumari, P.; Chaturvedi, A.; Mishra, A. K. Nanofibrous polyaniline thin film prepared by plasma-induced polymerization technique for detection of $NO_2$ gas. *Polymers for Advanced Technologies* **2010**, *21*, 615-620.

(103) Navale, S. T.; Mane, A. T.; Khuspe, G. D.; Chougule, M. A.; Patil, V. B. Room temperature $NO_2$ sensing properties of polythiophene films. *Synthetic Metals* **2014**, *195*, 228-233.

(104) Kamble, D. B.; Sharma, A. K.; Yadav, J. B.; Patil, V. B.; Devan, R. S.; Jatratkar, A. A.; Yewale, M. A.; Ganbavle, V. V.; Pawar, S. D. Facile chemical bath deposition method for interconnected nanofibrous polythiophene thin films and their use for highly efficient room temperature $NO_2$ sensor application. *Sensors and Actuators B: Chemical* **2017**, *244*, 522-530.

(105) Shaik, M.; Rao, V. K.; Sinha, A. K.; Murthy, K. S. R. C.; Jain, R. Sensitive detection of nitrogen dioxide gas at room temperature using poly(3,4-ethylenedioxythiophene) nanotubes. *Journal of Environmental Chemical Engineering* **2015**, *3*, 1947-1952.

(106) Lin, C.-Y.; Chen, J.-G.; Hu, C.-W.; Tunney, J. J.; Ho, K.-C. Using a PEDOT:PSS modified electrode for detecting nitric oxide gas. *Sensors and Actuators B: Chemical* **2009**, *140*, 402-406.

(107) Jeon, S. S.; An, H. H.; Yoon, C. S.; Im, S. S. Synthesis of ultra-thin polypyrrole nanosheets for chemical sensor applications. *Polymer* **2011**, *52*, 652-657.

(108) Nerkar, D.; Jaware, S.; Padhye, G. Fabrication of a Novel Flexible Room Temperature Hydrogen Sulfide ($H_2S$) Gas Sensor based on Polypyrrole Films. *International Journal of Science and Research (IJSR)* **2016**, *5*, 106-111.

(109) Misra, S. C. K.; Mathur, P.; Srivastava, B. K. Vacuum-deposited nanocrystalline polyaniline thin film sensors for detection of carbon monoxide. *Sensors and Actuators A: Physical* **2004**, *114*, 30-35.

(110) Srinives, S.; Sarkar, T.; Hernandez, R.; Mulchandani, A. A miniature chemiresistor sensor for carbon dioxide. *Analytica Chimica Acta* **2015**, *874*, 54-58.

(111) Chaudhary, V.; Kaur, A. Solitary surfactant assisted morphology dependent chemiresistive polyaniline sensors for room temperature monitoring of low parts per million sulfur dioxide. *Polymer International* **2015**, *64*, 1475-1481.

(112) Mabrook, M. F.; Pearson, C.; Petty, M. C. Inkjet-printed polypyrrole thin films for vapour sensing. *Sensors and Actuators B: Chemical* **2006**, *115*, 547-551.

(113) Ramesh Kumar, M.; Ryman, S.; Tareq, O.; Buchanan, D. A.; Freund, M. S. Chemical diversity in electrochemically deposited conducting polymer-based sensor arrays. *Sensors and Actuators B: Chemical* **2014**, *202*, 600-608.

(114) Iyogun, A. A.; Kumar, M. R.; Freund, M. S. Chemically diverse sensor arrays based on electrochemically copolymerized pyrrole and styrene derivatives. *Sensors and Actuators B: Chemical* **2015**, *215*, 510-517.

(115) Iyogun, A. A.; Buchanan, D. A.; Freund, M. S. Analyte discrimination with chemically diverse sensor array based on electrocopolymerized pyrrole and vinyl derivatives. *RSC Advances* **2016**, *6*, 32549-32559.

(116) Phasuksom, K.; Prissanaroon-Ouajai, W.; Sirivat, A. Electrical conductivity response of methanol sensor based on conductive polyindole. *Sensors and Actuators B: Chemical* **2018**, *262*, 1013-1023.

(117) Jiang, Y.; Tang, N.; Zhou, C.; Han, Z.; Qu, H.; Duan, X. A chemiresistive sensor array from conductive polymer nanowires fabricated by nanoscale soft lithography. *Nanoscale* **2018**, *10*, 20578-20586.

(118) Pavluchenko, A. S.; Mamykin, A. V.; Kukla, A. L.; Konoshchuk, N. V.; Posudievsky, O. Y.; Koshechko, V. G. Estimation of multicomponent organic solvent vapor mixture composition with electroconducting polymer chemiresistors. *Sensors and Actuators B: Chemical* **2016**, *232*, 203-218.

(119) Rañola, R. A. G.; Santiago, K. S.; Sevilla, F. B. Use of array of conducting polymers for differentiation of coconut oil products. *Talanta* **2016**, *146*, 75-82.

(120) Ghoorchian, A.; Alizadeh, N. Chemiresistor gas sensor based on sulfonated dye-doped modified conducting polypyrrole film for high sensitive detection of 2,4,6-trinitrotoluene in air. *Sensors and Actuators B: Chemical* **2018**, *255*, 826-835.

(121) Zhang, W.; Wu, Z.; Hu, J.; Cao, Y.; Guo, J.; Long, M.; Duan, H.; Jia, D. Flexible chemiresistive sensor of polyaniline coated filter paper prepared by spraying for fast and non-contact detection of nitroaromatic explosives. *Sensors and Actuators B: Chemical* **2020**, *304*, 127233.

(122) Kwon, O. S.; Park, C. S.; Park, S. J.; Noh, S.; Kim, S.; Kong, H. J.; Bae, J.; Lee, C.-S.; Yoon, H. Carboxylic Acid-Functionalized Conducting-Polymer Nanotubes as Highly Sensitive Nerve-Agent Chemiresistors. *Scientific Reports* **2016**, *6*, 33724.

(123) Zehra, N.; Kalita, A.; Malik, A. H.; Barman, U.; Adil Afroz, M.; Iyer, P. K. Conjugated Polymer-Based Electrical Sensor for Ultratrace Vapor-Phase Detection of Nerve Agent Mimics. *ACS Sensors* **2020**, *5*, 191-198.

(124) Cosnier, S.; Holzinger, M. Electrosynthesized polymers for biosensing. *Chemical Society Reviews* **2011**, *40*, 2146-2156.

(125) Anantha-Iyengar, G.; Shanmugasundaram, K.; Nallal, M.; Lee, K.-P.; Whitcombe, M. J.; Lakshmi, D.; Sai-Anand, G. Functionalized conjugated polymers for sensing and molecular imprinting applications. *Progress in Polymer Science* **2019**, *88*, 1-129.

(126) Aravinda, C. L.; Cosnier, S.; Chen, W.; Myung, N. V.; Mulchandani, A. Label-free detection of cupric ions and histidine-tagged proteins using single poly(pyrrole)-NTA chelator conducting polymer nanotube chemiresistive sensor. *Biosensors and Bioelectronics* **2009**, *24*, 1451-1455.

(127) Bangar, M. A.; Shirale, D. J.; Chen, W.; Myung, N. V.; Mulchandani, A. Single Conducting Polymer Nanowire Chemiresistive Label-Free Immunosensor for Cancer Biomarker. *Analytical Chemistry* **2009**, *81*, 2168-2175.

(128) García-Aljaro, C.; Bangar, M. A.; Baldrich, E.; Muñoz, F. J.; Mulchandani, A. Conducting polymer nanowire-based chemiresistive biosensor for the detection of bacterial spores. *Biosensors and Bioelectronics* **2010**, *25*, 2309-2312.

(129) Shirale, D. J.; Bangar, M. A.; Park, M.; Yates, M. V.; Chen, W.; Myung, N. V.; Mulchandani, A. Label-Free Chemiresistive Immunosensors for Viruses. *Environmental Science & Technology* **2010**, *44*, 9030-9035.

(130) Bhattacharyya, D.; Senecal, K.; Marek, P.; Senecal, A.; Gleason, K. K. High Surface Area Flexible Chemiresistive Biosensor by Oxidative Chemical Vapor Deposition. *Advanced Functional Materials* **2011**, *21*, 4328-4337.

(131) Kannan, B.; Williams, D. E.; Laslau, C.; Travas-Sejdic, J. A highly sensitive, label-free gene sensor based on a single conducting polymer nanowire. *Biosensors and Bioelectronics* **2012**, *35*, 258-264.

(132) Chartuprayoon, N.; Rheem, Y.; Ng, J. C. K.; Nam, J.; Chen, W.; Myung, N. V. Polypyrrole nanoribbon based chemiresistive immunosensors for viral plant pathogen detection. *Analytical Methods* **2013**, *5*, 3497-3502.

(133) Travas-Sejdic, J.; Aydemir, N.; Kannan, B.; Williams, D. E.; Malmström, J. Intrinsically conducting polymer nanowires for biosensing. *Journal of Materials Chemistry B* **2014**, *2*, 4593-4609.

(134) Flory, P. J. Molecular size distribution in three dimensional polymers. I. Gelation1. *Journal of the American Chemical Society* **1941**, *63*, 3083-3090.

(135) Stockmayer, W. H. Theory of molecular size distribution and gel formation in branched-chain polymers. *The Journal of chemical physics* **1943**, *11*, 45-55.

(136) Kirkpatrick, S. Percolation and conduction. *Reviews of Modern Physics* **1973**, *45*, 574-588.

(137) Bollobás, B.; Riordan, O.: *Percolation*; Cambridge University Press, 2006.

(138) Gelves, G. A.; Lin, B.; Sundararaj, U.; Haber, J. A. Low Electrical Percolation Threshold of Silver and Copper Nanowires in Polystyrene Composites. *Advanced Functional Materials* **2006**, *16*, 2423-2430.

(139) White, S. I.; Mutiso, R. M.; Vora, P. M.; Jahnke, D.; Hsu, S.; Kikkawa, J. M.; Li, J.; Fischer, J. E.; Winey, K. I. Electrical Percolation Behavior in Silver Nanowire–Polystyrene Composites: Simulation and Experiment. *Advanced Functional Materials* **2010**, *20*, 2709-2716.

(140) Dong, X. M.; Luo, Y.; Xie, L. N.; Fu, R. W.; Zhang, M. Q. Conductive carbon black-filled polymethacrylate composites as gas sensing materials: Effect of glass transition temperature. *Thin Solid Films* **2008**, *516*, 7886-7890.

(141) Marsden, A. J.; Papageorgiou, D. G.; Vallés, C.; Liscio, A.; Palermo, V.; Bissett, M. A.; Young, R. J.; Kinloch, I. A. Electrical percolation in graphene–polymer composites. *2D Materials* **2018**, *5*, 032003.

(142) Murphy, J. P.; Andriolo, J. M.; Sutton, N. J.; Wyss, G.; Skinner, J. L. Loading Dependent Electrical Properties of Hybrid Perovskite Composite Media. *MRS Advances* **2017**, *2*, 3069-3076.

(143) Tsuruta, A.; Mikami, M.; Kinemuchi, Y.; Terasaki, I.; Murayama, N.; Shin, W. High electrical conductivity of composite ceramics consisting of insulating oxide and ordered perovskite conducting oxide. *physica status solidi (a)* **2017**, *214*, 1600968.

(144) Chen, J.; Zhu, Y.; Huang, J.; Zhang, J.; Pan, D.; Zhou, J.; Ryu, J. E.; Umar, A.; Guo, Z. Advances in Responsively Conductive Polymer Composites and Sensing Applications. *Polymer Reviews* **2021**, *61*, 157-193.

(145) Boulerouah, A.; Longuemart, S.; Hus, P.; Sahraoui, A. H. Ethanol-sensing properties of potassium bromide/multi-walled carbon nanotube composites. *Journal of Materials Science* **2013**, *48*, 8023-8028.

(146) Freund, P.; Senkovska, I.; Kaskel, S. Switchable Conductive MOF–Nanocarbon Composite Coatings as Threshold Sensing Architectures. *ACS Applied Materials & Interfaces* **2017**, *9*, 43782-43789.

(147) Sahimi, M.: *Applications of percolation theory*; Taylor & Francis: London, 1994.

(148) Choi, H.-J.; Kim, M. S.; Ahn, D.; Yeo, S. Y.; Lee, S. Electrical percolation threshold of carbon black in a polymer matrix and its application to antistatic fibre. *Scientific Reports* **2019**, *9*, 6338.

(149) Merlini, C.; Rosa, B. S.; Müller, D.; Ecco, L. G.; Ramôa, S. D. A. S.; Barra, G. M. O. Polypyrrole nanoparticles coated amorphous short silica fibers: Synthesis and characterization. *Polymer Testing* **2012**, *31*, 971-977.

(150) Luong, N. D.; Korhonen, J. T.; Soininen, A. J.; Ruokolainen, J.; Johansson, L.-S.; Seppälä, J. Processable polyaniline suspensions through in situ polymerization onto nanocellulose. *European Polymer Journal* **2013**, *49*, 335-344.

(151) Ali, M. Z.; Ishak, K. M. K.; Zawawi, M. A. M.; Jaafar, M.; Ahmad, Z. Tunneling Percolation Mechanism of Conductivity for PEDOT:PSS in Hydrophilic PDMS Composite for the Fabrication of Highly Sensitive Strain Sensors. *Macromolecular Chemistry and Physics* **2022**, *223*, 2200077.

(152) Ramli, M. M.; Zhang, W.; Silva, S. R. P.; Henley, S. J. Dye-assisted dispersion of single-walled carbon nanotubes for solution fabrication of $NO_2$ sensors. *AIP Advances* **2012**, *2*, 032165.

(153) Ramli, M. M.; Isa, S. S. M.; Henley, S. J. Fabrication of multi-walled carbon nanotubes hydrogen sensor on plastic. *RSM 2013 IEEE Regional Symposium on Micro and Nanoelectronics* **2013**, 316-319.

(154) Kolmakov, A.; Klenov, D. O.; Lilach, Y.; Stemmer, S.; Moskovits, M. Enhanced Gas Sensing by Individual $SnO_2$ Nanowires and Nanobelts Functionalized with Pd Catalyst Particles. *Nano Letters* **2005**, *5*, 667-673.

(155) Kolmakov, A.; Klenov, D.; Lilach, Y.; Stemmer, S.; Moskovits, M. Surface sensitization of metal oxide quasi-1D sensors: in situ comparative study of pristine and Pd doped individual $SnO_2$ nanostructure. *IEEE Sensors* **2005**, 1201-1204.

(156) Tomeček, D.; Fitl, P.; Marešová, E.; Vlček, J.; Hofmann, J.; Vrňata, M. Silver phthalocyanine thin films carrying gold, palladium and silver nanoparticles for detection of taggants in explosives. *Thin Solid Films* **2017**, *630*, 31-37.

(157) Wang, H. L.; Toppare, L.; Fernandez, J. E. Conducting polymer blends: polythiophene and polypyrrole blends with polystyrene and poly(bisphenol A carbonate). *Macromolecules* **2002**, *23*, 1053-1059.

(158) Morsli, M.; Bonnet, A.; Samir, F.; Jousseaume, V.; Lefrant, S. Electrical conductivity and thermoelectric power of polybithiophenepolystyrene composites. *Synthetic Metals* **1996**, *76*, 273-276.

(159) Morsli, M.; Bonnet, A.; Samir, F.; Lefrant, S. Electrical properties of polybithiophene-polystyrene composites. *Journal of Applied Polymer Science* **1996**, *61*, 213-216.

(160) Nicho, M. E.; Rivera, L.; Hu, H. Polyaniline composite coatings with thermally stable electrical properties. *Advanced Materials for Optics and Electronics* **1999**, *9*, 47-53.

(161) Mpoukouvalas, K.; Wang, J.; Tilch, R.; Butt, H.-J.; Wegner, G. Impedance spectroscopy investigation of conjugated polymer coated core-shell nanoparticles. *Journal of Applied Physics* **2009**, *106*.

(162) Brezoi, D.-V.; Ion, R.-M. Phase evolution induced by polypyrrole in iron oxide–polypyrrole nanocomposite. *Sensors and Actuators B: Chemical* **2005**, *109*, 171-175.

(163) Luo, J.; Wang, Q.; Wang, X.; Li, J.; Zhao, X.; Wang, F. Water-resistant conducting hybrids from electrostatic interactions. *Journal of Polymer Science Part A: Polymer Chemistry* **2007**, *45*, 1424-1431.

(164) Tang, Q.; Sun, X.; Li, Q.; Lin, J.; Wu, J. Preparation and electrical conductivity of SiO2/polypyrrole nanocomposite. *Journal of Materials Science* **2009**, *44*, 849-854.

(165) Cao, Y.; Smith, P.; Heeger, A. J. Counter-ion induced processibility of conducting polyaniline and of conducting polyblends of polyaniline in bulk polymers. *Synthetic Metals* **1992**, *48*, 91-97.

(166) Hu, H.; Cadenas, J. L.; Saniger, J. M.; Nair, P. K. Electrically conducting polyaniline–poly(acrylic acid) blends. *Polymer International* **1998**, *45*, 262-270.

(167) Jousseaume, V.; Morsli, M.; Bonnet, A.; Tesson, O.; Lefrant, S. Electrical properties of polyaniline–polystyrene blends above the percolation threshold. *Journal of Applied Polymer Science* **1998**, *67*, 1205-1208.

(168) Min, G. Conducting Polymers and Their Applications in The Film Industry — Polyaniline/Polyimide Blended Films. *Synthetic Metals* **1999**, *102*, 1163-1166.

(169) Moulton, J.; Smith, P. Gel processing of electrically conductive blends of poly(3-octylthiophene) and ultrahigh molecular weight polyethylene. *Journal of Polymer Science Part B: Polymer Physics* **1992**, *30*, 871-878.

(170) Patil, R. C.; Kuratani, K.; Nakayama, M.; Ogura, K. Studies on CSA-induced processability of conducting poly(o-toluidine) and its polyblend with ABS. *Journal of Polymer Science Part A: Polymer Chemistry* **1999**, *37*, 2657-2665.

(171) Mendez, J. D.; Weder, C. Synthesis, electrical properties, and nanocomposites of poly(3,4-ethylenedioxythiophene) nanorods. *Polymer Chemistry* **2010**, *1*, 1237-1244.

(172) Watcharaphalakorn, S.; Ruangchuay, L.; Chotpattananont, D.; Sirivat, A.; Schwank, J. Polyaniline/polyimide blends as gas sensors and electrical conductivity response to CO–$N_2$ mixtures. *Polymer International* **2005**, *54*, 1126-1133.

(173) Costa, L. C.; Henry, F.; Valente, M. A.; Mendiratta, S. K.; Sombra, A. S. Electrical and dielectrical properties of the percolating system polystyrene/polypyrrole particles. *European Polymer Journal* **2002**, *38*, 1495-1499.

(174) Yin, X. H.; Yoshino, K.; Yamamoto, H.; Watanuki, T.; Isa, I.; Nakagawa, S.; Adachi, M. Electrical Conduction by Percolation Process in Insulating Polymer Containing Small Amount of Conducting Polymer. *Japanese Journal of Applied Physics* **1994**, *33*, 3597-3601.

(175) Yin, X. H.; Kobayashi, K.; Yoshino, K.; Yamamoto, H.; Watanuki, T.; Isa, I. Percolation conduction in polymer composites containing polypyrrole coated insulating polymer fiber and conducting polymer. *Synthetic Metals* **1995**, *69*, 367-368.

(176) Yin, X. H.; Yoshino, K.; Yamamoto, H.; Watanuki, T.; Isa, I.; Nakagawa, S.; Adachi, M. Electrical Conduction near Percolation Threshold in Polymer Composite Containing Conducting Polypyrrole-Coated Insulating Polymer Fiber. *Japanese Journal of Applied Physics* **1996**, *35*, 4692-4695.

(177) Zilberman, M.; Siegmann, A.; Narkis, M. Melt-processed electrically conductive polymer/polyaniline blends. *Journal of Macromolecular Science, Part B* **1998**, *37*, 301-318.

(178) Prokeš, J.; Křivka, I.; Stejskal, J. Control of Electrical Properties of Polyaniline. *Polymer International* **1997**, *43*, 117-125.

(179) Cassignol, C.; Cavarero, M.; Boudet, A.; Ricard, A. Microstructure–conductivity relationship in conducting polypyrrole/epoxy composites. *Polymer* **1999**, *40*, 1139-1151.

(180) Valenciano, G. R.; Job, A. E.; Mattoso, L. H. C. Improved conductivity of films of ultra high molecular weight polyethylene and polyaniline blends prepared from an m-cresol/decaline mixture. *Polymer* **2000**, *41*, 4757-4760.

(181) Barra, G. M. O.; Leyva, M. E.; Soares, B. G.; Sens, M. Solution-cast blends of polyaniline–DBSA with EVA copolymers. *Synthetic Metals* **2002**, *130*, 239-245.

(182) Plantard, G.; Papini-Arconada, M. Analysis of the radiative properties of insulating and conducting granular polymers and of their mixtures. *Powder Technology* **2002**, *128*, 287-295.

(183) Wen, T.-C.; Sivakumar, C.; Gopalan, A. Studies on processable conducting blend of poly(diphenylamine) and poly(vinylidene fluoride). *Materials Letters* **2002**, *54*, 430-441.

(184) Sivakumar, C.; Wen, T. C.; Gopalan, A.; Teng, H. Electroactive conducting blends of poly(o-toluidine) and poly(vinylidene fluoride) and characterisation. *Synthetic Metals* **2003**, *132*, 219-226.

(185) Huang, B.; Kang, G.; Ni, Y. Electrically Conductive Fibre Composites Prepared from Polypyrrole-Engineered Pulp Fibres. *The Canadian Journal of Chemical Engineering* **2005**, *83*, 896-903.

(186) Jing, X.; Wang, Y.; Zhang, B. Electrical conductivity and electromagnetic interference shielding of polyaniline/polyacrylate composite coatings. *Journal of Applied Polymer Science* **2005**, *98*, 2149-2156.

(187) Ebrahim, S. M.; Kashyout, A. B.; Soliman, M. M. Electrical and structural properties of polyaniline/cellulose triacetate blend films. *Journal of Polymer Research* **2007**, *14*, 423-429.
(188) Vicentini, D. S.; Barra, G. M. O.; Bertolino, J. R.; Pires, A. T. N. Polyaniline/thermoplastic polyurethane blends: Preparation and evaluation of electrical conductivity. *European Polymer Journal* **2007**, *43*, 4565-4572.
(189) Wang, Y.; Jing, X. Transparent conductive thin films based on polyaniline nanofibers. *Materials Science and Engineering: B* **2007**, *138*, 95-100.
(190) Niu, Y. Electromagnetic interference shielding with polyaniline nanofibers composite coatings. *Polymer Engineering & Science* **2008**, *48*, 355-359.
(191) Sudha, J. D.; Sivakala, S. Conducting polystyrene/polyaniline blend through template-assisted emulsion polymerization. *Colloid and Polymer Science* **2009**, *287*, 1347-1354.
(192) Cristovan, F. H.; Lemos, S. G.; Pereira, E. C. Systematic evaluation of the preparation of conducting PANI/ABS blends. *Journal of Applied Polymer Science* **2010**, *116*, 825-831.
(193) Li, X.-G.; Li, A.; Huang, M.-R.; Liao, Y.; Lu, Y.-G. Efficient and Scalable Synthesis of Pure Polypyrrole Nanoparticles Applicable for Advanced Nanocomposites and Carbon Nanoparticles. *The Journal of Physical Chemistry C* **2010**, *114*, 19244-19255.
(194) Kanhegaokar, S. A.; Chunji, G.; Choi, E.-Y.; Kwon, O.-P.; Lee, S.-H. Molecular composites created by the solution blending of polyaniline and sulfonated poly(ether sulfone). *Journal of Applied Polymer Science* **2011**, *120*, 1138-1144.
(195) Wojkiewicz, J. L.; Bliznyuk, V. N.; Carquigny, S.; Elkamchi, N.; Redon, N.; Lasri, T.; Pud, A. A.; Reynaud, S. Nanostructured polyaniline-based composites for ppb range ammonia sensing. *Sensors and Actuators B: Chemical* **2011**, *160*, 1394-1403.
(196) Kanhegaokar, S. A.; Choi, E.-Y.; Kwon, O. P.; Lee, S.-H. Preparation of compatible polyaniline/polyethersulfone solution blends. *Polymer Bulletin* **2012**, *69*, 95-104.
(197) Du, P.; Lin, X.; Zhang, X. Tunable electrical and mechanical responses of PDMS and polypyrrole nanowire composites. *Journal of Physics D: Applied Physics* **2013**, *46*, 195303.
(198) Tkalya, E.; Ghislandi, M.; Thielemans, W.; van der Schoot, P.; de With, G.; Koning, C. Cellulose Nanowhiskers Templating in Conductive Polymer Nanocomposites Reduces Electrical Percolation Threshold 5-Fold. *ACS Macro Letters* **2013**, *2*, 157-163.
(199) Vega-Rios, A.; Hernández-Escobar, C. A.; Zaragoza-Contreras, E. A.; Kobayashi, T. Electrical and electrochemical properties of polystyrene/polyaniline core–shell materials prepared with the use of a reactive surfactant as the polyaniline shell precursor. *Synthetic Metals* **2013**, *167*, 64-71.

(200) Arenas, M. C.; Sánchez, G.; Martínez-Álvarez, O.; Castaño, V. M. Electrical and morphological properties of polyaniline–polyvinyl alcohol in situ nanocomposites. *Composites Part B: Engineering* **2014**, *56*, 857-861.
(201) Merlini, C.; Barra, G. M. d. O.; Araujo, T. M.; Pegoretti, A. The effect of compressive stress on the electrically resistivity of poly(vinylidene fluoride)/polypyrrole blends. *Synthetic Metals* **2014**, *196*, 186-192.
(202) Ding, H.; Zhong, M.; Wu, H.; Park, S.; Mohin, J. W.; Klosterman, L.; Yang, Z.; Yang, H.; Matyjaszewski, K.; Bettinger, C. J. Elastomeric Conducting Polyaniline Formed Through Topological Control of Molecular Templates. *ACS Nano* **2016**, *10*, 5991-5998.
(203) Renna, L. A.; Bag, M.; Gehan, T. S.; Han, X.; Lahti, P. M.; Maroudas, D.; Venkataraman, D. Tunable Percolation in Semiconducting Binary Polymer Nanoparticle Glasses. *The Journal of Physical Chemistry B* **2016**, *120*, 2544-2556.
(204) Jerkovic, I.; Koncar, V.; Grancaric, A. M. New Textile Sensors for In Situ Structural Health Monitoring of Textile Reinforced Thermoplastic Composites Based on the Conductive Poly(3,4-ethylenedioxythiophene)-poly(styrenesulfonate) Polymer Complex. *Sensors* **2017**, *17*, 2297.
(205) Polpaya, I. C.; Rao, C. L.; Varughese, S. Strain induced insulator-to-conductor transition in conducting polymer composites from the auxetic behaviour of hierarchical microstructures. *Physical Chemistry Chemical Physics* **2017**, *19*, 19377-19385.
(206) Rodríguez-Cantó, P. J.; Martínez-Marco, M.; Sánchez-Royo, J. F.; Martínez-Pastor, J. P.; Abargues, R. In-situ synthesis of thiophene-based multifunctional polymeric networks with tunable conductivity and high photolithographic performance. *Polymer* **2017**, *108*, 413-422.
(207) Sousa, E. A.; Deniz, W. D. S.; Arlindo, E. P. S.; Sakamoto, W. K.; Fuzari, G. C. PVDF-PAni blend: a free-standing film with variable electrical resistance. *Polymer Bulletin* **2017**, *74*, 1483-1492.
(208) El Zein, A.; Huppé, C.; Cochrane, C. Development of a Flexible Strain Sensor Based on PEDOT:PSS for Thin Film Structures. *Sensors* **2017**, *17*, 1337.
(209) Zhang, L.; Lu, X.; Zhang, X.; Jin, L.; Xu, Z.; Cheng, Z. Y. All-organic dielectric nanocomposites using conducting polypyrrole nanoclips as filler. *Composites Science and Technology* **2018**, *167*, 285-293.
(210) Wang, Z.; Wang, T.; Zhuang, M.; Xu, H. Stretchable Polymer Composite with a 3D Segregated Structure of PEDOT:PSS for Multifunctional Touchless Sensing. *ACS Applied Materials & Interfaces* **2019**, *11*, 45301-45309.

(211) Arias-Ferreiro, G.; Ares-Pernas, A.; Dopico-García, M. S.; Lasagabáster-Latorre, A.; Abad, M.-J. Photocured conductive PANI/acrylate composites for digital light processing. Influence of HDODA crosslinker in rheological and physicochemical properties. *European Polymer Journal* **2020**, *136*, 109887.

(212) Kim, N.; Lienemann, S.; Petsagkourakis, I.; Alemu Mengistie, D.; Kee, S.; Ederth, T.; Gueskine, V.; Leclère, P.; Lazzaroni, R.; Crispin, X.; Tybrandt, K. Elastic conducting polymer composites in thermoelectric modules. *Nature communications* **2020**, *11*, 1424.

(213) Novikov, A.; Goding, J.; Chapman, C.; Cuttaz, E.; Green, R. A. Stretchable bioelectronics: Mitigating the challenges of the percolation threshold in conductive elastomers. *APL Materials* **2020**, *8*, 101105.

(214) Aksimentyeva, O. I.; Martyniuk, G. V. Percolation phenomena in the polymer composites with conducting polymer fillers. *Physics and Chemistry of Solid State* **2021**, *22*, 811-816.

(215) Lux, F. Models proposed to explain the electrical conductivity of mixtures made of conductive and insulating materials. *Journal of Materials Science* **1993**, *28*, 285-301.

(216) Catalanotti, G.; Katunin, A. Modelling the electro-mechanical properties of PPy/epoxy conductive composites. *Computational Materials Science* **2016**, *113*, 88-97.

(217) Katunin, A. Analysis of Critical Percolation Clusters of Mixtures of Conducting and Dielectric Polymers. *Journal of Applied Mathematics and Computational Mechanics* **2016**, *15*, 59-69.

(218) Katunin, A.: Generalized Chemical Distance Distribution in All-sided Critical Percolation Clusters. In *AIP Conference Proceedings*, 2016; Vol. 1790; pp 150002.

(219) Katunin, A.; Krukiewicz, K.; Catalanotti, G. Modeling and synthesis of all-polymeric conducting composite material for aircraft lightning strike protection applications. *Materials Today: Proceedings* **2017**, *4*, 8010-8015.

(220) Moučka, R.; Mravčáková, M.; Vilčáková, J.; Omastová, M.; Sáha, P. Electromagnetic absorption efficiency of polypropylene/montmorillonite/polypyrrole nanocomposites. *Materials & Design* **2011**, *32*, 2006-2011.

(221) Neelgund, G. M.; Bliznyuk, V. N.; Pud, A. A.; Fatyeyeva, K. Y.; Hrehorova, E.; Joyce, M. Formation of nanostructured composites with environmentally-dependent electrical properties based on poly(vinylidene fluoride)–polyaniline core–shell latex system. *Polymer* **2010**, *51*, 2000-2006.

(222) Das, M.; Roy, S. Polypyrrole and associated hybrid nanocomposites as chemiresistive gas sensors: A comprehensive review. *Materials Science in Semiconductor Processing* **2021**, *121*, 105332.
(223) Liu, X.; Zheng, W.; Kumar, R.; Kumar, M.; Zhang, J. Conducting polymer-based nanostructures for gas sensors. *Coordination Chemistry Reviews* **2022**, *462*, 214517.
(224) Ehsani, M.; Rahimi, P.; Joseph, Y. Structure–Function Relationships of Nanocarbon/Polymer Composites for Chemiresistive Sensing: A Review. *Sensors* **2021**, *21*, 3291.
(225) Wang, Y.-F.; Sekine, T.; Takeda, Y.; Yokosawa, K.; Matsui, H.; Kumaki, D.; Shiba, T.; Nishikawa, T.; Tokito, S. Fully Printed PEDOT:PSS-based Temperature Sensor with High Humidity Stability for Wireless Healthcare Monitoring. *Scientific Reports* **2020**, *10*, 2467.
(226) Liu, C.; Hayashi, K.; Toko, K. Electrochemical deposition of nanostructured polyaniline on an insulating substrate. *Electrochemistry Communications* **2010**, *12*, 36-39.
(227) Xu, K.; Zhu, L.; Li, J.; Tang, H. Effects of dopants on percolation behaviors and gas sensing characteristics of polyaniline film. *Electrochimica Acta* **2006**, *52*, 723-727.
(228) Han, D. H.; Kim, J. W.; Park, S. M. Electrochemistry of conductive polymers 38. Electrodeposited poly(3,4-ethylenedioxy-thiophene) studied by current sensing atomic force microscopy. *Journal of Physical Chemistry B* **2006**, *110*, 14874-14880.
(229) Del-Oso, J. A.; Frontana-Uribe, B. A.; Maldonado, J.-L.; Rivera, M.; Tapia-Tapia, M.; Roa-Morales, G. Electrochemical deposition of poly[ethylene-dioxythiophene] (PEDOT) films on ITO electrodes for organic photovoltaic cells: control of morphology, thickness, and electronic properties. *Journal of Solid State Electrochemistry* **2018**, *22*, 2025-2037.
(230) Holze, R.; Lippe, J. A method for electrochemical in situ conductivity measurements of electrochemically synthesized intrinsically conducting polymers. *Synthetic Metals* **1990**, *38*, 99-105.
(231) Kankare, J.; Kupila, E.-L. In-situ conductance measurement during electropolymerization. *Journal of Electroanalytical Chemistry* **1992**, *322*, 167-181.
(232) Porras-Gutiérrez, A. G.; Frontana-Uribe, B. A.; Gutiérrez-Granados, S.; Griveau, S.; Bedioui, F. In situ characterization by cyclic voltammetry and conductance of composites based on polypyrrole, multi-walled carbon nanotubes and cobalt phthalocyanine. *Electrochimica Acta* **2013**, *89*, 840-847.
(233) Salinas, G.; Frontana-Uribe, B. A. Analysis of Conjugated Polymers Conductivity by in situ Electrochemical-Conductance Method. *ChemElectroChem* **2019**, *6*, 4105-4117.

(234) Setka, M.; Calavia, R.; Vojkuvka, L.; Llobet, E.; Drbohlavova, J.; Vallejos, S. Raman and XPS studies of ammonia sensitive polypyrrole nanorods and nanoparticles. *Sci Rep* **2019**, *9*, 8465.

(235) Casanova-Chafer, J.; Umek, P.; Acosta, S.; Bittencourt, C.; Llobet, E. Graphene Loading with Polypyrrole Nanoparticles for Trace-Level Detection of Ammonia at Room Temperature. *ACS Appl Mater Interfaces* **2021**, *13*, 40909-40921.

(236) Salimi, M.; Rahmani, F.; Hosseini, S. M. R. M. Copper Fluoride Doped Polypyrrole for Portable and Enhanced Ammonia Sensing at Room Temperature. *ChemistrySelect* **2021**, *6*, 7829-7837.

(237) Šetka, M.; Drbohlavová, J.; Hubálek, J. Nanostructured Polypyrrole-Based Ammonia and Volatile Organic Compound Sensors. *Sensors* **2017**, *17*, 562.

(238) Gustafsson, G.; Lundström, I. The effect of ammonia on the physical properties of polypyrrole. *Synthetic Metals* **1987**, *21*, 203-208.

(239) Maksymiuk, K. Chemical Reactivity of Polypyrrole and Its Relevance to Polypyrrole Based Electrochemical Sensors. *Electroanalysis* **2006**, *18*, 1537-1551.

(240) Babaei, M.; Alizadeh, N. Methanol selective gas sensor based on nano-structured conducting polypyrrole prepared by electrochemically on interdigital electrodes for biodiesel analysis. *Sensors and Actuators B: Chemical* **2013**, *183*, 617-626.

(241) Zhou, J.; Cheng, X.-F.; Gao, B.-J.; Yu, C.; He, J.-H.; Xu, Q.-F.; Li, H.; Li, N.-J.; Chen, D.-Y.; Lu, J.-M. Detection of $NO_2$ Down to One ppb Using Ion-in-Conjugation-Inspired Polymer. *Small* **2019**, *15*, 1803896.

(242) Patois, T.; Sanchez, J.-B.; Berger, F.; Rauch, J.-Y.; Fievet, P.; Lakard, B. Ammonia gas sensors based on polypyrrole films: Influence of electrodeposition parameters. *Sensors and Actuators B: Chemical* **2012**, *171-172*, 431-439.

(243) Kwon, O. S.; Park, S. J.; Yoon, H.; Jang, J. Highly sensitive and selective chemiresistive sensors based on multidimensional polypyrrole nanotubes. *Chemical Communications* **2012**, *48*, 10526-10528.

(244) Hernandez, S. C.; Chaudhuri, D.; Chen, W.; Myung, N. V.; Mulchandani, A. Single Polypyrrole Nanowire Ammonia Gas Sensor. *Electroanalysis* **2007**, *19*, 2125-2130.

(245) Chartuprayoon, N.; Hangarter, C. M.; Rheem, Y.; Jung, H.; Myung, N. V. Wafer-Scale Fabrication of Single Polypyrrole Nanoribbon-Based Ammonia Sensor. *The Journal of Physical Chemistry C* **2010**, *114*, 11103-11108.

(246) Ishpal; Kaur, A. Spectroscopic and electrical sensing mechanism in oxidant-mediated polypyrrole nanofibers/nanoparticles for ammonia gas. *Journal of Nanoparticle Research* **2013**, *15*, 1637.

(247) Kalaleh, H.-A.; Masri, K. The role of butanol isomers on the performance of ammonia sensors based on polypyrrole prepared by microemulsion polymerization. *Journal of Materials Science: Materials in Electronics* **2021**, *32*, 5978-5988.

(248) Hien, H. T.; Van Tuan, C.; Anh Thu, D. T.; Ngan, P. Q.; Thai, G. H.; Doanh, S. C.; Giang, H. T.; Van, N. D.; Trung, T. Influence of surface morphology and doping of PPy film simultaneously polymerized by vapour phase oxidation on gas sensing. *Synthetic Metals* **2019**, *250*, 35-41.

(249) Lee, J. S.; Jun, J.; Shin, D. H.; Jang, J. Urchin-like polypyrrole nanoparticles for highly sensitive and selective chemiresistive sensor application. *Nanoscale* **2014**, *6*, 4188-4194.

(250) Li, J.; Hu, Y.; Yu, L.; Li, L.; Ji, D.; Li, L.; Hu, W.; Fuchs, H. Recent Advances of Nanospheres Lithography in Organic Electronics. *Small* **2021**, *17*, 2100724.

(251) Nguyen, V.-Q.; Schaming, D.; Martin, P.; Lacroix, J.-C. Highly Resolved Nanostructured PEDOT on Large Areas by Nanosphere Lithography and Electrodeposition. *ACS Applied Materials & Interfaces* **2015**, *7*, 21673-21681.

(252) Puzzo, D. P.; Arsenault, A. C.; Manners, I.; Ozin, G. A. Electroactive Inverse Opal: A Single Material for All Colors. *Angewandte Chemie International Edition* **2009**, *48*, 943-947.

(253) Cassagneau, T.; Caruso, F. Conjugated Polymer Inverse Opals for Potentiometric Biosensing. *Advanced Materials* **2002**, *14*, 1837-1841.

(254) Zhao, L.; Tong, L.; Li, C.; Gu, Z.; Shi, G. Polypyrrole actuators with inverse opal structures. *Journal of Materials Chemistry* **2009**, *19*, 1653-1658.

(255) Zhong, Q.; Xu, H.; Ding, H.; Bai, L.; Mu, Z.; Xie, Z.; Zhao, Y.; Gu, Z. Preparation of conducting polymer inverse opals and its application as ammonia sensor. *Colloids and Surfaces A: Physicochemical and Engineering Aspects* **2013**, *433*, 59-63.

(256) Cernat, A.; Le Goff, A.; Holzinger, M.; Sandulescu, R.; Cosnier, S. Micro- to nanostructured poly(pyrrole-nitrilotriacetic acid) films via nanosphere templates: applications to 3D enzyme attachment by affinity interactions. *Analytical and Bioanalytical Chemistry* **2014**, *406*, 1141-1147.

(257) Park, S. H.; Kim, O.-H.; Kang, J. S.; Lee, K. J.; Choi, J.-W.; Cho, Y.-H.; Sung, Y.-E. Poly(3,4-Ethylenedioxythiophene) Inverse Opal Electrode Fabricated from Poly(3,4-Ethylenedioxythiophene):Poly(Styrene Sulfonate)-Filled Polystyrene Template for Dye-Sensitized Solar Cells. *Electrochimica Acta* **2014**, *137*, 661-667.

(258) Szűcs, J.; Lindfors, T.; Bobacka, J.; Gyurcsányi, R. E. Ion-selective Electrodes with 3D Nanostructured Conducting Polymer Solid Contact. *Electroanalysis* **2016**, *28*, 778-786.

(259) Wu, P.; Guo, J.; Jiang, K.; Wang, J.; Jiang, L. Direct Water-Writing/Electroerasing Pattern on PEDOT Inverse Opals. *Advanced Functional Materials* **2019**, *29*, 1808473.

(260) Miah, M. R.; Yang, M.; Khandaker, S.; Bashar, M. M.; Alsukaibi, A. K. D.; Hassan, H. M. A.; Znad, H.; Awual, M. R. Polypyrrole-based sensors for volatile organic compounds (VOCs) sensing and capturing: A comprehensive review. *Sensors and Actuators A: Physical* **2022**, *347*, 113933.

(261) Kwak, D.; Lei, Y.; Maric, R. Ammonia gas sensors: A comprehensive review. *Talanta* **2019**, *204*, 713-730.

(262) Scott, R. W. J.; Yang, S. M.; Williams, D. E.; Ozin, G. A. Electronically addressable SnO2 inverted opal gas sensors fabricated on interdigitated gold microelectrodes. *Chemical Communications* **2003**, 688-689.

(263) Pikul, J. H.; Özerinç, S.; Liu, B.; Zhang, R.; Braun, P. V.; Deshpande, V. S.; King, W. P. High strength metallic wood from nanostructured nickel inverse opal materials. *Scientific Reports* **2019**, *9*, 719.

(264) Yang, X.; Jin, Y.; Zhu, Y.; Tang, L.; Li, C. Inverse Opal of Polyaniline for Biosensors Prepared by Electrochemical and Self-Assembly Techniques. *Journal of the Electrochemical Society* **2008**, *155*, J23.

(265) Li, W.; Lefferts, M. J.; Armitage, B. I.; Murugappan, K.; Castell, M. R. Polypyrrole Percolation Network Gas Sensors: Improved Reproducibility through Conductance Monitoring during Polymer Growth. *ACS Applied Polymer Materials* **2022**, *4*, 2536-2543.

(266) Tian, S.; Wang, J.; Jonas, U.; Knoll, W. Inverse Opals of Polyaniline and Its Copolymers Prepared by Electrochemical Techniques. *Chemistry of Materials* **2005**, *17*, 5726-5730.

(267) Tang, X.; Raskin, J.-P.; Kryvutsa, N.; Hermans, S.; Slobodian, O.; Nazarov, A. N.; Debliquy, M. An ammonia sensor composed of polypyrrole synthesized on reduced graphene oxide by electropolymerization. *Sensors and Actuators B: Chemical* **2020**, *305*, 127423.

(268) Penza, M.; Milella, E.; Alba, M. B.; Quirini, A.; Vasanelli, L. Selective $NH_3$ gas sensor based on Langmuir-Blodgett polypyrrole film. *Sensors and Actuators B: Chemical* **1997**, *40*, 205-209.

(269) Guernion, N.; Ewen, R. J.; Pihlainen, K.; Ratcliffe, N. M.; Teare, G. C. The fabrication and characterisation of a highly sensitive polypyrrole sensor and its electrical responses to amines of differing basicity at high humidities. *Synthetic Metals* **2002**, *126*, 301-310.

(270) Kharat, H. J.; Kakde, K. P.; Savale, P. A.; Datta, K.; Ghosh, P.; Shirsat, M. D. Synthesis of polypyrrole films for the development of ammonia sensor. *Polymers for Advanced Technologies* **2007**, *18*, 397-402.
(271) Carquigny, S.; Sanchez, J.-B.; Berger, F.; Lakard, B.; Lallemand, F. Ammonia gas sensor based on electrosynthesized polypyrrole films. *Talanta* **2009**, *78*, 199-206.
(272) Joshi, A.; Gangal, S. A.; Gupta, S. K. Ammonia sensing properties of polypyrrole thin films at room temperature. *Sensors and Actuators B: Chemical* **2011**, *156*, 938-942.
(273) Dunst, K. J.; Cysewska, K.; Kalinowski, P.; Jasiński, P. Polypyrrole based gas sensor for ammonia detection. *IOP Conference Series: Materials Science and Engineering* **2016**, *104*, 012028.
(274) Masri, K.; Kalaleh, H.-A.; Alhassan, A. Fabrication of Sensitive and Selective Ammonia Gas Sensors Based on Pyrrole Interfacial Polymerization. *Journal of Electronic Materials* **2019**, *48*, 5967-5974.
(275) Fernandez, F. D. M.; Khadka, R.; Yim, J.-H. Highly porous, soft, and flexible vapor-phase polymerized polypyrrole–styrene–ethylene–butylene–styrene hybrid scaffold as ammonia and strain sensor. *RSC Advances* **2020**, *10*, 22533-22541.
(276) Hong, Y.; Rozyyev, V.; Yavuz, C. T. Alkyl-Linked Porphyrin Porous Polymers for Gas Capture and Precious Metal Adsorption. *Small Science* **2021**, *1*, 2000078.
(277) Amini, A.; Jafari, A.; Vafaei, M.; Mahmoodian, M. Stability enhancement of polypyrrole thin film ammonia sensor by camphor sulfonic acid dopant. *Journal of Materials Science: Materials in Electronics* **2022**, *33*, 1293-1306.
(278) Wetchakun, K.; Samerjai, T.; Tamaekong, N.; Liewhiran, C.; Siriwong, C.; Kruefu, V.; Wisitsoraat, A.; Tuantranont, A.; Phanichphant, S. Semiconducting metal oxides as sensors for environmentally hazardous gases. *Sensors and Actuators B: Chemical* **2011**, *160*, 580-591.
(279) Gafare, M.; Dennis, J. O.; Khir, M. H. D. Detection of Ammonia in Exhaled Breath for Clinical Diagnosis- A Review. *3rd International Conference on Fundamental and Applied Sciences (Icfas 2014): Innovative Research in Applied Sciences for a Sustainable Future* **2014**, *1621*, 303-309.
(280) Pavel, I.-A.; Lakard, S.; Lakard, B. Flexible Sensors Based on Conductive Polymers. *Chemosensors* **2022**, *10*, 97.
(281) Wang, S.; Jiang, Y.; Liu, B.; Duan, Z.; Pan, H.; Yuan, Z.; Xie, G.; Wang, J.; Fang, Z.; Tai, H. Ultrathin $Nb_2CT_x$ nanosheets-supported polyaniline nanocomposite: Enabling ultrasensitive $NH_3$ detection. *Sensors and Actuators B: Chemical* **2021**, *343*, 130069.

(282) Tang, X. H.; Raskin, J. P.; Kryvutsa, N.; Hermans, S.; Slobodian, O.; Nazarov, A. N.; Debliquy, M. An ammonia sensor composed of polypyrrole synthesized on reduced graphene oxide by electropolymerization. *Sensors and Actuators B-Chemical* **2020**, *305*, 127423.

(283) Weber, I. C.; Derron, N.; Königstein, K.; Gerber, P. A.; Güntner, A. T.; Pratsinis, S. E. Monitoring Lipolysis by Sensing Breath Acetone down to Parts-per-Billion. *Small Science* **2021**, *1*, 2100004.

(284) She, C.; Li, G.; Zhang, W.; Xie, G.; Zhang, Y.; Li, L.; Yue, F.; Liu, S.; Jing, C.; Cheng, Y.; Chu, J. A flexible polypyrrole/silk-fiber ammonia sensor assisted by silica nanosphere template. *Sensors and Actuators A: Physical* **2021**, *317*, 112436.

(285) Geng, W.; Li, N.; Li, X.; Wang, R.; Tu, J.; Zhang, T. Effect of polymerization time on the humidity sensing properties of polypyrrole. *Sensors and Actuators B: Chemical* **2007**, *125*, 114-119.

(286) Joulazadeh, M.; Navarchian, A. H.; Niroomand, M. A Comparative Study on Humidity Sensing Performances of Polyaniline and Polypyrrole Nanostructures. *Advances in Polymer Technology* **2014**, *33*, 21461.

(287) Oh, S.-G.; Im, S.-S. Electroconductive polymer nanoparticles preparation and characterization of PANI and PEDOT nanoparticles. *Current Applied Physics* **2002**, *2*, 273-277.

(288) Mumtaz, M.; de Cuendias, A.; Putaux, J.-L.; Cloutet, E.; Cramail, H. Synthesis of PEDOT Nanoparticles and Vesicles by Dispersion Polymerization in Alcoholic Media. *Macromolecular Rapid Communications* **2006**, *27*, 1446-1453.

(289) Wu, C.-H.; Don, T.-M.; Chiu, W.-Y. Characterization and conversion determination of stable PEDOT latex nanoparticles synthesized by emulsion polymerization. *Polymer* **2011**, *52*, 1375-1384.

(290) Zhang, Y.; Liu, S.; Wang, L.; Luo, Y.; Tian, J.; Asiri, A. M.; Al-Youbi, A. O.; Sun, X. Novel Use of Poly(3,4-ethylenedioxythiophene) Nanoparticles for Fluorescent Nucleic Acid Detection. *ACS Combinatorial Science* **2012**, *14*, 191-196.

(291) Culebras, M.; Serrano-Claumarchirant, J. F.; Sanchis, M. J.; Landfester, K.; Cantarero, A.; Gómez, C. M.; Muñoz-Espí, R. Conducting PEDOT Nanoparticles: Controlling Colloidal Stability and Electrical Properties. *The Journal of Physical Chemistry C* **2018**, *122*, 19197-19203.

(292) Reddy, N. R.; Anandhan, S. Polyaniline/poly(styrene-co-acrylonitrile) blend nanofibers exhibit enhanced ammonia and nitrogen dioxide sensing characteristics. *Journal of Materials Science: Materials in Electronics* **2016**, *27*, 13329-13337.

(293) Surwade, S. P.; Agnihotra, S. R.; Dua, V.; Manohar, S. K. Nitrogen dioxide vapor detection using poly-o-toluidine. *Sensors and Actuators B: Chemical* **2009**, *143*, 454-457.
(294) Mane, A. T.; Navale, S. T.; Sen, S.; Aswal, D. K.; Gupta, S. K.; Patil, V. B. Nitrogen dioxide ($NO_2$) sensing performance of p-polypyrrole/n-tungsten oxide hybrid nanocomposites at room temperature. *Organic Electronics* **2015**, *16*, 195-204.
(295) Liu, B.; Liu, X.; Yuan, Z.; Jiang, Y.; Su, Y.; Ma, J.; Tai, H. A flexible $NO_2$ gas sensor based on polypyrrole/nitrogen-doped multiwall carbon nanotube operating at room temperature. *Sensors and Actuators B: Chemical* **2019**, *295*, 86-92.
(296) Guettiche, D.; Mekki, A.; Lilia, B.; Fatma-Zohra, T.; Boudjellal, A. Flexible chemiresistive nitrogen oxide sensors based on a nanocomposite of polypyrrole-reduced graphene oxide-functionalized carboxybenzene diazonium salts. *Journal of Materials Science: Materials in Electronics* **2021**, *32*, 10662-10677.
(297) Raj, K. A; Gorthala, G.; Ghosh, R.; Malakalapalli, R. R. Tetrazine-based 1D polymers for the selective chemiresistive sensing of nitrogen dioxide via the interplay between hydrogen bonding and n-heteroatom interactions. *Polymer Journal* **2022**, *54*, 1191-1201.
(298) Murugesan, T.; Kumar, R. R.; Anbalagan, A. k.; Lee, C.-H.; Lin, H.-N. Interlinked Polyaniline/ZnO Nanorod Composite for Selective $NO_2$ Gas Sensing at Room Temperature. *ACS Applied Nano Materials* **2022**, *5*, 4921-4930.
(299) Nagare, A. B.; Harale, N. S.; Dhas, S. D.; Shembade, U. V.; Ghatage, S. R.; Patil, P. S.; Moholkar, A. V. Facile synthesis of nanogranular PPy thin films for sensitive and selective detection of toxic $NO_2$ gas. *Inorganic Chemistry Communications* **2022**, *146*, 110067.
(300) Li, C.; Sun, Y.-Y.; Li, Y.-N.; Zhang, X.-F.; Deng, Z.-P.; Huo, L.-H.; Xu, Y.-M.; Gao, S. Low-temperature and high-response $NO_2$ sensor based on oxygen vacancy-enriched ZnO tubes inherited from waste chestnut mesocarps. *Sensors and Actuators B: Chemical* **2023**, *388*, 133838.
(301) Bang, J. H.; Mirzaei, A.; Han, S.; Lee, H. Y.; Shin, K. Y.; Kim, S. S.; Kim, H. W. Realisation of low-temperature and selective $NO_2$ sensing of $SnO_2$ nanowires via synergistic effects of Pt decoration and $Bi_2O_3$ branching. *Ceramics International* **2021**, *47*, 5099-5111.
(302) Gueye, M. N.; Carella, A.; Faure-Vincent, J.; Demadrille, R.; Simonato, J.-P. Progress in understanding structure and transport properties of PEDOT-based materials: A critical review. *Progress in Materials Science* **2020**, *108*, 100616.
(303) Tessler, N.; Preezant, Y.; Rappaport, N.; Roichman, Y. Charge Transport in Disordered Organic Materials and Its Relevance to Thin-Film Devices: A Tutorial Review. *Advanced Materials* **2009**, *21*, 2741-2761.

(304) Zuppiroli, L.; Bussac, M. N.; Paschen, S.; Chauvet, O.; Forro, L. Hopping in disordered conducting polymers. *Physical Review B* **1994**, *50*, 5196-5203.

(305) Cao, G.; Cai, S.; Chen, Y.; Zhou, D.; Zhang, H.; Tian, Y. Facile synthesis of highly conductive and dispersible PEDOT particles. *Polymer* **2022**, *252*, 124952.

(306) Oh, J. H.; Hong, S. Y.; Park, H.; Jin, S. W.; Jeong, Y. R.; Oh, S. Y.; Yun, J.; Lee, H.; Kim, J. W.; Ha, J. S. Fabrication of High-Sensitivity Skin-Attachable Temperature Sensors with Bioinspired Microstructured Adhesive. *ACS Applied Materials & Interfaces* **2018**, *10*, 7263-7270.

(307) Zhang, F.; Hu, H.; Islam, M.; Peng, S.; Wu, S.; Lim, S.; Zhou, Y.; Wang, C.-H. Multi-modal strain and temperature sensor by hybridizing reduced graphene oxide and PEDOT:PSS. *Composites Science and Technology* **2020**, *187*, 107959.

(308) Khalaf, A. M.; Issa, H. H.; RamíRez, J. L.; Mohamed, S. A. All Inkjet-Printed Temperature Sensors Based on PEDOT:PSS. *IEEE Access* **2022**, *10*, 61094-61100.

(309) Yu, Y.; Peng, S.; Blanloeuil, P.; Wu, S.; Wang, C. H. Wearable Temperature Sensors with Enhanced Sensitivity by Engineering Microcrack Morphology in PEDOT:PSS–PDMS Sensors. *ACS Applied Materials & Interfaces* **2020**, *12*, 36578-36588.

(310) Honda, W.; Harada, S.; Arie, T.; Akita, S.; Takei, K. Wearable, Human-Interactive, Health-Monitoring, Wireless Devices Fabricated by Macroscale Printing Techniques. *Advanced Functional Materials* **2014**, *24*, 3299-3304.

(311) Bali, C.; Brandlmaier, A.; Ganster, A.; Raab, O.; Zapf, J.; Hübler, A. Fully Inkjet-Printed Flexible Temperature Sensors Based on Carbon and PEDOT:PSS1. *Materials Today: Proceedings* **2016**, *3*, 739-745.

(312) Vuorinen, T.; Niittynen, J.; Kankkunen, T.; Kraft, T. M.; Mäntysalo, M. Inkjet-Printed Graphene/PEDOT:PSS Temperature Sensors on a Skin-Conformable Polyurethane Substrate. *Scientific Reports* **2016**, *6*, 35289.

(313) Lee, J.-W.; Han, D.-C.; Shin, H.-J.; Yeom, S.-H.; Ju, B.-K.; Lee, W. PEDOT:PSS-Based Temperature-Detection Thread for Wearable Devices. *Sensors* **2018**, *18*, 2996.

(314) Nitani, M.; Nakayama, K.; Maeda, K.; Omori, M.; Uno, M. Organic temperature sensors based on conductive polymers patterned by a selective-wetting method. *Organic Electronics* **2019**, *71*, 164-168.

(315) Zhang, Y.; Cui, Y. Development of Flexible and Wearable Temperature Sensors Based on PEDOT:PSS. *IEEE Transactions on Electron Devices* **2019**, *66*, 3129-3133.

(316) Pradhan, S.; Yadavalli, V. K. Photolithographically Printed Flexible Silk/PEDOT:PSS Temperature Sensors. *ACS Applied Electronic Materials* **2021**, *3*, 21-29.

(317) Song, J.; Wei, Y.; Xu, M.; Gao, J.; Luo, L.; Wu, H.; Li, X.; Li, Y.; Wang, X. Highly Sensitive Flexible Temperature Sensor Made Using PEDOT:PSS/PANI. *ACS Applied Polymer Materials* **2022**, *4*, 766-772.

(318) Khalaf, A. M.; Ramírez, J. L.; Mohamed, S. A.; Issa, H. H. Highly sensitive interdigitated thermistor based on PEDOT:PSS for human body temperature monitoring. *Flexible and Printed Electronics* **2022**, *7*, 045012.

(319) Li, F.; Xue, H.; Lin, X.; Zhao, H.; Zhang, T. Wearable Temperature Sensor with High Resolution for Skin Temperature Monitoring. *ACS Applied Materials & Interfaces* **2022**, *14*, 43844-43852.

(320) Seifi, M.; Hamedi, S.; Kordrostami, Z. Fabrication of a high-sensitive wearable temperature sensor with an improved response time based on PEDOT:PSS/rGO on a flexible kapton substrate. *Journal of Materials Science: Materials in Electronics* **2022**, *33*, 6954-6968.

(321) Aidit, S. N.; Rezali, F. A. M.; Nor, N. H. M.; Yusoff, N.; Ma, L.-Y.; Hatta, S. F. W. M.; Soin, N. Hydrothermal synthesis of zinc oxide/PEDOT:PSS composite for flexible temperature sensor application. *Flexible and Printed Electronics* **2023**, *8*, 025008.

(322) Wang, H.; Li, S.; Wang, Y.; Wang, H.; Shen, X.; Zhang, M.; Lu, H.; He, M.; Zhang, Y. Bioinspired Fluffy Fabric with In Situ Grown Carbon Nanotubes for Ultrasensitive Wearable Airflow Sensor. *Advanced Materials* **2020**, *32*, 1908214.

(323) Huang, L.; Liu, Y.; Li, G.; Song, Y.; Su, J.; Cheng, L.; Guo, W.; Zhao, G.; Shen, H.; Yan, Z.; Tang, B. Z.; Ye, R. Ultrasensitive, Fast-Responsive, Directional Airflow Sensing by Bioinspired Suspended Graphene Fibers. *Nano Letters* **2023**, *23*, 597-605.

(324) Parcell, J.; Aydemir, N.; Devaraj, H.; Travas-Sejdic, J.; Williams, D. E.; Aw, K. C. A novel air flow sensor from printed PEDOT micro-hairs. *Smart Materials and Structures* **2013**, *22*, 112001.

(325) Devaraj, H.; Aw, K. C.; Travas-Sejdic, J.; Sharma, R. N. Low velocity digital air flow sensor from 3D printed PEDOT:PSS micro-hair structures. *18th International Conference on Solid-State Sensors, Actuators and Microsystems* **2015**, 1097-1100.

(326) Wang, P.; Wang, M.; Zhu, J.; Wang, Y.; Gao, J.; Gao, C.; Gao, Q. Surface engineering via self-assembly on PEDOT: PSS fibers: Biomimetic fluff-like morphology and sensing application. *Chemical Engineering Journal* **2021**, *425*, 131551.

(327) Gao, Q.; Wang, Y.; Wang, P.; Shen, M.; Li, T.; Gao, C.; Zhu, J. Highly Stretchable, Conductive and Long-Term Stable PEDOT:PSS Fibers with Surface Arrays for Wearable Sensors. *Advanced Engineering Materials* **2022**, *24*, 2101448.

(328) Song, Y.; Chen, L.; Yang, Q.; Liu, G.; Yu, Q.; Xie, X.; Chen, C.; Liu, J.; Chao, G.; Chen, X.; Chang, M.-W. Graphene-Based Flexible Sensors for Respiratory and Airflow Monitoring. *ACS Applied Nano Materials* **2023**, *6*, 8937-8944.

(329) Li, W.; Lefferts, M. J.; Wang, Y.; Lister, A. M.; Forssberg, A.; Chen, R.; Wang, L.; Castell, M. R. Chemiresistive Polymer Percolation Network Gas Sensor Created with a Nanosphere Template. *Advanced Materials Interfaces* **2023**, *10*, 2202042.

(330) Patra, A.; Wijsboom, Y. H.; Zade, S. S.; Li, M.; Sheynin, Y.; Leitus, G.; Bendikov, M. Poly(3,4-ethylenedioxyselenophene). *Journal of the American Chemical Society* **2008**, *130*, 6734-6736.

(331) Lepeltier, M.; Hiltz, J.; Lockwood, T.; Belanger-Gariepy, F.; Perepichka, D. F. Towards crystal engineering of solid-state polymerization in dibromothiophenes. *Journal of Materials Chemistry* **2009**, *19*, 5167-5174.

(332) Wijsboom, Y. H.; Patra, A.; Zade, S. S.; Sheynin, Y.; Li, M.; Shimon, L. J. W.; Bendikov, M. Controlling Rigidity and Planarity in Conjugated Polymers: Poly(3,4-ethylenedithioselenophene). *Angewandte Chemie International Edition* **2009**, *48*, 5443-5447.

(333) Patra, A.; Wijsboom, Y. H.; Leitus, G.; Bendikov, M. Tuning the Band Gap of Low-Band-Gap Polyselenophenes and Polythiophenes: The Effect of the Heteroatom. *Chemistry of Materials* **2011**, *23*, 896-906.

(334) Chen, S.; Lu, B.; Duan, X.; Xu, J. Systematic study on chemical oxidative and solid-state polymerization of poly(3,4-ethylenedithiathiophene). *Journal of Polymer Science Part A: Polymer Chemistry* **2012**, *50*, 1967-1978.

(335) Pati, P. B.; Zade, S. S. Selective bromination of 2,5-bis(2-thienyl)pyrroles and solid-state polymerization through the β-carbon of pyrrole. *RSC Advances* **2014**, *4*, 17022-17027.

(336) Luo, Q.; Peng, K.; Zhang, J.; Xia, J. Synthesis of Metal-Containing Poly(thiophene methines) via Solid- and Melt-State Polymerization and Their Related Applications as Highly Sensitive $Ni^{2+}$ Chemosensors. *Organometallics* **2019**, *38*, 647-653.

(337) He, G.; Lu, Q.; Xu, F.; Zhang, D.; Li, Y.; Xia, J. Facile synthesis of poly(BODIPY)s via solid state polymerization and application in temperature sensor. *Polymer* **2022**, *241*, 124514.

(338) Koh, J. K.; Kim, J.; Kim, B.; Kim, J. H.; Kim, E. Highly Efficient, Iodine-Free Dye-Sensitized Solar Cells with Solid-State Synthesis of Conducting Polymers. *Advanced Materials* **2011**, *23*, 1641-1646.

(339) Kim, B.; Koh, J. K.; Kim, J.; Chi, W. S.; Kim, J. H.; Kim, E. Room Temperature Solid-State Synthesis of a Conductive Polymer for Applications in Stable $I_2$-Free Dye-Sensitized Solar Cells. *ChemSusChem* **2012**, *5*, 2173-2180.

(340) Yin, X.; Wu, F.; Fu, N.; Han, J.; Chen, D.; Xu, P.; He, M.; Lin, Y. Facile Synthesis of Poly(3,4-ethylenedioxythiophene) Film via Solid-State Polymerization as High-Performance Pt-Free Counter Electrodes for Plastic Dye-Sensitized Solar Cells. *ACS Applied Materials & Interfaces* **2013**, *5*, 8423-8429.

(341) Bhargav, R.; Bhardwaj, D.; Shahjad; Patra, A.; Chand, S. Poly(Styrene Sulfonate) Free Poly(3,4-Ethylenedioxythiophene) as a Robust and Solution-Processable Hole Transport Layer for Organic Solar Cells. *ChemistrySelect* **2016**, *1*, 1347-1352.

(342) Jiang, X.; Yu, Z.; Zhang, Y.; Lai, J.; Li, J.; Gurzadyan, G. G.; Yang, X.; Sun, L. High-Performance Regular Perovskite Solar Cells Employing Low-Cost Poly(ethylene-dioxythiophene) as a Hole-Transporting Material. *Scientific Reports* **2017**, *7*, 42564.

(343) Wu, F.; Xu, Z.; Wang, Y.; Wang, M. Electromagnetic interference shielding properties of solid-state polymerization conducting polymer. *RSC Advances* **2014**, *4*, 38797-38803.

(344) Wu, F.; Sun, M.; Jiang, W.; Zhang, K.; Xie, A.; Wang, Y.; Wang, M. A self-assembly method for the fabrication of a three-dimensional (3D) polypyrrole (PPy)/poly(3,4-ethylenedioxythiophene) (PEDOT) hybrid composite with excellent absorption performance against electromagnetic pollution. *Journal of Materials Chemistry C* **2016**, *4*, 82-88.

(345) Ding, B.; Chang, Z.; Wang, J.; Dou, H.; Zhang, X. An in situ confinement strategy to porous poly(3,4-ethylenedioxythiophene)/sulfur composites for lithium–sulfur batteries. *RSC Advances* **2016**, *6*, 47858-47863.

(346) McGraw, M.; Kolla, P.; Yao, B.; Cook, R.; Quiao, Q.; Wu, J.; Smirnova, A. One-step solid-state in-situ thermal polymerization of silicon-PEDOT nanocomposites for the application in lithium-ion battery anodes. *Polymer* **2016**, *99*, 488-495.

(347) Gao, X.; Dong, B.; Chen, S.; Chen, B.; Xiao, X.; Zhou, J.; Su, X.; Zou, D. Facile Preparation of Poly(3,4-ethylenedioxythiophene)/$MnO_2$ Composite Electrodes for Efficient Supercapacitors. *ChemElectroChem* **2016**, *3*, 1746-1752.

(348) Yu, X.; Su, X.; Yan, K.; Hu, H.; Peng, M.; Cai, X.; Zou, D. Stretchable, Conductive, and Stable PEDOT-Modified Textiles through a Novel In Situ Polymerization Process for Stretchable Supercapacitors. *Advanced Materials Technologies* **2016**, *1*, 1600009.

(349) Yan, B.; Matsushita, S.; Akagi, K. Aligned carbon and graphite fibers prepared from poly(3,4-ethylenedioxythiophene) single crystals synthesized by solid-state polymerization and their supercapacitor performance. *Journal of Materials Chemistry C* **2017**, *5*, 3823-3829.

(350) Ding, L.; Dai, Z.; Xiao, L.; Hong, H.; Wei, J.; Li, Y.; Hao, N.; Wang, K. Mass-produced flexible Br doped PEDOT modified carbon paper electrodes for constructing mercury ion photoelectrochemical sensor. *Sensors and Actuators B: Chemical* **2021**, *339*, 129871.

(351) Ngoensawat, U.; Pisuchpen, T.; Sritana-anant, Y.; Rodthongkum, N.; Hoven, V. P. Conductive electrospun composite fibers based on solid-state polymerized Poly(3,4-ethylenedioxythiophene) for simultaneous electrochemical detection of metal ions. *Talanta* **2022**, *241*, 123253.

(352) Gulprasertrat, N.; Chapromma, J.; Aree, T.; Sritana-anant, Y. Synthesis of functionalizable derivatives of 3,4-ethylenedioxythiophene and their solid-state polymerizations. *Journal of Applied Polymer Science* **2015**, *132*, 42233.

# Appendix

As Sigma-Aldrich can only provide limited information about dodecylbenzenesulfonic acid (DBSA) doped poly(3,4-ethylenedioxythiophene) (PEDOT) nanoparticles used in this thesis, experiments for material characterisation were conducted to further understand the particle size and morphology of these purchased nanoparticles.

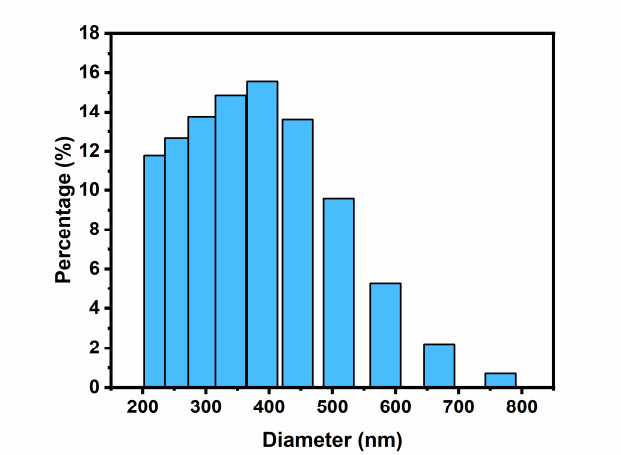



**Figure A1.** Particle size distribution of the PEDOT nanoparticles purchased from Sigma-Aldrich. The data obtained from the DLS measurement was taken by Liwei Dai and then further analysed by the author of this thesis.

First, a Horiba Partica LA-960 particle size distribution analyser with a measurement range from 10 nm to 5000 μm was used to analyse the particle size and size distribution of PEDOT nanoparticles. The dynamic light scattering (DLS) technique is applied in this analyser. The wavelength of the light source is 650 nm, and the measured particles are assumed to be spheres. During the measurement, PEDOT nanoparticles were dispersed in deionised water (refractive index: 1.33). A refractive index of 1.45 for PEDOT, obtained from the literature,[1] was applied to match the wavelength of the light source. The measurement was conducted at 25 °C by Liwei Dai, while further analysis was carried out by the author of this thesis. As shown in Figure A1,

the PEDOT nanoparticles purchased from Sigma-Aldrich exhibit a wide size distribution ranging from 226 to 766 nm. This range should be more informative than the vague value of particle diameter (around 400 nm) given by the supplier.

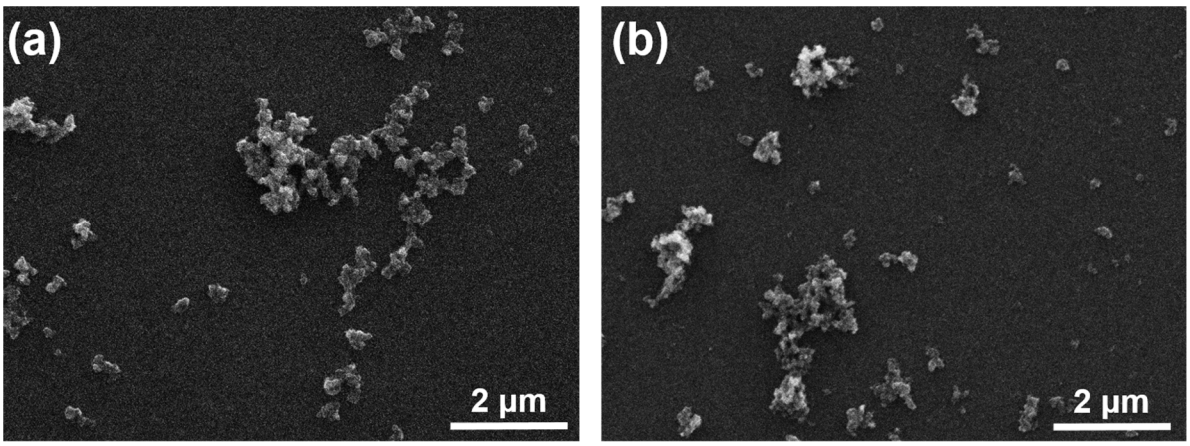



**Figure A2.** SEM images of PEDOT nanoparticles on ITO glass slides (a) before and (b) after the 24-hour THF bath. Images taken by Yu Wang.

Another method based on scanning electron microscopy (SEM) was attempted to double-check the size distribution. This method provides two-dimensional images of nanoparticles, and these images can be used to produce number-based size distributions. Also, these images can directly reflect the morphologies of nanoparticles. Samples for SEM were prepared via simple dip-coating. Clean indium tin oxide (ITO) coated glass slides (Sigma-Aldrich) were quickly extracted from the diluted PEDOT dispersion (0.02 wt% in water) used in Chapter 6, and they were then dried at ambient conditions. These samples were affixed onto a specimen stub to secure them in place. The SEM images were taken by Yu Wang using a Zeiss Merlin scanning electron microscope at an accelerating voltage of 12 kV. Similar to reported studies on PEDOT nanoparticles,[2-6] non-spherical nanoparticles and their aggregates are observed in Figure A2a. The poorly defined morphology of the purchased PEDOT nanoparticles should be related to the conditions of polymerisation. Some previous studies have demonstrated that

better defined morphologies of spherical shape can be achieved through suitable surfactant-oxidant systems,[2] ideal stabilisers,[3] and bi-oxidant systems.[4,6] It should be noted that the morphology of the purchased PEDOT nanoparticles limits the measurement method based on SEM. The particle aggregation makes it difficult to measure the size of each particle in the aggregates, and various diameters of these non-spherical nanoparticles can be measured through different directions.

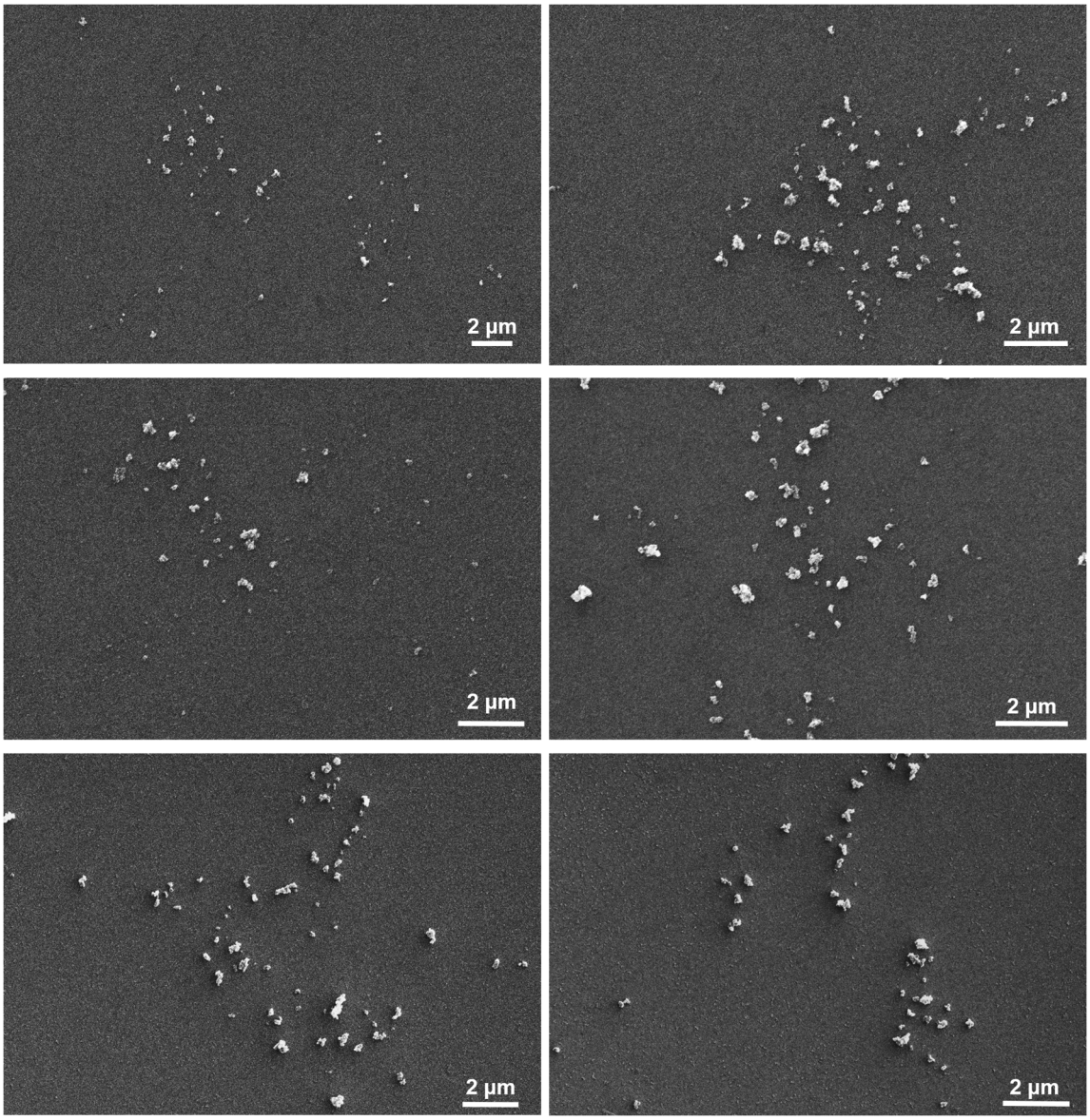



**Figure A3.** SEM images of PEDOT nanoparticles on ITO glass slides after the removal of PS nanospheres. Images taken by Yu Wang.

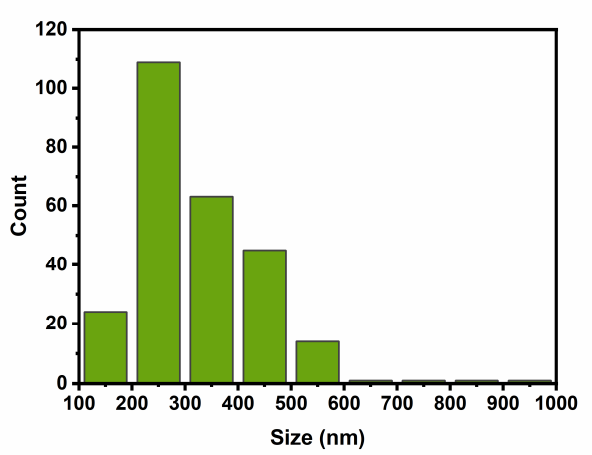



**Figure A4.** Particle size distribution of the PEDOT nanoparticles purchased from Sigma-Aldrich. This distribution was obtained based on the SEM images taken by Yu Wang (Figure A3). The particle sizes were measured by the author of this thesis using the software ImageJ.

Although it is impossible to tune the shape of purchased PEDOT nanoparticles, attempts can be made to reduce their possibility of aggregation as much as possible. According to the morphology study in Chapter 6 (Figure 6.2), fewer PEDOT nanoparticles aggregate at lower weight percentages of PEDOT possibly owing to the blocking effect of polystyrene (PS) nanospheres. Instead of the diluted PEDOT dispersion (0.02 wt% in water), thus, the sample preparation for SEM was updated using the mixture dispersion containing 0.002 wt% of PEDOT nanoparticles and 0.018 wt% PS nanospheres in water. Tetrahydrofuran (THF) was then used to dissolve the PS nanospheres, leaving the PEDOT nanoparticles on the substrate. After a 24-hour THF bath, the sample was carefully washed with THF and then dried at ambient conditions. For the sample without the introduction of PS (Figure A2a), no obvious changes in its morphology were observed after the THF treatment (Figure A2b), suggesting that THF has no obvious impacts on the PEDOT nanoparticles. After the removal of PS nanospheres, six SEM images of the sample prepared via the updated method (Figure A3) were randomly taken by Yu Wang using the Zeiss Merlin scanning electron microscope at an accelerating voltage of 12 kV. Then, the particle size was analysed by the author of this thesis using the software

ImageJ. As shown in Figure A4, the majority of the PEDOT nanoparticles exhibit a wide distribution from 150 to 550 nm. Trace portions over 600 nm are observed, possibly due to a small amount of particle aggregates.

To sum up, two methods based on DLS and SEM were used to measure the size distribution of the PEDOT nanoparticles purchased from Sigma-Aldrich. Both of these methods indicate that these nanoparticles exhibit wide ranges of size. It should be noted that larger sizes were obtained via the DLS method. According to the literature,[7] this could be attributed to potential factors, such as the assumption that measured particles are spherical, the possible aggregation of measured particles, and the difference between the hydrodynamic diameter and the imaged size of each measured particle. Although the DLS method can quickly estimate the size distribution, SEM images taken after the removal of PS nanospheres can better reflect both the size distribution and the morphology of the purchased PEDOT nanoparticles. Therefore, results obtained via the SEM method have been used to describe these nanoparticles used in this thesis. Rather than the spherical particles as expected, these PEDOT nanoparticles purchased from Sigma-Aldrich exhibit poorly defined morphologies. Their estimated mean size is 322 nm, and the standard deviation is 116 nm.

**References**

(1) Hoppe, H.; Sariciftci, N. S.; Meissner, D. Optical constants of conjugated polymer/fullerene based bulk-heterojunction organic solar cells. *Molecular Crystals and Liquid Crystals* **2002**, *385*, 113-119.

(2) Oh, S.-G.; Im, S.-S. Electroconductive polymer nanoparticles preparation and characterization of PANI and PEDOT nanoparticles. *Current Applied Physics* **2002**, *2*, 273-277.

(3) Mumtaz, M.; de Cuendias, A.; Putaux, J.-L.; Cloutet, E.; Cramail, H. Synthesis of PEDOT Nanoparticles and Vesicles by Dispersion Polymerisation in Alcoholic Media. *Macromolecular Rapid Communications* **2006**, *27*, 1446-1453.

(4) Wu, C.-H.; Don, T.-M.; Chiu, W.-Y. Characterization and conversion determination of stable PEDOT latex nanoparticles synthesized by emulsion polymerisation. *Polymer* **2011**, *52*, 1375-1384.

(5) Zhang, Y.; Liu, S.; Wang, L.; Luo, Y.; Tian, J.; Asiri, A. M.; Al-Youbi, A. O.; Sun, X. Novel Use of Poly(3,4-ethylenedioxythiophene) Nanoparticles for Fluorescent Nucleic Acid Detection. *ACS Combinatorial Science* **2012**, *14*, 191-196.

(6) Culebras, M.; Serrano-Claumarchirant, J. F.; Sanchis, M. J.; Landfester, K.; Cantarero, A.; Gómez, C. M.; Muñoz-Espí, R. Conducting PEDOT Nanoparticles: Controlling Colloidal Stability and Electrical Properties. *The Journal of Physical Chemistry C* **2018**, *122*, 19197-19203.

(7) Linkov, P.; Artemyev, M.; Efimov, A. E.; Nabiev, I. Comparative advantages and limitations of the basic metrology methods applied to the characterization of nanomaterials. *Nanoscale* **2013**, *5*, 8781-8798.